

Study of Magneto-dielectric property in Polymer nanocomposite system

Thesis Submitted For the Award of the Degree of

DOCTOR OF PHILOSOPHY

in

Physics

By

Simrandeep Kour

(11919276)

Dr. Rupam Mukherjee (23644)

Department of Physics (Assistant Professor)



L OVELY
P ROFESSIONAL
U NIVERSITY

Transforming Education Transforming India

**LOVELY PROFESSIONAL UNIVERSITY,
PUNJAB**

2023

*Dedicated to my loving parents, Mr. Kuldeep
Singh and Mrs. Manmeet Kour*

DECLARATION

I, hereby declare that the presented work in the thesis entitled "**Study of Magneto-dielectric property in Polymer nanocomposite system**" in fulfillment of the degree of **Doctor of Philosophy (Ph.D.)** is the outcome of the research work carried out by me under the supervision **Dr. Rupam Mukherjee**, working as Assistant Professor, in the Department of Physics, School of Chemical Engineering and Physical Sciences of Lovely Professional University, Punjab, India. In keeping with the general practice of reporting scientific observations, due to acknowledgments have been made whenever work described here has been based on findings of other investigator. This work has not been submitted in part or full to any other University or Institution for the award of any degree.

Simrandeep Kour

Reg. No: 11919276

Department of Physics

School of Chemical Engineering and Physical Sciences

Lovely Professional University

Jalandhar-Delhi, G.T. Road (NH-1), Phagwara

Punjab (INDIA)-144411

Date:



CERTIFICATE


This is to certify that the work reported in the Ph.D. thesis entitled "**Study of Magneto-dielectric property in Polymer nanocomposite system**" submitted in fulfillment of the requirement for the reward of degree of **Doctor of Philosophy (Ph.D.)** in the Department of Physics, School of Chemical Engineering and Physical Sciences of Lovely Professional University, is a research work carried out by **Ms. Simrandeep Kour**, (11919276); is a bonafide record of her original work carried out under my supervision and that no part of the thesis has been submitted for any other degree, diploma or equivalent course.

Dr. Rupam Mukherjee
(Supervisor)

Assistant Professor
Department of Physics
School of Chemical Engineering and Physical Sciences
Lovely Professional University
Jalandhar-Delhi, G.T. Road (NH-1), Phagwara
Punjab (INDIA)-144411



Date:


29/11/2023

Acknowledgements

I thank the almighty God for bestowing me with the blessing of being a learner and keeping me a knowledge seeker. May this little knowledge lead me and those who are directly or indirectly associated with me on the righteous path, here and hereafter.

I cordially express my profound regards and gratitude to my research supervisor Dr. Rupam Mukherjee, who paid immense attention and guided me to overcome my delusions and hurdles. His expert comments and suggestions made this work meaningful.

I am very much obliged to all my mentors and would like to express my love and gratitude, especially to my fiance Dr. Harsimran Singh for his affection and constant motivation.

I express my sincere thanks to the head of the department (HOD) Dr. Kailash C. Juglan and all other faculty members of the Physics Department for their help and support during this period. I would like to show my appreciation and gratitude to the respected panel members, Dr. Naresh Pal Singh Saini, Dr. Mukesh Kumar, and Dr. A.K. Srivastava, who helped me to shape my research objectives by providing their insightful and knowledgeable suggestions. My special thanks to all the research scholars, members of the technical and non-technical/non-teaching staff especially Nitin Kumar Yadav and Ramesh Kumar of the Department of Physics, Manoj Kumar of the Department of the Chemistry from the School of Chemical Engineering and Physical Sciences, Davinder Kumar of the School of Agriculture for their support and kind cooperation. Moreover, sincere thanks to all my dearest friends, Nitish Rajput, Hamnesh Mahajan, Ankur Nath, Manisha Thakur, and Vikrant Sharma who have uplifted and motivated me in and out in all possible ways and I would take this opportunity to thank them wholeheartedly. I consider it an appropriate occasion to record my deep sense of affection for my well-wishers Shruti Bakshi, Kiranjot Kour, and Anuj Garg who uplifted my spirits and eventually paved the path to my success.

Finally and most importantly, I would like to thank my parents who are always there for me and without them this piece of work was impossible. I shall always be indebted to them for their unstinted support, be it financially, morally, or inspirationally. May the Almighty God give them a happy life and bless them with good health.

Simrandeep Kour, (11919276)

PAPERS PUBLISHED

1. **Simrandeep Kour**, Sanat Kumar Adhikari, Maheshika Palihawadana, and Rupam Mukherjee. "The Dielectric, Magnetic, and Ferroelectric Analysis of $x\text{Ni}_{0.5}\text{Co}_{0.5}\text{Fe}_2\text{O}_4:(1-x)$ PANI Multiferroic Composites." *Journal of Inorganic and Organometallic Polymers and Materials* (2023): 1-12. <https://doi.org/10.1007/s10904-023-02602-2>
 2. **Simrandeep Kour**, Hammesh Mahajan, and Rupam Mukherjee. "Influence of sintering temperature on impedance and modulus spectroscopy of nickel-substituted cobalt ferrite." *Journal of Materials Science: Materials in Electronics* 34, no. 7 (2023): 594. <https://doi.org/10.1007/s10854-023-10030-8>
 3. **Simrandeep Kour**, and Rupam Mukherjee. "Effect of TiO_2 as Filler in NaCl: Possible Applications in Ionic Storage Systems." In *Journal of Physics: Conference Series*, vol. 2267, no. 1, p. 012092. IOP Publishing, (2022). <https://doi.org/10.1088/1742-6596/2267/1/012092>
 4. **Simrandeep Kour**, Rupam Mukherjee, and Nitish Kumar. "Synthesis of $\text{Ni}_{0.5}\text{Co}_{0.5}\text{Fe}_2\text{O}_4$ Ferrite and Effect of Annealing Temperature on the Structural, Morphological and Dielectric Analysis." *ECS Transactions* 107, no. 1 (2022): 19791. <https://doi.org/10.1149/10701.19791ecst>
 5. B. Sharma, R. Sharma, **Simrandeep Kour**, M. D. Sharma, O. Amin, A. R. Maity, and R. Mukherjee. "Fractional exponents of electrical and thermal conductivity of vanadium intercalated layered 2H-NbS₂ bulk crystal." *Indian Journal of Physics* 96, no. 5 (2022): 1335-1339. <https://doi.org/10.1007/s12648-021-02045-w>
 6. Hammesh Mahajan, Shammi Kumar, Anjori Sharma, Ibrahim Mohammed, Manisha Thakur, **Simrandeep Kour**, Amarjeet Kaur, and Ajeet Kumar Srivastava. "Structural, morphological, and electrochemical investigation of $\text{Mn}_{0.3}\text{Co}_{0.2}\text{Zn}_{0.5}\text{Fe}_2\text{O}_4$ -polyaniline nanocomposite for supercapacitor application." *Journal of Materials Science: Materials in Electronics* (2022): 1-14. <https://doi.org/10.1007/s10854-022-09335-x>
 7. **Simrandeep Kour**, O. Amin, B. Sharma, M. Kalyan, N. Kumari, R. Sharma, and R. Mukherjee. "Frequency dependent conductivity in vanadium intercalated MnPSe_3 bulk single crystal." *Journal of Emerging Technologies and Innovative Research* 6 (2019): 738-43.
-

ORAL AND POSTER PRESENTATIONS

1. **Simrandeep Kour**, presented a paper titled Synthesis of $\text{Ni}_{0.5}\text{Co}_{0.5}\text{Fe}_2\text{O}_4$ Ferrite and Effect of Annealing Temperature on the Structural, Morphological, and Dielectric Analysis, at the International Conference on Technologies for Smart Green Connected Societies (ICTSGS-1), 29-30 November 2021 conference led by Yamagata University Japan, Sponsored by ACS Publications and ECS Partners. (**Poster Presentation**)
2. **Simrandeep Kour**, presented a paper titled Effect of TiO_2 as Filler in NaCl: Possible Applications in Ionic Storage Systems, International Conference on “Recent Advances in Fundamental and Applied Sciences” (RAFAS-2021), 25-26 June 2021, Lovely Professional University, Punjab. (**Oral Presentation**)

AWARDS

- **ACS Best Poster Presentation Award**, (Simrandeep Kour, Lovely Professional University, India), on paper titled Synthesis of $\text{Ni}_{0.5}\text{Co}_{0.5}\text{Fe}_2\text{O}_4$ Ferrite and Effect of Annealing Temperature on the Structural, Morphological, and Dielectric Analysis, at the International Conference on Technologies for Smart Green Connected Societies (ICTSGS-1), 29-30 November 2021 conference led by Yamagata University Japan.

WORKSHOPS

1. Successfully completed **Manuscript Writing Workshop**, conducted on the 23rd and 24th of April in the year 2022, sponsored by Boxberg and SPAST Foundation, Hyderabad, India.
2. Participated in **XRD for Research and Orthogonal Data Analysis Workshop** from 6-7 July 2021, proudly brought to you by Malvern Panalytical and Indian Institute of Technology, Jammu.
3. Attended two days Online Workshop on **Material Characterization Techniques** from 20 to 22 July 2020, organized by Chitkara University Research and Innovation Network (CURIN) Chitkara University, Punjab.

SHORT COURSE

- Participated in the One Week Short Term Course on “**Recent Trends in Advanced Materials and Devices**” organized by the Department of Physics and Department of Electronics & Communication Engineering, Dr. B R Ambedkar National Institute of Technology Jalandhar held during September 21, 2020, to September 25, 2020.
-

Contents

Acknowledgements

Contents

List of Figures

Abstract	1
1 Introduction	3
1.1 Importance of Energy Storage in 21 st Century	3
1.2 Importance of the Dielectric Constant	5
1.2.1 Dielectric Polymer Composites	11
1.3 Study of Magneto-dielectrics: single-phase and heterogeneous systems	12
1.3.1 Single-phase and heterogeneous systems	15
1.4 Multiferroic: A Unique and Novel Property	17
1.4.1 Magneto-Electric coupling	18
1.5 Composites and its matrices: Hybrid Composites	19
1.5.1 Matrix of Polymer	21
1.5.2 Reinforcement: Nanoparticles as Reinforcement	24
1.5.3 Magnetic Nanoparticles	25
1.5.3.1 Types of Magnetic Semiconductor Nanoparticles	25
1.5.4 Hybrid Nanocomposite: Polymer matrix based material system	32
1.6 Percolation phenomenon: Percolation Threshold in composites	34
2 Review of Literature, Research Gaps, and Research Objectives	36
2.1 Literature Review	36
2.2 Research Gaps	50
2.3 Research Objectives	52
3 Materials and Methodology	53
3.1 Materials	53
3.1.1 Titanium dioxide (TiO ₂)	54

3.1.2	Sodium Chloride (NaCl)	55
3.1.3	Nickel Cobalt Ferrite (NiCoFe ₂ O ₄)	56
3.1.4	Polyaniline (PANI)	57
3.2	Methodology	59
3.2.1	Synthesis of Spinel ferrite	59
3.2.1.1	Sol-Gel Auto Combustion Method	60
3.2.2	Sample Preparation NiCoFe ₂ O ₄ (NCF)	61
3.2.3	Synthesis of Polymer (Polyaniline)	62
3.2.4	Sample Preparation Polyaniline (PANI) by Chemical Oxidative Polymerization (COP)	64
3.2.5	Synthesis of Spinel Ferrite (NCF)-Polyaniline (PANI) Nanocomposite	65
3.2.5.1	Physical Blending Method	66
3.2.6	Sample Preparation of Hybrid (NCF-PANI) Nanocomposite	66
4	Physiochemical Characterization Techniques of Materials	69
4.1	X-Ray Diffraction (XRD)	70
4.2	Fourier Transform Infrared Spectroscopy (FTIR)	73
4.3	X-ray Photoelectron Spectroscopy (XPS)	74
4.4	Field Emission Scanning Electron Microscopy (FESEM)	76
4.5	Energy dispersive X-ray spectroscopy (EDS)	78
4.6	High-Resolution Transmission Electron Microscopy (HRTEM)	79
4.7	Superconducting Quantum Interference Device (SQUID)	81
4.8	Impedance Spectroscopy	83
4.8.1	4 K CCR for zero Field resistivity, Dielectric, and P-E loop measurement	83
4.9	Instrumentation	85
4.9.1	Mortar and Pestle	85
4.9.2	Cold Press Die-set	85
4.9.3	KBr Press	87
5	Influence of TiO₂ as a reinforcement in a NaCl matrix	88
5.1	Introduction	89
5.2	Experimental	92
5.2.1	Titanium dioxide (TiO ₂) nanoparticles	92
5.2.2	TiO ₂ (x)NaCl nanocomposites	93
5.3	Results and Discussion	93
5.3.1	X-Ray Diffraction (XRD)	93
5.3.2	The Field Emission Scanning Electron Microscopy (FESEM)	96
5.3.3	Dielectric Analysis	97
5.3.3.1	Effective dielectric Constant vs Frequency	97
5.3.3.2	Dielectric Loss vs Frequency	99
5.3.3.3	Percolation assisted Dielectric constant	100
5.3.3.4	A.C conductivity	101
5.4	Conclusion	102

6	The Structural, Morphological, and Dielectric Analysis of Ni-Co Ferrites	104
6.1	Introduction	105
6.2	Experimental	107
6.2.1	<i>Material synthesis</i>	107
6.3	Results and Discussion	109
6.3.1	<i>Structural analysis</i>	109
6.3.2	<i>Morphological Analysis</i>	112
6.3.3	<i>Dielectric Analysis</i>	114
6.4	Conclusion	117
7	Complex impedance and electric modulus analysis of nickel-substituted cobalt ferrite	118
7.1	Introduction	119
7.2	Experimental	122
7.2.1	Synthesis of Ni-Co ferrite	123
7.3	Results and Discussion	124
7.3.1	Phase and Structural analysis	124
7.3.2	Morphological and Elemental Analysis	129
7.3.3	Complex Impedance analysis	134
7.3.4	Complex Modulus analysis	137
7.4	Conclusion	139
8	Multiferroic Magnetoelectric Coupling in hybrid nanocomposite system	140
8.1	Introduction	141
8.2	Experimental	144
8.2.1	Polyaniline (PANI) Nanoparticles	145
8.2.2	Ni _{0.5} Co _{0.5} Fe ₂ O ₄ (NCF) Nanoparticles	145
8.2.3	xNCF:(1-x)PANI Nanocomposite	147
8.3	Results and Discussion	148
8.3.1	X-Ray Diffraction (XRD) Analysis	148
8.3.2	Field Emission Scanning Electron Microscope (FESEM) and Energy Dispersive X-ray (EDAX) Analysis	150
8.3.3	Dielectric Analysis	152
8.3.4	Magnetic Analysis	155
8.3.5	Ferroelectric Analysis	158
8.4	Conclusion	160
9	Summary and Future Scope	162
	Future Scope	165

Contents

Bibliography	166
List of Publications	212

List of Figures

1.1	Applications for energy storage capacitors.	4
1.2	Illustration of the Parallel-Plate Capacitor.	6
1.3	Types of dielectric polarization, in the unpolarized state ($\vec{E} = 0$) and the polarized state ($\vec{E} > 0$)	9
1.4	Enhancement of Dielectric constant by Percolative approach.	10
1.5	Formation of Magnetodielectric effect in heterogeneous system	14
1.6	Possible cross-couplings in Multiferroics	18
1.7	Composites progressively classified according to the types of Matrix	20
1.8	Structural representation of intrinsically conductive polymers (ICPs)	23
1.9	Summary of Magnetic Semiconductor nanoparticles	26
1.10	Classification of Ferrites	28
1.11	Structure of Spinel ferrite cubic crystal.	30
1.12	classification of spinel ferrites.	31
1.13	Hybrid nanocomposite.	33
3.1	Bulk TiO ₂ in powder form.	55
3.2	NaCl from Loba Chemie in powder form.	56
3.3	Bulk Ni _{0.5} Co _{0.5} Fe ₂ O ₄ in powder form.	57
3.4	Bulk PANI (Emeraldine Base) in powder form.	58
3.5	Techniques for Spinel ferrite synthesis.	60
3.6	Schematic of Sol-gel auto-combustion for the synthesis NPs.	61
3.7	The detailed synthesis of NiCoFe ₂ O ₄ (NCF) spinel ferrites via sol-gel auto-combustion method.	62
3.8	Different routes for synthesis of PANI	63
3.9	Chemical oxidative polymerization method for preparation of polyaniline.	65
3.10	Blending method for synthesis of the hybrid nanocomposite.	67
3.11	Synthesis of xNCF:(1-x)PANI Nanocomposite via Physical blending method.	68
3.12	Fabrication of working electrode for xNCF:(1-x)PANI (x = 0.3) nanocomposite.	69
4.1	(a) Schematic representation for the generation of X-rays, and (b) concept diagram explaining the generation of K _α and K _β X-rays. (c) The complete schematic representation for the X-ray generation and diffracted rays' detection during the XRD experiment.	71
4.2	Schematic representation of FTIR spectrometer.	73

4.3	(a) Schematic illustration shows the XPS measurements' instrumental arrangement. (b) Various sample properties identification using XPS measurements.	75
4.4	(a) FESEM column showing the different components, and (b) the findings of FESEM measurements are shown pictorially.	77
4.5	(a) The schematic description for the working of the EDAX setup. (b) The graphical representation displays the interaction volume of incident electrons.	78
4.6	(a) Schematic diagram of HRTEM instrumentation showing different lens and detectors arrangement. (b) HRTEM allows for the investigation of various properties of samples, such as crystal structure, lattice defects, and composition, at a high level of resolution.	80
4.7	Quantum Design MPMS3 (SQUID) Superconducting Quantum Interference Device Magnetometer at IIT Roorkee	82
4.8	4 K CCR for zero Field resistivity, Dielectric, and P-E loop measurements at UGC-DAE CSR Kolkata	84
4.9	The agate mortar and pestle used for fine grinding of powders.	85
4.10	Cold Press Dye-set of 12 mm diameter.	86
4.11	KBr press instrument	87
5.1	(A) The XRD structure of NaCl (Halite), (B) The XRD structure of TiO ₂ (Anatase), (C) The XRD pattern of TiO ₂ (x)NaCl composite; where x (%)=50.	94
5.2	FESEM images at 700 °C (a) TiO ₂ Nanoparticles, (b) TiO ₂ (x)NaCl Nanocomposite; x (%) = 50.	97
5.3	Room temperature Dielectric constant (κ) as the function of oscillating frequencies for x concentrations of TiO ₂ (x)NaCl.	98
5.4	Room temperature Dielectric Loss as a function of oscillating frequencies for various concentrations of TiO ₂ (x)NaCl.	99
5.5	Percolation assisted Dielectric constant at 300 K.	100
5.6	Room temperature Ac conductivity vs frequency for a varying concentration of x (%) TiO ₂	101
6.1	Schematic illustration of the sol-gel auto-combustion procedure for synthesized material.	108
6.2	Structural confirmation for as-synthesized material for different annealing temperature. (a) XRD patterns of Ni _{0.5} Co _{0.5} Fe ₂ O ₄ , (b) FTIR spectra of Ni _{0.5} Co _{0.5} Fe ₂ O ₄ samples.	111
6.3	Morphological investigations for as-synthesized material for different annealing temperature. (a) FESEM image of Ni _{0.5} Co _{0.5} Fe ₂ O ₄ at 850 °C, (b) FESEM image of Ni _{0.5} Co _{0.5} Fe ₂ O ₄ at 1050 °C, (c) FESEM image of Ni _{0.5} Co _{0.5} Fe ₂ O ₄ at 1150 °C.	113
6.4	(a) EDAX spectra of Ni _{0.5} Co _{0.5} Fe ₂ O ₄ for different annealing temperature, (b) Elemental mapping images of Ni _{0.5} Co _{0.5} Fe ₂ O ₄ at 1150 °C.	114
6.5	Dielectric analysis for as-synthesized material for different annealing temperatures. (a) Dielectric permittivity vs Frequency of Ni _{0.5} Co _{0.5} Fe ₂ O ₄ , (b) Frequency-dependent AC conductivity of Ni _{0.5} Co _{0.5} Fe ₂ O ₄ samples.	116

7.1	The scheme illustrates the synthesis procedure of the Ni-Co ferrites.	124
7.2	a) The XRD of $\text{Ni}_{0.5}\text{Co}_{0.5}\text{Fe}_2\text{O}_4$ ferrite samples for all sintering temperatures, b) Density (D_x) vs sintering temperature ($^\circ\text{C}$).	124
7.3	The deconvoluted XPS spectra of a) Full scan, b) C 1s, c) O 1s, d) Fe 2p, e) Co 2p, and f) Ni 2p XPS spectrum at 1150 $^\circ\text{C}$ of ‘as synthesized’ $\text{Ni}_{0.5}\text{Co}_{0.5}\text{Fe}_2\text{O}_4$ samples	127
7.4	FESEM micrograph of $\text{Ni}_{0.5}\text{Co}_{0.5}\text{Fe}_2\text{O}_4$ samples at various sintering temperatures	129
7.5	a) EDAX spectra of $\text{Ni}_{0.5}\text{Co}_{0.5}\text{Fe}_2\text{O}_4$ samples at sintering temperatures 850 $^\circ\text{C}$ and 1150 $^\circ\text{C}$, b) Elemental mapping images of $\text{Ni}_{0.5}\text{Co}_{0.5}\text{Fe}_2\text{O}_4$ samples at 1150 $^\circ\text{C}$	131
7.6	a) TEM micrographs of $\text{Ni}_{0.5}\text{Co}_{0.5}\text{Fe}_2\text{O}_4$ nanoparticles at 1150 $^\circ\text{C}$, b) The average grain size (nm) distribution of scans, c) High-resolution TEM pictures demonstrating the arrangement of single direction-oriented planes, d) The SAED pattern suggesting the formation of a single-phase of as-prepared $\text{Ni}_{0.5}\text{Co}_{0.5}\text{Fe}_2\text{O}_4$ sample at 1150 $^\circ\text{C}$	133
7.7	a) Z' vs Frequency, b) Z'' vs Frequency, and c) Nyquist plots of $\text{Ni}_{0.5}\text{Co}_{0.5}\text{Fe}_2\text{O}_4$ samples at all sintering temperatures.	135
7.8	a) M' vs Frequency, b) M'' vs Frequency, and c) Complex Modulus plots of $\text{Ni}_{0.5}\text{Co}_{0.5}\text{Fe}_2\text{O}_4$ samples at all sintering temperatures.	138
7.9	a) Variation of Z'' and M'' versus frequency of $\text{Ni}_{0.5}\text{Co}_{0.5}\text{Fe}_2\text{O}_4$ sample sintered temperature at 1150 $^\circ\text{C}$	138
8.1	Synthesis of xNCF:(1-x)PANI Nanocomposite.	148
8.2	XRD patterns of NCF, PANI, and xNCF:(1-x)PANI nanocomposite.	149
8.3	FESEM micrographs of (a) PANI, (b) NCF, (c) xNCF:(1-x)PANI; x=0.3 nanocomposite, and (d) EDAX scan of x = 0.3 nanocomposite.	151
8.4	Dielectric analysis of xNCF:(1-x)PANI samples, (a) ϵ' vs T (K), (b) $\text{Tan}\delta$ vs T (K), (c) σ (Sm^{-1}) vs T (K), (d) Room temperature permittivity ϵ' vs Freq. (Hz) of samples.	153
8.5	Real permittivity (ϵ') vs wt. fraction of NCF (x) samples at 300 K.	154
8.6	(a) Room temperature M-H curve of xNCF:(1-x)PANI samples, (b) Magnetified view of M-H curves. Temperature-dependent M-T curves (ZFC–FCC) of (c) NCF, and (d) x= 0.3 nanocomposite.	156
8.7	P–E hysteresis loop at room temperature (a) PANI, (b) xNCF:(1-x)PANI samples, (c) Temperature-dependant P–E hysteresis loop for nanocomposite (x= 0.3), and (d) Remnant Polarization P_r vs wt. fraction of NCF (x).	159

Abstract

For a future that undoubtedly includes a trillion ubiquitous electronic devices, the field of nanotechnology provides a variety of channels for the fabrication of novel and accessible devices. Hybrid (Organic-Inorganic) nanocomposite capacitors are fascinating since they could possibly reduce the number of discrete components on printed electronic circuit boards. The installation of embedded capacitors for nano packaging applications in combination with integrated circuits marks its unique way in the nanotechnology world. The idea of forming a dielectric nanocomposite through the integration of colloidal nanoparticle fillers and polymer hosts serves well with the idea of tuning the electrical properties and being compatible to nanomanufacturing. Multiferroics, in which the possible overlapping of magnetic permeability with permittivity can yield output for magnetodielectrics and magnetoelectrics, which are currently being investigated in nanocomposite systems (polymers and transition metals). These devices go beyond basic capacitors. The main focus of this doctoral thesis is to develop such performing energy storage hybrid composites that could erase the need for external peripherals in the potential magnetic/multiferroic industries.

In the present research work, our study aims to investigate the dielectric property of insulating polyaniline (PANI) (being intrinsically conducting in nature) in the presence of varying weight fractions of ferromagnetic ferrite $\text{Ni}_{0.5}\text{Co}_{0.5}\text{Fe}_2\text{O}_4$ (NCF), which possess significant characteristics of high magneto-crystalline isotropy and high resistivity. These composites exhibit novel multiferroic properties at room temperature.

Firstly, the samples have been prepared individually in pristine form, followed by hybrid composites by employing convenient and low-cost methods such as the sol-gel auto combustion and chemical oxidative polymerization approaches. The two differently prepared samples are mentioned below.

- Synthesis of nickel cobalt spinel ferrite, $\text{Ni}_{0.5}\text{Co}_{0.5}\text{Fe}_2\text{O}_4$, prepared and sintered at varying temperatures 850 °C to 1150 °C for 4 hrs to obtain the homogeneous and single-phase nanoparticles.
- The synthesis of dedoped polyaniline in emeraldine base (EB) form using the cost-effective approach via chemical oxidative polymerization (COP), followed by the fabrication of $x\text{NCF}:(1-x)\text{PANI}$ hybrid nanocomposites at different weight fractions.

The above-prepared materials were then initially analyzed at structural (XRD, FTIR, XPS), morphological (FESEM, EDX), and elemental aspects to confirm the elements' homogeneity and purity. The vigorous investigation of dielectric and magnetic properties at low and room temperatures confirms the presence of novel multiferroicity in the as-prepared materials, resulting in the evolution of fascinating phenomena that have occurred when polymer-based multiferroic hybrid nanocomposites are taken into consideration. Further, it has deepened the urge to understand the coupling between ferroelectricity and ferromagnetism at room temperature in these synthetic heterostructures.

Hence, the thesis primarily focuses to investigate the dielectric property of insulating PANI in the presence of varying weight fractions of ferromagnetic ceramic NCF. Here $\text{Ni}_{0.5}\text{Co}_{0.5}\text{Fe}_2\text{O}_4$ (NCF) is an outstanding magnetic material possessing significant high magneto-crystalline isotropy and high resistivity characteristics. In our composite system, NCF is ferromagnetic in behavior at room temperature with a transition temperature of around 310 K, which also exhibits novel multiferroic properties at room temperature. To the extent that we are aware, these novel characteristics have not been explored in the literature yet. Moreover, the main purpose of introducing the magnetic ceramic fillers into the polymer host matrix is not well explored. This aims to increase the interaction between magnetic and dielectric particles, which can affect the charge dynamics and lead to lower charge leakage which also enhances the charge density. In the context of the above discussion, we have synthesized and characterized flexible $x\text{NCF}:(1-x)\text{PANI}$ nanocomposites, which further paves the research flow toward clean energy materials and offer efficient performance for sensing and energy storage applications.

Chapter 1

Introduction

1.1 Importance of Energy Storage in 21st Century

As per the rules set out in the Paris Agreement, carbon dioxide emissions need to decrease $\sim 45\%$ by 2030 and approach net zero by 2050, which could limit global warming to $< 1.50\text{ }^\circ\text{C}$ [1][2]. Renewable resource technologies, such as the ones based on sunlight, tides, and wind are essential for achieving these goals. However, due to the intermittent nature of renewable energy sources, there are still many barriers to their replacement of traditionally high CO₂-emitting sectors based on natural gas and coal, which still account for an immense and substantial share of energy generation. To simultaneously move towards alternatives to fossil fuels and avoid the unpredictability of clean energy sources, energy-harvesting technology, and energy storage devices must be coupled. Therefore, green technology is rapidly evolving into a vital facilitator for sustainable renewable technologies. Energy-storing technologies, such as batteries, electrochemical super-capacitors, and electrostatic capacitors, occupy a larger space in energy-harvesting technology [3][4][5][6]. These latter ones are electrical energy storage units that fall under the class of passive components, which are widely used in electronics.

Additionally, today's growing demand for compact and miniature devices had led us to pack billions of transistors into $1\text{mm} \times 1\text{mm}$ microchips, which is responsible for the functioning of nearly all modern devices from an automobile to supercomputers. Therefore, BaTiO_3 (BT), the standard ferroelectric (FE) ceramic, is employed in the annual production of over three billion and more multilayer ceramic capacitors (MLCCs) [7][8][9][10][11][12]. Additionally, non-polarized electrostatic or dielectric capacitors have an advantage over Li-ion batteries or fuel cells due to their high power density ($\sim 10^4$ - 10^5 W/kg) and faster charging/discharging characteristics ($\sim \mu\text{s}$), which are beneficial for pulse power applications and power electronics in electrical vehicles (EVs), as seen in (Figure 1.1), [4][13][14][15][16].

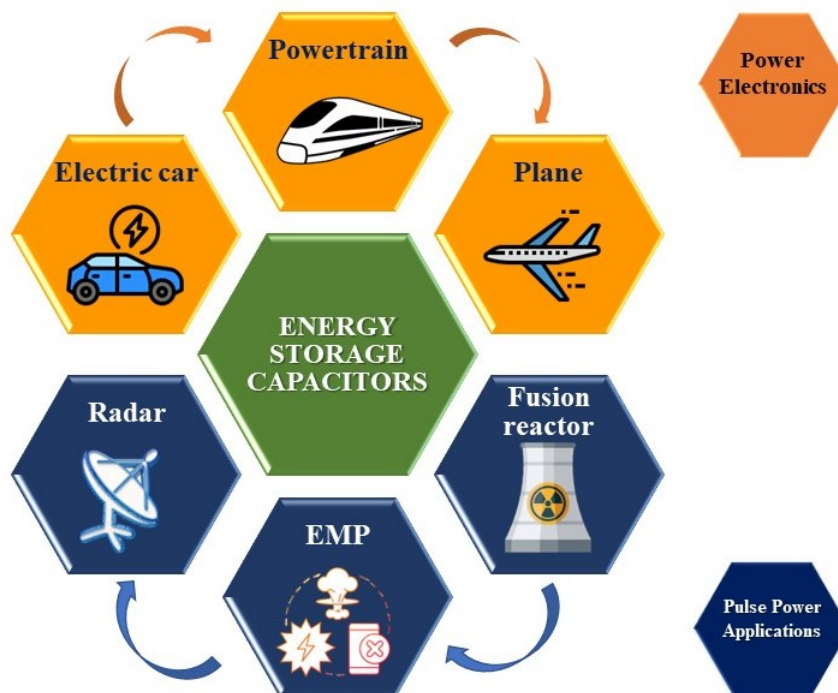


FIGURE 1.1: Applications for energy storage capacitors.

As a result, electrostatic capacitors are emerging as practical substitutes for applications involving energy storage within which high power density and high energy density could

be combined, which plays a significant role in technological requirements. For practical applications such as dielectric capacitors, some of the vital factors like resistance, stability, temperature/frequency, fatigue, lifetime reliability, manufacturing cost, and equivalent series resistance are equally essential apart from high energy density and a rapid charging-discharging rate.

One of the crucial parameters of large volumetric capacitors is the thickness, and it can prove detrimental to the whole gadget if the size is shrunk below a limiting thickness. When a capacitor's thickness is decreased, it either becomes more prone to charge leakage or shorting between electrodes, which degrades the capacitance of the capacitor for a storage device. The volumetric capacitance has been increased to 10^2 cm^3 due to the development of super-capacitors, double-layered capacitors, and other conventional methods, making it an average performer for an energy storage devices [3]. Furthermore, the electrolyte in electrolytic capacitors has a tendency to deteriorate or evaporate over time and is incompatible with AC power sources. Therefore, the other typical way to boost capacitance is to increase the material's dielectric constant by a larger amount rather than adjusting the cross-sectional area's geometry or the space between the plates. Following the parallel plate configuration (as shown in Figure 1.2), we know that the capacitance is given by Equation 1.1,

$$C = \epsilon_r \epsilon_0 \frac{A}{d} \quad (1.1)$$

Where C is the capacitance, A is the cross-sectional area between two plates, ϵ_r is the dielectric constant (relative permittivity) of the material, ϵ_0 is the dielectric permittivity in free space ($8.85 \times 10^{-12} \text{ Fm}^{-1}$), and d is the distance between the plates.

1.2 Importance of the Dielectric Constant

From the equation, it is clear that a capacitor's capacitance (C) is directly proportional to the material's dielectric constant. In general, a dielectric is a non-conductive material or

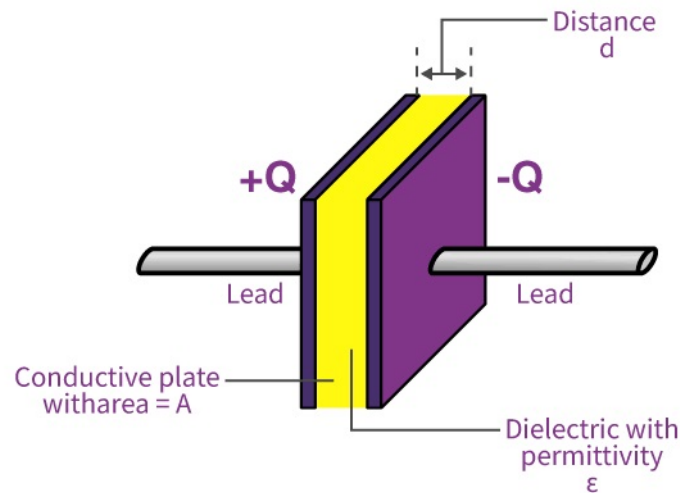
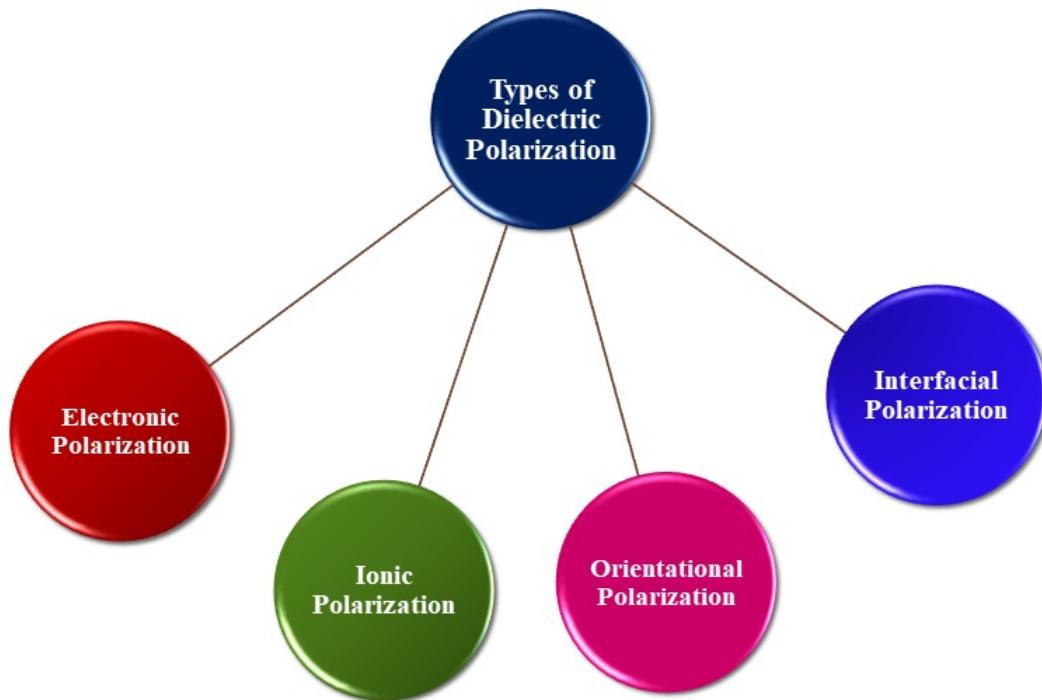


FIGURE 1.2: Illustration of the Parallel-Plate Capacitor.

substance that does not allow the flow of electrical charges easily through it. On applying an electric field, the electrons of the dielectric material become polarized, creating an opposing electric field. Applying an electric field on the dielectric leads to an increase in the condenser's capacitance, which is similar to charging the two surfaces of the dielectric that are directly close to the condenser's plates with charges of opposite signs. This buildup of unbalanced negative and positively charged plates on the surface of the dielectric and condenser causes a reduction of the initial charges q . Further, dielectric polarization (P) is caused by a little deviation of both negative and positive charges from their usual equilibrium positions. Consequently, dielectric polarization due to the electric field results in an increased condenser's capacitance. Instead, the substance is electrically neutral without the application of an electric field, and in any tiny volume of it, the centers of all positive and negative charges coincide.

Additionally, the various polarizations that can occur in dielectric materials as a result of the direction of dipoles parallel to the applied field includes, Electronic polarization or atomic polarization, Ionic polarization, Orientational polarization, and Interfacial Polarization or space-charge polarization (occurs in heterogeneous materials). The schematic

illustration of types of dielectric polarization in the unpolarized state ($\vec{E} = 0$) and the polarized state ($\vec{E} > 0$) is shown in Figure 1.3.



- **Electronic Polarization** - When an external electric field is applied, the center of positive (+) and negative (-) charges of an atom become distorted from their original positions and up to a given distance, induce a displacement in the direction of the applied electric field, as shown in Figure 1.3, While the negative charges shift in the opposite direction and form a dipole, the positive charges move in the direction of the electric field. The induced dipole is proportional to the applied electric field, $\vec{p} \propto \vec{E}$, and $\vec{p} = \alpha \vec{E}$. Here, α is called atomic polarizability.
- **Ionic Polarization** - When there is an ionic link between two ions (a cation and an anion). The minimal energy needed to break an ionic connection or threshold energy, exists in the ionic bond. If we apply the electric field less than the threshold field then the bond acts as a spring. By stretching and contracting in reaction to an applied external electric field, the ions connected to this bond fluctuate around

their equilibrium position. The center of the masses of both negative and positive charges combine to form a dipole moment, which is separated as a result of the ions being stretched out of their equilibrium. The polarization so produced is called ionic polarization.

- **Orientalional Polarization** - is a type of polarization that occurs in dielectric materials due to the alignment of polar molecules or ions in an external electric field. When a dielectric material containing polar molecules or ions is placed in an electric field, the molecules or ions tend to align themselves with the direction of the field, creating an induced electric dipole moment. This dipole moment is opposite to the applied electric field and reduces the overall electric field strength inside the material. The degree of orientational polarization depends on the strength of the electric field and the orientation of the polar molecules or ions. The time it takes for the molecules or ions to align themselves with the electric field is called the relaxation time, and it is a function of the viscosity and temperature of the dielectric material. For instance, water (H_2O) has a dipole moment of 1.85 D ('D' stands for Debye, measurement unit for dipole moment).
- **Interfacial Polarization** - For heterogeneous materials or composite materials phenomenon governing the Maxwell-Wagner-Sillars interfacial polarization or Space-charge polarization can be observed. Interfacial polarisation causes novel dielectric properties to manifest that resemble molecular relaxation processes but do not directly correlate with them physically. Interfacial polarisation can also alter the dielectric spectra of molecular relaxation processes, appearing to move their frequency positions and produce broadening effects. [17]. In general, interfacial polarization arises at significantly lower frequencies. The essential concept underlying the phenomenon of interfacial polarization has to do with the variation in the dielectric loss that happens across an internal interface that separates the locally different dielectric phases of a composite material.

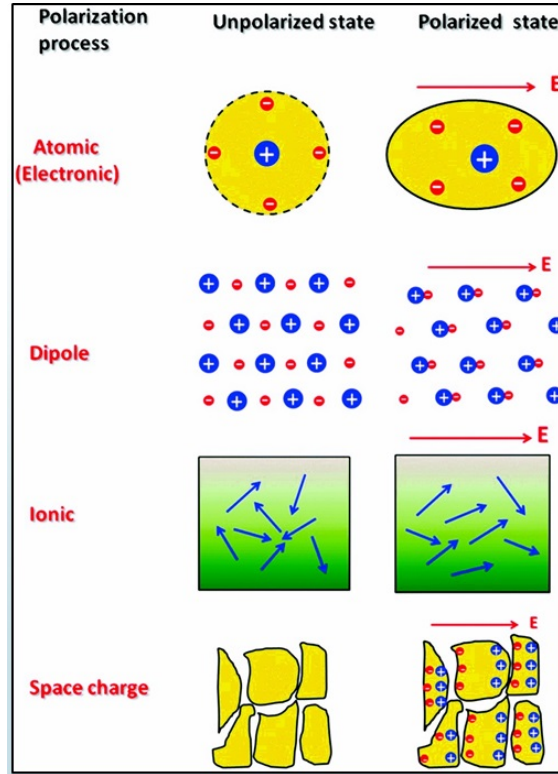


FIGURE 1.3: Types of dielectric polarization, in the unpolarized state ($\vec{E} = 0$) and the polarized state ($\vec{E} > 0$) [18].

Unfortunately, only a few ceramics and polymers having a high dielectric constant fulfill the requirement in high-energy-density capacitors (known as super- or ultracapacitors). The importance of the interface between the ceramic phase and the polymer phase has been extensively studied theoretically since this interface is crucial in determining how well dielectric materials perform. These models additionally include the "interphase" with the filler and polymer phases as separate phases. To investigate the complicated permittivity of the composite system, Todd et al. established the "interphase power law" model [19]. The model accounts for the volume fractions of the polymer, filler, and interface region as well as permittivity. Experimental findings have been compared with the effective permittivity estimated by the model.

Eventually, the dielectric constant of a composite system made up of a dielectric matrix and metal nanoparticles approaching the percolation threshold increased quickly

as a result of the alternative method provided by A. L. Efros (2011) for achieving high volumetric capacities [20]. In this percolative approach, there is a formation of an infinite conducting cluster approaching the threshold which results in the divergence of dielectric constant K leading to a large increase in capacitance, as seen in Figure 1.4. The divergence

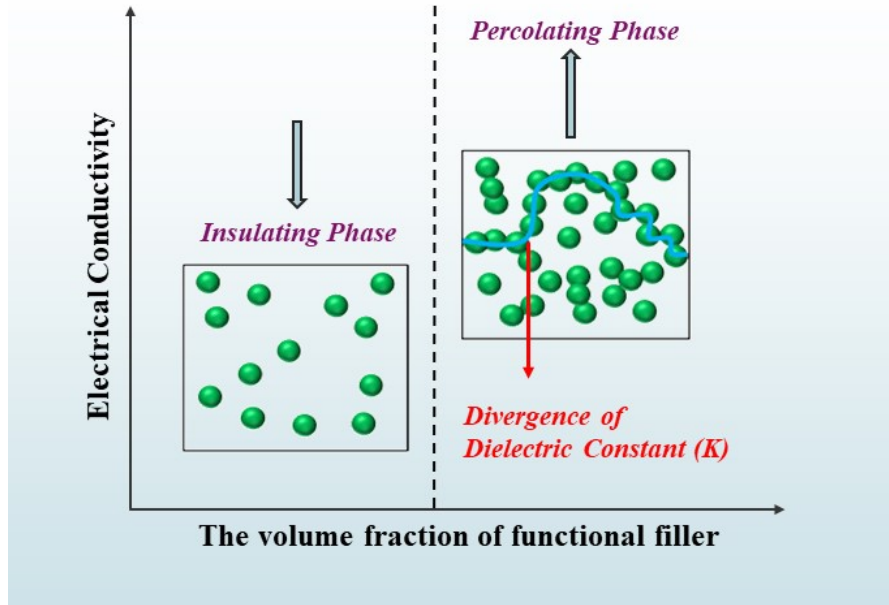


FIGURE 1.4: Enhancement of Dielectric constant by Percolative approach.

of the dielectric constant is established by introducing metallic fillers in the dielectric component system. This increase of dielectric constant K is due to the fractal geometry of metallic clusters near the threshold, which follows a power law behavior at the percolation threshold, and is given as

$$K \propto 1/(P - P_c)^\mu \quad (1.2)$$

where P represents metallic volume fraction, P_c is percolation threshold and μ represents critical exponent.

1.2.1 Dielectric Polymer Composites

In response to the growing demand for energy storage devices with high energy densities, polymer composite systems have been created that unite the ability to process and break down the field strength of polymers with the high dielectric constant of ceramic fillers. Ideally, the fillers would aid in enhancing the composite system's effective dielectric constant while maintaining polymer's high inherent breakdown strength. As studied by Tuncer et al., the investigation of the dielectric characteristics of CoFe_2O_4 nanoparticle incorporated in a matrix of poly (methyl methacrylate) nanodielectric system [21]. They revealed that the composite system's relaxation behavior at high frequencies differs from the unfilled polymer's. This phenomenon gave rise to interfacial polarization. Furthermore, it must be possible to improve the effective dielectric constant, without doing so at the expense of an unacceptable rise in energy dissipation, (i.e., dielectric loss). As a result, an extensive amount of research is being done to create better materials for polymer composites by having a deeper comprehension of the fundamental processes influencing breakdown field strength and dielectric permittivity of the composites. Therefore, since these problems are probably related to the polymer-filler interface, as a result, research aiming to gain a better physiochemical knowledge of the filler-polymer interfaces is a prime matter.

Most recent research focuses on ferroelectric metal oxide-based dielectric polymer composites that aim to increase the dielectric permittivity of $\text{Pb}(\text{Mg}_{0.33}\text{Nb}_{0.77})\text{O}_3\text{-PbTiO}_3$ (PMNT), $\text{Pb}(\text{Zr, Ti})\text{O}_3$ (PZT), and BaTiO_3 (BT). It is highly desirable to incorporate inorganic fillers with dielectric properties on a scale of several hundred to several thousand into polymers, which generally have dielectric constants below 10, in order to increase the composite's effective dielectric constant. Particularly, since the filler's permittivity is significantly higher compared to that of the polymer matrix, the majority increase in the actual dielectric constant is brought on by an increase in the standard field within the polymer matrix, with only a small amount of energy being stored in the high permittivity phase. Additionally, significant disparity in dielectric permittivity between the two phases

can result in exceedingly inhomogeneous electric fields. Ultimately, the production of a homogeneous composite is hampered by incompatibility between the hydrophilic metal oxide filler and the organophilic polymer matrix. Therefore, a key area of research in this area continues to be on modulating the inorganic filler's surface to make it compatible with the polymer matrix.

1.3 Study of Magneto-dielectrics: single-phase and heterogeneous systems

There is considerable interest in understanding new systems where the effect of magnetic fields on dielectric characteristics develops a rich flavor of physics. The phenomenon can further show exotic effects if the dielectric constant and magnetism of the material are coupled. Especially when the dielectric materials lack good insulating properties, this type of contribution grows stronger. Magnetodielectric (MD) materials are a kind of multi-purpose composite dielectrics that contain magnetic particles as fillers. Certainly, the hunt for convenient materials has been the prime focus, where ferromagnetic compounds that show an efficient magnetodielectric effect is the need, such as ϵ -Fe₂O₃, [22] double perovskites La₂CoMnO₆ thin films [23], and terbium iron garnet [24]. Modulating a material's dielectric characteristics when a magnetic field is applied has proven to be challenging both technologically and scientifically [25]. There are two primary methods for magnetically altering a material's capacitive or dielectric property,

- (a) Tuning the functioning of the interface in multilayer systems, and
- (b) Enhancing the magneto-dielectric property in materials (ferromagnetic) proximal to their ferromagnetic transitions [26][27].

Therefore, improved magnetodielectric materials can be a powerful tool to unfold various potential applications such as devising new devices including magnetic sensors, tunable

filters, spintronics, and tunable filters. Unlike materials exhibiting the magnetoelectric effect which requires strong symmetry restrictions, the magnetodielectric effect can be found in any insulating magnet. This non-requirement of symmetry actually expands the search for viable magneto-dielectrics and provides feasibility to engineer many other systems with improved material properties. Due to crystal symmetry limitations, single-phase magneto-dielectrics often have a modest magneto-dielectric effect (MDE) at room temperature, which further restricts the utilization of such material in diverse technological devices [28]. Generally, novel composites of technical significance can be developed by combining two materials with exceptional electrical characteristics. The incorporation of a second phase can synergistically enhance the desired electrical feature of the resulting composite material [29][30]. Apparently, the easiest way to produce a large MDE approximately at room temperature is to combine materials with intriguing dielectric and magnetic characteristics [31][32]. In our case, the heterogeneous composites make good insulators, with polymer as a dielectric matrix and ferrite as a magnetic filler having dielectric losses of less than 1. Below are the two primary methods that cause a large magneto-dielectric effect in composites [33][34].

- (i) Maxwell-Wagner effects in combination with magnetoresistance (MR).
- (ii) Interface coupling via strain transfer induced by a magnetic field.

Firstly, there is a diverse availability of materials for MR-related MDE. [35]. The magnetostrictive effect may further orient the spins of magnetic nanoparticles in heterogeneous systems, which will affect the polarization by redistributing charges and dipoles into the polymer matrix. Due to this, a correlation between ferroelectric/piezoelectric polarization and magnetostriction can occur, producing the observable magnetodielectric effect. However, in the latter scenario, a magnetic and an electric substance coexist in the system while adhering to the composite's principles. This is the most common way, a strain is induced in the composite's magnetostrictive phase on the application of magnetic field applied to magneto-dielectrics, as can be seen in Figure 1.5. This interface stress might

cause dielectric polarization in the corresponding component of the composite system, which will cause a significant MDE reaction [36][37]. The advantage of this mixture is the abundant availability of conducting ferromagnetic materials with large magnetic moments. This component can be incorporated into a matrix of dielectric material in tiny volume fractions to achieve a greater magnetodielectric effect.

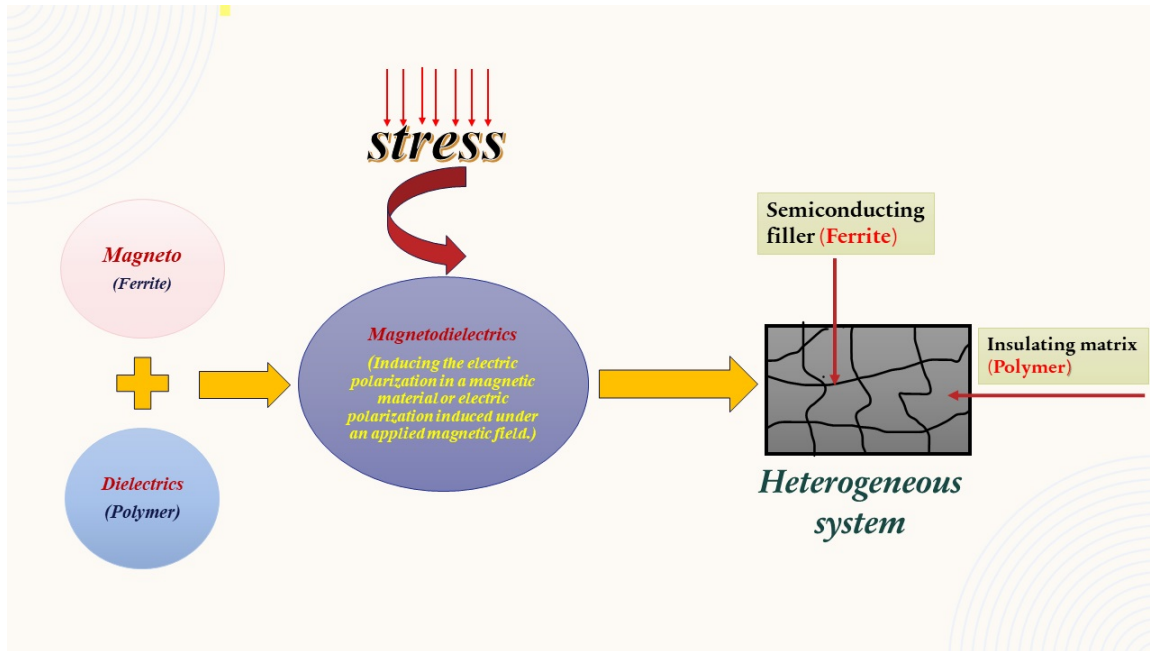


FIGURE 1.5: Formation of Magnetodielectric effect in heterogeneous system

Here, one should be extra cautious in interpreting magneto-capacitive signals as an indicator of magneto-dielectric effects. Since a magnetic field helps to orient magnetic moments in a preferred direction, the dielectric constant of conductors is indirectly changed by the field. This is known to be actual **magnetodielectric effect** and is observed in a wide range of materials. For example in a single-phase system BiMnO_3 , A site occupied by lone pair (ferroelectric) and B site has magnetic ordering. At a glance, it is difficult to believe any material exhibiting magnetodielectric effect [38][39]. Because magnetism depends on the spin degree of freedom while the dielectric property is associated with the charge degree of freedom. However, since the electrons possess both charge and spin, there are a number of mechanisms that supports spin-charge coupling. The drawback of this strategy is that achieving the magnetodielectric effect cannot only be done through

magnetoelectric coupling. The difference in magnetoresistive artifacts in between bulk and interface conductance can also lead to extrinsic magnetodielectric effects. Further, it is important to carefully distinguish between the interfacial extrinsic magnetocapacitance and the intrinsic magnetoelectric coupling. For device applications, compared to composite systems with extrinsic effects, these intrinsic systems have faster switching speeds and less dielectric loss [40][41][42].

Typically, ceramic-based materials are used to develop magneto-dielectric composites, but they lag in certain spheres. For the most part, processing at high temperatures is required for ceramic MDs. On the contrary, establishing components with the desired dimensions is challenging due to the poor machinability of ceramics. By incorporating magnetic components into dielectric polymers, polymer-based composites can be used to solve these issues. They have advantages such as low processing temperatures, a wide variety of versatility, a large dielectric breakdown field, cost-effectiveness, etc [43]. Following this, due to their synergistic and flexible characteristics, researchers explored many ways to produce polymer nanocomposites [44][43][45][46][47]. By combining various kinds of polymers with magnetodielectric oxides, several researchers have produced novel composites with appealing electrical characteristics [48][49]. In light of this context, the current work investigates the feasibility of creating thin pellets of a functional gradient polymer nanocomposite for dielectric analysis.

1.3.1 Single-phase and heterogeneous systems

In our work we would like to study the magnetodielectric effect on both single phase and a better heterogeneous composite systems where enhancement of dielectric permittivity by many folds of magnitude can be observed. So far scientists from all over the world have found strong magnetoelectric coupling in many interesting systems such as TeCuO_3 , $\text{Ni}_3\text{V}_2\text{O}_8$, BaTiO_3 , BiFeO_3 which belongs to single phase and correspondingly in heterogeneous or multi-phase systems such as CCTO/RuO_2 , $\text{LaFeO}_3/\text{PVDF}$, $\text{NiNbO}_3/\text{BaTiO}_3$.

Nath et al. has shown that the surface modified LaFeO_3 nanoparticles in matrix of PVDF polymer matrix has improved the dielectric constant and lowers the dielectric loss, thus paving a perfect way for the development of memory storage device. Grain boundary effect also known as Maxwell-Wagner effect is held responsible for the increase of dielectric properties in this well-dispersed medium. The positive change in the dielectric constant is also found to be proportional to the magnetic field intensity. Similarly in a single phase BiFeO_3 (BFO) nanoceramics (Kumari et al.), confirmed that the system display a multi-ferroic behavior as analyzed from magnetoelectric response. From magnetic measurements bulk BiFeO_3 shows antiferromagnetic behavior which mainly arises due to Dzyaloshinskii-Moriya exchange interaction. Along with the magnetic ordering, ferroelectric behavior appears in BiFeO_3 is due to Bi 6p and O 2p orbital hybridization, thus building a strong spin-charge coupling within BFO system. In another interesting system where MnFe_2O_4 (MFO) and Fe_2O_3 (FO) are independently dispersed in an organic long chain molecular matrix and magnetoelectric study was performed by Lawes et al. Experimentally magnetodielectric parameter (MD) is calculated from the following Equation 1.3,

$$MD = [\epsilon'(H) - \epsilon'(0)]/\epsilon'(0) \quad (1.3)$$

where $\epsilon'(H)$ is the real permittivity when the magnetic field is applied and $\epsilon'(0)$ is the permittivity in zero fields. Chatterjee et al. have further reported a large negative magnetodielectric effect of around 52.2 % in the NiO nanoparticle system which is mainly attributed to electron hopping between Ni^{2+} and Ni^{3+} sites leading to the formation of space charge polarization at the interface of NiO nanoparticles. The high magnitude is mainly due to strong competition between the anti-ferromagnetic and ferromagnetic phases which makes the NiO system more magnetic. Much of the research on novel functional materials such as magneto-dielectric, multiferroics, and magneto-electric attracts significant attention. These materials possess both ferromagnetism/ferroelectric characteristics in a single-phase or in artificially engineered composites [50]. However, at room temperature (RT) single-phase materials have weak coupling characteristics, which makes them

unstable for real-world applications [28]. To this, an alternative strategy of fabricating artificial multi-phase or heterogeneous systems helps to achieve the aim [29][30]. Hence novel heterogeneous systems can be fabricated in which individual phases are separately optimized for achieving potential multiferroic properties at room temperature and below.

1.4 Multiferroic: A Unique and Novel Property

Multiferroics are materials that combine at least two 'ferro' characteristics (ferroelastic, ferroelectric, ferromagnetic) into a single component. They are among the new smart materials that have received the most attention because of the vast potential for sensing, energy transformation, and harvesting technologies [51][52][53] due to their capacity to function across a wide variety of frequencies, fields, temperatures, etc., such functioning elements are alluring [54][55][56]. In terms of science and technology, multiferroic materials are most fascinating because they can exhibit numerous order states, which, are essential because of the order states' cross-coupling with one another. The ability to directly manipulate ferroelectric and ferromagnetic properties by applying mechanical stress from external sources is made possible by the coupling between the ferro-phases and piezoelectric qualities. The complex coupling can be seen in Figure 1.6.

- Magneto-Electric-: the interaction or cross-coupling of electric polarization and electric field-strain.
- Magneto-Dielectric-: coupling between magnetization- magnetic field- strain
- Elasto-magnetolectric-: coupling between stress-strain electric polarization- magnetization.

Thus, the coexistence of ferroelectric and ferromagnetic traits in these multiferroic materials results in the above novel combinations of properties, such as a magneto-dielectric

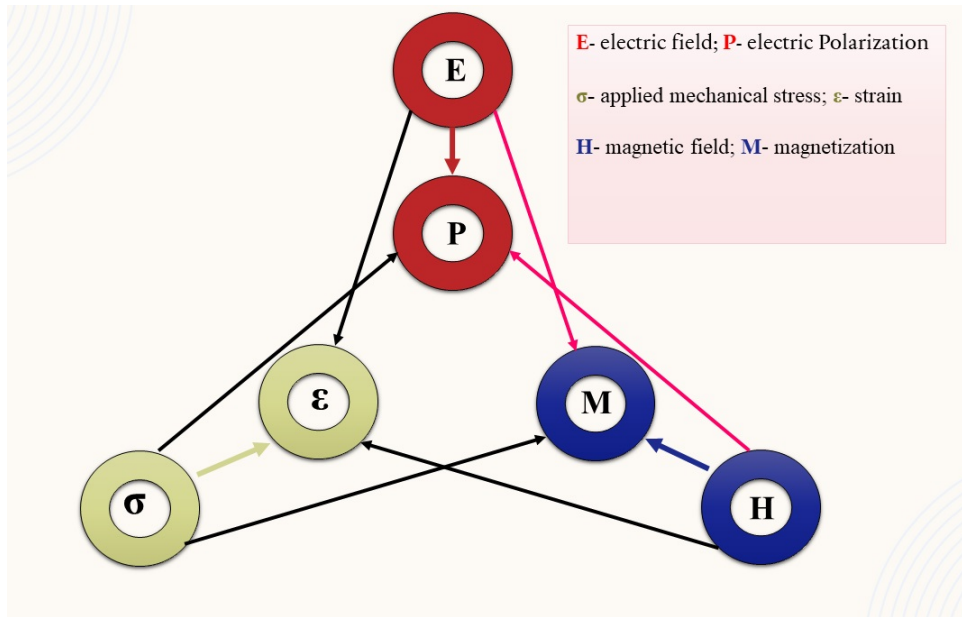


FIGURE 1.6: Possible cross-couplings in Multiferroics

effect and a magneto-electric effect, etc. Hence, the present study focuses on magneto-dielectric and magneto-electric effects, exhibited due to the coexistence of ferromagnetic and ferroelectric properties which directly corresponds to the multiferroic nature of our samples.

1.4.1 Magneto-Electric coupling

Multiferroics have a greater magnetoelectric (ME) effect than naturally occurring multiferroic materials do [54]. The solid composite multiferroics that combine magnetostrictive and piezoelectric phases as nanocomposites, generate the highest values of ME coupling [55][56]. The sintered composite consists of a densely packed blend of ferroelectric (FE) and ferromagnetic (FM) characteristics that serve as an instructive example. Due to this close contact between the grains, a piezo effect occurs when an external field-induced mechanical stress caused by a constraint on one specific composite component exerts pressure on an adjacent component.

The early 2000s saw a massive inclination towards ME composites, with the new experiments on the ME effect related to the magnetostrictive material $\text{Tb}(1-x)\text{Dy}_x\text{Fe}_2$ (Terfenol-D). Following that, a variety of composites employing the ferromagnetic phases, e.g., CFO, LaMnO_3 (LMO), and Terfenol-D, and the ferroelectric phase, BTO, polyvinylidene fluoride (PVDF), have been deeply explored over the past few years. In composite multiferroics, a piezopolymer holds the FM and FE particles together [57]. The interphase interaction is increased by the matrix's piezo effect, which also improves MEE. In contrast to solid nanocomposites, polymer multiferroics can deform without breaking, making them a practical alternative for flexible electronics. The composite frameworks open up novel possibilities for modifying the ME coupling by cautiously selecting specific phase features including connectivity, microstructure, and volume fraction. Additionally, polymer-based composites are an excellent option for achieving large ME coupling considering they are simple to fabricate and have enhanced mechanical properties [58].

Thus, a ceramic-polymer multiferroic, consisting of ferromagnetic and ferroelectric particles, is the prime focus of the current study's application of the molecular dynamics method. Both the particles and the polymer beads are regarded as molecular building blocks joined by "virtual springs," which are structural components. Given that the model allows for elastic interaction among the particles, which are also connected by electromagnetic dipole-dipole interactions, demonstrating ME coupling.

1.5 Composites and its matrices: Hybrid Composites

A remarkable genre of engineering substances, known as Composite evolved around the middle of 20th century, offering up new possibilities for modern science and technology [59]. Combining at least two materials, often with contrasting features, yields composite materials, which have a substantial ratio of strength to a weight which offers feasibility

and flexibility in the material [60]. These substances are employed to develop exceptional characteristics of corrosion-resistant, weight, rigidity, conductivity, durability, or strength. There are two distinct elements in all composite materials: a matrix (emerges as a "continuous phase"), & a reinforcement or filler (appears as a discontinuous phase and behaves like a binding agent,). In general, a substance is considered composite if it satisfies the criteria of comprising at least two physically distinct & mechanically separable elements [61]. It consists of a number of chemically distinct phases that are insoluble in one another and can be distinguished by an interface. Engineers can modify the qualities to satisfy particular demands by judiciously selecting the polymer (matrix), the ceramic (reinforcement), and the synthesis method [62]. Increasing the surface-to-volume ratio will enhance the matrix's and the reinforcement's surface area of interaction, which is responsible for the changes inside the new nanocomposite. Hence, based on material comprising the matrix, composites tend to be categorized, as shown in Figure 1.7,

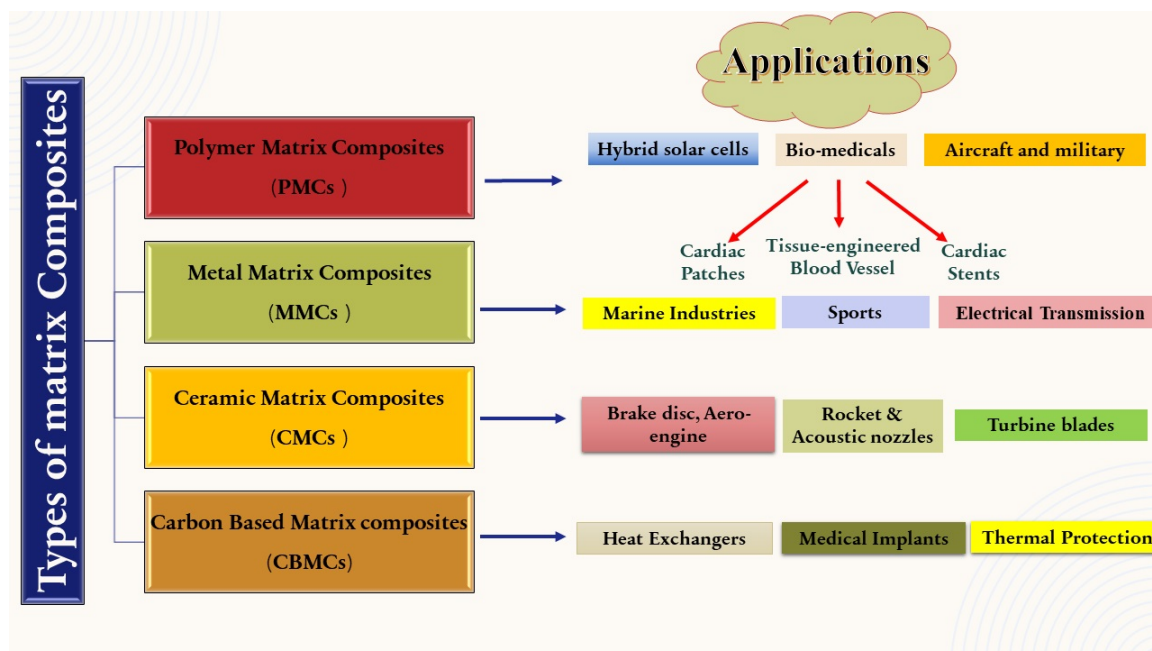


FIGURE 1.7: Composites progressively classified according to the types of Matrix

1.5.1 Matrix of Polymer

Despite the fact that any substance can serve as a composite matrix, metals, ceramics, and polymers are the most frequently used materials in this capacity. The majority of matrix materials used in composites are polymers [63]. Due to their exceptional qualities, such as adhesion, and toughness, polymer matrices (PMs) are frequently employed as a matrix for the creation of composite materials [64]. In composites, the matrix of polymer behaves (as the continuous phase) that maintains the reinforcement part in place. Additionally, the majority of deteriorating procedures (including delamination, high-temperature creep, chemical resistance, and water absorption) are determined by matrix properties [65]. Modern commercial high-power capacitors are primarily composed of low-dielectric-constants, considering various matrices of polymer, (e.g. poly (vinyl alcohol), poly (ethylene glycol), polyethylene (glycol), poly (ethylene terephthalate), poly (propylene), and others because of their high dielectric breakdown strength. Among these, PVDF and its co-polymers have been widely selected as appealing options because of their assured properties; high dielectric constant, low crystallinity, low T_g (glass transition temperature), high degree of compactness, and large-scale dipole moment, attractive thermal and electrochemical stability [66][67]. Hence, it has been utilized as one of the significant ferroelectric polymers in non-volatile memories, energy storage capacitors, nano-generators, touch sensors, and many more [68]. Due to their massive and invasive use in applications today, PVDF has been used and exploited largely. Therefore, alternative materials or polymers are introduced in order to increase dielectric strength for energy storage applications. Strongly correlated electron systems are a kind of unconventional electronic material where the study of the effect of magnetoelectric coupling in multiferroic hybrid composites where polymer, as a matrix is taken into consideration, is very limited. Alternatively, chemical modifications have been introduced which has resulted in the improved dielectric strength of polymers, investigated by Job et al. Their investigation suggests the in-situ polymerization of a layer of polyaniline (PANI) which increases the breakdown strength of poly(ethylene terephthalate) (PET) films.

Furthermore, due to advancements in science and technology, two distinct groups of conductive substances incorporating polymer as a matrix has emerged: **Intrinsic and Extrinsic conductors**.

- **Intrinsic conductors:** the conjugated polymers are the intrinsic conducting polymers that have a generalized feature, i.e., the successive alternation of a single bond with double bonds along the main chains. The ability of the π electron to be transported to adjacent carbon, allowing the electron flow, is able to explain the inherent electrical conductivity in that context [69][70]. However, this mechanism results in a low conductivity (between 10^{-10} to 10^1 S/cm), so it is necessary to produce a charge carrier by oxidizing (p-doping) or reducing (n-doping) the polymer using chemical or electrochemical methods, which are typically reversible processes [71][72].
- **Extrinsic conductors:** Extrinsic conductors feature a polymer matrix consisting of composite materials that are often thermoplastic polymers and fillers. These polymers are insulators that permit their electrical conduction through the incorporation of a conducting mediator into their polymeric chains [69]

They are used in a variety of applications, including organic photovoltaics [73], stretchable electronic devices, organic light-emitting diodes [74], supercapacitors [75], fuel cells [76], and electrochemical sensors [77]. Thus, making a composite system with polymer polyaniline (PANI) and correlated systems like transition metals and metal oxides, e.g., (Nickel, Chromium, Neodymium), Haematite, Nickel-cobalt ferrites, are expected to yield some interesting rich phenomenons. The real competition between intrinsic and extrinsic effects on magnetodielectric properties in hybrid composite systems can help us comprehend the source of the magnetoelectric coupling within the sample.

According to the recent literature, magnetodielectric properties have been carried out in single-phase correlated electron systems, for example, Sr_2IrO_4 , BaIrO_3 , $\text{Ha}_2\text{BaNiO}_5$, and NiO. In our system, the electronic structure of PANI, the polymer itself can exist in

three different phases which are emeraldine, lucoemeraldine, and perni-graniline, depending on synthesis. Among them, the Emeraldine base is regarded to be more stable at room temperature, and the fact that upon doping with acid (protonation), the emeraldine base becomes highly electrically conducting. Whereas Lucoemeraldine and pernigraniline always behave as an insulator despite protonation. It would be interesting to see how mobile charges in conducting PANI as a matrix interact with the correlated electron system. The electronic properties are governed by occupied oxygen 2p states, empty 4s metal orbitals, and partially occupied metal 3d states. Moreover, unlike conventional band structures, Mott-Hubbard assets strong atomic d-d coulombic interaction, leading to a spin-polarized band gap. The magnetism which originates due to this band gap in the correlated system can affect the behavior of mobile charges of PANI, thus paving a direct path for spin-charge coupling. Figure 1.8 illustrates some of the intrinsically conducting materials, from which Polyaniline (PANI) has been investigated as a part of nanocomposites in the present study.

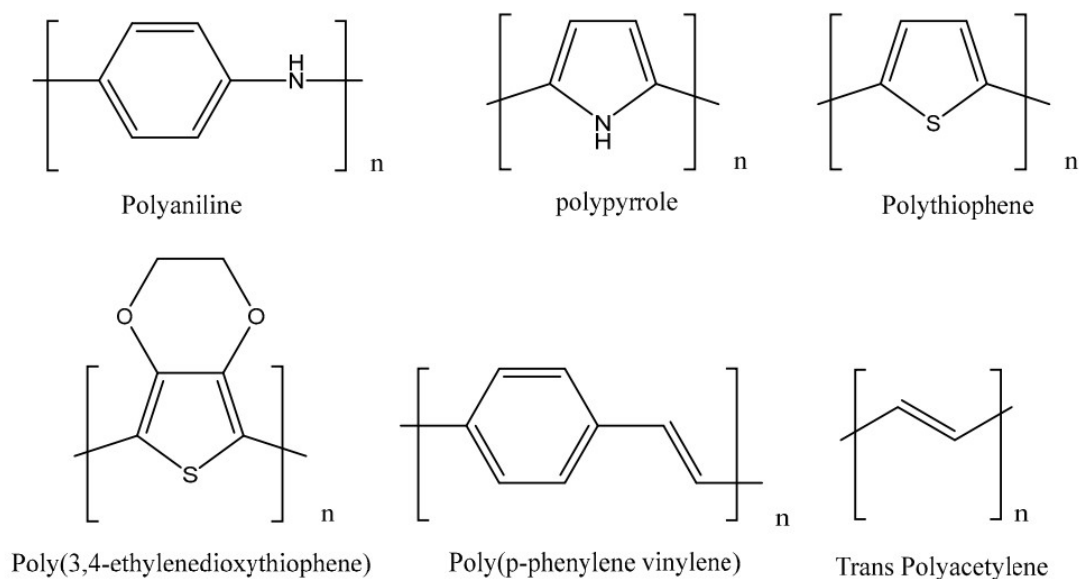


FIGURE 1.8: Structural representation of intrinsically conducting polymers (ICPs)

1.5.2 Reinforcement: Nanoparticles as Reinforcement

To further improve the physical qualities of the resultant composite system, reinforcement materials or composite fillers are incorporated into the matrix material [78]. In other words, these materials are more rigid, strong, and stiff than the matrix, the reinforcing phase offers strength and stiffness [79]. These fillers or reinforcing materials can be categorized based on their physical and chemical structure, but generally based on the shape of the particles, they have been categorized [80]. Apparently, polymeric matrices frequently have reinforcement applied to them to enhance their chemical and physical characteristics. The most desired goal among these properties has been the optimization of the characteristics, which has prompted the employment of reinforcements ranging from (glass and carbon fibers) inorganic fibers to (aramid) organic fibers and (SiO_2 , CaCO_3 , etc) inorganic particles, and carbon black/silicate sheets [81]. Regardless of having substances with outstanding characteristics, their real-world applications are limited by some aspects that significantly raise their costs, such as manufacturing challenges or material incompatibilities.

The ultrafine particles identified as nanoparticles (NPs) range in size from 1 to 100 nm [82]. The polymeric matrix might include these NPs as filler [83]. Therefore, a nanocomposite is formed after incorporating NPs into the polymer matrix (PM). This nanocomposite has a particular structure and possesses physical characteristics that are dependent on the amount and kind of introduced nanometric charge [84]. NPs exhibit a large number of the atoms that compose them and are part of their surface. This makes these atoms easily able to interact with the matrix in which they are embedded [85]. Thus, the use of NPs is important as it lowers the composite's cost. Additionally, they are easily accessible in the necessary quantities, sizes, and shapes [86].

1.5.3 Magnetic Nanoparticles

Superparamagnetism or magnetic behavior that combines the properties of ferromagnetism and paramagnetism is an excellent characteristic of magnetic nanoparticles (MNPs) [87]. Nowadays, superparamagnetic nanoparticles have a variety of applications ranging from biological treatment, electronics, drug delivery, physiochemical spheres, and many others [88] [89] [90] [91]. In general, switching from ferro- or ferri-magnetic to super-para-magnetic as a result of size reduction causes the material's magnetic behavior to alter, with each particle's magnetic moment oscillating in the direction of a net magnetic moment of zero due to the influence of thermal energy [92]. Technologies can potentially be improved as a result of MNPs' unique physicochemical characteristics, huge surface areas, simplicity in the synthesis process, and alternation in intrinsic characteristics. These MNPs also have remarkable synergistic union capability with other chemicals, such as polymers [91].

1.5.3.1 Types of Magnetic Semiconductor Nanoparticles

Figure 1.9 summarises the type of magnetic semiconductor nanoparticles that have been outlined in this section, along with their properties and uses.

- Metal and Metal oxide nanoparticles
- Ferrite
- Manganite

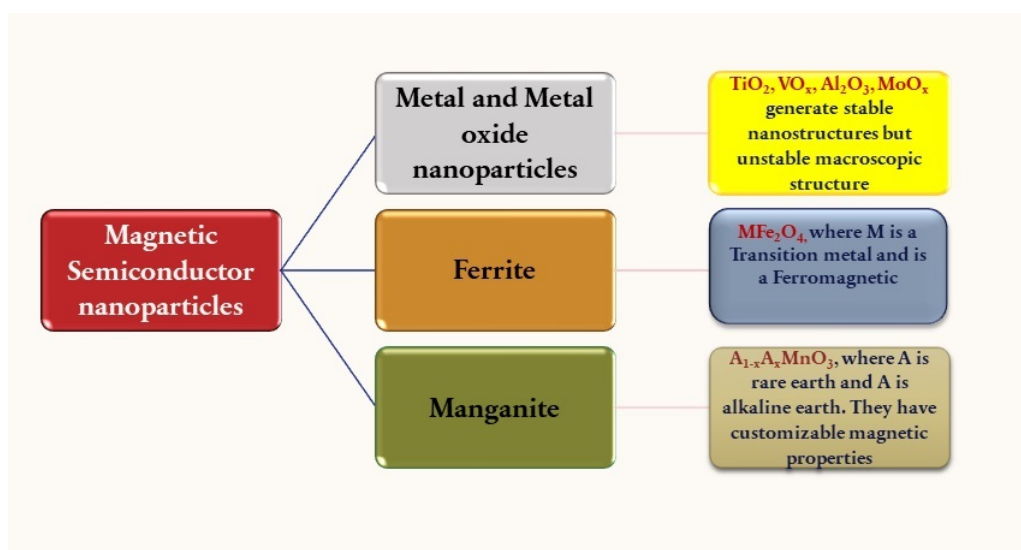


FIGURE 1.9: Summary of Magnetic Semiconductor nanoparticles

(I) *Ferrite*

The history of ferrites (magnetic oxides) and their applications have been known for several centuries ago. The loadstone (magnetite, Fe_3O_4), a natural non-metallic solid, may attract iron and be first described in known Greek writings about 800 B.C. Much later, the first application of magnetite was as 'Lodestones' used by early navigators to locate magnetic North. That is the first scientific significance was appreciated, after the first technical magnetic material because it formed the first compass (Crangle, 1977). The first scientific study of magnetism named *De Magnete* was published by William Gilbert in 1600. Later, in 1819 Hans Christian Oersted observed that an electric current in a wire affected a magnetic compass needle. Naturally occurring magnetite is a weak 'hard' ferrite. 'Hard' ferrites possess a magnetism that is essentially permanent. Originally manufactured in a few select shapes and sizes, primarily for inductor and antenna applications, 'soft' ferrite has

for a variety of uses, multiplied in countless sizes and shapes. Primarily, ferrites utilized in different electronic applications are: power applications, EMI suppression, and low-level applications. Ferrites continue to find more and more uses in electrical circuitry. Ferrite components are the preferred option for both traditional and novel applications due to the large range of feasible geometries, constant developments in material properties, and their comparative cost-effectiveness.

In general, ferrites are ceramic substances with a dark grey or black appearance that is extremely hard and brittle. It is possible to classify ferrites as magnetic materials since they display ferrimagnetic behavior and are made primarily of oxides with ferric ions as the major component. They are formed due to compressing a mixture of raw material of powders into the desired shape, which is then sintered into a ceramic component. The forces that exist between metallic ions holding specific locations in relation to oxygen ions in the oxide's crystal structure give rise to magnetic characteristics. Further, commercial ferrites fall into three key categories, each with a distinctive crystal structure, which are as follows:

- a) Microwave ferrites (such as YIG), have a garnet structure, which is soft ferrite in nature.
- b) NiCo-, MnZn-, and MgMnZn- ferrites are a couple of soft ferrites having a cubic spinel structure.
- c) Ba and Sr hexaferrite's are examples of hard ferrites with magnetoplumbite (hexagonal) structures.

Ferrites are the only material that exhibits such a broad range of characteristics, employing them for various significant applications [93].

(II) *Classification of Ferrite*

Ferrites consist of iron oxide as their main element and other metal oxides. Depending upon the crystal structure, ferrites are of the following types, as illustrated in Figure 1.10.

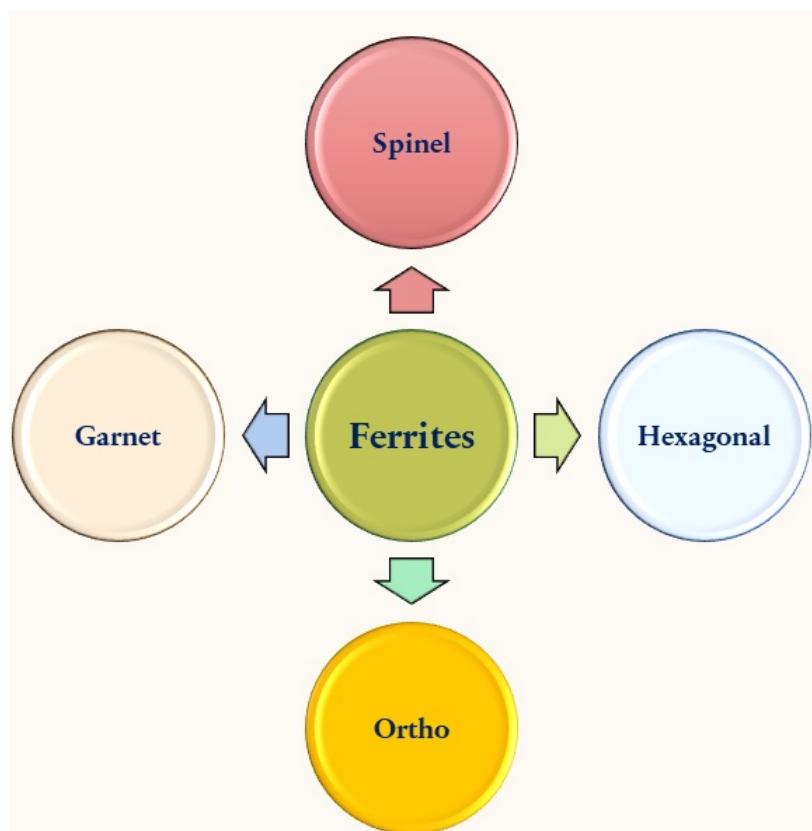


FIGURE 1.10: Classification of Ferrites

1) Spinel Ferrite: In reality, spinel ferrites are a form of naturally occurring ferrites, i.e., $\text{FeO}\cdot\text{Fe}_2\text{O}_3$. The spinel mineral (MgAl_2O_4 or $\text{MgO}\cdot\text{Al}_2\text{O}_3$), which crystallizes in the cubic system, is the source of the spinel structure. Bragg and Nishikawa were the first to determine this crystal structure. The magnetic spinel has the same general formula as the mineral spinel $\text{MO}\cdot\text{Fe}_2\text{O}_3$ or MFe_2O_4 , depending on whether M is the divalent metal ion. The smallest unit of the spinel lattice has cubic symmetry and contains eight “molecules” of MFe_2O_4 .

2) Garnet Ferrite: Large trivalent rare earth ions with strong magnetic moments can be accommodated by these ferrites. The general formula is $\mathbf{M}_3\mathbf{Fe}_5\mathbf{O}_{12}$. The silicate garnet mineral's structure can be observed in garnet ferrites. Magnetic garnets have a 12-sided or dodecahedral crystal structure similar to that of the garnet stone.

3) Ortho Ferrite: The typical formula for ortho-ferrites is \mathbf{RFeO}_3 , where R is yttrium or a rare earth ion. These cubic ferrites have a somewhat deformed perovskite structure but are nonetheless cubic ferrites. The term "perovskite structure" refers to the atomic configuration of oxides with the formula \mathbf{RMO}_3 , such as \mathbf{BaTiO}_3 , \mathbf{PbTiO}_3 , etc. Often, a material with a complex molecular structure consistent with cubic symmetry will acquire this arrangement. Contrary to cubic structures, this one is orthorhombic. Out of these above ferrites, spinel ferrite has pulled in the focal point of numerous scientists in light of its immense scope of utilizations in high-performance energy storage devices.

4) Hexagonal Ferrite: Hexagonal ferrites are a large subgroup of iron oxides that have significant scientific and practical value. Because oxygen-mediated antiferromagnetic superexchange is the predominant interaction between magnetic ions in these systems, they are ferrimagnetic. They deliver a diversity of properties; the structure and specific composition define these features and magnetic structures. The M, W, Y, Z, and U compounds are further categories under which these ferrites are classified.

(III) *Spinel Ferrite: Its Crystal structure and Classification*

Bragg and Nishikawa were the first to notice the spinel structure of ferrite. Spinel ferrite crystallizes into a cubic structure when it crystallizes in the space group $Fd\bar{3}m$ [94]. The 56 atoms that consist of the eight formula units of spinel ferrite are divided into 32 oxygen anions, which assume a close-packed cubic structure, and the remaining metal cations, which are found on 8 of the 64 possible tetrahedral (A) sites and 16 of the 32 octahedral (B) sites.

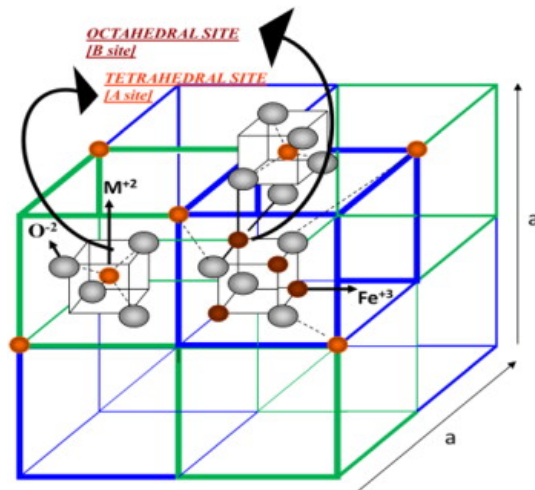


FIGURE 1.11: Structure of Spinel ferrite cubic crystal.

[95]

The unit cell of a spinel structure is shown in Figure 1.11. The ionic locations differ when two octants share a face or a corner, but they remain the same by sharing an edge. The ions' positions in two neighboring octants are therefore all that is required to provide an accurate depiction. Each octant in this structure has four oxygen ions, which are big spheres, arranged on the body diagonals and positioned at the corners of a tetrahedron. An A-site is stated to be occupied by a metal ion that is present in the center of the right-hand octant and is surrounded by a tetrahedron of oxygen ions. An octahedron made of six oxygen ions, one of which is illustrated, is surrounded by four metal ions in the left-hand octant. According to reports, these ions reside at B-sites. Normal spinel structure refers to ferrites with M^{2+} in the A-site (tetrahedral) and Fe^{3+} in the B-site (octahedral). The spinel ferrites are represented by the general formula $M_x^{2+}Fe_{1-x}^{3+}[M_{1-x}^{2+}Fe_{1+x}^{3+}]O_4^{2-}$. Here 'M' is a divalent cation, and 'x' is the inversion factor that further decides the divisions of spinel ferrites.

Based on the distribution of metal cations, three kinds of spinel ferrites can be identified, as shown in Figure 1.12, viz. normal, inverse, and mixed [96].

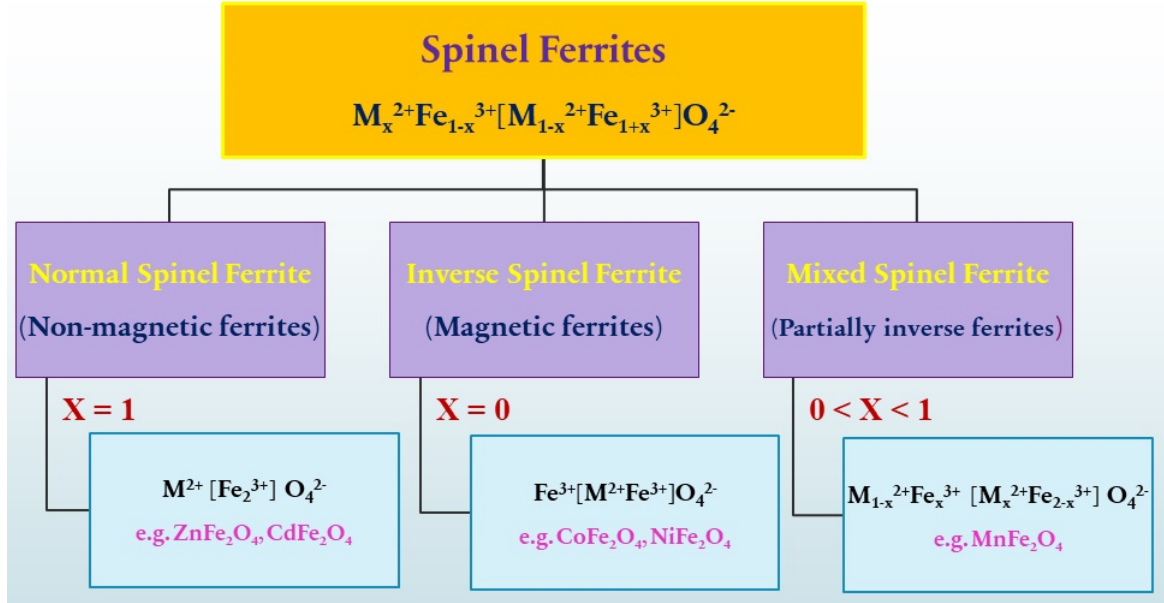


FIGURE 1.12: classification of spinel ferrites.

(a) Normal Spinel Ferrite: The normal spinel ferrite structural formula is denoted by $M^{2+}[Fe_2^{3+}]O_4^{2-}$. All divalent metal cations (M^{2+}) occupy A or tetrahedral sites, whereas trivalent metal cations (Fe^{3+}) occupy B or octahedral sites in the normal spinel ferrite.

(b) Inverse Spinel Ferrite: The inverse spinel ferrite structural formula is denoted by $Fe^{3+}[M^{2+}Fe^{3+}]O_4^{2-}$. All divalent metal cations (M^{2+}) occupy B or octahedral sites, while trivalent metal cations (Fe^{3+}) equally occupy A or tetrahedral and B or octahedral sites in the inverse spinel ferrite. Nickel ferrite ($NiFe_2O_4$) and cobalt ferrite ($CoFe_2O_4$) belong to the category of inverse spinel ferrite.

Among the various spinel ferrites, we report the synthesis of inverse spinel ferrite ($NiCoFe_2O_4$). These ferrites have been widely employed due to their attractive and wide scopes [97][98][99]. $CoFe_2O_4$ and $NiFe_2O_4$ are represented by $(Fe^{3+})[Co^{2+}Fe^{3+}]O_4$ and $(Fe^{3+})[Ni^{2+}Fe^{3+}]O_4$, respectively, as part of spinel-type crystal structures [100][101]. Cobalt ferrites are suitable for strain sensors and actuators due to their greater magnetostriction values [102]. The permittivity values of cobalt ferrite NPs were found to be lower than those of bulk $CoFe_2O_4$, according to a study investigated by Gopalan et al

[103]. Similar to spinel ferrite, another promising material to employ in the following applications is nickel ferrite. In addition to having a high electrical resistivity, nickel ferrite also has a high Curie temperature, saturation magnetization, and a low eddy current and dielectric losses [104][105]. Additionally, NiFe_2O_4 has a dielectric structure with grain boundaries and grains with varying conductivity [106]. According to the analysis, mixed ferrite has superior characteristics and stability depending on the final composition's cation stoichiometry and type. Various researchers have reported their work on the specific stoichiometric $\text{Ni}_{0.5}\text{Co}_{0.5}\text{Fe}_2\text{O}_4$ NPs using multiple dry and wet chemical synthesis methods (Chapter 3) depending on different parameters, such as magnetic properties, temperature variation, etc. Thus, our work reports the study of compositions in the hybrid nanocomposite system comprising ferroelectric as well as conducting polymers (PANI) depicting the synthesis, structural morphological, and multiferroic properties have remained scarce till today.

(c) Mixed Spinel Ferrite: Last but not the least, the mixed spinel ferrite structural formula is denoted by $\text{M}_{1-x}^{2+}\text{Fe}_x^{3+}[\text{M}_x^{2+}\text{Fe}_{2-x}^{3+}]\text{O}_4^{2-}$. Both divalent metal cations (M^{2+}) and trivalent metal cations (Fe^{3+}) occupy A or tetrahedral and B or octahedral sites in the mixed spinel ferrite. Manganese ferrite (MnFe_2O_4) belongs to the category of mixed spinel ferrite.

1.5.4 Hybrid Nanocomposite: Polymer matrix based material system

Hybrid compounds are not just a physical combination of various constituents. The resultant hybrid materials typically gain new properties after merging the multiscale components (reinforcements), and these characteristics can be modified by the unique physiochemical characteristics of individual materials, structures, and interfaces between various components [107]. Currently, investigations have been conducted on the utilization of standard polymers in composites, resulting in a particular class of hybrid substances known

as polymers/hybrid composites (PCs), Figure 1.13 [108]. The composition of the PCs depends upon the interaction between the inorganic and organic phases, such as the dispersion method used during its production, mixing, morphology, arrangement, and the surface characteristics, in a variety of the NPs, that will influence the significant properties of the prepared PNCs. The uniform dispersion of nanofillers in a polymer possess one of the biggest challenges in the production of PNCs [109]. Despite the fact that polymers make an ideal matrix for NCs, still they lack magnetic characteristics.

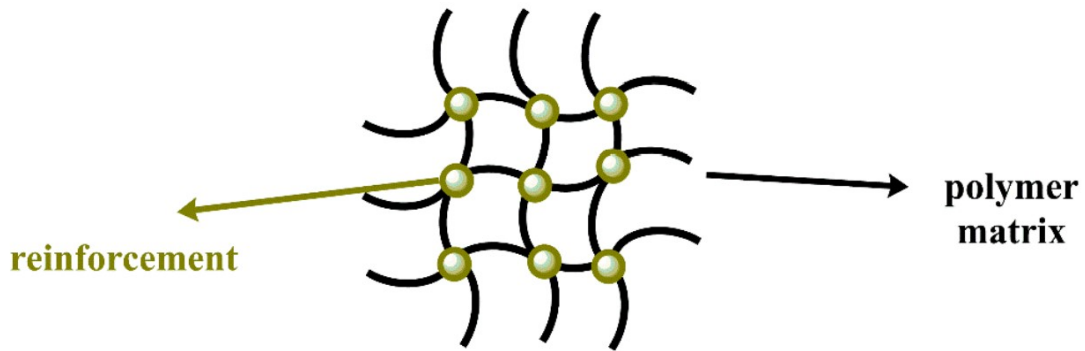


FIGURE 1.13: Hybrid nanocomposite.

As a result, an ideal approach of adding fillers that have magnetic properties into the matrix (polymer) enhances the NCs' features. To build integrated functional systems with supplementary magnetic properties, nanosized ferro-electric, and ferri-magnetic particles are added into the developed matrices [110]. As previously mentioned, Ferrite comprises the characteristics of a magnetic substance with an electrical insulator. It is an appropriate option as it is simple to obtain, inexpensive, and flexible in modulating their magnetic and electromagnetic properties [111]. The amount of ferrite incorporated into the polymer matrix determines how ferrite-reinforced composite materials function.

Thus, our study aims to investigate the dielectric property of insulating polyaniline (PANI) (being intrinsically conducting in nature) in the presence of varying weight fractions of ferromagnetic ferrite $\text{Ni}_{0.5}\text{Co}_{0.5}\text{Fe}_2\text{O}_4$ (NCF), which has significant characteristics of high magneto-crystalline isotropy and high resistivity. These composites exhibit novel

multiferroic properties at room temperature. To our ability and understanding, no reports of such characteristics have yet appeared in the literature.

1.6 Percolation phenomenon: Percolation Threshold in composites

The percolation phenomenon was first introduced by Stockmayer and Flory in 1943, and 1941, respectively, shortly after they explored the polymerization process. The basis for the percolation process is the polymerization process, in which small molecules join by linking chemical bonding resulting in a dense network of single molecules. Broadbent and Hammersley (1957) introduced the percolation theory to mathematics for the first time. "They demonstrated that the percolation process is the outcome of a geometrical phase shift in an irregular medium, and interestingly, the modification in the system's physical and transport characteristics complies with scaling and universal power law principles." Typically, there are two types of percolation processes,

- **Lattice (site bond) percolation model:** Consider a normal 2-d lattice wherein every lattice point can either be inhabited by an insulated particle having probability $(1-P)$ or an electrically conducting particle having probability P . Each lattice site's occupation is indifferent to the likelihood that it will be occupied in adjacent areas. When a continuous group of conducting sites crosses the whole lattice system, the electric current in this system travels from one side of the lattice to the another. Given that the clusters are made up of the nearest neighbors, this phenomenon in the system is known as site percolation. Bond percolation occurs when the cluster emerges by the nearest neighbors' bonds in which there is a probability of q for the bond connecting the sites to be occupied at random.

- **Continuum percolation model:** The fact that the allocation of numbers of coordination fluctuates from site to a site in the context of percolation in a continual medium, that renders the issue, in fact, more intriguing. The component placements in this instance are not constrained to the discrete sites of a normal lattice. For illustration, consider an electrically conducting sheet with a random pattern of round holes. The sheet becomes insulating at the critical concentration of holes (P_C), regardless of whether the sites or bonds are occupied. The "Swiss cheese model" refers to how closely this resembles Swiss cheese. To explain the elastic or transport properties in a porous media, this model is suitable.

The percolation threshold has historically drawn attention in composite systems. Near the percolation threshold, a variety of composite material physical parameters, including resistivity, dielectric constant, heat capacity, and thermal conductivity, have a significant impact. Additionally, the type of conductance in the composite system can be impacted by the dimensions, shape, and position of the filler particles, as well as the quantity of each present in the system. For example, If the matrix itself acts as insulation and the conducting nanoparticles are sphere-shaped, it is possible to examine the electrically conductive properties of disorderly nanocomposites, by incorporating the factor of spheres. It is well known that the thresholds for percolation and conductivity of electricity for ceramic-based polymer composites are significantly influenced by the dispersion condition or level of agglomeration of ceramics.

Chapter 2

Review of Literature, Research Gaps, and Research Objectives

2.1 Literature Review

- **Z. Chchiyai, et.al. (2023)** reported that the AB_2O_4 -type spinel oxides, based on transition metals, for lithium-ion batteries (LIBs) that could serve as anodes. For concentrations ($x = 0, 0.25, 0.5, 0.75, 1, \text{ and } 1.25$) samples were produced using a simple sol-gel synthesis procedure. All compounds formed cubic spinel structures with the space group of $Fd\bar{3}m$, according to X-ray diffraction studies, and Raman scattering spectroscopy verified that all samples had cubic $Fd\bar{3}m$ symmetry. The produced spinels are clearly linked nanoparticles with a crystalline face-centered cubic structure with nanosized pores, as shown by scanning electron microscopy. This structure is found to be extremely stable, thermally. By cycling the lithium-ion batteries' charge and discharge, the electrochemical characteristics of anodes composed of Mn-doped spinel ferrites were examined. Significant improvements were made to the efficiency and stability during the charge-discharge operations, by Mn doping, which ensures excellent cycling stability and good rate capability for

the compound where $x = 1$, sustaining a specific capacity at 307 mAh g^{-1} after 50 cycles. Cyclical voltammetry data at various scan rates were used to analyze the mechanism of Li-ion storage. The current work recommends spinel oxides as an effective, affordable, and environmentally friendly alternative anode material for LIBs” [112].

- **G. Vinod, et.al. (2023)** discovered the effect of Dy^{3+} ion substitution on the structural, optical, electrical, and magnetic properties of $\text{Cu}_{0.8}\text{Cd}_{0.2}\text{Fe}_2\text{O}_4$ nano-ferrites. A series of Dy_{3+} doped Cu–Cd nano-ferrites with the chemical composition of $\text{Cu}_{0.8}\text{Cd}_{0.2}\text{Dy}_x\text{Fe}_{2-x}\text{O}_4$ ($x = 0.00, 0.025, 0.05, 0.075, \text{ and } 0.10$) were fabricated by CSGAC (citrate sol-gel auto combustion) technique using the respected elements in their nitrate state and grounded powders and were calcined at $650 \text{ }^\circ\text{C}$ for 4 h. By Using P-XRD, FE-SEM, HR-TEM, FTIR, UV-Vis, ESR, VSM, and I-V measurements, the structural, optical, magnetic, and electrical characteristics of these ferrite nanoparticles (NPs) were analyzed. P-XRD data has been used to investigate the purity of the crystal structure, phase formation, and different structural properties of Cu-Cd-Dy nano-particles. Between 13.82 and 18.32 nm is the size range of the examined crystals. Particle sizes of 40–60 nm and grain sizes of 48–80 nm from FE–SEM images, respectively, had been estimated. The spine structure can be observed in measured FTIR spectra when functional groups and metal-oxide stretching bonds were present. With a concentration of Dy^{3+} , the coercivity (H_c) decreased from 557.29-183.89 Oe at 300 K and from 749.85-410.72 Oe at 15 K, respectively. At a temperature of 300 K for $x = 0.025$, the maximum saturation magnetization is 32.53 emu/g , whereas at a temperature of 15 K for $x = 0.1$, it is 38.85 emu/g . The application of Dy^{3+} doped $\text{Cu}_{0.8}\text{Cd}_{0.2}\text{Fe}_2\text{O}_4$ nanoparticles in highly dense recording media was demonstrated by the findings of the current studied samples, with improved H_c , M_s , and M_r values at low temperature 15 K then the same values at the average room temperature of 300 K [113].

- **N. Venkatesh, et.al. (2023)** synthesized gadolinium-substituted magnesium nano ferrites with composition $\text{MgGd}_x\text{Fe}_{2-x}\text{O}_4$ ($X=0.0-1.0$ with 0.025 variations) via citrate gel auto-combustion method. The influence of Gd^{3+} substitution on the photocatalytic, structural, magnetic, and electrical properties of Mg nano ferrites was analyzed. To gain insight into the magnetic, structural, optical and electrical characteristics of the synthesized materials, measurements such as XRD, SEM, FTIR, UV-vis, VSM, and dielectric transport were used. In order to determine the sample's X-ray densities, crystallinity, lattice parameters, and unit cell volume, the XRD analytical technique was used. A crystalline size in the range of 15–19 nm was produced by Scherrer's formula. The formation of spinel structure was identified using FTIR spectroscopy, which revealed two unique absorption bands at octahedral and tetrahedral locations, respectively, with wave numbers close to 400 cm^{-1} and close to 600 cm^{-1} . Peaks in the 400 nm region of the PL spectrum were observed and displayed fluorescence properties. The photocatalytic activity of the synthesized materials was estimated using methylene blue and acid red, and pure Mg ferrite showed high degradation activity with low crystalline size. The variation of samples from hard to soft magnetic materials could be found using VSM research. The nano-ferrites' frequency-dependent AC conductivity (σ_c) increased with temperature. With rising frequency, dielectric properties such as the dielectric constant and dielectric loss ($\tan \delta$) are lowered. Dielectric tests have shown that the hopping process of electrons results in dielectric dispersion between Fe^{2+} and Fe^{3+} ions [114].
- **D. Hamad, et.al. (2023)** investigated the morphological and magnetic characteristics of $\text{Cd}_{1-x}\text{Co}_x\text{Fe}_2\text{O}_4$ nanoferrite system with ($0.0 < x < 1.0$ mole), prepared by the hydrothermal technique. The structure of the synthesized nano ferrite as a result of the X-ray diffraction (XRD) reveals that cadmium–cobalt nano ferrites possess fcc CdO, hexagonal Fe_2O_3 , hexagonal CoFe_2O_4 phases. To determine the typical grain size, they used High-Resolution Transmission Electron Microscope (HRTEM)

images. Using the Fourier Transform Infrared (FTIR) method, (M-O) the metal-oxide bonds were verified. Since the magnetization saturation rises linearly with Co concentration, this outstanding rise constitutes the greater value for a particular sample that has been recorded [115].

- **B. Sapkota, et.al. (2022)** proposed their study on the fabrication and investigation of magnetoelectric properties in flexible PVDF-TrFE/Cobalt ferrite nanocomposite films, using a blade coating process. Here, the ferroelectric matrix was taken into consideration. A two-step procedure was used to create the nanocomposite films. The first step involved developing cobalt ferrite NPs by sonochemical method, and the second process involved adding different weight fractions (0, 3, 6, and 9 %) of the CoFe_2O_4 nanoparticles to the PVDF-TrFE to develop the composites. X-ray diffraction proved PVDF-ferroelectric TrFE's polar phase (XRD). When 5 wt. % CFN was loaded into PVDF-TrFE composite films as compared to PVDF-TrFE films, it significantly improved maximum polarization, according to research on the ferroelectric characteristics of pure polymer/composite films. The authors outlined a method for creating pure PVDF-TrFE films with outstanding optical quality and without any pinholes. The mechanical investigations ultimately demonstrated that adding nanoparticles to the co-polymer matrix boosts the strength of the films by 5 % before it starts to decline. Thus, it was found that the developed films might work well with flexible electronics [116].
- **S.I Ahmad (2022)** reviewed the types of ferrites, their structure, room, and magnetic dielectric properties of pristine at low-temperature, of metal-doped Cobalt ferrite (CFO). The author discusses an overview of XRD and the influence of calcination temperature on FTIR processes. Dielectric, electric, magnetic, and impedance spectroscopic properties at low temperature (FC) and zero fields (ZFC) have been investigated for pure and doped CFO. In conclusion, this review summarizes recent research on CFO nanoparticles while describing CFO's structural, room temperature, and low temperature magnetic, and dielectric properties [117].

- **D.R. Lekshmi, et.al. (2022)** synthesized "an axially anisotropic magnetodielectric composite formed from polymethyl methacrylate (PMMA) and NiFe₂O₄ (NFO) was developed with the goal of achieving miniature antennas. By varying the volume % of NFO (5, 10, 15, and 20 vol %), which was incorporated into the PMMA matrix, (0-3) thin film composites were fabricated. The investigation was carried out for individual composites for dielectric, structural, magnetic, and magnetocapacitance measurements. Researchers theoretically simulated an 830 MHz microstrip patch antenna that would serve as the antenna substrate. When compared to typical values of permittivity and permeability by dielectric substrates, it is in approximation equal to unity, this MD antenna impressively scaled up by 95.46 % [118].
- **Rekha Gupta, et.al. (2022)** studied the magnetoelectric coupling phenomenon in multiferroics because it has a variety of uses in electrically tunable microwave devices, spintronic devices, and data storage. Since the discovery of magnetoelectric coupling in a variety of single-phase and multiferroic composites in Cr₂O₃ in order to generate a stable magnetoelectric coupling at room temperature, many of these have been converted into device applications. Various device applications of multiferroic materials result from various magnetoelectric coupling phenomena. The author succinctly reviews several major findings on room-temperature magnetoelectric coupling [119].
- **D.R. Fierro, et.al. (2022)** studied nanocomposite materials, like similar composite materials on a macroscale scale, have grown significantly because the reinforcement resolves for matrix flaws to provide substances with improved thermal, electrical, and mechanical properties. Consequently, attention and deep study into polymeric composites strengthened with different kinds of nanoparticles have increased. The nanoparticles which exhibit dual behavior - both magnetic and semiconductor, are among those polymeric matrices that have best distinguished themselves in the electronics sector. The development of daily electrical devices like televisions, laptops, and cell phones has made excellent use of this characteristic. This review thus

compiles the synthetic techniques for creating polymer nanocomposites with dual magnetic and semiconductor properties, as well as their potential uses in electronic domains and recent pertinent developments [120].

- **S. Kangishwar, et.al. (2022)** studied polymer matrix composites, which have improved durability and corrosion resistance than many other materials and useful design flexibility. Due to their better mechanical qualities and relative simplicity of manufacture, these materials are thus acknowledged as advanced composite materials. Because of this, producers are already using these sophisticated composites for a variety of applications in numerous industries. The review focuses on diverse matrices and reinforcement combinations utilized for various applications taking into account their qualities, such as in the civil engineering industry, bio-medical application energy harvesting, and biotechnology. Also, the multiple uses of polymer matrix composites in the modern world and the difficulties they provide in a variety of settings are discussed [121].
- **X. Liang, et.al. (2021)** proposed their review in extremely fascinating areas of multiferroics. Following the resurgence of multiferroic laminated materials, with high ME coupling coefficients has been a considerable study of magnetoelectric (ME) materials and devices. New multifunctional gadgets in the next generation heavily rely on the presence of two or more ferroic characteristics in ME systems. Numerous ME systems, such as thin-film substances or single-phase and thin-film composites like magnetostrictive/piezoelectric heterostructures, exhibit strong ME coupling. Many device applications, including voltage-adjustable inductors, that are small, light, & energy-efficient, have drawn an ever-increasing amount of attention based on the coupling processes. Next-generation magnetic devices have a lot of potential thanks to these innovative ME materials. The authors attempted to summarize the discoveries in magneto-electric materials, with a focus on nano-films composites. There are also a few unanswered queries and potential future paths for the community to offer [122].

- **I. Petrila, et.al. (2021)** employed a sol-gel procedure to examine the influence due to the sintering of $\text{Cu}_{0.5}\text{Zn}_{0.5}\text{Fe}_2\text{O}_4$ on the electrical, structural, and magnetic characteristics. XRD demonstrates the crystallite size and phase of the prepared samples. SEM and AFM reveal the impact of sintering on several aspects viz. size of the crystallite, homogeneity, and porosity. At ambient temperature, relative permittivity, relative permeability, and electrical conductivity were computed with frequency. Eventually, at varying levels of humidity, an evaluation of relative permittivity, electrical conductivity, and temporal response has been done. Consequently, the prepared sample would have the possibility to be used in humidity sensors [123].
- **A. Manikandan, et.al. (2020)** in the current study studied magnetic Fe_3O_4 NPs and non-toxic luminous ZnO NPs were separately created using the co-precipitation approach. Both of these NPs were incorporated in a silica matrix to create the $\text{ZnO@Fe}_3\text{O}_4$ nanocomposite (NCs). Powder XRD demonstrates that the cubic inverse spinel structure of Fe_3O_4 and the hexagonal wurtzite structure of ZnO were formed. The prepared $\text{ZnO@Fe}_3\text{O}_4$ NCs combined both phases. In samples of ZnO NPs, and $\text{ZnO@Fe}_3\text{O}_4$ NCs, Fe_3O_4 NPs, metal-oxygen stretching bands were detected in FT-IR spectra with absorption peaks. The superparamagnetic properties of magnetite and $\text{ZnO@Fe}_3\text{O}_4$ were demonstrated by VSM data, while $\text{ZnO@Fe}_3\text{O}_4$ NC saturation values were significantly reduced. ZnO and $\text{ZnO@Fe}_3\text{O}_4$'s photoluminescence (PL) spectra demonstrated that both samples have excellent luminescence properties. Comparing $\text{ZnO@Fe}_3\text{O}_4$ NCs to bare ZnO NPs, the PL intensity of the latter has decreased. $\text{ZnO@Fe}_3\text{O}_4$ still has excellent luminous properties, though. The application of the $\text{ZnO@Fe}_3\text{O}_4$ NCs was successfully demonstrated. As a result, it can be applied to optical imaging applications as well as MRI contrast agents [124].
- **Debajyoti Nath, et.al. (2020)** had synthesized the polymer-based hybrid nanocomposites of LaFeO_3 , poly(vinylidene fluoride) (PVDF) via pyrophoric and polymerization reaction processes. "The study of $x\text{LFO}-(1-x)\text{PVDF}$ nanocomposites with

variables fractions ($x = 0.5, 0.6,$ and 0.7) were carried out via impedance and modulus spectroscopy. The improved dielectric properties for hybrid nanocomposites were studied through surface modification and LaFeO_3 (LFO) distribution inside the polymer. The XRD pattern reveals the accurate formation of phases. No phase segregation of hybrid materials was present. Thus, the study focuses on the electrical, and dielectric properties and their dependence on the magnetic field in a system potentially capable of industrial applications” [125].

- **S. Ikram, et.al. (2020)** assessed the impact on the dielectric, magnetic, electrical, and structural characteristics of the doping of the rare earth metal cations. XRD scans and subsequent FTIR analyses verified the spinel ferrite in the cubic structure of all as-produced systems. The type of dopant RE^{3+} ions has an influence on the lattice constant, and crystallite size. Secondary phases on doping La exist for $x > 0.2$ owing to the La larger radius than the Ce. The spin order coupled with RE^{3+} ionic radius was affected by decreasing crystallite size, resulting in a reduction in magnetization. The decrement in the coercivity and increment in the permeability was examined for the dopant having a short radius. The dielectric constant, as well as dielectric loss, dropped with the decrement in the frequency. These ferrites NPs were applicable for microwave and high-frequency appliances according to their described properties [126].
- **R.P. Patil, et.al. (2020)** synthesized Mn-doped LiFe_2O_4 NPs by employing the sol-gel procedure. The prepared sample is sintered in air at various temperatures. FTIR, SEM, and XRD have been utilized for the examination of morphological and structural characteristics. All of the samples had a nanocrystalline single cubic phase structure, as per the XRD pattern. The SEM method is used to provide morphological investigations of produced nanocrystalline materials. It can be observed that when the sintering temperature rises, the average grain size grows dramatically. According to FT-IR investigations, the spinel phase forms at a higher sintering temperature [127].

- **Ajith. S. Kumar, et.al. (2019)** manufactured the composite systems by employing piezoelectric (BCZT)/magnetostrictive CFO) with respect to the CFO weight fraction. Despite having strong magnetocapacitance (MC) characteristics (*sim* 35 %), composite systems are unreliable for calculating the ME coupling coefficient (MECC) quantitatively because of potential stray contributions from magnetoresistance and magnetostriction. The magnetic, ferroelectric, electrical, and magneto-electric (ME) characteristics of the system are studied and reported with respect to variable ferrite concentration. In order to measure magnetoelectric coupling, a dynamic approach is selected. Every mixture displayed rather strong ME coupling. The ME coupling is discovered to increase with ferrite fraction, with a composite of 0.6BCZT and 0.4CFO exhibiting the maximum ME coupling with 15 mV/(cm Oe). These materials are used for magnetic field sensors to energy harvesters applications [128].
- **I. Hussain Lone, et.al. (2019)** reports the development of different kinds of nano-materials which possess both electric and magnetic properties at the nanoscale. This review article discusses the wide range of applications and active research that such materials with magnetic and electric characteristics have. Even in materials where the magnetic property would alter by an electric field or vice versa, these materials induce new features that are crucial in electronic and magnetic devices. The demand for such ferroic qualities for scientific applications is urgent, and their discovery opens up a brand-new field with great promise for the development of cutting-edge materials both technically and economically. Recent research has focused on the actual mechanism through which the multiferroic characteristics exist, and novel metal oxide compounds have been found. This work has explored the fundamentals and structural variations of ternary transition metal oxides, which have unique features in storage systems like magnetic read heads and hard disc platters [129].

- **D. Kumar Rana, et.al. (2019)** successfully synthesized Polyvinylidene fluoride and bismuth ferrite (BiFeO_3)(BFO) flexible nanocomposites films with varying concentrations of BFO nanoparticles via the two-stage sol-gel method of a bottom-up approach. The XRD confirmed the phase purity of BiFeO_3 NPs, distinct phases of crystallinity for PVDF-BFO composites. Also, the particle size of BiFeO_3 is obtained with a particle distribution pattern, which is estimated to be 34 nm in size and had been obtained from (TEM) analysis. The room temperature ferromagnetic and ferroelectric ordering of composites has been confirmed by magnetic and electric hysteresis loops respectively. On addition of the bismuth ferrite nanoparticles into the PVDF matrix, increases the storage density of composites. The magnetodielectric coupling measurement, whose maximum value is seen 0.04 % at 7.9 wt. % of BFO nanoparticles inserted into the matrix confirms the presence of multiferroicity in the nanocomposite. Therefore, the establishment of room-temperature multiferroic nature in polymer composites suggests that it may be improved for use in spintronic devices, flexible electronics, and energy storage in the future [130].
- **Papia Dutta, et.al. (2019)** investigated the magnetoimpedance and magnetodielectric characteristics in LaFeO_3 (1-x) %/organic paraffin wax (x) %, where (x= 0.2, 0.4, 0.8, 1.0) at room temperature. The introduction of a dielectric non-magnetic layer over the surface in LaFeO_3 NPs was done in order to study the modifications in the conduction mechanism. The enhancement of MI (227 %)and MD (76%) effected at low-frequency regions are achieved at (0.5 %) nanocomposite of piezomagnetic materials. Also, the XRD confirms only the existence of LFO peaks and FESEM analysis of the particle size in nanometres at varying magnifications for x = 0.5%. The AC electrical studies reported the conduction system controlled through impedance spectroscopy, which was found to be minimum for x = 0.5 % composite. Thus, the successful synthesis of hybrid nanocompobehavior found to be of massive interest for energy storage and sensor-based applications [131].

- **B. karthikeyan, et.al. (2019)** presented their study on the various chemical synthesis methods of nanohybrid preparation. The author emphasized today's societal needs which are, the miniaturization of electronic devices, which could determine the new generation materials by investigating novel as well as simple nanohybrid preparation methods. The bottom-up processes such as ultra-sonochemical synthesis, seed growth mechanism, co-precipitation method, hydrothermal routes, and sol-gel approach techniques had been studied. The sol-gel technique is immensely utilized in nanostructure preparation consisting of multiple parts, and the resultant is formed because of slow reaction kinetics. Similarly, the hydrothermal method is the most successful way out for the synthesis of innovative nanohybrids for cosmetology applications, etc. As a result, the bottom-up technique, that has been employed by researchers to amalgamate the atomic molecules of the nanoscale industry in the most regulated manner, was found to be the best of all the approaches under study [132].
- **S. Hcini, et.al. (2018)** exploited the sol-gel approach for the production of $\text{Ni}_{0.4}\text{Cd}_{0.3}\text{Zn}_{0.3}\text{Fe}_2\text{O}_4$ and investigated the critical, magneto-caloric, magnetic, and structural characteristics of the temperature. The increment in the size of the crystal and lattice constant was perceived with a rise in the temperature. The developed samples contained transitions from FM-PM are noticed in the magnetic investigation. The enhancement in the relative cooling power, entropy, Curie temperature, and magnetization was manifested with the enhancement in the temperature. Owing to the enhancement in the size of the crystal, there arises variability in the critical exponents [133].
- **F.Madidi, et.al. (2018)** presented a study that reports the electrical characteristics at vulcanized (RTV) silicon rubber SR reinforced with variable TiO_2 concentrations. To achieve this, Triton X-100 a surfactant was added to improve the spreading of micro-NPs across the surface in order to produce homogeneous composites for the improvement of permittivity from 4.2 to 5.2 at 70 Hz across the samples. The study

also proposed, at 165 Hz and 20 wt.% TiO₂, the portion of permittivity that is frequency-dependent is quadrupled for two sizes of particles: 25nm and 1 μ m". Thus, it was observed that the dielectric properties were improved by using 5 wt. % and 10 wt. % TiO₂ nano- and microparticles, which can be significant for high-voltage electrical insulation [134].

- **H. Palneedi, et.al. (2016)** published their review article on multiferroic magnetoelectric (ME) composites, which are interesting materials for coupled electrical and magnetical devices. It is crucial to choose a combination of piezoelectric and magnetostrictive materials with feasible properties and adopt a suitable fabrication approach to configure the constituents of the composite, optimize interfacial coupling, and other dynamic parameters. In order to develop a thorough understanding of the contributing factors in order to achieve strong ME coupling and high-performance ME composites. Thus, reasons are briefly summarised by authors, along with information on fabrication procedures, characterization methods, and concepts on converse (electric to magnetic) & direct (magnetic to electric) ME devices. In general, overall investigations into ME composite systems have proved to be significant for science and technology [135].
- **Chaturmukha, et.al. (2016)** evaluated the dielectric characteristics of polyaniline/titanium dioxide (PANI/TiO₂) nanocomposites, which were successfully synthesized by polymerization technique. The (1-x)PANI-xTiO₂ nanocomposites of different compositions were prepared by various weight % of TiO₂ = 10%, 20%, 30%, 40%, and 50% with respect to aniline monomer. The powdered samples were analyzed via XRD and SEM. Further, dielectric characteristics and AC conductivity are studied in the range of frequency (1 kHz - 10 MHz). Thus, it was observed that at higher frequencies(>106 Hz), nanocomposites exhibit zero dielectric loss and maximum value of conductivity σ_{ac} , for a concentration of 20% of TiO₂ in polyaniline [136].

- **A.P. Pereira Fulco, et.al. (2015)** investigated "polymeric composite materials, which offer various advantages for applications due to the combination of properties, which includes high specific mechanical strength and elastic modulus, and corrosion resistance. Nondestructive evaluation (NDE) techniques that rely on magnetic sensors cannot be used on these materials since they are not magnetic. Characterization of circular plates with notches of diameters 1, 5, and 10 mm was carried out using the magnetic flux leakage technique. For the barium ferrite, the impact of particle size on the magnetic characteristics of the composites was also examined. The findings showed a strong link between the magnetic signals that were detected and the presence of notches. The detection of the tiniest notch was made more difficult by smaller average particle sizes. With regard to the intermediate and larger size notches, it produced a better signal-to-noise ratio" [111].
- **M. Rahimi et.al.(2013)** utilized a wet chemistry (sol-gel) approach for the preparation of $\text{Ni}_{0.3}\text{Zn}_{0.7}\text{Fe}_2\text{O}_4$ ferrite NPs. The prepared sample's magnetic and structural characteristics are highly influenced by the temperature (sintering). The development of the single-phase in the prepared samples was ratified by the XRD. The typical crystallite size was estimated to be in between 12 and 60 nm. As crystallite size, the M_s also enhances, whereas H_c first inclined and then declined, according to magnetic investigations of sintered samples at various temperatures. The findings of AC susceptibility studies on $\text{Ni}_{0.3}\text{Zn}_{0.7}\text{Fe}_2\text{O}_4$ NPs reveal that the NPs interaction (magnetic) may cause superspin glasses-like behavior [137].
- **Qian Liu, et.al. (2011)** proposed the study of the colossal magnetodielectric effect under the influence of the magnetoelectric effect. The choice of the sample was $\text{Pb}(\text{Zr}, \text{Ti})\text{O}_3/\text{Tefenol-D}$ laminate composite, in which a strong ME effect was revealed, attributing to the colossal MD effect at low external ac magnetic field at normal room temperature. On applying a magnetic field to a ME composite, a polarisation induced on the surface of the sample impacts dielectric constant. The capacitive or dielectric permittivity of the composites is tailored by the application

of a low magnetic field. Thus results discussed above are essential for understanding the MD and ME effects relationship [138].

- **Sreemanta Mitra, et.al. (2011)** synthesized Polyvinyl alcohol (PVA) solidified in a solution containing dispersed graphene nanosheets to form films with a width of 120 μm . The graphene-PVA contact produces localized states that are the cause of the electrical conductivity. A Debye-type relaxation phenomenon occurred due to dielectric permittivity data with respect to frequency. The nanocomposites displayed a magnetodielectric effect on increasing magnetic field (2 T), with the dielectric constant increasing by 1.8 %. Maxwell-Wagner polarisation was applied to explain the effect using a 2D-composite model. This category of composite is useful for nanogenerator applications [139].
- **Cesar Morales, et.al. (2011)** reported the study of tunable magnetodielectric polymer composites with evenly dispersed Fe_3O_4 magnetic nanoparticles of 8 nm diameter and of 1-6 GHz frequency range, which through raising the relative permittivity as well as relative permeability of the composite material, could improve its microwave properties. The relative permeability and permittivity of the composites are determined by using a conformal mapping method. Therefore, these qualities are highlighted in the design of adjustable RF elements like attenuators, antennas, and switches [140].
- **S.D. Bhame, et.al. (2008)** evaluated the magnetostrictive behavior of cobalt ferrite made using a conventional ceramic technique to the sintering temperature and stay time. The results of this investigation show that the microstructure of the resultant sintered product has a significant impact on the quantity of magnetostriction. When the sintered material contains tiny, homogeneous grains with a less permeable structure, the magnetostrictive strain rises. Considering samples that were sintered at a lower temperature of 1100 $^\circ\text{C}$, higher magnetostriction is produced". These findings are further supported by an examination of the microstructural and magnetostrictive characteristics of various additives during sintering [141].

- **O.P. Dimitriev, (2004)** ”investigated the effect of PANI films doped in transition metal salts in order to increase the conductivity. The author reported that emeraldine base (EB) could interact with various transition metal salts, forming an insoluble precipitate in the DMFA solution. The two extreme cases of doping were further separated based on their electrode potentials and the use of inorganic salt. Complex conductivity measurements, morphological analyses, and UV-vis-IR spectroscopy were all carried out. Thus, transition-metal salts (chlorides or nitrates) can be added to PANI as dopants to change the film’s shape and molecular structure” [142].
- **Ashis Dey, et.al (2004)** had synthesized PANI/TiO₂ nanocomposites from a solution of TiO₂ nanoparticles. The study of the transport and dielectric properties of these nanocomposites at low temperatures and low frequency had been described. The study of dc and ac conductivity of varying concentrations of PANI with respect to frequency/temperature had been analyzed. Therefore, a huge dielectric constant ~ 4000 is estimated at 300 K, along with the maximum permittivity for PANI(370) and TiO₂(115). Thus materials with such large dielectric constants can be used in the fields of memory storages, microactuators, and semiconductor devices [143].

2.2 Research Gaps

After surveying numerous pieces of literature in the field of the hybrid multiferroic nanocomposites, their route of synthesis, characterizations, and applications for energy storage capacitors, below are the mentioned research gaps, which are listed as follows:

- (a) Energy storage composites with large dielectric constants are very limited in the present literature. There are plenty of ways to improve volumetric capacitance which needs systematic study of dielectric response on different kinds of composite systems.

-
- (b) The percolative technique is less likely to be investigated in the literature to attain high volumetric capacities based on the rapid growth of a composite system's dielectric constant. Moreover, this phenomenon can gain a rich flavor of physics by showing various exotic effects, as if the dielectric constant and magnetism of the material are coupled with each other for analysis.
 - (c) Development of magnetodielectric materials involves a couple of ways. The study of the magnetodielectrics in hybrid nanocomposite systems can broaden the search for improved magnetodielectric materials and can give better flexibility for fabricating new devices and systems with improved magnetic-insulating material properties.
 - (d) Strongly correlated electron systems such as NiO/PVDF, NiCoFe₂O₄/PANI, etc., are another kind of unconventional electronic material where the study of multiferroic properties and the effect of magnetoelectric coupling is very limited.
 - (e) Today ample literature on magnetodielectric properties of single-phase systems has been carried out. However, for the multiphase/heterogenous systems, a detailed study of novel dielectric and multiferroic properties has been lacking in many ways.

To overcome these research gaps, the following research objectives have been framed.

2.3 Research Objectives

The primary objectives of the current research's investigation are:

- (1) To synthesize a hybrid nanocomposite, comprising polymer polyaniline (PANI) along with transitional metals in order to yield some interesting rich phenomenon.
- (2) The characterization of nanocomposite system, along with the study of the magnetodielectric effect on both single phase and in better heterogeneous composite systems.
- (3) The study of the origin of the magnetoelectric coupling effect in the nanocomposite system.
- (4) The study of percolation and finding percolation threshold in magnetodielectrics.

Chapter 3

Materials and Methodology

3.1 Materials

The materials utilised in our conducted experiments are the types of composite dielectric systems, which are synthesized for the purpose of increasing the dielectric constant of the composite systems for their use in high-energy storage applications. The composite dielectric systems are synthesized by combining both the host (metals, polymers) and filler (ceramics) materials into a matrix. Several combinations, including dielectric-dielectric, dielectric conductor, and dielectric-semiconductor phases, could constitute this host-filler inclusion system. A structured matrix of a certain type may be included in the constituent phases to produce desired dielectric properties, or the inclusions may be distributed randomly throughout the host medium or form a structural embedding system made up of multi-layer "layups" by the component phases. Therefore, a composite dielectric can be thought of generally as a mixing medium that is largely heterogeneous and may also be anisotropic and nonlinear.

Out of these systems, we have specifically worked on both single-phase ($\text{NiCoFe}_2\text{O}_4$) and heterogeneous systems, such as ionic composites (NaCl-TiO_2), hybrid composites

(NiCoFe₂O₄-PANI) and various others. The aspect ratio of all these components has been different and is measured by considering weight fraction (wt. %). Below are the following synthesized and used materials,

3.1.1 Titanium dioxide (TiO₂)

TiO₂ has several properties that make it well-suited for use as a dielectric material. It bears a high dielectric constant, which indicates its capacity to store a large amount of electrical energy for a given voltage. It also has a high breakdown voltage, which means that it can withstand high electric fields without breaking down.

Titanium dioxide (TiO₂) has a crystalline structure and exists in several forms (polymorphs). Generally, TiO₂ exists in rutile, anatase, and brookite polymorphs, each with its own unique crystal structure.

- Being the most stable, rutile has a tetragonal crystal structure. and commonly occurring form of TiO₂.
- Additionally, anatase has a tetragonal crystal structure and is often used as a photocatalyst, due to its high surface area and reactivity with light.
- Brookite TiO₂ has an orthorhombic crystal structure and is the least common form of TiO₂. It is less stable than rutile or anatase but can be synthesized under specific conditions.

All forms of TiO₂ are composed of titanium and oxygen atoms arranged in a crystal lattice structure. The variations in crystal shape and concentration of the polymorphs result in differences in their physio-chemical properties, which signifies their importance for various industries.

In our project, we have synthesized TiO₂ in Anatase and Rutile polymorphs. The detailed study of polymorphs, synthesis, and their application as dielectric material is

mentioned in Chapter 5. The below Figure 3.1 depicts the synthesized TiO_2 in powder form.



FIGURE 3.1: Bulk TiO_2 in powder form.

3.1.2 Sodium Chloride (NaCl)

In different chemical applications, such as capacitors, batteries, and the electrochemical industry, electrolytic solutions, and the solid-electrolyte interface are crucial. Since Na is vastly available in a variety of forms (such as sea salt and rock salt), it is a cost-effective substance. Na is an alkali metal in Group 1 of the periodic table, just like Li.

TiO_2 serves as a filler in the ionic matrix of NaCl in our work, and Chapter 5 places a lot of attention on the research of the composite systems' dielectric characteristics. For potential use in ionic storage systems, the composite systems $\text{TiO}_2(x)\text{NaCl}$ were also characterised by XRD, FTIR, and FESEM analyses. Sodium chloride [99.5% AR/ACS (NaCl)] from Loba Chemie Pvt. Ltd. is shown in powder form in Figure 3.2 below.



FIGURE 3.2: NaCl from Loba Chemie in powder form.

3.1.3 Nickel Cobalt Ferrite ($\text{NiCoFe}_2\text{O}_4$)

Nickel cobalt ferrite ($\text{NiCoFe}_2\text{O}_4$) is a type of spinel ferrite with a chemical composition of $\text{Ni}_{1-x}\text{Co}_x\text{Fe}_2\text{O}_4$, where x is the ratio of nickel to cobalt, and for the sake of uniformity, its value is 0.5. $\text{NiCoFe}_2\text{O}_4$ possesses significant characteristics of high magneto-crystalline isotropy and high resistivity. Moreover, their fascinating properties make them ideal for diverse applications, such as magnetic data storage, microwave devices, magnetic sensors, and others. The below Figure 3.3 depicts the synthesized $\text{Ni}_{0.5}\text{Co}_{0.5}\text{Fe}_2\text{O}_4$ in powder form.

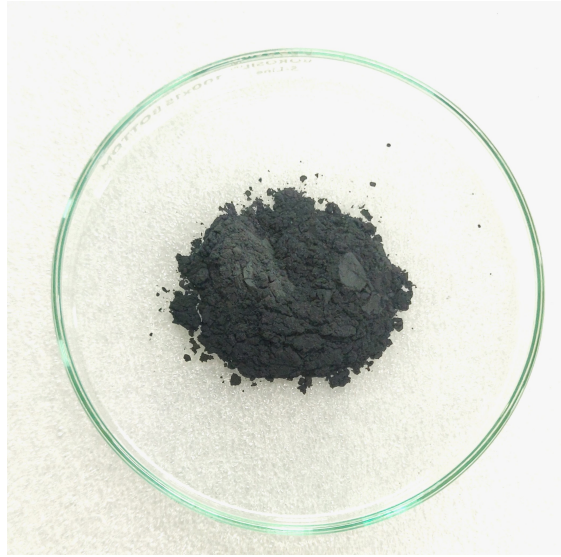


FIGURE 3.3: Bulk Ni_{0.5}Co_{0.5}Fe₂O₄ in powder form.

3.1.4 Polyaniline (PANI)

Polyaniline is a conductive polymer that belongs to the family of organic semiconductors. It is a synthetic polymer made by the polymerization of aniline, (an aromatic amine). Polyaniline can exist in several different forms, including emeraldine base, emeraldine salt, pernigraniline base, pernigraniline salt, and lucoemeraldine, which differ in their physical and electronic properties, depending on the synthesis.

One of the unique properties of polyaniline is its tunable electrical conductivity. Depending on the doping level, it can exhibit either metallic or semiconducting behavior. This property makes it useful for a variety of applications, such as in electronic devices, sensors, and batteries.

Polyaniline is also known for its environmental stability, biocompatibility, and ease of processing. It can be easily synthesized through chemical or electrochemical polymerization methods, and its structure can be tailored to meet the requirements of potential applications in energy storage, such as in supercapacitors and batteries, due to its high specific capacitance and charge-discharge efficiency.

In our system, polyaniline (PANI) has been synthesized in a stable form. Among all the forms of PANI, the Emeraldine base is regarded to be more stable at room temperature, and the fact that upon doping with acid (protonation), Emeraldine base becomes highly electrically conducting, known as Emeraldine Salt. Therefore, to improve the dielectric properties of PANI, we have synthesized PANI of emeraldine base (EB) via de-doping of emeraldine salt (ES), where electrical conductivity is found to be reduced in the order of 10^{-8} S m^{-1} at room temperature. The below Figure 3.4 depicts the synthesized PANI (Emeraldine Base) in powder form.

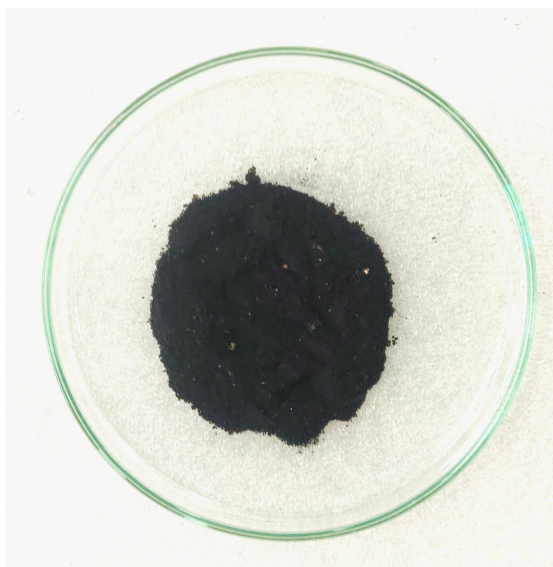


FIGURE 3.4: Bulk PANI (Emeraldine Base) in powder form.

3.2 Methodology

The methodology or synthesis process plays a vital role in the production of spinel ferrite, polyaniline (PANI), and spinel ferrite-PANI nanocomposite (NC). Various well-known properties of the spinel ferrite viz. structural, morphological, magnetic, and dielectric were highly influenced by the methodology utilized. However, these above properties also have a greater impact on the composition, type of dopant used, and sintering temperature of the prepared material. For the preparation of the PANI, an appropriate selection of dopant, oxidant, temperature, and synthesis techniques is required. For preparing the NC (spinel ferrite-PANI) a facile and quick synthesis procedure should be chosen for excellent entanglement of PANI with spinel ferrite nanoparticles (NPs). Furthermore, for the dielectric electrode preparation, the material relies heavily on the type of the conducting substrate, binder, and the substance's surface. As per our ability and extent, the best synthesis techniques for the synthesis of our materials are, sol-gel auto combustion, chemical oxidative polymerization (COP), and physical blending, which have been employed for the synthesis of the spinel ferrite, PANI, and spinel ferrite-PANI NC respectively. The detailed procedures for the preparation of the materials by these above-selected techniques along with the properties are mentioned one by one below.

3.2.1 Synthesis of Spinel ferrite

Figure 3.5 illustrated a variety of techniques are available to synthesize spinel ferrite, including hydrothermal, sol-gel, co-precipitation, ceramic, microwave, solid-state, and spray pyrolysis.

The sol-gel method is preferred over the other methods mentioned above due to its low cost, formulation of products with nanosized structures, homogeneity, formulation of thin films, mass production, reduction of the crystallization temperature, formulation of products with porous structures, minimal time required for product synthesis, and

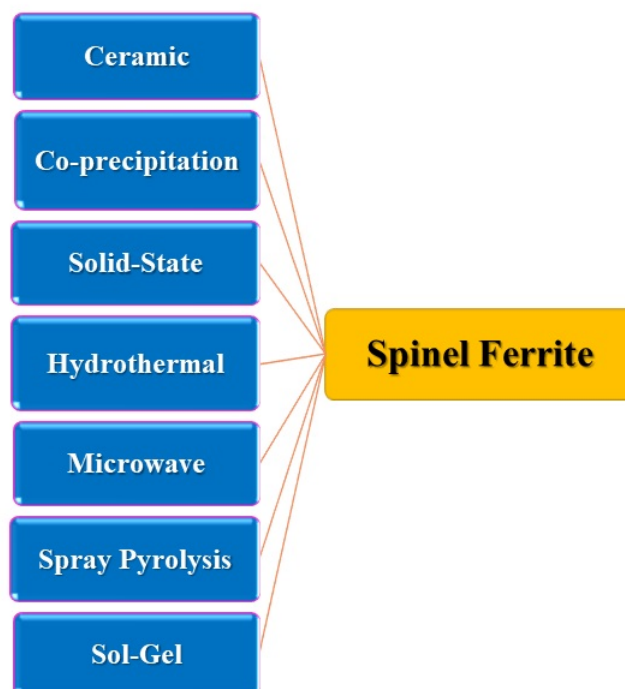


FIGURE 3.5: Techniques for Spinel ferrite synthesis.

formulation of immaculate products. Furthermore, this process is environmentally friendly because it uses water extracted from distillation as a solvent in the sol-gel [144].

3.2.1.1 Sol-Gel Auto Combustion Method

The wet chemical process known as the sol-gel auto-combustion method is the most widely used and simple approach for the creation of nanoparticles. It is mainly used for metal oxide synthesis. The popularity and wide acceptance of this method are attributed to its great advantages over other methods of synthesis such as the hydrothermal method, ceramic method, solid-state reaction method, and co-precipitation method. The advantages of the sol-gel process include regulated porosity and particle size, low operating temperatures, a minimal amount of costly supplies needed, high homogeneity, and the ability to synthesize thin films. The beginning of this process as depicted in Figure 3.6 is to convert monomers or starting material into a colloidal solution (sol) which acts as a precursor for the further formation of a gel [145].

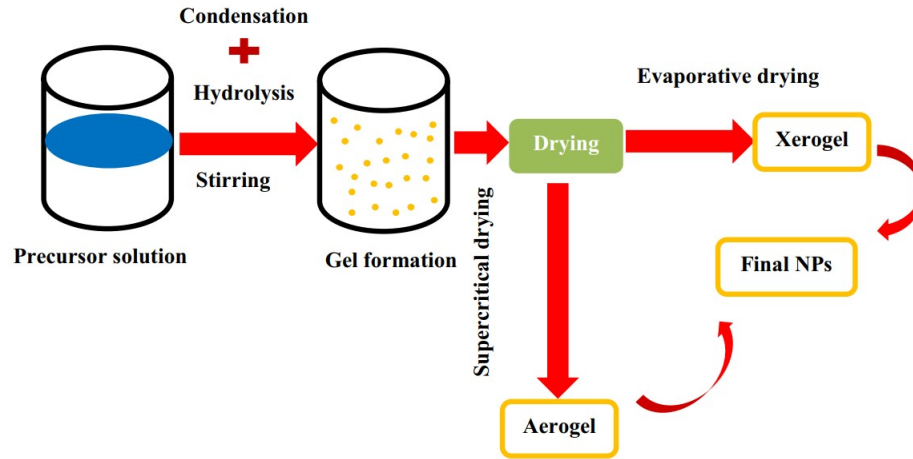


FIGURE 3.6: Schematic of Sol-gel auto-combustion for the synthesis NPs. [146]

The raw material such as metal nitrates or alkoxides is usually dissolved in a liquid medium such as ethylene glycol, distilled water, or a suitable acid to form a “sol” which is succeeded by aging and then heating of the sol to get what is named as “gel”, further drying or heating the gel at higher temperatures evaporate the liquid medium and transform the gel into a “precursor”. A sol is a colloid suspended in a liquid, however, a gel is a suspension that maintains its shape, thus the name “sol-gel”. The hydrolysis, condensation, and polymerization of monomers produce particles and particle agglomeration, followed mostly by the creation of a network that spreads across the liquid media, resulting in the formulation of a gel using the sol-gel auto-combustion method. Hydrolysis is a chemical breakdown of a compound when reacts with water whereas condensation is the conversion of a gas or vapor into liquid.

3.2.2 Sample Preparation $\text{NiCoFe}_2\text{O}_4$ (NCF)

Figure 3.7 illustrated, the sol-gel auto-combustion method for the synthesis of NCF spinel ferrites. AR-grade chemicals are employed in this method of production.

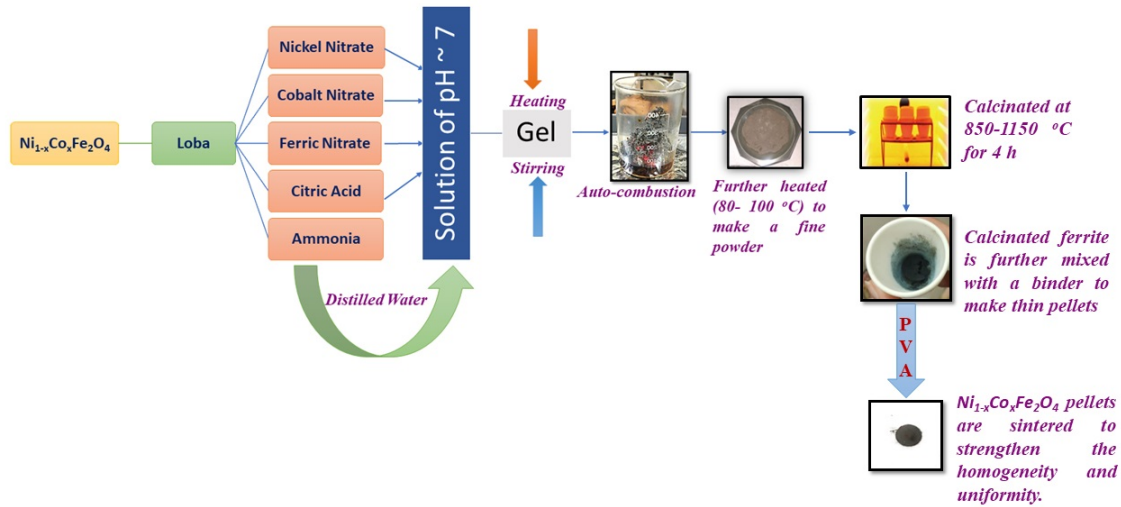


FIGURE 3.7: The detailed synthesis of $\text{NiCoFe}_2\text{O}_4$ (NCF) spinel ferrites via sol-gel auto-combustion method.

3.2.3 Synthesis of Polymer (Polyaniline)

As shown in Figure 3.8, the polyaniline (PANI) synthesis methods revealed by various research groups can be categorized as: (a) with oxidant and (b) without oxidant. The first part involves interfacial polymerization, enzymatic polymerization, solid-state polymerization, chemical oxidative polymerization (COP), microemulsion polymerization, plasma polymerization, electrospinning technique, and ultrasonic irradiation, while the latter part involves only electrochemical polymerization [147].

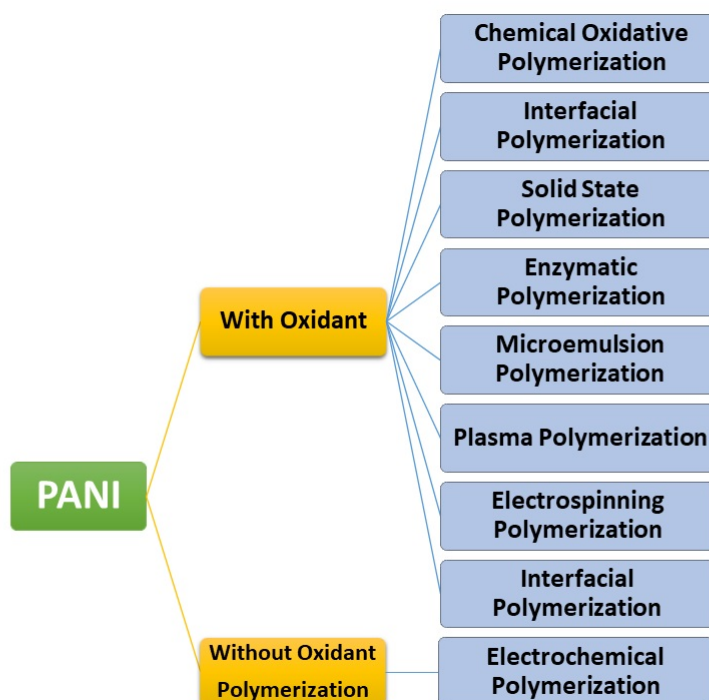


FIGURE 3.8: Different routes for synthesis of PANI

Because of its advantages and widespread use among the aforementioned procedures, chemical oxidative polymerization (COP) is suggested. [148][149][150]:

- The COP is a facile synthesis technique that yields immaculate PANI in bulk amounts.
- In COP the starting material used was cost-effective.
- The COP controls the growth and alignment of the PANI nanofibers.
- The COP will take less than 1 h to complete the polymerization of PANI.
- In the COP technique, the oxidant part could be cycled.
- The dosage of the oxidant utilised in the COP is extremely low due to its decreased molecular weight.
- Unlike other synthesis techniques, the PANI prepared by the COP technique can be deposited on both the conducting as well as non-conducting substrates.

- The PANI prepared by the COP technique doesn't require the nasty or toxic solvent for the preparation of PANI ink which is to be loaded on conducting substrate surface by utilizing spin or dip coating.

3.2.4 Sample Preparation Polyaniline (PANI) by Chemical Oxidative Polymerization (COP)

Polyaniline (PANI) is produced in an aqueous environment utilizing the dopants (HCl) and an oxidant (APS) in chemical oxidation polymerization (COP) [150][151]. The oxidant might remove a proton from the aniline monomer at this stage without forming a bond with the final product.

The monomer [aniline], oxidant [$K_3(Fe(CN)_6$, $(NH_4)_2S_2O_8$, $Ce(SO_4)_2$, H_2O_2 , $NaVO_3$, KIO_3 , $K_2Cr_2O_7$], and dopant [HCl, H_2SO_4] are involved for the chemical production of PANI. The most widely utilized and facile technique for the production of the PANI is the COP. In this technique, the monomer of aniline acts as a neutralizer by interacting with the doping reagent. The polymerization phenomenon occurs at different temperatures when the oxidizing reagent is added drop by drop to the aforementioned (aniline+HCl) solution. After 3 h, the PANI polymerization is pretty much under completion, and the resulting PANI is still in aqueous form. The PANI residues are collected by filtering the PANI solution, which is then washed repeatedly with distilled water to obtain a pristine PANI. The resulting PANI residue is then rinsed with acetone to render the colorless filtrate and ensure that all non-reactive elements are eliminated. The final PANI is emeraldine salt (ES) with a slime-green colour which is unstable in nature [152]. As a result, the ES state transforms to the emeraldine base (EB) state of PANI at ambient temperature, which itself is inherently stable, enabling these precipitates to reach equilibrium by dedoping with an adequate quantity of ammonia (NH_4OH) [153]. Figure 3.9 depicts the detailed synthesis of polyaniline (ES & EB) utilizing the chemical oxidative polymerization method,

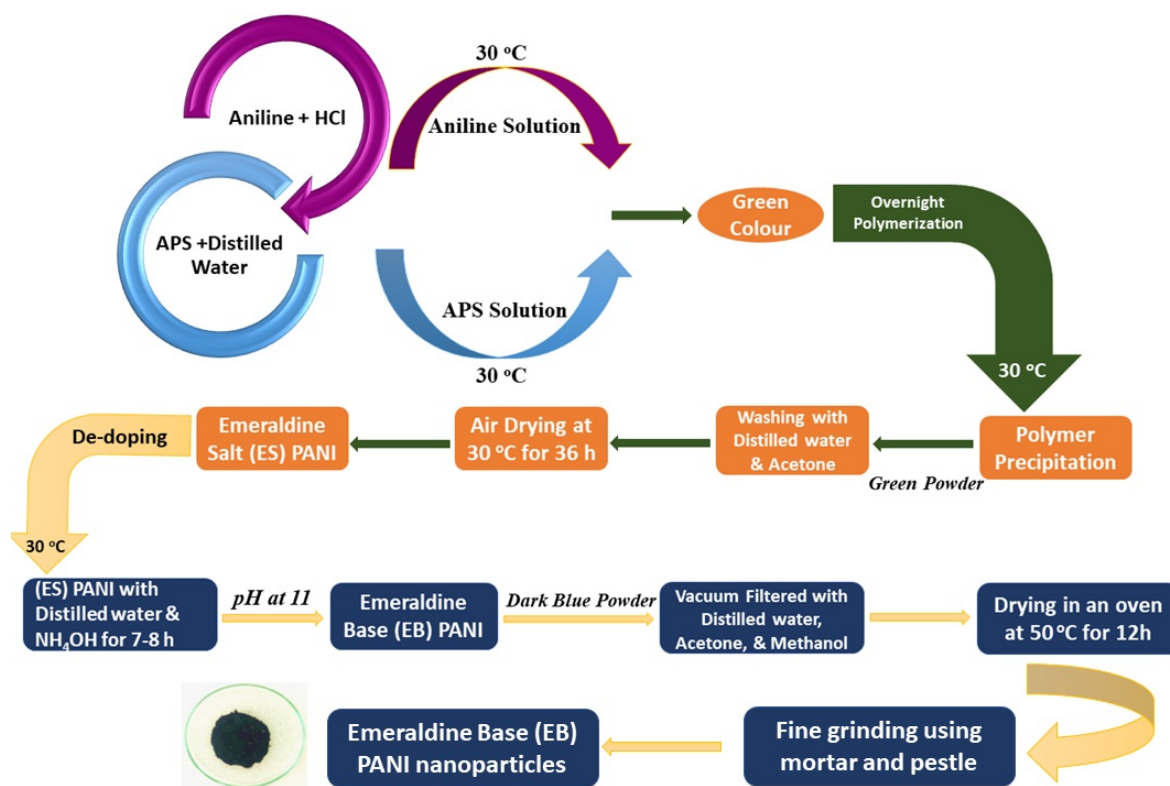
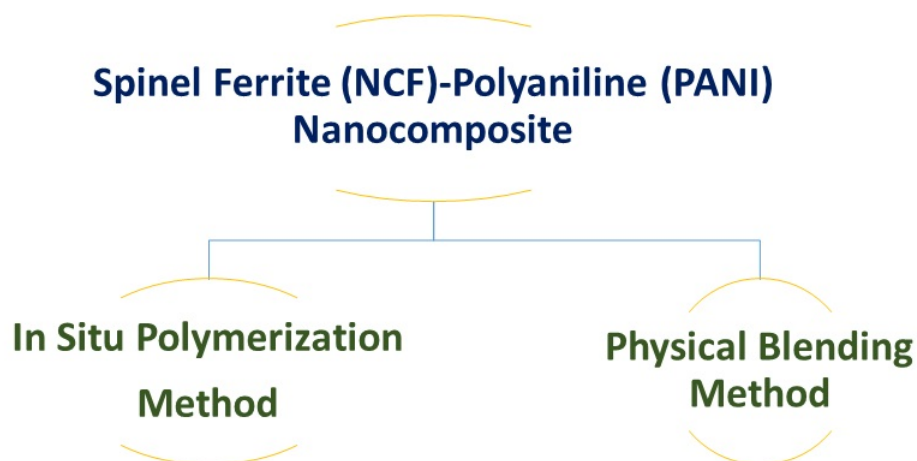


FIGURE 3.9: Chemical oxidative polymerization method for preparation of polyaniline.

3.2.5 Synthesis of Spinel Ferrite (NCF)-Polyaniline (PANI) Nanocomposite

In situ, polymerization and physical blending, also known as direct compounding, are the two main approaches used by scientists to create polymer PANI-based nanocomposite materials [154].

Depending on the kind of nanoparticles and polymeric matrix utilized, in addition to the desired qualities for the end product, a suitable approach has been implemented. Since it requires little effort, little time, and minimal expenses, the physical blending method is frequently employed to create PANI-based nanocomposite materials. In addition, compared to the in situ polymerization process, it is much more difficult to achieve a suitable dispersion of the nanomaterials in the PANI matrix when using the blending method.



3.2.5.1 Physical Blending Method

Physical Blending, sometimes known as direct compounding, is considered to be a facile and quick procedure to produce polymer nanocomposites (NCs). The solution, emulsion, melt, mechanical, and physical are the commonly known blending procedures, as illustrated in Figure 3.10. These blending procedures deal with the direct insertion of nanoparticles (NPs) into the polymer matrix in the required proportion. The preforms of polymers and NPs are prepared separately in this case before being blended together to produce the NCs. Aside from the benefits, there are also drawbacks to this procedure, as it results in non-uniform dissemination of NPs inside the polymer matrix owing to NPs agglomeration [155]. Regardless of the drawbacks mentioned above, the blending procedures continue to be utilized for the production of polymer NCs.

3.2.6 Sample Preparation of Hybrid (NCF-PANI) Nanocomposite

Recently, many polymer-ceramic composites have been successfully prepared, for the construction of traditional high-dielectric-constant polymer-ceramic nanocomposites. A great

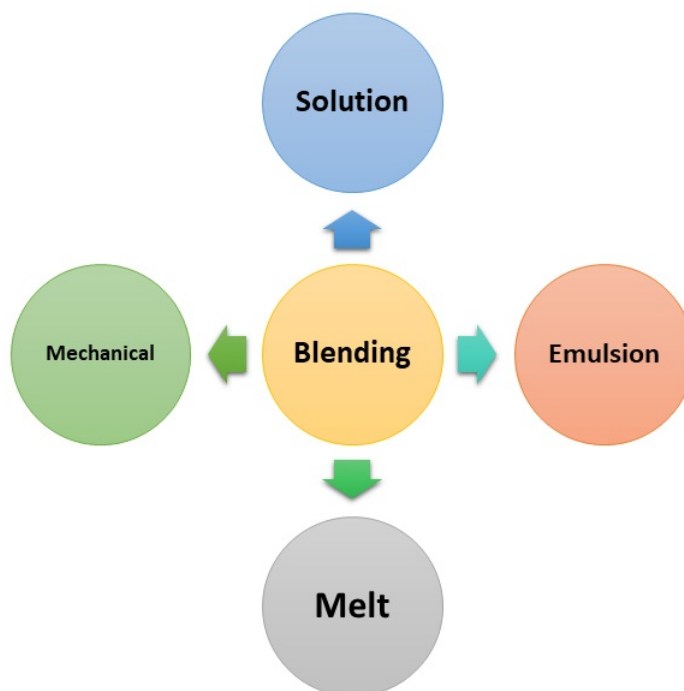


FIGURE 3.10: Blending method for synthesis of the hybrid nanocomposite.

challenge during the preparation of such polymer-ceramic composite films is how to homogeneously disperse fillers in the polymer matrix, which is responsible for the final properties of the composite.

The present work reports the preparation of hybrid composites $x\text{NCF}:(1-x)\text{PANI}$ via one of the ternary blend preparation methods known as physical blending. Additionally, it is also expected that combining two components with different degradation characteristics would alter the original characteristics of the components. Thus, the composites here are prepared by fine grinding and homogenous mixing of NCF ferrite in the polymer PANI matrix via mortar and pestle. Additionally, followed by mechanically pressing the samples using the cold-press technique via KBr mechanical press instrument. The $x\text{NCF}:(1x)\text{PANI}$ nanocomposites are prepared with respective weight fractions (wt.) of $x = 0, 0.1, 0.3, 0.5, 0.7,$ and 1 , where x is the NCF ferrite in the polymer matrix of PANI, as can be seen in the Figure 3.11.

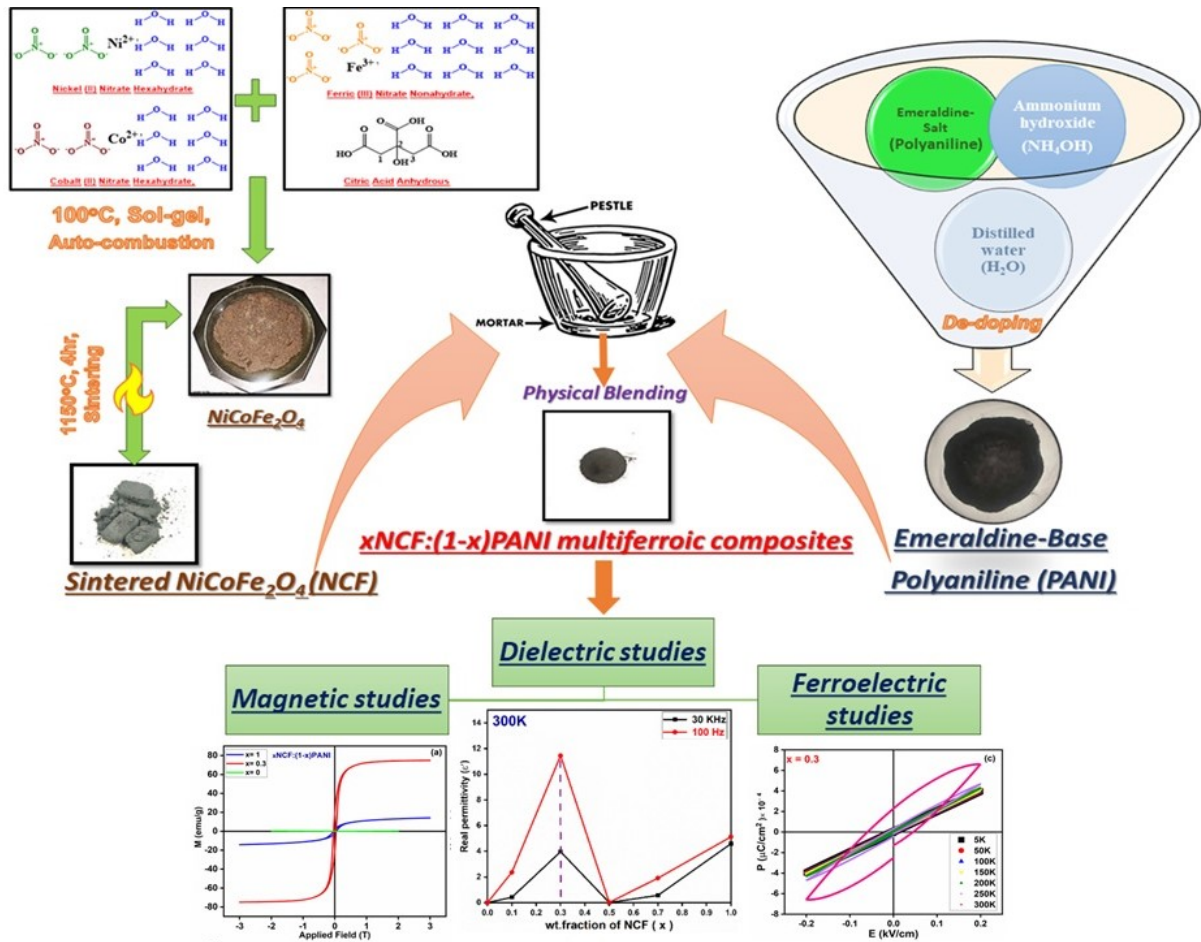


FIGURE 3.11: Synthesis of $x\text{NCF}:(1-x)\text{PANI}$ Nanocomposite via Physical blending method.

After the synthesis of hybrid nanocomposites, the nanocomposites as electrodes are fabricated. These electrodes are created using Ted Pella, Inc.'s Pelco conductive silver paint, which serves as the connection for the instrumentation. Figure 3.12 represents one of the working electrodes for the dielectric study.

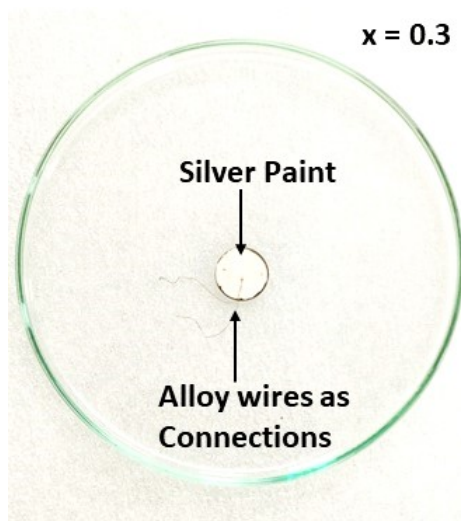


FIGURE 3.12: Fabrication of working electrode for $x\text{NCF}:(1-x)\text{PANI}$ ($x = 0.3$) nanocomposite.

Chapter 4

Physiochemical Characterization Techniques of Materials

4.1 X-Ray Diffraction (XRD)

One of the best methods for figuring out the materials' structure is the XRD process. The chemical substance may be recognized by XRD based on its crystal structure, and multiple phases of the same molecule can also be detected [156][157][158]. X-rays are electromagnetic radiation beams with short wavelengths and high energy. When a high-speed electron via a high-voltage acceleration field collides with a target (metal), X-rays are created. The kinetic energy of moving electrons transforms into X-ray radiation as a result of their fast deceleration.

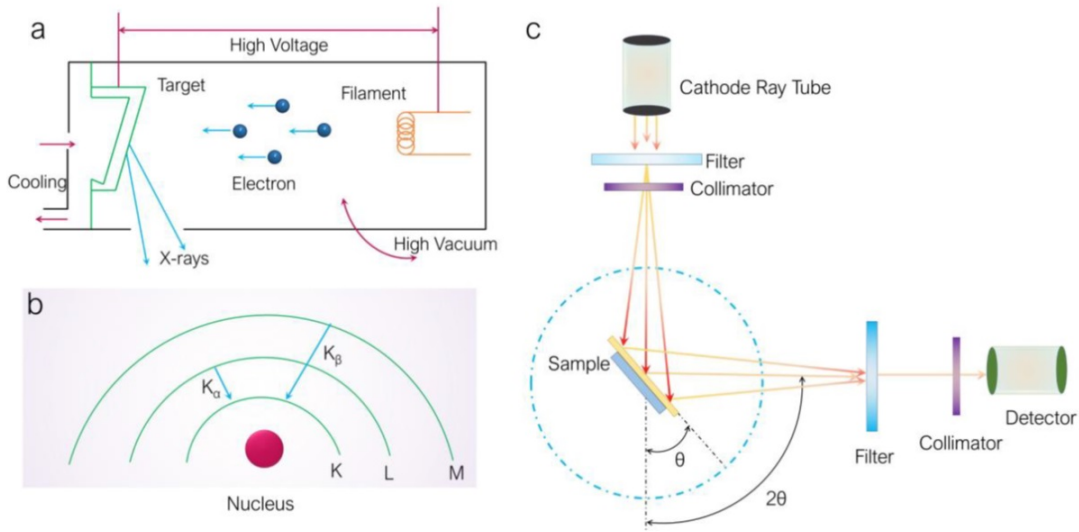


FIGURE 4.1: (a) Schematic representation for the generation of X-rays, and (b) concept diagram explaining the generation of K_{α} and K_{β} X-rays. (c) The complete schematic representation for the X-ray generation and diffracted rays' detection during the XRD experiment.

The X-rays wavelength radiation (λ in nm) can be related to the accelerating voltage of the electrons (V) by the following Equation 4.1 [157],

$$\lambda = (1.2398 * 10^3)/V \quad (4.1)$$

An X-ray tube (XRT) is needed in order to produce X-rays. Figure 4.1a illustrates the basic construction of an XRT, which consists of a stream of accelerated electrons and two metal electrodes in a vacuum. The application of a very high voltage between these two electrodes rapidly hit the fast-moving electron on the metal target (copper, iron, molybdenum, chromium). The windows of the XRT allow the X-rays that are created at the collision site to pass through. Although the XRT produces X-rays with a variety of wavelengths, only monochromatic X-ray radiation is necessary for the XRD methods. By removing other radiations from the spectrum using a nickel filter, monochromatic radiation is created.

Figure 4.2b provides an illustration of the fundamentals of characteristic X-ray production. A vacancy is generated when an incoming electron with sufficient energy knocks an electron from an atom's inner shell into a higher state, filling it with an electron from the outer shell. Radiation with a distinctive wavelength that is in the X-ray energy range is emitted as a result of the transition of electrons from a higher energy shell to a lower energy shell. The highly intense Cu K α radiation is widely used to characterize the samples. The crystal structure and phase detection of material are identified by determining the d spacing, and the obtained peaks are recognized by matching the ICDD (International Centre for Diffraction Data) database, also known as (JCPDS) Joint Committee on Powder Diffraction Standards.

Bragg's law governs the fundamental rule of X-ray diffraction in the crystalline structure, where λ is the source's wavelength, d is the interlayer spacing, n is an integer (order of diffraction), and θ is the incident angle. Bragg's law is given by Equation 4.2 [159][160]:

$$2d\sin\theta = n\lambda \quad (4.2)$$

Using Scherrer's formula and equation 4.3, it is possible to determine the sample's crystallite size from the full width at half maximum (FWHM) of the strongest diffraction line. [161]:

$$D = (K\lambda)/\beta \cos\theta \quad (4.3)$$

Here, D is grain size, β is FWHM of the peak in radians, θ is Bragg's angle, and K is constant. The 'K' value range varies from 0.89 to 1.39, but it is most commonly very close to 1.

4.2 Fourier Transform Infrared Spectroscopy (FTIR)

In order to determine the covalent bonds and functional group information of the prepared samples, Fourier-Transform Infrared Spectroscopy (FTIR) is an effective analytic technique. The spontaneous orientation of the dipole moment in materials is studied by the non-destructive tool using infrared spectroscopy that can provide information about inter-atomic forces within the crystal lattice. There are six different ways an organic/inorganic compound can vibrate: symmetrical and anti-symmetrical stretching, wagging, rocking, scissoring, and twisting [162]. FTIR spectrometer; of Perkin Elmer company is used for characterization, as shown in Figure 4.2.

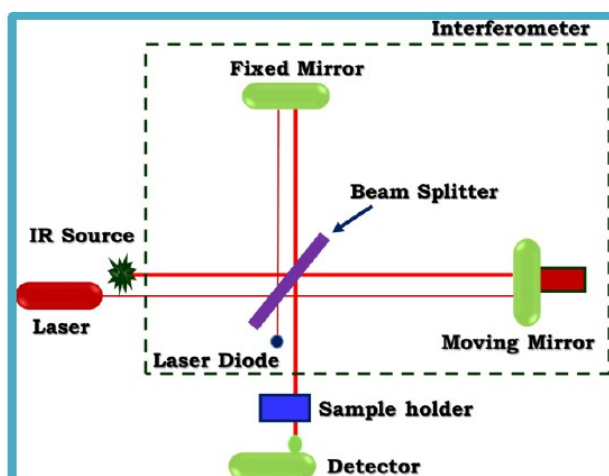


FIGURE 4.2: Schematic representation of FTIR spectrometer. [163]

The infrared vibrational frequencies and inter-atomic forces are correlated, so it is used to investigate functional groups in the material. According to the Planck-Einstein relation, energy transfer between different energy states of molecules can be written as the following Equation:

$$\Delta E = h\nu \quad (4.4)$$

Here ΔE , h , and ν represent the change in energy, Planck constant, and frequency respectively. The positive ΔE means the molecule absorbs energy; when ΔE is negative, it emits

energy in the form of radiation, and thus emission spectrum is obtained. When Equation (4.4) is satisfied, an absorption spectrum is obtained, which is particular to a molecule under investigation. The spectrum is normally presented as an intensity plot versus frequency and absorption peaks obtain when Equation (4.4) is satisfied. A spectrum close to a visible region (comparatively small portion) is used for spectroscopic investigations. This portion incorporates UV-VIS and IR regions (10 nm to 1 mm). The different absorption spectra can be observed from atoms and molecules, because of the nature of energy levels in transition. The transition of electrons between orbitals of atoms takes place due to the absorption of energy. However, the atoms vibrate in a molecule and it moves due to the absorption of energy [164]. A few transition energies such as rotational, vibrational, and electronic are possible to measure. Usually, translational energy can be ignored, since it is sufficiently small. The vibrational spectrum is believed to be a unique physical characteristic of molecules. Therefore, the IR spectrum is supposed to be a fingerprint for material identification [165].

4.3 X-ray Photoelectron Spectroscopy (XPS)

An analytical method used to determine a sample's chemical composition and electronic structure is called X-ray photoelectron spectroscopy (XPS). It works by bombarding a sample with X-rays, which causes the electrons in the outermost shell (the valence electrons) of the atoms in the sample to be emitted. These emitted electrons are analyzed to determine their kinetic energy and angle of emission, from which the sample's chemical composition and electronic structure can be inferred [166][167]. The working principle of XPS is based on the photoelectric effect, which is the phenomenon in which electrons are emitted from a material when it is irradiated with electromagnetic radiation [168]. In the case of XPS, the electromagnetic radiation used is X-rays. When the X-rays interact with the sample, they cause the valence electrons to be emitted, and these electrons are collected and analyzed.

The kinetic energy (K.E) of the emitted electrons is related to the binding energy of the electrons in the sample, which can be used to identify the elements present in the sample and the chemical state of the atoms. The emission angle is also used to identify the location of the atoms within the sample. This is achieved by exposing the sample to mono-energetic Al $k\alpha$ X-rays, which induces photoelectron emission from the surface. An electron energy analyzer is then utilized to measure the energy of the produced photoelectrons. The resulting binding energy-dependent intensity plot makes it possible to ascertain the surface's chemical state, elemental breakdown, and quantities of elements. [169]. Additionally, the kinetic energy of the emitted photoelectrons can be used to determine their binding energy and identify elements present in the sample. Different components of the XPS instrument are shown in Figure 4.3a.

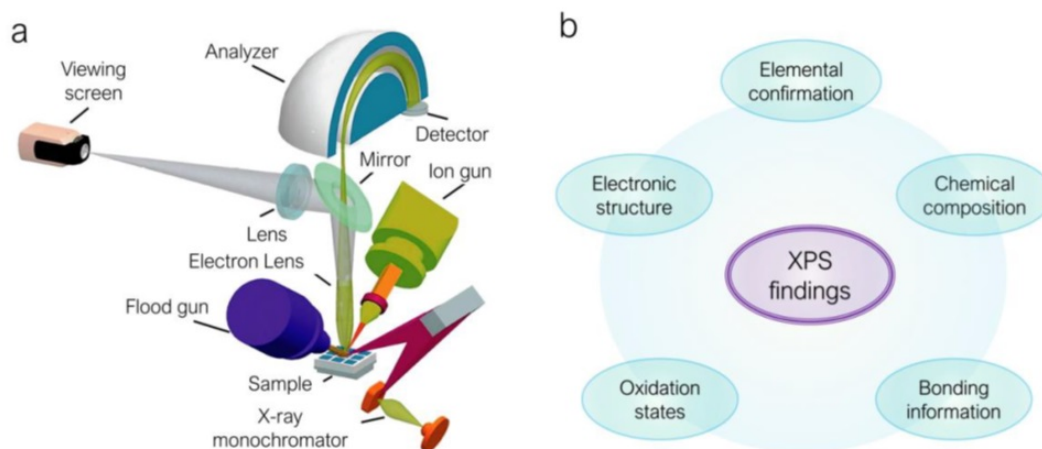


FIGURE 4.3: (a) Schematic illustration shows the XPS measurements' instrumental arrangement. (b) Various sample properties identification using XPS measurements.

The key findings of XPS measurements are displayed schematically in Figure 4.3b. The main advantages include determining the material's chemical state by observing slight shifts in the elemental binding energy, known as chemical shifts, caused by differences in the chemical environment of the elements in compounds. The semi-empirical formula for the material under investigation can also be predicted based on the findings.

4.4 Field Emission Scanning Electron Microscopy (FESEM)

Field-emission scanning electron microscopy (FESEM) is an analytical characterization that uses a beam of electrons to create detailed images of a sample's surface [170]. This scanning electron microscopy (SEM) type utilizes a field emission gun as the electron source. The electron gun uses an electric field to emit a highly focused beam of electrons, which is then directed onto the sample surface. The sample emits secondary electrons (SEs) from the surface whenever the beam of electrons encounters it. These SEs are collected and used to create a representation of the sample's surface. The sample's arrangement, framework, and primary electron beam's energy all affect how many SEs are released. As the electrons are focused on a small area, the resolution of the images obtained is high, and the details of the sample surface can be seen clearly. It is used to study materials' microstructure, morphology, and composition at high resolution [171].

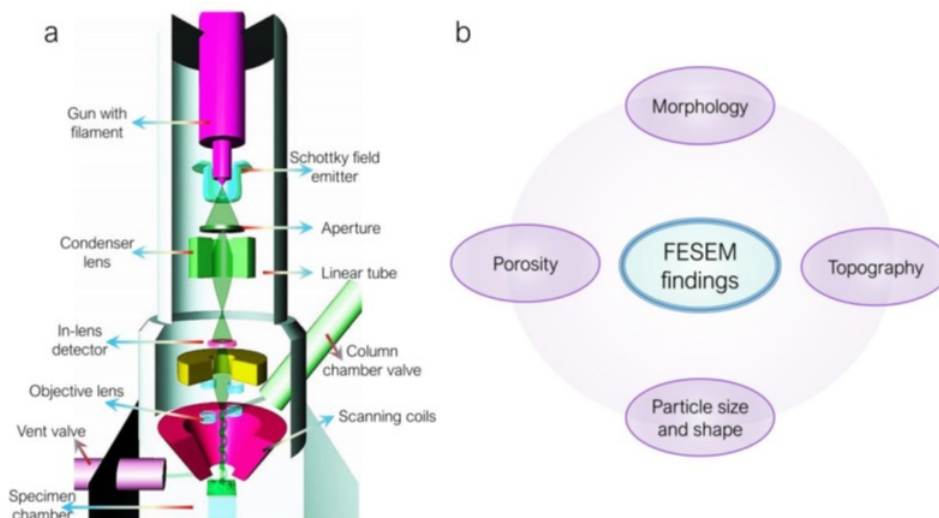


FIGURE 4.4: (a) FESEM column showing the different components, and (b) the findings of FESEM measurements are shown pictorially.

The schematic representation of the different components of the FESEM instrument is shown in Figure 4.4a. The gun produces a beam of electrons in order to focus on the sample, where the aperture and condenser lens are employed. The objective lens further aligns the broadness of the beam on the sample. The scanning coils are used for rastering the sample area. The sample findings like morphology, topography, particle size, and shape, and for microporous materials, the porosity can be seen visually by the FESEM images (Figure 4.4b). Thus, FESEM is a powerful analytical technique that utilizes a beam of electrons to create detailed images of a sample's surface. It is based on how the sample and the electron source interact, and it uses the secondary electrons emitted from the sample surface to create an image. The electron beam is highly focused, resulting in the images' high resolution. It can be used to study materials' microstructure, morphology, and composition at high resolution.

4.5 Energy dispersive X-ray spectroscopy (EDS)

As previously discussed, when electrons interact with a solid, they generate a variety of indications, including secondary electrons (SEs) and X-rays, and back-scattered electrons (BSEs), which are characteristic of the atoms in the host framework. Among these signals, X-rays are used to detect and quantify the elements present in the sample for compositional analysis. It is worth noting that the signals created by how electrons interact with substances, such as X-rays, SEs, and backscattered electrons (BSEs), provide valuable information [172]. The X-ray signals, in particular, are used for elemental analysis and quantification. The EDS measurements allow identifying the different elements in the sample under investigation, their chemical composition, and their distribution in the different parts of the sample. Figure 4.5a briefly depicts the working of the EDS measurements.

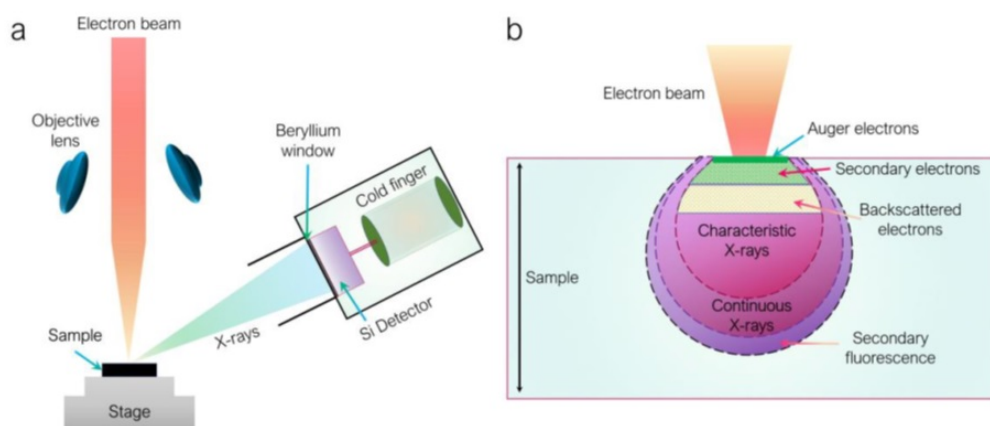


FIGURE 4.5: (a) The schematic description for the working of the EDAX setup. (b) The graphical representation displays the interaction volume of incident electrons.

Figure 4.5b shows the sample's interaction volume with the incident electron beam. The generation of Auger electrons occurs at the surface's uppermost 3-5 nm, whereas the emission of secondary electrons is observed at a slightly more profound level of 50 nm. Furthermore, backscattered electrons are emitted from a depth of approximately 500 nm. The characteristic and continuous X-rays are generated from the deeper regions in the 1-2 μm [173][174]. It is essential to note that EDS has certain limitations in terms of sensitivity. One of the limitations is that when an element's concentration in the sample is inadequate, the X-rays' energy may not be enough to accurately establish the element's composition, thus making it challenging to detect elements that are present in small concentrations. Additionally, EDS is not typically effective for elements with atomic numbers that are too low, such as hydrogen and helium, which have only one shell ($n=1$) and lack core electrons that can be removed to produce X-ray emission. This makes it challenging to detect these elements using EDS. Furthermore, elements like lithium and beryllium, which have atomic numbers that are too low, may not emit enough energy for EDS to measure them accurately. Thus, it may be challenging to test for their presence using this technique.

4.6 High-Resolution Transmission Electron Microscopy (HRTEM)

HRTEM is a powerful technique for the characterization of materials at the nanoscale. It is based on the transmission of a highly-coherent electron beam through a thin sample, which is then projected onto a detector, typically a CCD camera or a film. The high-resolution capability of HRTEM is achieved by using electron lenses with high numerical apertures, which result in a minimal probe size and a high electron wavelength. One of the main advantages of HRTEM is its ability to provide atomic-scale imaging and structural information. The high resolution of the technique allows for the identification of crystal lattice planes and the determination of crystal structures and defects [175][176]. Additionally,

HRTEM can be used to study materials' composition and chemical bonding and samples' electronic structure and properties. Various components of the HRTEM instrument are shown in Figure 4.6a. Further, the different findings of HRTEM are pictorially represented in Figure 4.6b. The HRTEM provides highly detailed and accurate information about the samples under investigation.

HRTEM can also be combined with other techniques, such as electron energy loss spectroscopy (EELS), to provide complementary information about the samples. EELS can be used to analyze the chemical composition of samples, while the scanning TEM (STEM) mode helps in contrast imaging and elemental mappings at the atomic scale [177][178][179].

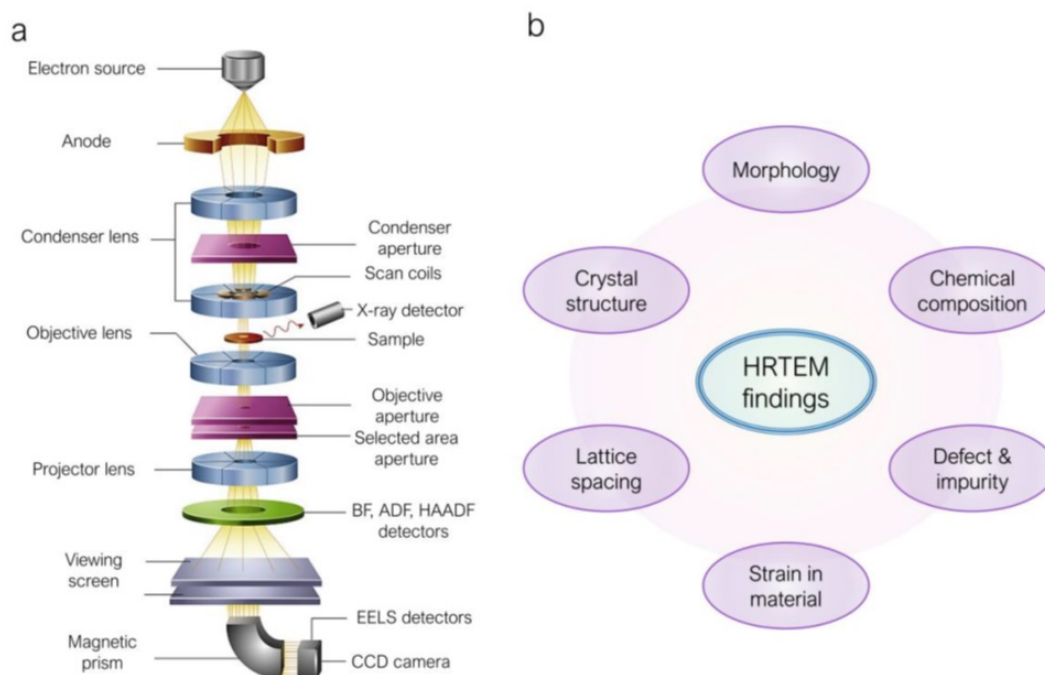


FIGURE 4.6: (a) Schematic diagram of HRTEM instrumentation showing different lens and detectors arrangement. (b) HRTEM allows for the investigation of various properties of samples, such as crystal structure, lattice defects, and composition, at a high level of resolution.

Despite its many advantages, HRTEM also has some limitations. One of the main limitations is that the samples must be thin, typically less than 100 nm, in order to obtain high-resolution images. This can be challenging for certain types of samples, such as thick films or powders. Additionally, HRTEM requires the use of highly-coherent electron sources, which can be costly and difficult to maintain.

4.7 Superconducting Quantum Interference Device (SQUID)

(SQUID) Magnetometer is used by the Quantum Design MPMS3 to track minute variations in magnetic flux and as a result, learn about the magnetic characteristics of samples. It monitors the sample's magnetic moment and has a very high sensitivity for magnetic measurements. The magnetization and magnetic susceptibility may be calculated from this. DC analysis and vibrating sample magnetometry (VSM) were included in MPMS3.

The SQUID magnetometer may be used for a variety of tasks, such as measuring minute amounts of paramagnetic ions, characterising various magnetic materials, and counting unpaired electrons quantitatively in samples. In important fields including high-temperature superconductivity, biology, and magnetic recording media, the MPMS3 offers solutions for a special class of sensitive magnetic measurements. The modular MPMS3 design incorporates an advanced computer operating system, a high-field superconducting magnet bore-mounted temperature control device, and a SQUID detecting system. Privately developed software that runs within the user-friendly MS Windows environment enables complete automation of all system settings while regulating measurements, facilitating rapid and simple data gathering and analysis. Following are the specifications of the SQUID instrument, Maximum Sample Size should be 9 mm, High homogeneity magnet configuration should be ± 7.0 Tesla, Field Uniformity can be 0.01% over 4 cm, Maximum sensitivity of the instrument is in the range of 10^{-8} emu, Temperature Range should be

1.8 – 400 K, Sample Requirements should be around 20 to 40 mg in powder form. The snapshot of the MPMS3 Quantum Design, which uses a Superconducting Quantum Interference Device (SQUID) Magnetometer at IIT Roorkee, can be seen in Figure 4.7.



FIGURE 4.7: Quantum Design MPMS3 (SQUID) Superconducting Quantum Interference Device Magnetometer at IIT Roorkee

4.8 Impedance Spectroscopy

The most accurate method for determining a material's resistance and capacitance qualities is called impedance spectroscopy, and it involves applying a sinusoidal AC excitation signal that ranges from 2 to 10 mV. You may create an impedance spectrum by changing the frequency across a predetermined range. It is also used to investigate how temperature and frequency affect dielectric reactions. By measuring the in- and out-of-phase current responses, the capacitance and resistance of the system may be determined. One of the most used techniques for evaluating electrodes for energy storage applications is impedance spectroscopy (IS).

In our project, Impedance spectroscopy is used to analyze the electrical behavior to distinguish between the contributions of the grains, grain boundaries, and electrodes to the overall conductivity of the materials (Chapter 7).

4.8.1 4 K CCR for zero Field resistivity, Dielectric, and P-E loop measurement

The following instrument is used both for the study of the dielectric and ferroelectric properties, below room temperature by keeping it in a closed cyclic refrigerator (4 K CCR).

For the study of electrical measurements, the flat surfaces of pellets acted as electrodes, where the conductive silver paste was applied on both faces of polymer-ceramic samples, and further kept for air drying. Temperature and frequency-dependent dielectric measurements are performed for nanocomposites via 4 K CCR (closed cyclic refrigerator) instrument at temperature and frequency ranges of 5 K to 300 K and 100 Hz to 1 MHz respectively. The temperature and frequency-dependent (P–E) hysteresis loops are measured using a cryocooler model SRDK-205 circuit via 4 K CCR at 5 K-300 K and

50 Hz-250 Hz respectively. The preferred mode of sample used in the instrument is in the form of pellets and thin films. Figure 4.8, shows the instrument at UGC-DAE CSR Kolkata, for CCR measurement of zero-field resistivity at 4 K, dielectric, and P-E loop analysis.

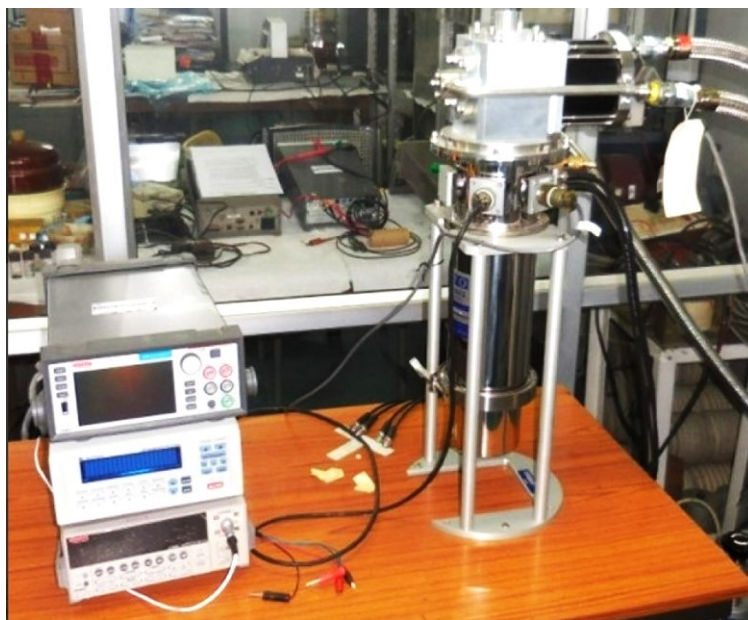


FIGURE 4.8: 4 K CCR for zero Field resistivity, Dielectric, and P-E loop measurements at UGC-DAE CSR Kolkata

4.9 Instrumentation

The weight proportion of the metallic component was changed to create a collection of composite samples. The range of the weight (wt.) fractions (x) is 0 to 1, or 0 to 100 %. The formula for the metallic component's weight fraction is provided as wt. fraction = $(mx)/[mx + m(1-x)]$. Here, m represents the powder's overall mass. The photos of every piece of experimental equipment are displayed below.

4.9.1 Mortar and Pestle

Laboratory mortar and pestle are a pair of tools used to finely crush and grind substances into a powder or paste. A porcelain mortar and pestle set are sufficient for most laboratory applications, as unglazed porcelain is hard enough to crush most materials while being resistant to high temperatures. For labs concerned with contamination, an agate mortar and pestle set is preferred, as polished agate is an economical material with low porosity. Figure 4.9, represents the used agate mortar and pestle in the laboratory.



FIGURE 4.9: The agate mortar and pestle used for fine grinding of powders.

4.9.2 Cold Press Die-set

The powder is compressed into the desired number of pellets using pressure in the dry pellet pressing die-set. A cold press die-set with a 12 mm diameter has been employed in

our project. Moreover, to grind the desired materials into the correct granularity of powder (from millimeters to microns), the use of methods such as powder processing, ball milling, sol-gel process, etc, in combination with agate mortar and pestle sets are preferred. Figure 4.10, represents the used Cold Press Dye-set (diameter of 12 mm) in the laboratory.



FIGURE 4.10: Cold Press Dye-set of 12 mm diameter.

4.9.3 KBr Press

It is a small hydraulic press that is efficient at producing pressure in the range of Tons. It has a variety of ranges that can make pellets of specimens for characterizations. Figure 4.11, represents the KBr press.



FIGURE 4.11: KBr press instrument

Chapter 5

Influence of TiO_2 as a reinforcement in a NaCl matrix

Abstract

Energy storage in sustainable nanotechnologies is increasingly being done with high-dielectric capacitors. When TiO_2 is used as a filler in the NaCl bulk matrix, we see a significant increase in the dielectric constant by 3 orders at frequency 1 kHz with just a mild loss. The TiO_2 nanoparticles are produced using the sol-gel method and then added to the ionic matrix of NaCl, which is denoted as $\text{TiO}_2(x)\text{NaCl}$, in variable weight percentages x . With different fractions of TiO_2 and a frequency range below 25 kHz, characteristics like dissipation loss, dielectric constant, and ac conductivity are measured. The initial dielectric peak at $x = 50$ is caused by percolation-type behavior, which is indicated by a steady rise in the dielectric constant as filler concentration at low frequency increases. For $x < 45$, it is discovered that the dielectric loss is approximately 1, whereas it tends to rise with a higher filler fraction. Additionally, as shown by the AC conductivity test, the frequency-dependent polarisation in this composite system also explains the hopping-type behavior of mobile charge carriers provided by TiO_2 . X-ray diffraction and field emission scanning electron microscopy are also employed to characterize the materials in order to

study their structure and shape. Overall, TiO₂ inclusion significantly enhances the ionic matrix's dielectric behavior at low frequency, qualifying it as a super dielectric material (SDM).

5.1 Introduction

Green technology is currently a rapidly growing field aiming to improve our surroundings by making us less dependent on non-renewable energy resources as they are furiously consumed at a faster rate than ever [180][181][182]. Large volumetric capacitors are one such green device that is used in a multitude of applications such as renewable energy as energy storage sources. Earlier, it had been widely observed that storage devices like Memory chips which use just a single capacitor to represent 1 or 0 illustrate the unsustainable approach to green technology. Since millions of capacitors tend to occupy at least a few tenths of a square m of the total area, the situation has been alarming considering the growing demand for miniature devices in form of ICs (Integrated circuits). This has left us with no other alternative rather by putting billions of transistors on 1mm*1mm chip responsible for the functioning of nearly all modern devices from an automobile to supercomputers. Given the above, storage devices with efficient storage and low power consumption and losses should be considered.

Capacitors being one of them, with large volumetric capacitance or High-K dielectric materials can be a prominent as well as effective way out. Capacitors on other hand can prove detrimental to the whole gadget if the size is shrunk below a limiting thickness. On reducing the thickness, capacitors are either likely to suffer from charge leakage or prone to shorting between electrodes, thus devaluing the actual storage ability of a capacitor. The development of super-capacitors or double-layered capacitors and other traditional approaches have so far raised the volumetric capacitance to 10^2 cm^3 , thus making it an average performer among energy storage devices [3]. Moreover, the electrolyte in the electrolytic capacitors tends to degrade or evaporate with time and does not make it

compatible with an AC power source as well. The other unconventional approach to increase the capacitance is by improving the magnitude of a material's dielectric constant itself rather than tweaking the geometrical cross-sectional area or the distance between the plates. Following the equation (1) of parallel plate configuration, we know that,

$$C = \kappa\epsilon_0 \frac{A}{d} \quad (5.1)$$

where κ is the dielectric constant, ϵ_0 is the free space permittivity, A is the cross-sectional area and d is the distance between the plates. Therefore, it becomes evident from equation (5.1) that, the material's dielectric constant has a direct relationship with the capacitor's capacitance C , which assures the only solution left, is to develop higher- k materials to enable the capacitor dielectric to maintain a robust thickness while still providing sufficient charge storage with a continuously shrinking area [20].

In optoelectronics and storage devices, transition metal oxides have a wide range of applications that have been extensively studied by numerous researchers for about 30 years. In the last ten years, titanium dioxide (TiO_2) became the most well-known and widely used of all the transition metal oxides. The fact lies in the production of (TiO_2) titanium dioxide, because of its common nontoxicity, chemical stability, availability, polymorphism, optoelectronics as well as high photocatalytic properties, low cost, and as high dielectric constant (κ) value material. Since titanium dioxide (TiO_2) is polymorphous in nature, it has different dielectric constant (κ) values for its polymorphs (Anatase, Brookite, and Rutile), where rutile being the most thermodynamically stable phase is studied widely. Due to its high dielectric constant, titanium dioxide in the form of rutile can be used as a filler in hybrid (or organic-inorganic) composites as well as low-temperature cofired ceramics (LTCC) [183] [184] [185]. The dielectric constants of the components—polymer matrix, ionic matrix, and inorganic filler—which make up a composite material determine its dielectric characteristics. As a result, TiO_2 nanoparticles in rutile form having a nanoscale size, low dispersity, and high values of dielectric permittivity are essential for use in present electronics [186]. Numerous authors have reported on the improvement in the

dielectric properties and the study of composites using TiO_2 as filler in organic/ionic matrix, organic-organic matrix, and organic-inorganic matrix. Researchers investigated the structural, ionic conduction, morphological, and dielectric polarization with an increase in nano-filler concentration of TiO_2 [187] [188]. By improving sodium chloride (NaCl) by functionalizing it with two of the oxides, Marie Bermeo et al. demonstrated their work for hygroscopic materials. He analyzed that NaCl- TiO_2 and NaCl- SiO_2 exhibited fascinating hydrophilic properties, compared to the individual NaCl [189]. S. Devikala, et.al worked on the corrosion resistant behavior of the polyvinyl alcohol/ TiO_2 composites in the vicinity of NaCl matrix for the prevention of corrosion in marine structures from the seawater [190]. Given the above-mentioned literature in this field, diverse research has been conducted on the NaCl- TiO_2 composite along with other organic-inorganic blends in the composite system. Yet, no valid report is available on the dielectric study of $\text{TiO}_2(x)\text{NaCl}$ composite system (x is the varying weight percentage in the ionic matrix) for the possible applications in ionic storage systems.

In this work, an optimized method for the production of titanium dioxide (TiO_2) has been preferred. Nanostructured TiO_2 can be produced by various wet chemistry methods like precipitation, thermohydrolysis, sol-gel, and hydrothermal route processes. Here sol-gel being the most convenient process has been used for the synthesis of TiO_2 , which acts as a filler in the ionic matrix of NaCl. Further research is done on the composite system's dielectric properties in order to determine potential applications in ionic storage systems. From the Group-1 elements (the alkali metals), Lithium has been potentially used as well as exploited for energy storage devices. Recently, scientists have created lithium-metal batteries which are more stable, powerful, and long-lasting, they can even charge an electric car in a few minutes. However, the increasing demand has led to the degradation of lithium resources, which has compelled scientists to rethink the feasibility and availability of Li [191]. Na is the most abundant alkali metal present in the Earth's crust. Also, it exists in a variety of forms (such as sea salt and rock salt). Therefore, it is thought to be a suitable candidate close to Li in Group 1 of the periodic table. The composite system

TiO₂(x)NaCl was further characterized using XRD, FTIR, and FESEM. Along with the study of the samples' dielectric properties, the samples' structure and morphology were also examined.

5.2 Experimental

5.2.1 *Titanium dioxide (TiO₂) nanoparticles*

Titanium (IV) isopropoxide (97 %, Ti (CH(CH₃)₂), Ethanol (96 % (CH₃CH₂OH)) were preferred by Sigma-Aldrich, whereas Sodium chloride (99.5 % AR/ACS (NaCl)) and Hydrochloric acid (37 % AR) from Loba Chemie Pvt. Ltd. were used. The usage of all reagents was unpurified and they were all commercially available.

Using a sol-gel method, titanium (IV) isopropoxide (TTIP) was dissolved in 100 % ethanol and stirred using a magnetic stirrer for at least 30 minutes to form the nanoparticles of titanium dioxide, maintaining the temperature range from 60-80 °C of the solution. The pH value of the solution was measured at 6 using litmus paper. In the next step, a mixture of hydrochloric acid (HCl) and distilled water, while maintaining a pH value of 1, has been added to the (TTIP + ethanol) solution dropwise under constant stirring. The concentration of hydrochloric acid (HCl) was 0.5 M and Table 5.1, illustrates the amount of other materials used. After 2 hours of vigorous swirling at 80 °C using a magnetic stirrer, a homogeneous solution was produced. A sol was created and aged for 24 hours to produce the gel-like structure. The structure's pale pink color denotes its acidic nature. The gel was centrifuged for 15 min. at 100 rpm to separate out the nanoparticles, and it was then dried for 30 min. at 80 °C to completely evaporate the water and organic material. To produce the necessary TiO₂ nanoparticles, the residual powder was calcined in the muffle furnace at 450 °C for three hours.

Table 5.1. Materials in molar concentration (M).

S.No.	Materials	Concentration (M)
1)	TTIP	1
2)	Ethanol	4
3)	Distilled water	10
4)	HCl	0.5

5.2.2 $TiO_2(x)NaCl$ nanocomposites

Once the synthesis of TiO_2 nanoparticles has been completed, the $TiO_2(x)NaCl$ nanocomposites were prepared by mechanical blending via mortar pestle and, the KBr mechanical press instrument. The pure Sodium chloride (99.5 % AR/ACS (NaCl)) and TiO_2 nanoparticles synthesized, was used with varying weight percentage $xTiO_2$ for the formation of composites. Further, all the composites prepared with varying weight percentages (%) TiO_2 ($x= 0, 10, 50, 80, 100$) were taken into consideration for analysis and investigation.

5.3 Results and Discussion

5.3.1 X-Ray Diffraction (XRD)

The XRD patterns for powdered samples NaCl, TiO_2 nanoparticles, and the composite $TiO_2(x)NaCl$ are shown in Figure 5.1. The powdered samples were analyzed using $Cu-K\alpha$ X-rays of wavelength (λ) = 1.5406 Å for confirming the presence of TiO_2 and NaCl crystal structures. Figure 5.1 (A) represents the NaCl (Halite) crystal structure in the cubic system, with a face-centered lattice fcc (space group Fm3m) typically for (111), and lattice parameter $a_o = 5.64$ Å as confirmed from the literature [192] and in agreement with the JCPDS card no. 01-070-2509 NaCl (Halite). The strong diffraction peaks appeared at 2θ with 31.68° , 45.15° , 66.17° , corresponds to the crystal planes of (200), (220), and

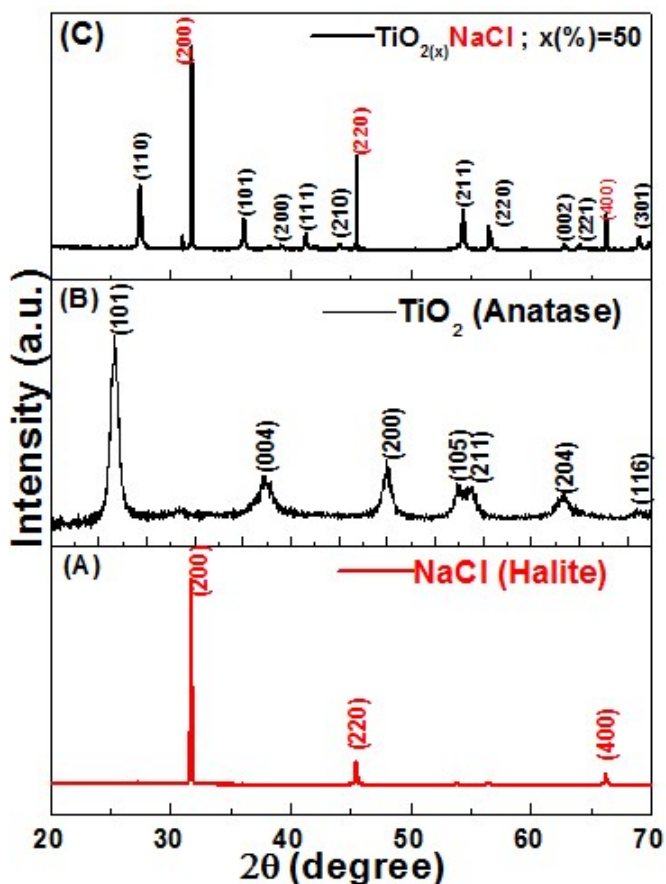


FIGURE 5.1: (A) The XRD structure of NaCl (Halite), (B) The XRD structure of TiO₂ (Anatase), (C) The XRD pattern of TiO₂(x)NaCl composite; where x (%)=50.

(400) respectively, which is in agreement with the reported literature [193] for the NaCl (Halite) sample. The XRD pattern of TiO₂ (Anatase) is represented in Figure 5.1 (B). The experimental XRD pattern for TiO₂ (Anatase) is in agreement with the JCPDS card no. 21-1272 (TiO₂ Anatase) [194] and literature [195]. The peaks that appeared at 2θ confirm the presence of TiO₂ nanoparticles in the anatase phase at the calcinated temperature 450 °C.

The peaks at 2θ with 25.31° , 37.77° , 48.11° , 53.99° , 55.07° , 62.53° , 68.96° value corresponds to the crystal planes of (101) (004) (200) (105) (211) (204) (116) respectively, indicating purely the TiO₂ (Anatase) nanoparticles at temperature 450 °C. Akarsu, et.al confirms the XRD pattern with similar 2θ values and crystal planes for the pure anatase

form of TiO₂ nanoparticles [195]. The XRD pattern for the nano-composite TiO₂NaCl; x (%) = 50 is shown in the Figure 5.1 (C), confirming the presence of both TiO₂ as well as NaCl samples. The phase composition of the nano-composite TiO₂(x)NaCl is also mentioned. The peaks for the composite system are confirmed from the JCPDS card no.86-0148; TiO₂ (Rutile) and 01-070-2509; NaCl (Halite), annealed at the temperature 700 °C appeared at 2θ with 27.45°, 31.63°, 36.16°, 39.12°, 41.33°, 43.99°, 45.45°, 54.36°, 56.49°, 62.63°, 64.17°, 66.35°, and 69.07° values, which corresponds to the crystal planes along with the phase composition mentioned in the Table 5.2.

Table 5.2. Phase composition of the composite annealed at 700 °C.

S.No.	Crystal Planes	2θ (Degree)	Phase composition
1)	(110)	27.45	Rutile
2)	(200)	31.63	Halite
3)	(101)	36.16	Rutile
4)	(200)	39.12	Rutile
5)	(111)	41.33	Rutile
6)	(210)	43.99	Rutile
7)	(220)	45.45	Halite
8)	(211)	54.36	Rutile
9)	(220)	56.49	Rutile
10)	(002)	62.63	Rutile
11)	(221)	64.17	Rutile
12)	(400)	66.35	Halite
13)	(301)	69.07	Rutile

Given the above, it is clearly seen that the phase transition of TiO₂ from the anatase phase to the rutile phase takes place when annealed at the higher temperature. The anatase to rutile change could be influenced by several factors including particle size, particle shape, and the presence of 112 facets [196]. Here, the anatase to rutile percentage decreased when

a higher temperature than 500 °C is provided, as seen in the data pattern of the XRD composite in Figure 5.1 (C), annealed at 700 °C. Therefore, the phase change at higher temperatures is one of the reasons for the new peaks appearing in the XRD structure of the composite. Also, it is observed for the anatase phase Figure 5.2 (B), the peaks are quite wide which indicates incomplete crystallization because it has an amorphous component [197]. But as soon as the higher temperature is provided (above 500 °C), the crystallinity of TiO₂ was improved along with the phase change from anatase to rutile, obtaining the sharper peaks, indicating the significance of the temperature parameter for phase transformation of TiO₂ nanoparticles. Nevertheless, the same cannot be illustrated for the ionic matrix of NaCl (Halite) in the composite system, since the phase change for NaCl (Halite) occurs at or above 800 °C. Sol-gel microencapsulation of high-temperature phase change materials (PCMs) utilizing molten salts was the technique utilized by Arconada et al. for analyzing their work [198]. NaCl is a well-known phase change material because its melting point (800 °C) enables it to operate using novel thermodynamic cycles at a higher temperature than common molten salts like NaNO₃. Hence, NaCl (Halite) did not show any phase transformation (no new peaks), whereas TiO₂ did transform into a rutile phase for the composite system, when annealed for higher temperatures.

5.3.2 The Field Emission Scanning Electron Microscopy (FESEM)

Figure 5.2, illustrates the morphology of the synthesized (a) TiO₂ nanoparticles, and (b) TiO₂(x)NaCl nanocomposite at x (%) = 50, further annealed at 700 °C for 1 hour. Figure 5.2 (a) presents the images of TiO₂ nanoparticles calcined at 700 °C, which illustrates the regular, even size (100 nm) of the particles. The result confirms the width of the rutile peak diffraction from XRD, indicating the bigger crystalline size at 700 °C. As demonstrated in Figure 5.2 (a), the effects of heat treatment on the particle size of TiO₂ nanoparticles are explained by the tendency of the particle size to rise with an increase in the calcination

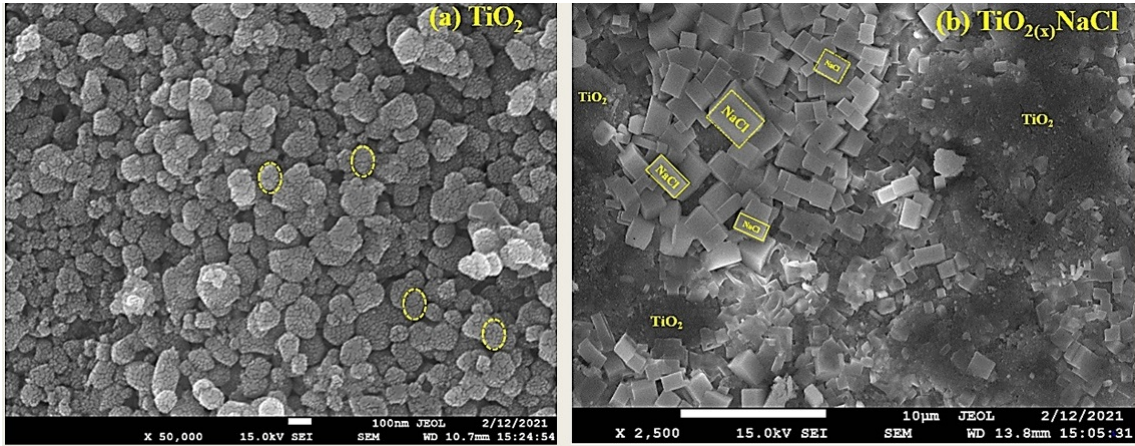


FIGURE 5.2: FESEM images at 700 °C (a) TiO₂ Nanoparticles, (b) TiO₂(x)NaCl Nanocomposite; x (%) = 50.

temperature. The literature provides evidence that while the calcination temperature has no effect on the nanoparticles' morphology, which retains its atypical spherical forms after calcination, [199] it does have an impact on their particle size. Figure 5.2 (b) represents the TiO₂(x)NaCl nanocomposite; x (%) = 50, annealed at 700 °C, which illustrates the presence of TiO₂ nanoparticles around the ionic matrix of NaCl, with much smaller in size. Here the morphology of NaCl nanoparticles illustrates the presence of cubic structures and is well crystallized. On the contrary, inhomogeneous morphology can be seen for TiO₂ nanoparticles in the nanocomposite system.

5.3.3 Dielectric Analysis

5.3.3.1 Effective dielectric Constant vs Frequency

The dielectric study illustrates the relaxation behavior of TiO₂ filler in an ionic matrix. Using a precision LCR meter (SM6019) at 300 K with test frequencies standard 100 Hz to 25 kHz in 11 steps, and an additional user-defined, from 500 possible frequencies between 100 Hz and 25 kHz, parameters such as real parts and imaginary parts of dielectric permittivity, and Ac conductivity are measured. An internal bias voltage of 2 V and ac supply of 230 V was applied throughout the dielectric measurement. Figure 5.3, represents

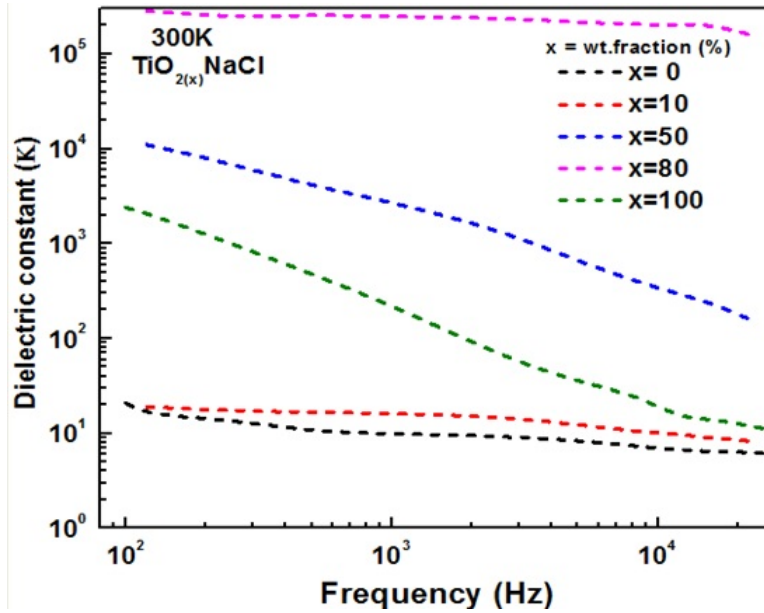


FIGURE 5.3: Room temperature Dielectric constant (κ) as the function of oscillating frequencies for x concentrations of $\text{TiO}_2(x)\text{NaCl}$.

the logarithmic variation of the dielectric constant (K) of $\text{TiO}_2(x)\text{NaCl}$, where x (%) = 0, 10, 50, 80, and 100 for the composite system, as a function of frequency at 300 K. In this instance, TiO_2 is introduced as an additive (filler) to the NaCl ionic matrix. It is observed that with an increase in filler concentration, the effective dielectric constant first increases and then decreases significantly when $x > 80$. Interestingly, the enhancement of dielectric behavior for the varying concentrations of (x) for $\text{TiO}_2(x)\text{NaCl}$ composite is noticed near the percolation threshold $x > 50$. The effective dielectric value for the varying concentrations of (x) for $\text{TiO}_2(x)\text{NaCl}$ composite is calculated using Equation (5.1).

At 300K and frequencies between 10^2 and 10^5 Hz, the theoretical static value of the dielectric constant is determined to be 5.9 for NaCl crystals [200]. Whereas the measured value of the dielectric constant in the frequency range of 100 Hz to 25 kHz for Pure NaCl is found to be ~ 21 for low-frequency values, and for higher frequencies it tends to saturate, approaching ~ 6 dielectric value. This accounts for the reason, why Pure NaCl has a larger dielectric constant for smaller values, as dipolar polarisation is present due to the broken inversion symmetry [201]. From the graph, it is also observed that on adding the higher nanofiller TiO_2 concentration, the dielectric value for x (%) = 50 and 80 increases

abruptly from 10^4 to 10^5 for lower value frequencies and slowly decreases with increase in frequency. This can be stated as, for the lower value frequencies, dipoles begin to lag behind since the weak dependence of dielectric constant leads to a slight decrease in the (κ) value for low frequencies. On the contrary, for the higher value frequencies dipoles can no longer follow the field [202] due to weak dipolar interaction and saturates. Higher permittivity values at low regions can be understood by the development and buildup of charges at the interfaces between the composite system (space charge polarization) or at the grain boundaries between NaCl and TiO₂ [203], known as Maxwell-Wegner effect [204][205]. The space charge zones in this phenomenon, also known as the Non-Debye type of behavioral patterns, are explained by ion diffusion with relation to frequency [203].

5.3.3.2 Dielectric Loss vs Frequency

Figure 5.4, shows the imaginary part of the dielectric permittivity as a function of oscillating frequency at 300 K. The imaginary part of the dielectric permittivity for TiO₂(x)NaCl,

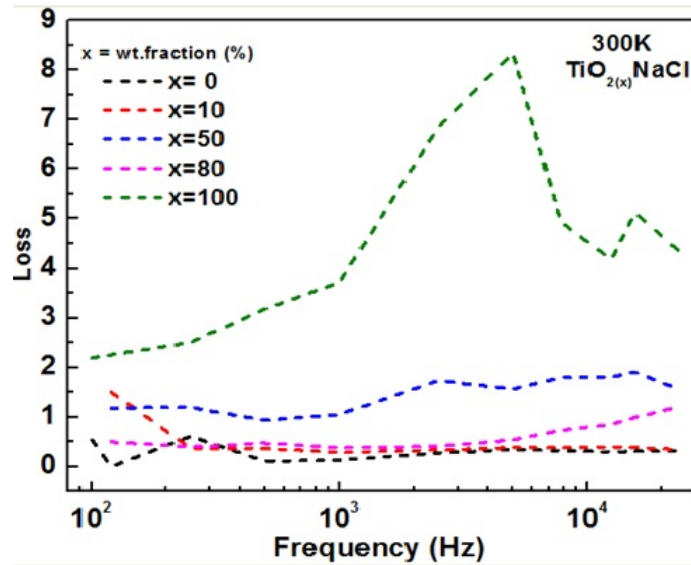


FIGURE 5.4: Room temperature Dielectric Loss as a function of oscillating frequencies for various concentrations of TiO₂(x)NaCl.

x (%) = 10, 50 80 composite is approximately less than 1 for low frequencies and approaches ~ 1 for higher frequencies. For Pure NaCl, the dielectric loss is observed to be

almost 0 for both low and high frequency, which is due to the fewer conduction molecules present in the ionic compound (Pure NaCl). Whereas at the lower frequencies for Pure TiO_2 , the loss increases with an increase in frequency, followed by a peak at a higher frequency regime, indicating the hopping-type behavior of conduction molecules.

5.3.3.3 Percolation assisted Dielectric constant

The effect on real part and imaginary part of dielectric permittivity of composite via the addition of TiO_2 nanofiller in the ionic matrix of NaCl is further analyzed with respect to wt. fraction (%) of filler concentration for specific frequencies at room temperature 300 K, as illustrated in Figure 5.5. With the increase of nano-filler TiO_2 concentration,

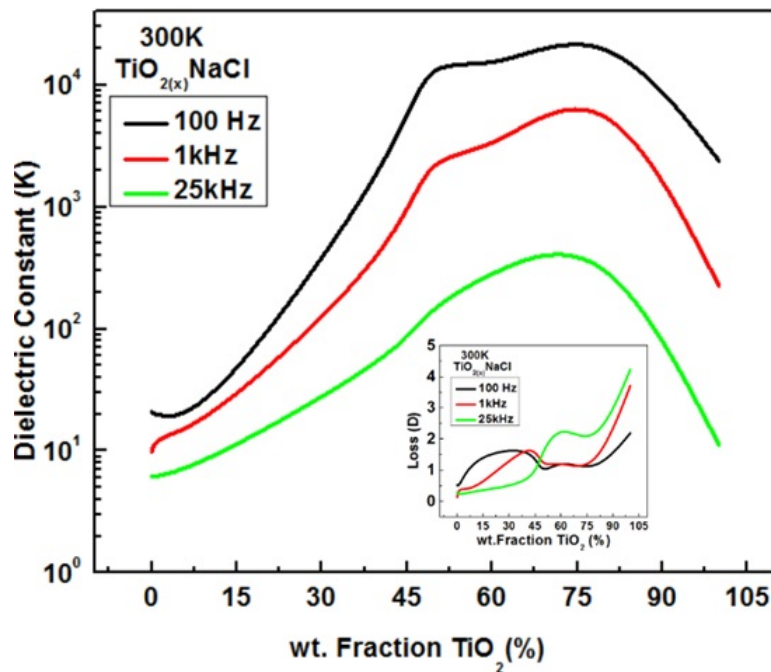


FIGURE 5.5: Percolation assisted Dielectric constant at 300 K.

the real part of dielectric permittivity (κ) is found to increase significantly. When TiO_2 is introduced as a filler to the NaCl bulk matrix, a significant increase in the dielectric constant of 3 order magnitude at 1 kHz with minimal loss. The initial dielectric peak at x (%) = 50 is explained by percolation-type behavior, as seen by the steadily rising

permittivity at low-frequency regions. When the filler fraction increases, the dielectric loss typically increases and is found to be approximately 1 for $x < 50$. Additionally, the further increase in (κ) in relation to filler concentration ($x < 80$) causes an acceleration of the space charge region, which results in an increase in equivalent capacitance [206]. This supports the second dielectric constant peak exhibited in Figure 5.5. This illustrates that the concentration $50 > x < 80$ of TiO_2 nanofiller with respect to frequencies has the maximum number of micro capacitors, with a moderate amount of losses. Additionally, the TiO_2 -contributed frequency-dependent polarisation in this composite system explains the hopping-type behavior of mobile charge carriers. To shed more light on the carrier dynamics, ac conductivity measurement is also performed in the same ambient condition.

5.3.3.4 *A.C conductivity*

The effect of TiO_2 nanofiller concentration in the $\text{TiO}_2(x)\text{NaCl}$ nanocomposite for the varying concentration of x (%) = 0, 10, 50, 80, 100 is further verified by temperature-dependent measurement of AC conductivity 300 K as shown in Figure 5.6. The variation

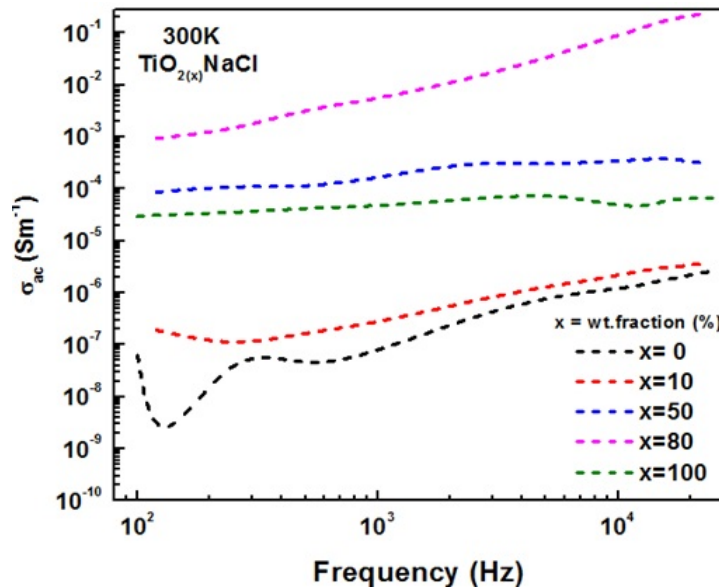


FIGURE 5.6: Room temperature Ac conductivity vs frequency for a varying concentration of x (%) TiO_2 .

of Ac conductivity (σ) with frequency is calculated using, $\sigma_{ac} = \epsilon_r \epsilon_o \omega \tan \delta$.

Where ϵ_o is the permittivity of the free space, ϵ_r is the dielectric constant of the sample, $\tan \delta$ is the dielectric loss and ω is the angular frequency ($\omega = 2\pi f$). The AC conductivity of pure TiO_2 (green line) is higher than that of pure NaCl (black line) in all frequency regimes, as can be seen from the logarithmic plot of Figure 5.6. Furthermore, pure TiO_2 exhibits strong frequency dependence throughout the whole frequency range, in contrast to the conductivity of TiO_2 , which is found to be frequency independent. Charge conductivity is observed to increase when filler content (x) increases since TiO_2 at 300 K contributes more charge carriers. The existence of hopping-type conductivity across conducting zones is also implied by a steady increase in charge conductivity with frequency [187]. The highest conductivity of charge carriers is shown at $x = 80$, further supporting the subsequent peak of the permittivity, after which the system percolates classically.

5.4 Conclusion

TiO_2 nanoparticles and $\text{TiO}_2(x)\text{NaCl}$ nanocomposite with varying concentration of x (%) = 0, 10, 50, 80, 100 have been successfully synthesized using sol-gel process and mechanical blending technique respectively. The effect of TiO_2 nanofiller in the bulk matrix of ionic compound NaCl, on the morphological, structural, and dielectric polarization, along with the effect of ac conductivity was studied. The XRD pattern confirms the presence of (A) NaCl (Halite), (B) TiO_2 (Anatase), and (C) $\text{TiO}_2(x)\text{NaCl}$ for concentration x (%) = 50 at their respective temperatures (300 K, 723.15 K, and 973.15 K) and phases. The dielectric studies for the varying concentrations of $\text{TiO}_2(x)\text{NaCl}$ nanocomposite reveal the rise in the real permittivity, with a moderate rise in loss with the increase in nanofiller concentration of TiO_2 . Particularly, $\text{TiO}_2(x)\text{NaCl}$ nanocomposite for a higher concentration of nanofiller TiO_2 , $x > 50$ tends to have the high dielectric value (κ) $> 10^4$ for low frequencies regions at temperature 300 K with moderate dielectric losses < 1 . An increase in a greater concentration of x is seen to cause a discernible change in ac conductivity. Hence, the

conductivity rises swiftly with increasing frequency for higher concentrations of x. Overall, TiO₂ incorporation as a nanofiller enhances the characteristics of ionic storage devices, self-heating sensors, volatile organic compound (VOC) sensors, etc.

Chapter 6

The Structural, Morphological, and Dielectric Analysis of Ni-Co Ferrites

Abstract

In the current investigation, Pechini's approach was used to develop nickel-substituted cobalt ferrite nanoparticles. At annealing temperatures of about 1000 °C, the presence of single-phased nanoparticles appears, and with an increase in annealing temperature at 1150 °C, the crystallinity nature further improves. With rising annealing temperatures, it becomes apparent that the average crystallite size improves. XRD investigation indicated that the strain in the crystalline particles decreases with increasing temperatures. FESEM images of nanoparticles reveal a cuboidal form with significant size. A pure single phase of the necessary elements is present in grown nanoparticles, as further evidenced by the EDAX spectrum. Impedance spectroscopy was used to examine the dielectric characteristics. Different annealed temperatures were studied for frequencies ranging 100 Hz to 1 MHz at room temperature. According to the correlated barrier hopping (CBH) model and

the Maxwell-Wagner two-layer model for space charge theory, the frequency-dependent dielectric characteristics vary as the annealing temperature rises.

6.1 Introduction

Over the past few decades, there has been an increase in studies towards the formation and characterization of ferrites with nanoscale dimensions, and a variety of novel technological uses for these materials have been found. The large range of possible technological uses for ferrites has been increased by the ability to precisely control their structural, magnetic, optical, chemical, and electrical properties by judiciously selecting the synthesis parameters [207][208][209]. Due to their environmentally friendly synthesis and wide range of uses, ferrites CuFe_2O_4 , CoFe_2O_4 , ZnFe_2O_4 , NiFe_2O_4 , and MnFe_2O_4 have received a lot of interest [210][211] [212][213][209], as NiFe_2O_4 and CoFe_2O_4 are grown in spinel category crystal structures, that has been represented by $(\text{Fe}^{3+}) [\text{Ni}^{2+}\text{Fe}^{3+}]\text{O}_4$, and $(\text{Fe}^{3+}) [\text{Co}^{2+}\text{Fe}^{3+}]\text{O}_4$ respectively [100][101]. Recently, nanoparticles (NPs) of cobalt ferrites-based materials have gained tremendous interest due to their important conducting and insulating properties. Cobalt ferrites can be employed for applications such as strain sensors and actuators as they have higher magnetostriction values [102]. The small Co^{2+} ion that occupies the tetrahedral site in CoFe_2O_4 lowers the lattice constant, which makes it easier for electrons to move between Fe^{3+} and Fe^{2+} and serves as an origin of charge carrier, improving CoFe_2O_4 's dielectric behavior [214]. Lower dielectric constant values were reported for CoFe_2O_4 NPs compared to bulk CoFe_2O_4 synthesized via the sol-gel process investigated by Gopalan et al. [103]. Similarly, nickel ferrite is likewise an ideal choice for purposes involving the spinel ferrite family. Nickel ferrite has a high Curie temperature, high saturation magnetization, high electrical resistivity, low eddy current, and low dielectric losses [104][105]. Additionally, the dielectric structure of NiFe_2O_4 includes grains and grain boundaries with varying conductivity [106]. Electrical conduction and dielectric polarisation are ensured by the electron exchange between Fe^{2+} and Fe^{3+}

ions and the hole exchange between Ni^{3+} and Ni^{2+} ions. Lower polarization occurs at high frequencies because the electron/hole hopping frequency does not match the applied electric field [106]. The investigation of the reports suggests that mixed ferrite has outstanding features and is comparatively stable based on the final stoichiometry and type of compositions' cation. Nanocrystalline mixed Ni-Co ferrites' electrical, dielectric, and magnetic properties were recently documented by a handful of research groups [97][98][99]. The structural and dielectric characteristics of NPs of $\text{Co}_{(0.5-x)}\text{Ni}_x\text{Zn}_{0.5}\text{Fe}_2\text{O}_4$ ($x = 0$ to 0.3) were examined by Kumar et al.[215], via the co-precipitation approach. Sawal et al. [216] compared the influence on the structural and magnetic characteristics of nano-sized as prepared $\text{Ni}_{0.5}\text{Co}_{0.5}\text{Fe}_2\text{O}_4$ ferrite and its sintered counterpart. Various researchers have reported their work on the specific stoichiometric $\text{Ni}_{0.5}\text{Co}_{0.5}\text{Fe}_2\text{O}_4$ NPs using multiple dry and wet chemical synthesis methods and the temperature variation concerning different sintered samples. However, information regarding the formation of stoichiometric $\text{Ni}_{0.5}\text{Co}_{0.5}\text{Fe}_2\text{O}_4$ nanoparticles in a pure phase of the spinel system and the influence on morphological, dielectric, and structural studies due to annealing temperature have remained scarce till today.

The current study seeks to investigate the $\text{Ni}_{0.5}\text{Co}_{0.5}\text{Fe}_2\text{O}_4$ synthesis by using the simple and affordable method of sol-gel auto-combustion that results in the production of nano-powders with absolute purity and homogeneity. Along with the influence of sintering at different temperatures on the synthesized NPs for obtaining the desired single-phase system. Ferrite as a single-phase system was obtained at a temperature around 1000 °C. The fundamental goal of the work is to obtain various sizes NPs and investigate how they affect the dielectric characteristics using impedance spectroscopy for various storage device applications. On the contrary, there is a fair amount of exploration in understanding and synthesizing new materials, that paves the way for research in areas where the influence of magnetic field on dielectric properties eventually gains a rich flavor of physics for materials, such as Magneto-dielectrics.

6.2 Experimental

Analytical grades of materials were used to synthesize NCF $[\text{Ni}_{0.5}\text{Co}_{0.5}\text{Fe}_2\text{O}_4]$ spinel ferrite NPs. Nickel (II) Nitrate Hexahydrate, 98+ % $[\text{Ni}(\text{NO}_3)_2 \cdot 6\text{H}_2\text{O}]$, Cobalt (II) Nitrate Hexahydrate, 98 % $[\text{Co}(\text{NO}_3)_2 \cdot 6\text{H}_2\text{O}]$, Ferric (III) Nitrate Nonahydrate, 98 % $[\text{Fe}(\text{NO}_3)_3 \cdot 9\text{H}_2\text{O}]$, Citric Acid Anhydrous, 99.5 % $[\text{C}_6\text{H}_8\text{O}_7]$ and Ammonium Hydroxide $[\text{NH}_4\text{OH}]$, 25 % Solution from Loba Chemie Pvt. Ltd. were used.

The dielectric and AC measurements have been performed using an impedance analyzer (FRA32M) in the 100 Hz to 1 MHz range (Potentiostat Galvanostat, by NOVA software). The characteristics via. Impedance spectroscopy provides powerful techniques for understanding energy conversion and storage studies. A Perkin Elmer Spectrum two device was used to measure the main transmission bands found in the FTIR. X-ray diffraction (XRD; Bruker) with $\text{Cu-K}\alpha$ ($\lambda = 1.5406 \text{ \AA}$) radiation analyzed the structural characteristics of the samples. Using Field Effect Scanning Electron Microscopy (FE-SEM), Energy Dispersive X-ray Analysis (EDAX), and an Au sputter coater (FE-SEM; JEOL JSM-7610F Plus EDAX; OXFORD EDAX LN2 free, Au Coater; JEOL Smart Coater), the surface morphology of the samples was examined.

6.2.1 *Material synthesis*

Pechini's method, commonly known as the sol-gel auto-combustion route, was employed to synthesize nickel-cobalt ferrite $[\text{Ni}_{0.5}\text{Co}_{0.5}\text{Fe}_2\text{O}_4]$ utilizing fuel as citric acid. The desired concentration of metal nitrates viz, $[\text{Co}(\text{NO}_3)_2 \cdot 6\text{H}_2\text{O}]$, $[\text{Ni}(\text{NO}_3)_2 \cdot 6\text{H}_2\text{O}]$, and $[\text{Fe}(\text{NO}_3)_3 \cdot 9\text{H}_2\text{O}]$. Here citric acid was utilized as a reducer and (all AR grades) as an oxidant. Metal nitrates and citric acid were considered to be in a 1:1 ratio. All metal nitrates and fuel in fixed stoichiometric quantities were weighed, mixed, and dissolved in 100 ml of double-distilled water along with heat and continue stirring on a hot magnetic stirrer to obtain a homogenous solution. In order to keep the pH level at 7, the solution was also vigorously

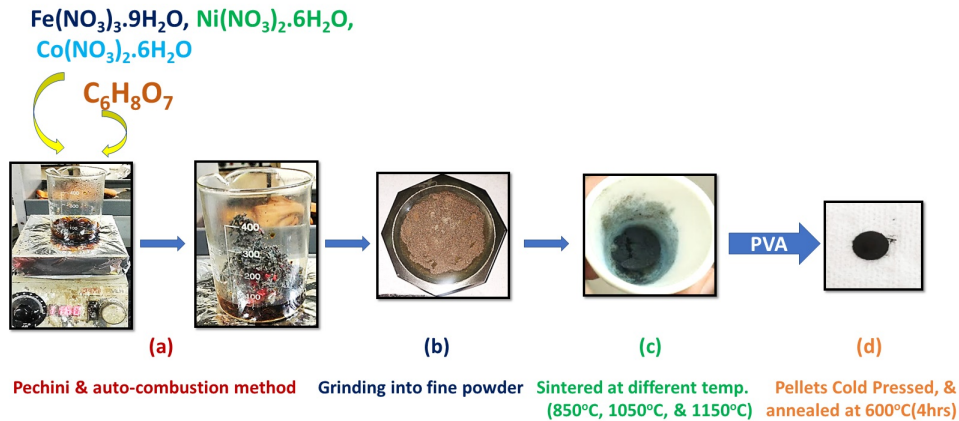
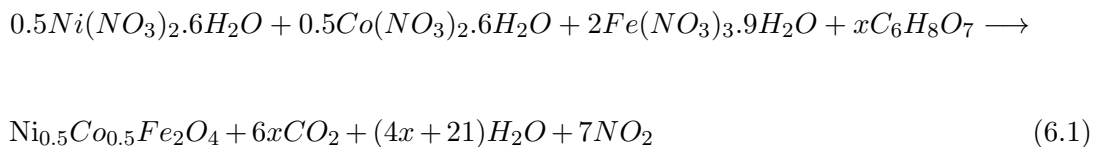


FIGURE 6.1: Schematic illustration of the sol-gel auto-combustion procedure for synthesized material.

stirred simultaneously with a drop-by-drop liquid ammonium hydroxide $[\text{NH}_4\text{OH}]$ solution. This homogenous mixture was then heated with continuous stirring, transforming the solution into xerogel. The flammable xerogel is heated until it ignites and undergoes auto-combustion, resulting in the formation of dark-colored, fluffy, powdered nanoscale ferrites. The unburned carbonaceous particles were evaporated from the burnt powder by calcining it for 4 hrs at 850 °C in the muffle furnace after being homogenized through grinding. The unheated powder was further sintered above 1000 °C for 4-5 hours to obtain the pure single-phase ferrite NPs. The sintered powder ferrite was then pressed into pellets via cold-pressed method using a suitable binder and pre-sintering the obtained pellets at 600 °C for 4 hours to evaporate the binder material for the efficient study of the ferrites. The schematic representation of the synthesis process is shown in Figure 6.1. Equation (6.1) can be used to explain the most probable reaction that will take place during the combustion reaction.



6.3 Results and Discussion

6.3.1 *Structural analysis*

XRD and FTIR characterizations were used to investigate whether annealing temperatures influenced the structural characteristics of the prepared samples. Room temperature XRD results of all samples were recorded in the 2θ range of $10^\circ - 70^\circ$ with Cu-K α radiation ($\lambda = 1.5405 \text{ \AA}$). The XRD patterns of Ni_{0.5}Co_{0.5}Fe₂O₄ (at 850 °C, 1050 °C, and 1150 °C) respectively are shown in Figure 6.2(a). The X-ray diffraction lines corresponding to NiFe₂O₄ and CoFe₂O₄ attributes to (111) and (220) particularly, followed by (311), (222), (400), (422), (511), and (440) crystal planes, as confirmed with standard JCPDF values (74-2081 and 79-1744) respectively. However, on sintering the ferrite initially at 850 °C, ferrite formation with magnetite as secondary phases occurs α -Fe₂O₃ as confirmed from the JCPDF card no. (39-1346). The formation of α -Fe₂O₃ at temperature 850 °C occurred most likely as a result of extra iron atoms in the reaction mixture that were not involved in the final ferrite's production. The excess Fe³⁺ cations in the reaction mixture will produce α -Fe₂O₃ as a secondary phase in Ni_{0.5}Co_{0.5}Fe₂O₄ ferrite if a portion of the Ni²⁺ cations is reduced to nickel or a proportion of the Co²⁺ cations, is reduced to cobalt [99]. As the sintering temperature is increased above 1000 °C particularly, peaks tend to get sharper and less rounded as crystallinity rises, indicating a successful synthesis of a single-phase spinel structure with cubic symmetry (Fd-3m space group) [217]. The crystallite sizes and lattice constant (a_0) for the highest diffraction peak (311) are estimated utilizing Debye Scherrer's formula, equation [6.2], which confirms the nanocrystalline nature of the incorporated samples as reported in TABLE 6.1.

$$D = K\lambda/\beta\cos\theta \quad (6.2)$$

where 'K' is the Scherrer's constant, ' λ ' is the X-ray's wavelength, ' β ' is the full width at half maxima ' θ ' is Bragg's angle. The average crystallite sizes (D) with different sintering

temperatures for the samples increased from 48.4 nm at (850 °C) to 71.3 nm at (1150 °C). This is demonstrated by the fact that enhanced crystallinity and an inactive surface layer of crystals caused the strength of diffraction peaks to increase at high annealing temperatures. In contrast, the processes of coalescence were enhanced, which enabled the growth in particle size [218]. In order to control crystallinity and crystallite size, the annealing temperature is therefore extremely important. Further, values of lattice strain inside the samples exhibited by distinct annealing temperatures can be evaluated using (W-H) the Williamson-Hall relation, from equations (6.3), reported in TABLE 6.1.

$$\varepsilon = \beta/4\tan\theta \quad (6.3)$$

where ε ' is the strain-induced inside the samples, ' β ' is the full width at half maximum of diffraction peaks, and ' θ ' is Bragg's angle.

Table 6.1. The lattice constant (a_0), interlayer spacing (d), unit cell volume (V), lattice strain (ε), FWHM (β), and Crystallite size (D) of $\text{Ni}_{0.5}\text{Co}_{0.5}\text{Fe}_2\text{O}_4$ samples for the most intense peak (311) of XRD reflection.

Sintering temperature ($^{\circ}\text{C}$)	d (\AA)	a_0 (\AA)	V (\AA^3)	D (nm)	β	ε
850	2.517	8.349	582.07	48.4	0.172	0.00234
1050	2.515	8.350	582.09	68.3	0.122	0.00166
1150	2.524	8.372	586.83	71.3	0.117	0.00159

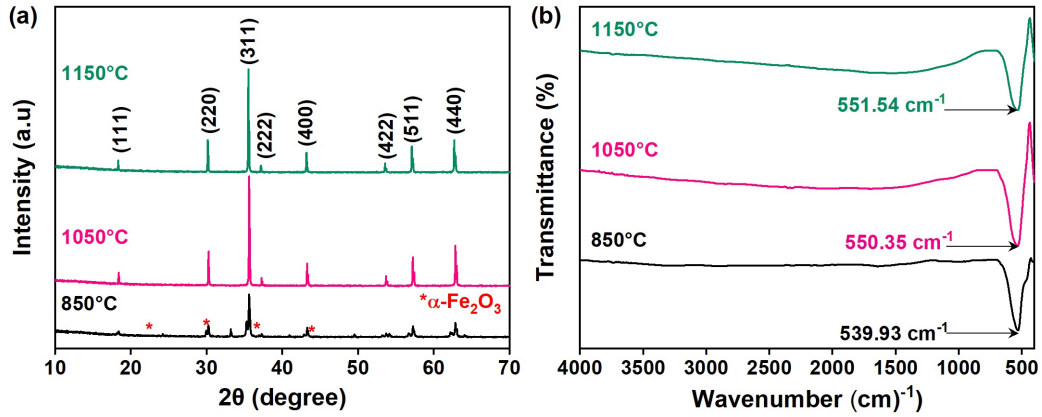


FIGURE 6.2: Structural confirmation for as-synthesized material for different annealing temperature. (a) XRD patterns of $\text{Ni}_{0.5}\text{Co}_{0.5}\text{Fe}_2\text{O}_4$, (b) FTIR spectra of $\text{Ni}_{0.5}\text{Co}_{0.5}\text{Fe}_2\text{O}_4$ samples.

$\text{Ni}_{0.5}\text{Co}_{0.5}\text{Fe}_2\text{O}_4$ ferrites FTIR spectra were examined at varying annealed temperatures in the range of 4000 - 400 cm^{-1} . In order to analyze the variation caused by the temperature difference, Figure 6.2(b) illustrates the FTIR spectra of all the ferrites that were made similarly but annealed at various temperatures. The absorption bands between (600-400 cm^{-1}) are attributed to the vibrations of stretching at the tetrahedral and octahedral locations. Each spectrum shows two distinct absorption bands that are typically found in cubic spinel ferrites and are located between (601-593) cm^{-1} and below 402 cm^{-1} , indicating the cubic spinel structures for ferrites [219]. The frequency band at ~ 400 cm^{-1} is related to cation-anion bond ($M_B\text{-O}$) vibrations that stretch at octahedral sites of the ferrite samples, while the absorption band at ~ 600 cm^{-1} is caused by cation-anion bond ($M_A\text{-O}$) vibrations that stretch at tetrahedral sites [220].

6.3.2 *Morphological Analysis*

The FESEM images investigated the ferrites' physical texture, morphology, and particle size. The FESEM microscope and their particle size histogram for all the samples, are shown in Figure 6.3. All of the scans showed that the samples feature cuboidal-shaped grains that are nanosized, non-uniform, and inhomogeneous with a significant level of amalgamation and agglomeration. This agglomeration in the samples may be caused due to the unavailability of surfactant during synthesis and due to the magnetic interaction between the NPs [221]. Therefore, it is evident from FESEM micrographs that the grains of the synthesized spinel ferrites are at the nanoscale with vivid pores, which certainly makes it beneficial for gas sensing applications due to the significant specific surface area of the smaller grains. Due to the production of a large number of gases during burning, which can partially prevent NP agglomeration and lead to porous materials, the nanosized nature of particles can be attributed [222]. The presence of gaps and pores in samples could be explained by the release of gases during burning, including (CO_2 , NO_2 , H_2O , etc.) [223][224]. Further, with the rise in the annealing temperature, particle size tends to increase, which corresponds to the fact that, on sintering, the NPs coalesce, resulting in higher particle sizes in the agglomerates. The corresponding histograms obtained from the FESEM pictures approached nearly depicting the highest average particle size for the different annealed ferrites at 850 °C to 1150 °C, obtained in the vicinity of ~ 59 to 316 nm respectively as can be seen from Figure 6.3 (a-c). The average particle size for all the samples was calculated from the histogram estimated from the FESEM micrograph using ImageJ software, and the values were reported in TABLE 6.2.

Table 6.2. Particle size from FESEM micrographs of the $\text{Ni}_{0.5}\text{Co}_{0.5}\text{Fe}_2\text{O}_4$ samples.

Sintering temperature ($^{\circ}\text{C}$)	Particle size (nm)
850	59.13
1050	237.03
1150	316

It was observed from the table that the particle size calculated from the FESEM micrograph using ImageJ software was not the same as the crystallite size determined by Debye-Scherrer formulas utilizing the XRD spectrum, as reported in TABLE 6.1. The XRD spectrum showed that the crystallite size was significantly less than the particle size inferred from the FESEM image. This revealed that the samples' particle size and crystallite size are entirely different from each other. Thus, two or more crystallites or grains combined to form particles result in larger particle sizes, as evidenced by FESEM images. Further, the elemental composition were obtained for all the samples by the EDAX

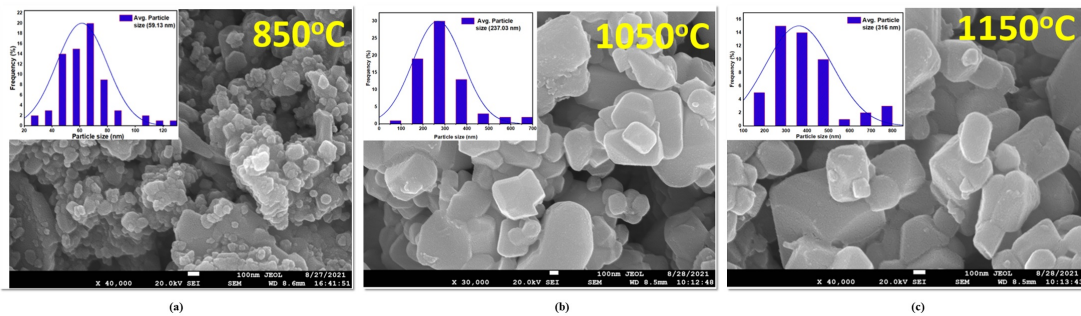


FIGURE 6.3: Morphological investigations for as-synthesized material for different annealing temperature. (a) FESEM image of $\text{Ni}_{0.5}\text{Co}_{0.5}\text{Fe}_2\text{O}_4$ at 850 $^{\circ}\text{C}$, (b) FESEM image of $\text{Ni}_{0.5}\text{Co}_{0.5}\text{Fe}_2\text{O}_4$ at 1050 $^{\circ}\text{C}$, (c) FESEM image of $\text{Ni}_{0.5}\text{Co}_{0.5}\text{Fe}_2\text{O}_4$ at 1150 $^{\circ}\text{C}$.

spectra, as shown in Figure 6.4 (a). All the samples confirm the constituent sample's composition and stoichiometric ratio. The EDAX spectra of $\text{Ni}_{0.5}\text{Co}_{0.5}\text{Fe}_2\text{O}_4$ spinel ferrite confirm Ni, Co, Fe, and O elements and some impurity elements such as Zn and Mn at (850 $^{\circ}\text{C}$) low annealing temperature. Additionally, during the preparation of the sample, an impurity element like carbon might have been accidentally deposited on the surface.

Figure 6.4 (b), shows the elemental mapping of the $\text{Ni}_{0.5}\text{Co}_{0.5}\text{Fe}_2\text{O}_4$ spinel ferrite for 1150 °C temperature, which confirms the presence of Ni, Fe, Co, and O elements and their equal distribution in the respective spinel ferrite purely. Therefore, with the increase in the annealing temperature, it is evident that particle size tends to increase with sintering, which corresponds to the fact that, merging NPs agglomerates with greater particle sizes, resulting in a purely single phase of ferrites.

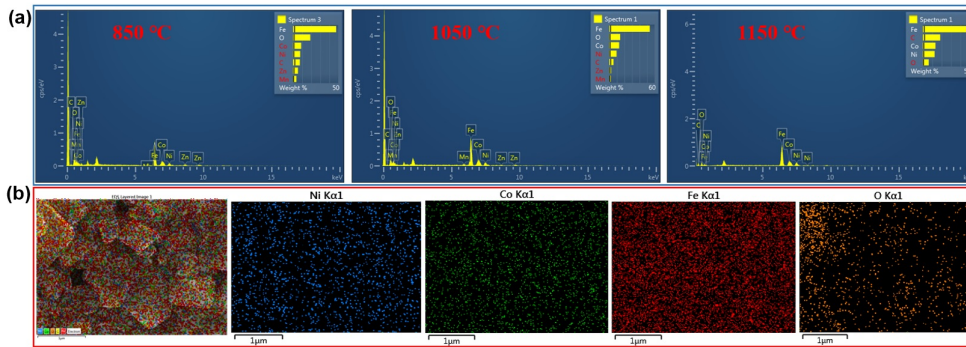


FIGURE 6.4: (a) EDAX spectra of $\text{Ni}_{0.5}\text{Co}_{0.5}\text{Fe}_2\text{O}_4$ for different annealing temperature, (b) Elemental mapping images of $\text{Ni}_{0.5}\text{Co}_{0.5}\text{Fe}_2\text{O}_4$ at 1150 °C.

6.3.3 Dielectric Analysis

The impedance spectroscopy was utilized to study the dielectric properties and AC conductivity. Specifically, the dielectric constant (ϵ'), dielectric loss ($\tan \delta$) and AC conductivity (σ_{ac}) was estimated from complex impedance data using impedance spectroscopy for any material; as shown in equations (6.4) and (6.5) respectively, that provides insightful data on polarization behavior, dielectric relaxation, and conduction mechanisms.

$$\varepsilon' = t/(\omega A \epsilon_o) * Z''/(Z'^2 + Z''^2), \varepsilon'' = t/(\omega A \epsilon_o) * Z'/(Z'^2 + Z''^2), \tan \delta = \varepsilon''/\varepsilon' \quad (6.4)$$

Figure 6.5(a) depicts the frequency-dependent fluctuation of the dielectric constant at various annealing temperatures. As can be observed, the dielectric constant increases at all temperatures in the low-frequency area but drops sharply as the frequency rises. The electric dipole's inability to adapt to changes in the applied AC electric field is the cause, which is why the dielectric constant drops as the frequency rises. Additionally, the Maxwell-Wagner (MW) phenomenon for interfacial polarisation with Koop's phenomenon explains the real permittivity (ε') with respect to frequency [104][225][226]. This concept proposes that the dielectric materials are composed of a significant quantity of thin grain borders (grain boundaries) separating well-conducting grains with low conductivity. This method results in larger permittivity and significant polarization. Here, it can also be seen that the magnitude of the dielectric constant drops as the annealing temperature rises from 30k at 850 °C to 15k at 1150 °C for 100 Hz. This is evident in Figure 6.5(a), since the size of the particle decreases from 71.3 nm (at 1150 °C)- 48.4 nm (at 850 °C), the dielectric permittivity rises. Therefore, the correlated barrier hopping (CBH) model can explain the improvement of the dielectric characteristics as the particle size decreases [227]. This model shows how the ions or charges can leap across an anisotropic barrier (or potential well) that separates them from one another. The particle's size decreases to 48.4 nm, resulting in a single-domain, despite a reduction in the number of domains. For the barrier to be removed and the dielectric permittivity to be increased, the presence of a weak field is essential [228].

The dielectric losses ($\tan \delta$) as a function of frequency at various annealing temperatures are shown in the inset of Figure 6.5(a). The value of $\tan \delta$ is high at lower frequencies and rapidly declines as the frequency rises. Here, the dielectric losses show the same pattern as the dielectric constant, except for 1050 °C of annealed temperature for ferrite. At low frequencies, it displays the highest loss tangent value, which is 63.9. Due to the high

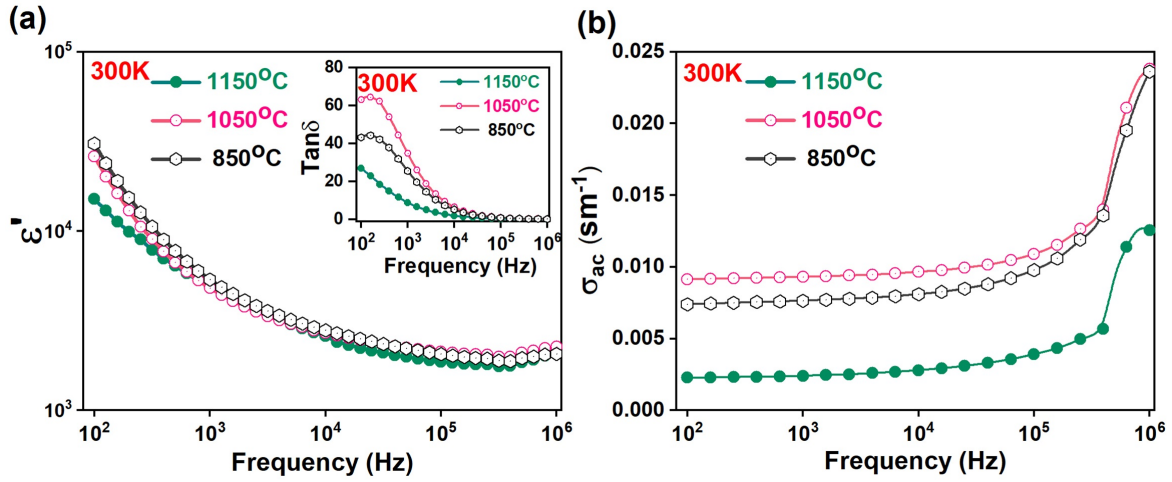


FIGURE 6.5: Dielectric analysis for as-synthesized material for different annealing temperatures. (a) Dielectric permittivity vs Frequency of $\text{Ni}_{0.5}\text{Co}_{0.5}\text{Fe}_2\text{O}_4$, (b) Frequency-dependent AC conductivity of $\text{Ni}_{0.5}\text{Co}_{0.5}\text{Fe}_2\text{O}_4$ samples.

resistivity of the material's grain boundaries, which make the exchange of electrons between Fe^{3+} and Fe^{2+} ions more energy-intensive, the high value of a loss and its tangent is attributable to these factors. The idea of the conduction mechanism within the ferrites at higher frequencies is provided by higher values, where a small amount of energy is needed for electron exchange between Fe ions, leading to a small amount of energy loss and a low value of electrical resistivity. Additionally, the variation of AC conductivity as a function of frequency, as shown in Figure 6.5(b), is further estimated by equation (6.5), which is necessary to comprehend the conduction mechanism and type of polarons responsible for conduction.

$$\sigma_{ac} = t/A * Z' / (Z'^2 + Z''^2) \quad (6.5)$$

As can be observed, the frequency has a linear effect on the AC conductivity. The exchange of electrons between ions of the same element with differing valences causes the conductivity to rise. The conductive grains become more active upon application of the ac field, hence enhancing the hopping between Fe^{2+} and Fe^{3+} ions and raising the hopping conduction. Following this, conductivity was observed to rise gradually on a regular basis [229][230][231]. Moreover, the variation in AC conductivity to annealing temperature

is because of the correlated barrier hopping (CBH) mechanism [227]. Further, complex impedance spectroscopy also allows for the investigation of the real and imaginary components of complex impedance in addition to the investigation of dielectric characteristics. The separation of grain, grain boundary, and electrode characteristics is ensured using complex impedance spectroscopy. When the electrical processes inside the system are modeled in terms of their equivalent circuit, it also provides insight into their ability to relate to the sample [232]. Therefore, It is evident to study the dielectric properties which are further used in energy storage devices, since the grain boundaries between these structures consist of well-conducting grains [233][234][235]

6.4 Conclusion

The Pechini technique uses citric acid as fuel and has been used to create nickel-cobalt ferrite powders. The nano-crystalline nature of the nickel-cobalt ferrite particles is confirmed by the characterization techniques, such as XRD and FESEM. The highest particle size of ferrite is ~ 71 nm at an annealing temperature of 1150 °C. Also, the pure single phase of ferrites was observed at a high annealing temperature (1150 °C). Due to the annealing temperature, the real permittivity appears to be variable. The maximum permittivity (D.C) is obtained to be $\sim 15k$ at 1150 °C. Therefore, of all the reports available in the literature, the high annealing temperature at 1150 °C is promoted to be one of the most suitable temperatures for the effective analysis of (Ni-Co) ferrite NPs.

Chapter 7

Complex impedance and electric modulus analysis of nickel-substituted cobalt ferrite

Abstract

This article describes the successful production of spinel ferrite $\text{Ni}_{0.5}\text{Co}_{0.5}\text{Fe}_2\text{O}_4$ samples by employing the sol-gel auto-combustion technique. XRD was used to validate the crystal structure of inverse spinel ferrite in all $\text{Ni}_{0.5}\text{Co}_{0.5}\text{Fe}_2\text{O}_4$ samples. Here, it is discovered that there is an inverse relationship between the computed theoretical density (D_x) and the crystallize size (D). As the sintering temperature increases from 850 °C to 1150 °C, crystallize size (D) increases. At 1150 °C, the ideal sintering temperature, XPS verifies the existence of a single phase in samples. EDAX and FESEM both confirm the modification in morphology and elemental composition of $\text{Ni}_{0.5}\text{Co}_{0.5}\text{Fe}_2\text{O}_4$. Furthermore, TEM reveals an even distribution of cuboidal shape grains with an average grain size of about 84 nm for the $\text{Ni}_{0.5}\text{Co}_{0.5}\text{Fe}_2\text{O}_4$ sample at an optimized temperature of 1150 °C. Additionally, the SAED pattern indicates an even distribution of bright spots, confirming

a significant amount of crystallization and a single-phase formation. A relaxation phenomenon with a non-Debye-type origin emanating from grain boundaries is also revealed by Complex Impedance and Modulus Spectroscopy. Space charge polarization is observed in frequency-dependent complex impedance and modulus examinations as the sintering temperature rises. It is proposed that the compound's enhanced dielectric properties reveal substantial results of sintering the compound at the required temperature, which is beneficial for magnetodielectric materials, spintronic devices, sensors, and other applications.

7.1 Introduction

Spinel ferrites are highly significant due to their remarkable magnetic and dielectric properties [236]. The materials have a wide variety of functional uses in the area of transformers, microwave devices, electrical sensors, and information storage media [236][237][238]. The single spinel ferrite crystallographic unit cell has eight formulae units of AF_2O_4 (where A is one or more divalent metal cations such as Ni^{2+} , Co^{2+} , Mn^{2+} , Mg^{2+} . Metal (divalent or trivalent) cation presence at lattice sites has been investigated using crystal field theory [239], resulting in many types of crystal arrangements such as inverse, normal, or mixed. Furthermore, these cations have a significant impact on their capability to modify chemical, structural, magnetic, optical, and electrical characteristics. In addition, the presence of metal (divalent or trivalent) cations in these tetrahedral and octahedral sites is affected by a number of important factors, including elemental composition, pH effects, preparation method, sintering time, and sintering temperature [240][241][242][243]. The sintering temperature has a considerable influence on the many structural parameters such as crystallinity, density, phase, crystallite size, porosity, and so on, which enhances the physicochemical characteristics. Additionally, the ferrite's magnetic porosity makes it suitable for a variety of applications, including supercapacitors, sensing applications, memory-based technology, solar cells, corrosion protection coatings, and many

more [244][245][246]. Several other groups have pointed out the significance of sintering temperatures [247]. Here, the increase in sintering temperature corresponds to an increase in particle grain size along with the saturation magnetism values of the mixed ferrite. Brajesh Nandan et al. investigated the impact of sintering on the magnetic and structural and characteristics of $\text{Ni}_{0.5}\text{Co}_{0.5}\text{Fe}_2\text{O}_4$ ferrites [218]. Furthermore, Iqbal et al. emphasized the investigation of the impact of reaction time and temperature on the appearance of L-cysteine surface-capped chalcocite (Cu_2S) snowflakes, dendrites, and nano-leaves, as well as the visible-light photodegradation of the methyl orange dye [248].

Further, the diverse versatility of ferrites can also be achieved by selecting an efficient and convenient synthesis method. Several techniques, including the hydrothermal method, microwave combustion, co-precipitation method, solid-state reaction, spray pyrolysis, and sol-gel auto-combustion, can be used to develop spinel nano ferrites [249][250][251][252][253]. The method of preparation has a large influence on structural parameters such as morphology, size, chemical homogeneity, and surface state. Of the various methods available for spinel ferrites synthesis, the sol-gel auto-combustion method proves to be the most cost-effective and convenient one. The low cost of this approach contributes to its cost-effectiveness, the quick and bulk availability of the precursors used for synthesizing ferrites [254]. Furthermore, this method has been regarded as a convenient chemical route because it provides numerous advantages such as improved reactant mixing with massive chemical homogeneity in the product and lowering the crystallization temperature [255][256]. In addition, the use of distilled water as a solvent leads to this methodology being clean and environmentally friendly from a natural standpoint [144].

Among the numerous spinel ferrites, the Ni-Co ferrites have been widely employed due to their attractive and wide scopes [97][98][99]. The CoFe_2O_4 has an inverse structure in which the small Co^{2+} ion occupying the tetrahedral site reduces the lattice constant, allowing electron hopping between Fe^{3+} and Fe^{2+} ions and acting as a charge carrier source, strengthening the dielectric behavior of CoFe_2O_4 [214]. NiFe_2O_4 also exhibits a dielectric structure with distinct conducting grains and grain boundaries. The electron

exchange between Fe^{2+} and Fe^{3+} ions, as well as the hole exchange between Ni^{3+} and Ni^{2+} ions, ensures electrical conduction and dielectric polarization, useful for various electrical applications [106]. Moreover, in our system nickel as a dopant is chosen because it is a soft ferrite with high magneto-crystalline isotropy while maintaining high resistivity [106], whereas cobalt ferrite as a host material is a hard ferrite with high magneto-crystalline anisotropy, high coercivity, and moderate saturation magnetization [214]. Further, at this particular stoichiometric concentration $x = 0.5$, the cationic distribution is found to be uniform and yields a narrow crystalline grains size distribution that makes our mixed ferrite chemically and mechanically stable.

In addition, (CIS) is a crucial method for identifying the source of the conducting process and the electrical characteristics of ferrite ceramics in terms of microstructure and composition by observing the contributions from grains, grain borders, or electrodes [257]. It also includes resistive (real component) and reactive (imaginary component) data which contributions to conductivity under applied fields. The macroscopic bulk materials are most convenient for complex (CIS) characterization, especially for a conventional parallel-plate capacitor (RC) measurement geometry, where RC is the measured resistance and capacitance, respectively, that allows quick characterization of the resistive and capacitive properties of different areas in the sample. Furthermore, the complex impedance analysis can provide basic information about the dielectric characteristics of materials, since dielectric characteristics provide fundamental information about the materials [258]. As a result, the report containing complex dielectric analysis has already been published previously [229].

Further, such diverse properties exhibited by Ni-Co-ferrite encouraged us to explore the system in our work. The current study describes the effective synthesis of $\text{Ni}_{0.5}\text{Co}_{0.5}\text{Fe}_2\text{O}_4$ by employing the sol-gel auto-combustion process, which results in the formation of grains with absolute single-phase and homogeneity at the optimized sintering temperature of 1150 °C. However, to the utmost of our understanding, the research due to the impact of sintering temperature on the impedance and modulus properties using complex impedance

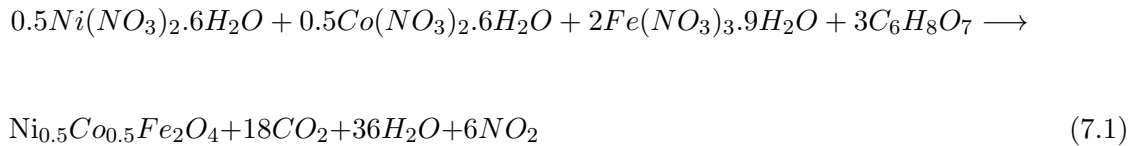
spectroscopy for mixed ferrite $\text{Ni}_{0.5}\text{Co}_{0.5}\text{Fe}_2\text{O}_4$ is not available in the literature till today. The detailed complex impedance formalism and frequency-dependent relaxation procedure at room temperature with respect to various sintering temperatures such as 850 °C, 1050 °C, and 1150 °C have been reported in this paper. Ferrite as a single-phase system is obtained at a temperature above 1000 °C. Therefore, the findings demonstrate that the synthesized Ni-Co ferrite exhibits unique features making our sample a suitable choice for their scope in magnetic, optoelectronic, and electric devices such as microwave absorption applications, inductors, sensors, developing magnetodielectric materials, and many more. Moreover, the transition of polycrystalline ferrites to single-phase ferrite along with rising grain size due to the influence of sintering temperature is uniquely fascinating to analyze.

7.2 Experimental

X-ray diffraction (XRD; Bruker) with $\text{Cu-K}\alpha$ ($\lambda = 1.5406 \text{ \AA}$) was used to evaluate the structural properties of heat-treated materials. FESEM in conjunction with EDAX was used to examine the surface morphology of the samples (FE-SEM; JEOL JSM-7610F Plus EDAX; OXFORD EDAX LN2 free). TEM (JEOL JEM 2100 Plus) confirms the form and size of grains as determined by XRD and FESEM images. XPS (Thermo Scientific NEXA Surface analyzer) via Avantage Data system software was utilized to analyze the chemical states. For the study of electrical measurements, the flat surfaces of pellets acted as electrodes, where the conductive silver paste was applied on both faces of ceramic samples and were air dried. The complex impedance measurements were performed with an impedance analyzer (FRA32M) in frequencies ranging from 100 Hz to 1 MHz (Potentiostat Galvano stat, using NOVA software).

7.2.1 Synthesis of Ni-Co ferrite

The successful synthesis of spinel ferrite ($\text{Ni}_{0.5}\text{Co}_{0.5}\text{Fe}_2\text{O}_4$) powders by using the sol-gel auto-combustion route, also known as Pechini's method have been reported. The aqueous solution of metal salts and iron is prepared homogeneously in distilled water with required stoichiometric proportions, under continuous magnetic stirring. To maintain a molar ratio of 1:1, the pulverized citric acid is introduced to the salt solution with cations. The solution was maintained at a pH of 7 by adding ammonium hydroxide in droplet form at 90 °C to 95 °C for 2 h under continuous magnetic stirring. Due to excessive heating, surplus water evaporates and the liquid is turned into xerogel. Further, the xerogel is dried over a hot plate at 100 °C for 1–2 h, which leads to an auto-combustion process, converting xerogel into brown fluffy powder forming the nanoparticles. Pre-sintering was done at 100 °C for 48 h, in order to evaporate any excess moisture. By then, a pre-sintered powder sample was further sintered at different temperatures such as 850 °C, 1050 °C, and 1150 °C. Furthermore, the sintering temperature and heating rate of the $\text{Ni}_{0.5}\text{Co}_{0.5}\text{Fe}_2\text{O}_4$ sample are kept constant at 12 °C per min for at least 4 hrs, respectively, to obtain the high crystalline and single-phase ferrite. The synthesis technique is depicted schematically in Figure 7.1. The required stoichiometric reaction occurring during the combustion synthesis is explained in Equation (7.1).



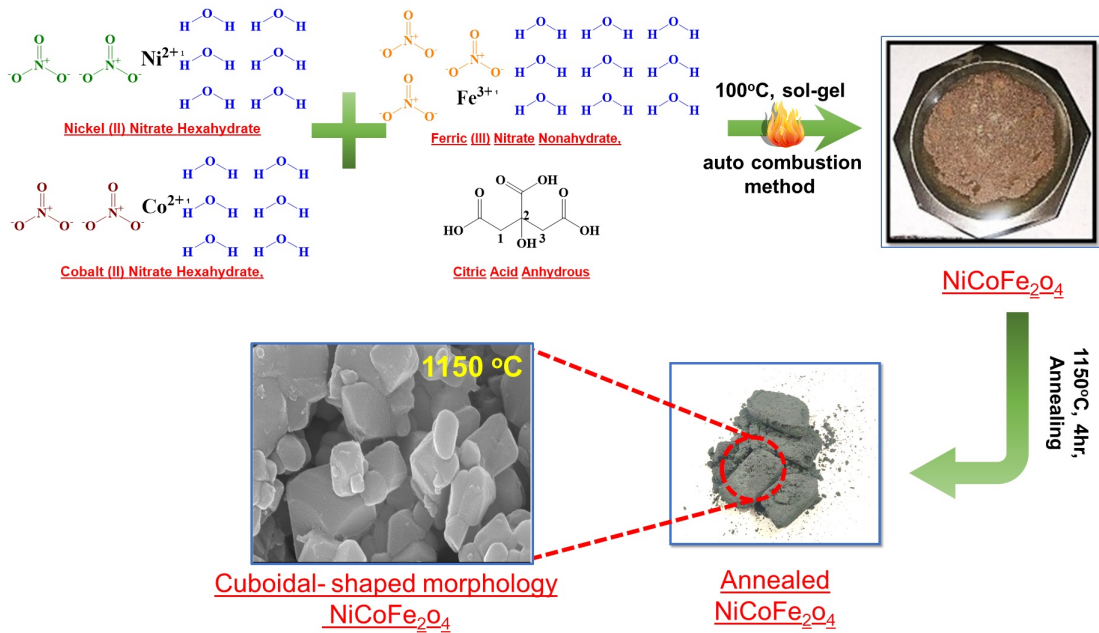


FIGURE 7.1: The scheme illustrates the synthesis procedure of the Ni-Co ferrites.

7.3 Results and Discussion

7.3.1 Phase and Structural analysis

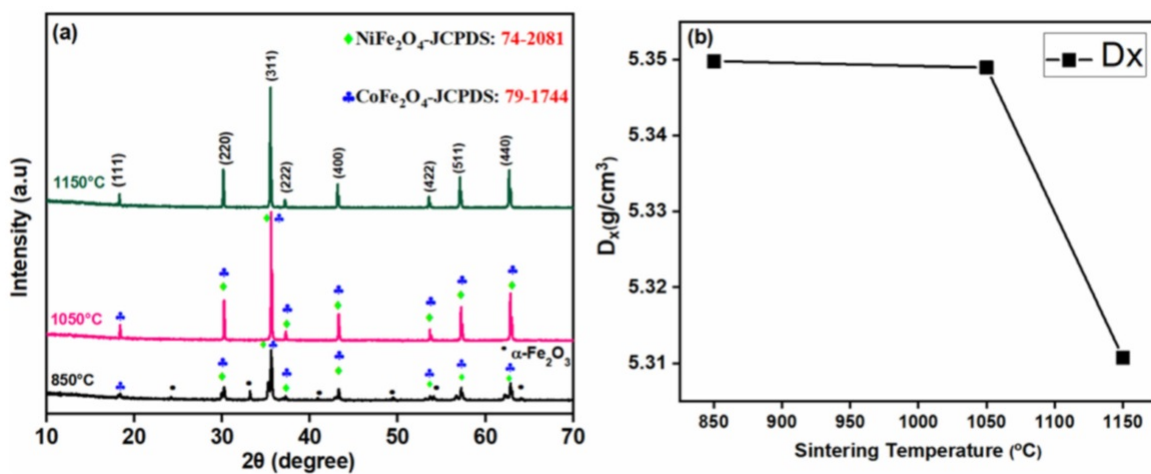


FIGURE 7.2: a) The XRD of Ni_{0.5}Co_{0.5}Fe₂O₄ ferrite samples for all sintering temperatures, b) Density (D_x) vs sintering temperature (°C).

Figure 7.2a depicts the XRD scans of samples of $\text{Ni}_{0.5}\text{Co}_{0.5}\text{Fe}_2\text{O}_4$ sintered at temperatures of 850 °C, 1050 °C, and 1150 °C. The crystallite size (D) and theoretical density (D_x) is estimated from the following Equation (7.2).

$$D_{(311)} = k\lambda/(\beta\cos\theta), D_x = ZM/N_A V_{cell} \quad (7.2)$$

Here, (D_x) is the theoretical density, N_A is Avogadro's number (6.023×10^{23}), M is molecular weight, Z is the number of molecules per unit cell, and V_{cell} is cell volume. For the most intense diffraction peak (311) the crystallite size (D) was determined. Here, λ is the X-ray's wavelength of the radiation, K is a constant ($K = 0.9$), θ is the Bragg's angle, and β is the full width at half maxima (FWHM). The sharp XRD spectra for the sintered samples reveal that the crystallinity increases, eliminating the extra impurity peaks such as $\alpha\text{-Fe}_2\text{O}_3$ with increasing sintering temperature. The majority of diffraction peaks correspond to the spinel structure as confirmed from standard JCPDS values 74-2081 and 79-1744 having cubic $Fd\text{-}3m$ space group [259][260]. The peak intensity of the samples sintered at 1050 °C and 1150 °C is found to be higher than the sample at 850 °C. This is due to the fact that when the sintering temperature rises, the diffraction peaks narrow and sharpen, suggesting an increase in the crystallinity and particle size of the samples. Furthermore, as reported by Trentler et al. [261], the sharp intensity of diffraction peaks is due to an inactive surface layer of crystals/the presence of high surface and bulk mobility in a solid phase, due to the higher orientation of atoms in the crystal structure. Furthermore, the enhanced crystalline nature of sintered samples corresponds to the improvement in coalescence processes due to nuclei size enlargement, enabling a rise in particle size and thus increasing peak intensity at higher sintering temperatures [262]. The detailed investigation and explanation of the structural properties with respect to the sintering temperature of the as-deposited samples can be confirmed from previously published work [229].

Table 7.1. The structural characteristics of $\text{Ni}_{0.5}\text{Co}_{0.5}\text{Fe}_2\text{O}_4$ samples at various sintering temperatures.

Sintering temperature ($^{\circ}\text{C}$)	$2\theta(^{\circ})$	$a_0 (\text{\AA})$	$V (\text{\AA})^3$	D (nm)	$D_x(\text{g}/\text{cm}^3)$
850	35.63	8.34	582.07	48	5.35
1050	35.63	8.35	582.18	68	5.34
1150	35.53	8.37	586.37	71	5.31

The structural parameters as calculated are tabulated in Table 7.1. It shows the values of X-ray density (D_x) that decline from 5.35 to 5.31 g/cm^3 as the sintering temperature increases from 850 $^{\circ}\text{C}$ to 1150 $^{\circ}\text{C}$, the variation is illustrated in Figure 7.2b, This variance is ascribed to an increase in volume because heat energy provides a force that forces grain boundaries to form across pores during the sintering process, causing the pore volume to contract and the materials to become denser. Further, the heating rate throughout all the sintering temperatures is used at 12 $^{\circ}\text{C}$ per min. The high heating rate would entrap the gas inside the material and produces intragranular pores [263]. Moreover, the density for the $\text{Ni}_{0.5}\text{Co}_{0.5}\text{Fe}_2\text{O}_4$ sample at 1150 $^{\circ}\text{C}$ drops to 5.31 g/cm^3 , resulting in increased grain size contrary to lower sintering temperatures. This eventually leads to an increase in intergranular spacing due to which porosity also increases. Therefore, at higher sintering temperatures, the density gets decreased, resulting in increased intragranular porosity due to discontinuous grain growth [264]. This implies that the sintering temperature has a significant impact on the crystallinity, crystallite size, and density of the materials.

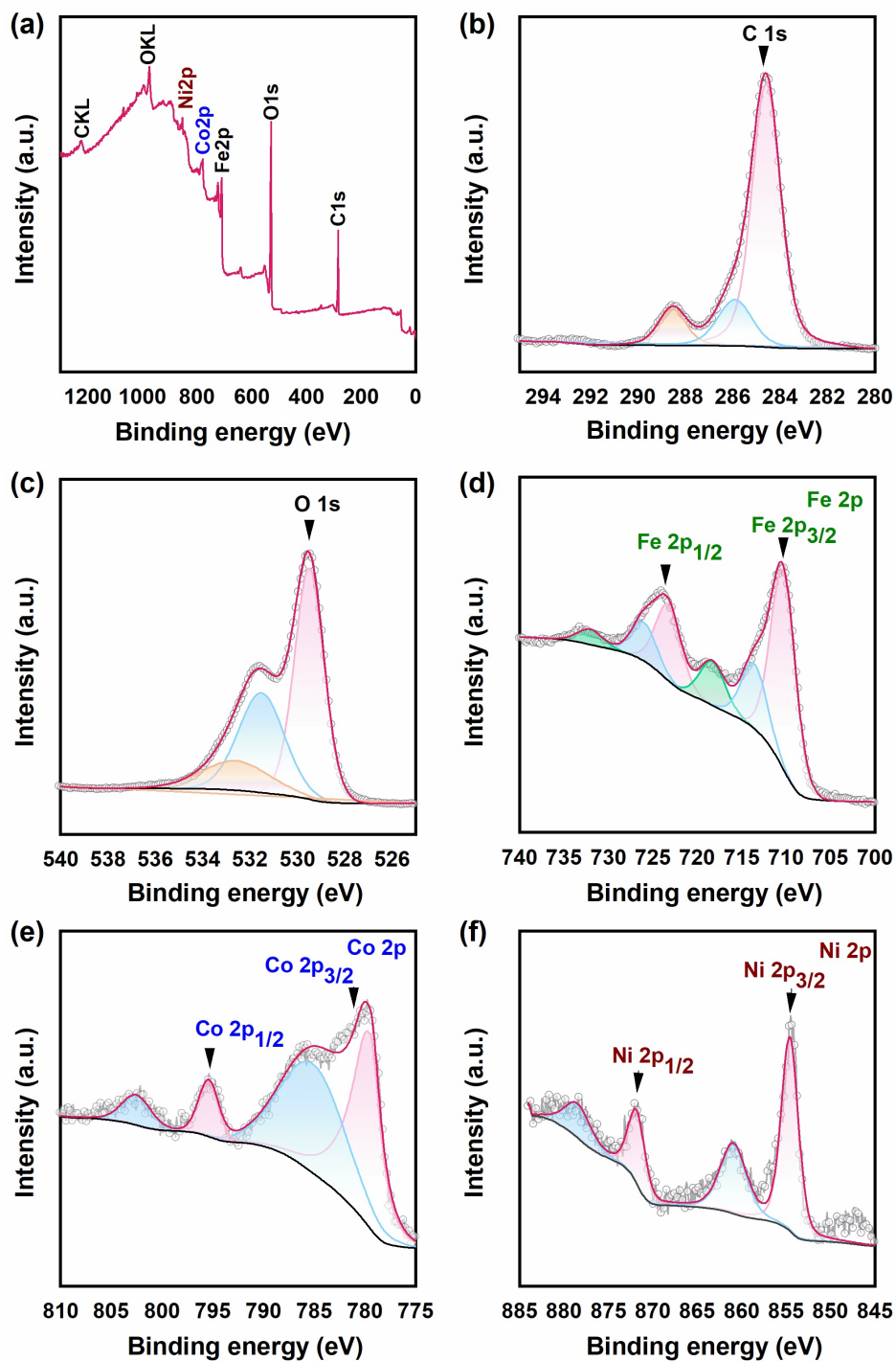


FIGURE 7.3: The deconvoluted XPS spectra of a) Full scan, b) C 1s, c) O 1s, d) Fe 2p, e) Co 2p, and f) Ni 2p XPS spectrum at 1150 °C of ‘as synthesized’ $\text{Ni}_{0.5}\text{Co}_{0.5}\text{Fe}_2\text{O}_4$ samples

The XPS spectra in Fig. 3 confirm the oxidation states of all the components of the synthesized $\text{Ni}_{0.5}\text{Co}_{0.5}\text{Fe}_2\text{O}_4$ samples at all sintering temperatures, i.e., 850 °C, 1050 °C, and 1150 °C. The full XPS scan (Figure 7.3a) of $\text{Ni}_{0.5}\text{Co}_{0.5}\text{Fe}_2\text{O}_4$ spectra and the deconvoluted core level XPS scans of Co 2p, Ni 2p, O 1s, Fe 2p, and C 1s of the prepared sample $\text{Ni}_{0.5}\text{Co}_{0.5}\text{Fe}_2\text{O}_4$ at 1150 °C are pictorially illustrated in Figure 7.3. The existence of all desired components Co, Fe, Ni, and O are purely observed at the highest sintering temperature of 1150 °C. Charge correction calibration for the complete spectrum data was performed using a constant value of 284.8 eV for the carbon 1s peak [265]. The two broader auger peaks OKL and CKL, which appeared in the whole scan spectrum as well, were visible at higher binding energies of 998.9 eV and 1200 eV, respectively. These peaks are generated by the detection of auger electrons which are generally produced by auto-ionization. Generally, the binding energy assigned to the auger transition may be due to the “shake-up” and “shake-off” contribution to the auger peaks. These processes of shake-off and shake-up feature incomplete electronic transitions. Given that there is a limited probability that a charged particle (after photoionization) will remain left in a particular excited energy state a few eV above its initial state due to ion excitation by the outgoing photoelectron, this reduces the kinetic energy of the emitted photoelectron and is visible as a “shake-up” peak at higher binding energy than the main line [266]. Similarly, where more than one electron is ejected at the time of photoionization, it may result in broad structures or contribute to the inelastic background in a spectrum resulting in shake-off events. Here, the appearance of auger peaks (as seen in Figure 7.3a), on the higher-binding (low-kinetic) energy side identifies it as a “shake-up” rather than a “shake-off” charge process [267]. Further, the curve-fitting approach adopted for various deconvoluted scans such as Fe 2p_{3/2} and Co 2p_{3/2} following the calculated components and their intensity ratio is in accord with the curve-fitting data reported in the literature, which provides enough evidence of the presence of desired elements [268]. This means that heat treatment is important in determining the formation of a single phase of as-prepared material $\text{Ni}_{0.5}\text{Co}_{0.5}\text{Fe}_2\text{O}_4$ samples.

The binding energy of the Ni $2p_{3/2}$ peak (Figure 7.3f) is 854.9 eV, while the peak for Ni $2p_{1/2}$ is 872.5 eV [269]. At 795.5 eV and 780 eV, respectively, the typical binding energy peaks for Co $2p_{1/2}$ and Co $2p_{3/2}$ are detected from Figure 7.3e [270], establishing the existence of cobalt in the + 2 oxidation state. The presence of Co in the + 2 oxidation state is also supported by satellite peaks at binding energies of 786.8 and 802.7 eV. The high-resolution XPS peaks (Figure 7.3d) at 725.4 eV and 710.2 eV correspond to the Fe $2p_{1/2}$ and Fe $2p_{3/2}$, respectively. In addition, a satellite peak with a binding energy of 716.8 eV is seen. A satellite peak for Fe $2p_{1/2}$ was seen, which is characteristic of Fe in a trivalent oxidation state [265][45]. Figure 7.3c shows that the binding energy of the oxygen species corresponding to O 1s is 529.7 eV, which is attributable to lattice oxygen. The greater binding energy (531.3 eV) peak, on the other hand, is attributable to lower coordinated lattice oxygen, demonstrating structural defects [271][272]. The entire spectrum data set had been optimized for charge correction for the carbon 1s peak, which had a consistent value of 284.8 eV throughout [273].

7.3.2 Morphological and Elemental Analysis

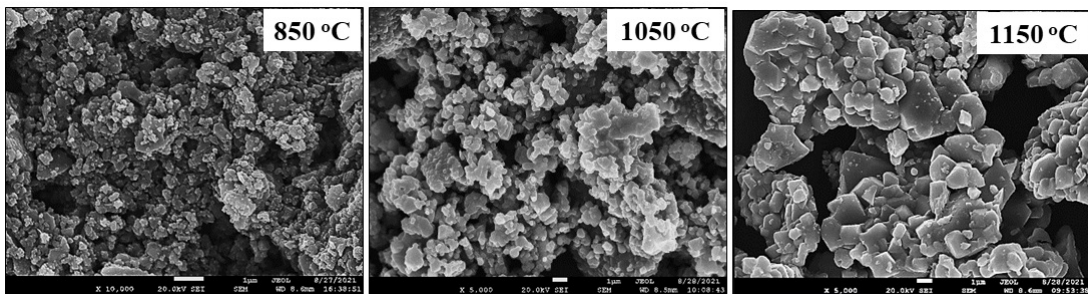


FIGURE 7.4: FESEM micrograph of $\text{Ni}_{0.5}\text{Co}_{0.5}\text{Fe}_2\text{O}_4$ samples at various sintering temperatures

Figure 7.4 depicts the FESEM micrographs for $\text{Ni}_{0.5}\text{Co}_{0.5}\text{Fe}_2\text{O}_4$ samples at all sintering temperatures 850 °C, 1050 °C, and 1150 °C. The results obtained at a low sintering temperature 850 °C, yield non-uniform coalesced globular grains of a few hundred nanometers that indicate the incomplete formation of grains. As the sintering temperature increases,

the morphology transforms into segregated cuboidal-shaped grains with distinct edges. This is due to the presence of non-homogeneous grains at low temperatures. Moreover, these effects are much more reliable for spinel ferrites, as it is worth noting that the heat treatment caused the particles to aggregate as a function of the sintering temperature. Therefore, on increasing the sintering temperature, the homogeneity of grains increases. Agglomeration rises as particle size grows due to magnetic interactions between nanoparticles [274][275]. Thus, the morphology transforms into segregated cuboidal-shaped grains at the highest sintering temperature. The FESEM images are further analyzed using ImageJ software that calculates the average particle size of about 59 nm, 237 nm, and 316 nm for the respective sintering temperatures 850 °C, 1050 °C, and 1150 °C. Therefore, on sintering the nanoparticles merge and agglomerate which facilitates an increase in particle size. The particles join together and enlarging of particle size occurs due to increasing sintering temperature at 1150 °C. Further, the porous nature avowed by the FESEM micrographs may find its applicability in energy storage devices viz. batteries and supercapacitors [275].

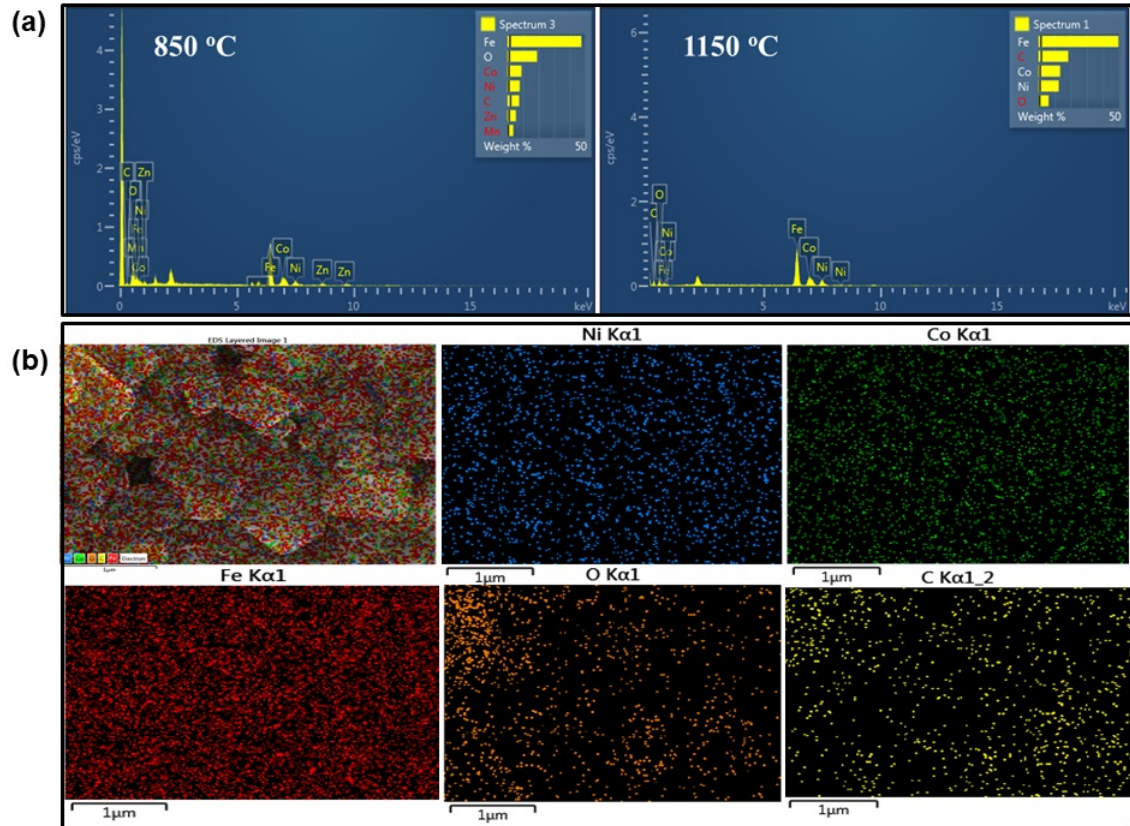


FIGURE 7.5: a) EDAX spectra of $\text{Ni}_{0.5}\text{Co}_{0.5}\text{Fe}_2\text{O}_4$ samples at sintering temperatures 850 °C and 1150 °C, b) Elemental mapping images of $\text{Ni}_{0.5}\text{Co}_{0.5}\text{Fe}_2\text{O}_4$ samples at 1150 °C.

Table 7.2. Elemental analysis, experimental and theoretical values of atomic % of $\text{Ni}_{0.5}\text{Co}_{0.5}\text{Fe}_2\text{O}_4$ samples at different sintering temperatures

Sintering Temperature (°C)	Value	Elements atomic %					Total atomic %
		Ni	Co	Fe	O	C	
850	Experimental	4.31	4.91	27.50	38.30	20.15	95.17
	Theoretical	4.53	5.15	28.90	40.24	21.18	100
1050	Experimental	5.85	7.97	34.76	32.39	16.56	97.53
	Theoretical	6.00	8.17	35.64	33.22	16.97	100
1150	Experimental	6.53	6.98	27.34	11.98	47.18	100
	Theoretical	2.06	2.20	9.07	13.87	72.80	100

Fig. 7.5a depicts the EDAX spectrum of $\text{Ni}_{0.5}\text{Co}_{0.5}\text{Fe}_2\text{O}_4$ samples at 850 °C and 1150 °C. Figure 7.5b displays elemental mapping for the Ni-Co ferrite sample at the highest sintering temperature of 1150 °C, which demonstrates the presence of the desired elements Fe, Co, Ni, C, and O. The experimental and theoretical values of the atomic percent (at. %) of Ni-Co spinel ferrite for all sintering temperatures, are reported in Table 7.2. The observed data show a minor difference between the experimental and theoretical atomic percent (at. %). This could be attributed to the nano ferrites' surface crystallographic flaw, as well as the presence of foreign components such as carbon [276][277]. The experimental values acquired from EDAX scans are nearly in agreement with the theoretical compositional analysis (Figure 7.5b), as it affirms the presence of a single-phase ferrite system due to the impact of sintering temperature. Therefore, on increasing the sintering temperature to 1150 °C, impurities are removed and single-phase grains of the spinel system are confirmed.

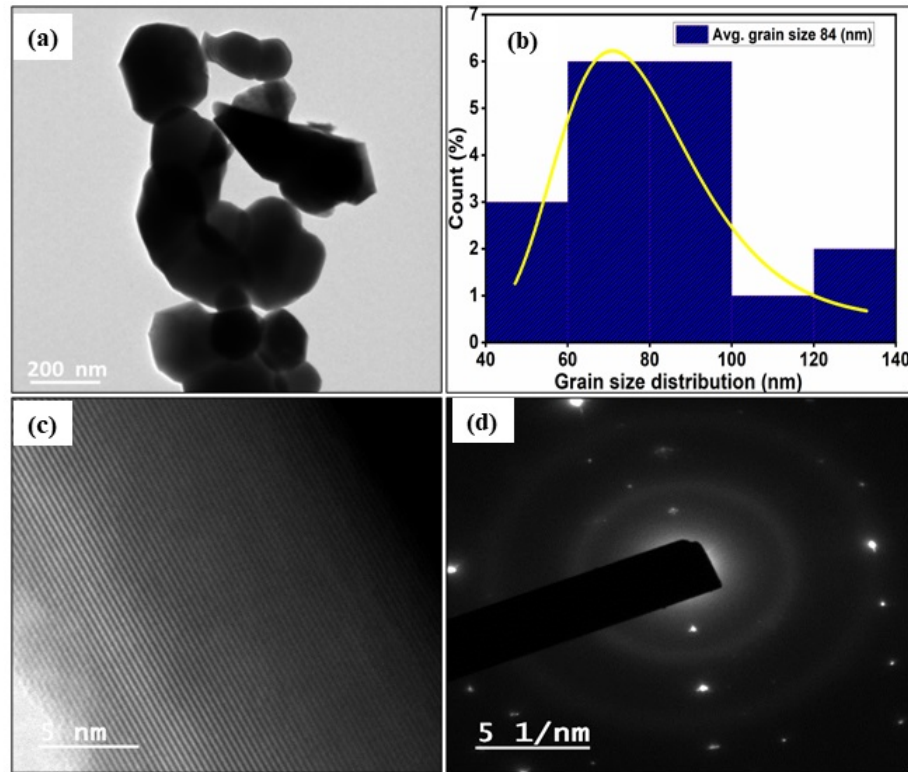


FIGURE 7.6: a) TEM micrographs of $\text{Ni}_{0.5}\text{Co}_{0.5}\text{Fe}_2\text{O}_4$ nanoparticles at $1150\text{ }^\circ\text{C}$, b) The average grain size (nm) distribution of scans, c) High-resolution TEM pictures demonstrating the arrangement of single direction-oriented planes, d) The SAED pattern suggesting the formation of a single-phase of as-prepared $\text{Ni}_{0.5}\text{Co}_{0.5}\text{Fe}_2\text{O}_4$ sample at $1150\text{ }^\circ\text{C}$.

The insight details of the $\text{Ni}_{0.5}\text{Co}_{0.5}\text{Fe}_2\text{O}_4$ ferrite samples are further inspected by Transmission electron microscopy (TEM). Here the optimized $\text{Ni}_{0.5}\text{Co}_{0.5}\text{Fe}_2\text{O}_4$ ferrite sample at the optimal sintering temperature of $1150\text{ }^\circ\text{C}$ is considered. Figure 7.6a shows the TEM micrographs that are used to evaluate the morphology and size of the studied samples. Although, due to the high agglomeration of grains, the individual grain size is not visible in the TEM images. Here, the TEM technique provides information from a very narrow portion of the sample. In our case, about 500 nm area of the sample was studied for average grain size distribution. The number of particles in this area is about 18, which are then analyzed for average size histogram via ImageJ software, as illustrated in Figure 7.6b. In contrast, some of the particle sizes and shapes are visible, and based on apparent particle size and shape; the agglomerated particles were measured [278]. Thus,

the TEM results obtained support the XRD predicted size. Figure 7.6c illustrates the well-defined and uniform lattice fringes obtained from high-resolution TEM images that show the single-direction oriented planes, suggesting the formation of a single-phase of $\text{Ni}_{0.5}\text{Co}_{0.5}\text{Fe}_2\text{O}_4$ sample at the highest sintering temperature. The SAED pattern as displayed in Figure 7.6d, shows the bright spots' regular distribution, confirming once more the substantial amount of crystallisation and single-phase production. This confirms the influence of sintering at the highest temperature, as the SAED pattern corresponds to the ferrite sample's single-phase crystalline structure, similar to results obtained for other ferrite samples [279][280].

7.3.3 Complex Impedance analysis

Impedance spectroscopy is used to analyze the electrical behavior of materials to identify the impact of grains, grain boundaries, and electrodes on overall conductivity. Figure 7.7a,b displays the variance in the real and imaginary parts of the evaluated ferrites' complex impedance (Z^*) for all the sintering temperatures with respect to frequencies. Similar literature on impedance spectroscopy had also been studied earlier, for several distinct types of samples such as manganite of $\text{Gd}_{0.95}\text{Ca}_{0.05}\text{MnO}_3$ [281], crystals of $\text{Pb}_x\text{Co}_{1-x}\text{C}_4\text{H}_2\text{O}_6 \cdot n\text{H}_2\text{O}$ [282] and bulk ferrite of $\text{Zn}_x\text{Co}_{1-x}\text{FeAlO}_4$ [283], and many more [284].

As seen below, both the resistive and reactive impedance components are included in the complex impedance (Z^*) which is given as, $Z^* = Z' - jZ''$ [285]. The horizontal element of the complex impedance is given by $Z' = |Z^*| \cos\theta$, which is used to denote the resistive component, and the imaginary part is supplied by $Z'' = Z'' = |Z^*| \sin\theta$, which is used to denote the reactive (capacitive) component. Grain and grain boundaries entangled with dielectric and electric modulus properties, on the other hand, are in agreement with Equation (7.3), since these two components integrate the impedance effects of resistance

and capacitance.

$$\tan\delta = (\epsilon''/\epsilon') = (Z''/Z') = (M''/M) \quad (7.3)$$

Figure 7.7a depicts the variation in the real component of complex impedance (Z') with regard to the frequency of the studied ferrites for all sintering temperatures. At low-frequency regions, Z' has a higher value with dispersed behavior and remains constant up to 10^4 Hz, after which the Z' drops continuously at higher frequencies. The relaxation frequency can also be observed where Z' tends to drop and shift to a higher frequency side. This decrease in Z' values is mostly due to a rise in charge carrier mobility and a drop in trapped charge density [285]. Further Figure 7.7a, illustrates that with an increase in sintering temperature, Z' increases which subsequently confirms the decrease in conductivity of the sintered ferrites [229].

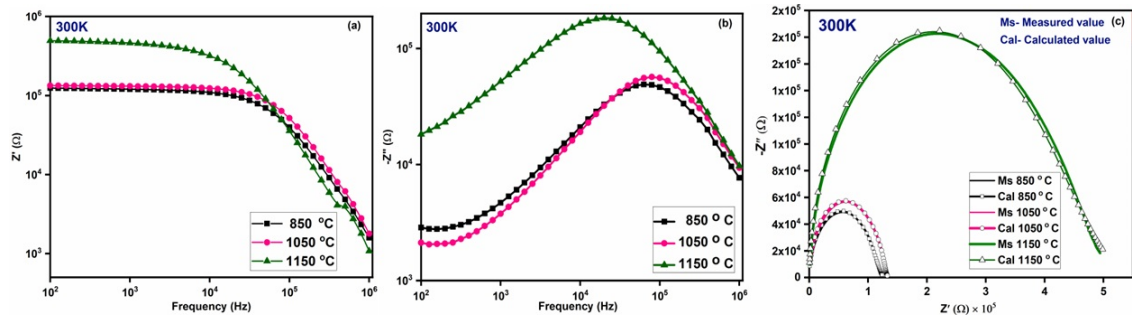


FIGURE 7.7: a) Z' vs Frequency, b) Z'' vs Frequency, and c) Nyquist plots of $\text{Ni}_{0.5}\text{Co}_{0.5}\text{Fe}_2\text{O}_4$ samples at all sintering temperatures.

Figure 7.7b depicts a change in the complex impedance's imaginary component (Z'') for $\text{Ni}_{0.5}\text{Co}_{0.5}\text{Fe}_2\text{O}_4$ samples for all sintering temperatures. The spectra explicitly characterize the location and strength of the relaxation peak, which is observed to vary with sintering temperature. Since the maximum values of Z'' shift to the low-frequency side with increasing sintering temperature. This peak shift corresponds to non-Debye relaxations [257][286]. This pattern of behavior demonstrates the existence of a relaxation effect in the ferrites, confirming the non-Debye type of relaxation in the system as the center of all peaks doesn't exist at the same frequency for all sintering temperatures. Therefore, it is evident that Z''_{max} rises with an increase in temperature, which reveals the rise in the

resistance of sintered ferrite samples. As a result, for all spectra, the elongation of position and strength of the relaxation peak for ferrites change for different sintering temperatures. Moreover, at low sintering temperatures, a significant broadening of peaks can be observed. In contrast, the impedance curves appear to merge for all compositions and the broadening of the peak decreases, suggesting the temperature-dependent relaxation process in the ferrites. Along with the peak broadening, the height of the relaxation peaks is also affected. The peak height of the relaxation peaks increases as the sintering temperature rises, showing an increase in resistive characteristics. Furthermore, emphasises the significance of space-charge polarisation, which is only considered significant when the conductivity of the grains and grain boundaries differ by significant magnitudes. [286].

In addition, the Nyquist impedance plots for $\text{Ni}_{0.5}\text{Co}_{0.5}\text{Fe}_2\text{O}_4$ samples (Figure 7.7c) has been fitted via ZSimDemo 3.20d software at room temperature for all sintering temperatures at a frequency range of 100 Hz-1 MHz. The graphs depict the overall response of an RC circuit with a parallel-connected resistor and capacitor, which illustrates the contribution of grain and grain boundary resistance [287]. The plot shows semicircular arcs as it starts at the origin and makes an intercept on the real axis with a distinct radius for all the sintering temperatures. The diameter of the semicircle arcs increases with increasing sintering temperature, which is due to an increase in grain resistance [288]. Also, an abrupt increase of the diameter at an optimal sintering temperature of 1150 °C indicates the minimal contribution to electrical conductivity from grains, as the grain size tends to increase and the size of grain boundaries decreases. However, the fall of grain boundary resistance suggests less hopping of mobile charge carriers aiding the material to behave as a weak semiconductor. Similar behavior of impedance spectra with a single semicircle was observed for other cases of nanocrystalline ferrites [289][290]. The primary cause of semicircle arc separation is considered to be a variation in relaxation time. Further, to shed more light on the transport behavior, complex modulus spectroscopy is studied on the grown sintered samples.

7.3.4 Complex Modulus analysis

As a result of differing relaxation time constants, complex modulus spectroscopy provides an alternate strategy for exploring the electrical properties of the material particularly the relaxation time and ion/carrier hopping rate [291]. The comparison of modulus spectroscopy to impedance spectroscopy lies over the advantage, in terms of grain boundary conduction and electrode polarization discrimination. The complex dielectric modulus can be represented by, $M^* = M' - jM''$ where M' and M'' is the real component and imaginary component of the dielectric modulus. The complex dielectric modulus is defined as the reciprocal of complex permittivity and is calculated using Equation 7.4,

$$M' = \epsilon' / (\epsilon'^2 + \epsilon''^2), M'' = \epsilon'' / (\epsilon'^2 + \epsilon''^2) \quad (7.4)$$

Figure 7.8a illustrates that both the real (M') component and imaginary (M'') component of the modulus are frequency-dependent, which has significance in studying the relaxation process of the materials. Figure 7.8a further shows that M' responds effectively to high-frequency zones, with the largest value of M' at 1150 °C. This suggests that at high frequencies, ϵ' has a lower value [229]. The inadequate strength of the restorative force, as well as the release of space charge polarization near the grain boundary, aid in the saturation of the force. This occurrence happens at higher frequencies while also ensuring the materials' frequency-independent electrical characteristics [292][293]. Figure 7.8b illustrates the frequency-dependent M'' . The hopping mechanism appears to show peaking behavior since it clearly describes the charge carrier shift. The charge carriers clearly contribute to the switching process that covers vast distances at low frequencies, illustrated in the above image. Charge carriers, on the other hand, travel small distances at higher frequencies, indicating polarisation relaxation [292][293].

Further, Figure 7.8c clearly illustrates the complex modulus spectra of M'' vs M' , (also known as Nyquist plot) drawn at all sintering temperatures for Ni-Co ferrite samples. This

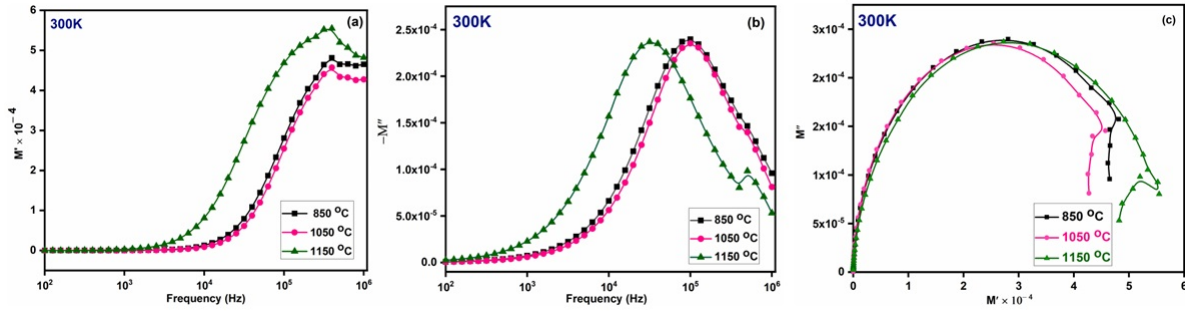


FIGURE 7.8: a) M' vs Frequency, b) M'' vs Frequency, and c) Complex Modulus plots of $\text{Ni}_{0.5}\text{Co}_{0.5}\text{Fe}_2\text{O}_4$ samples at all sintering temperatures.

separation is expected to be caused by the grain and grain boundaries [294][295]. The non-overlapping semicircular pattern indicates a non-Debye type relaxation.

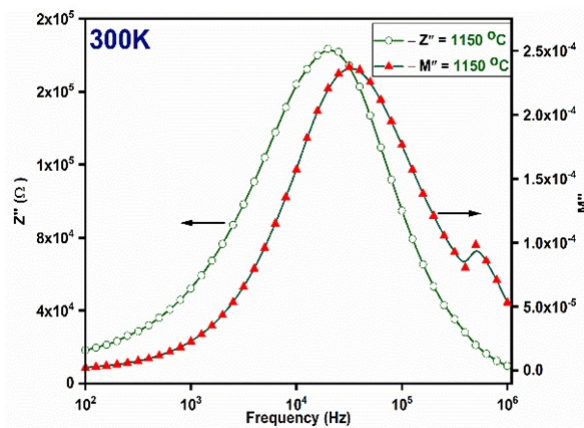


FIGURE 7.9: a) Variation of Z'' and M'' versus frequency of $\text{Ni}_{0.5}\text{Co}_{0.5}\text{Fe}_2\text{O}_4$ sample sintered temperature at $1150\text{ }^\circ\text{C}$.

Additionally, Figure 7.9 illustrates the variation of Z'' and M'' versus frequency combined plots of $\text{Ni}_{0.5}\text{Co}_{0.5}\text{Fe}_2\text{O}_4$ samples at $1150\text{ }^\circ\text{C}$. Similar combined plots for other temperatures reveal a similar pattern, except the fact that the difference between the two peak frequencies increases as the sintering temperature rises. As a result, the two peaks (Z'' and M'') are distinct, confirming the non-Debye type relaxation behavior.

7.4 Conclusion

The sol-gel auto-combustion process has been employed to effectively synthesize spinel ferrite $\text{Ni}_{0.5}\text{Co}_{0.5}\text{Fe}_2\text{O}_4$ nanoparticles with variable sintering temperatures. Scherrer's equation evaluates the crystallite size (D) (48.4 –71.3 nm) in the nano-size range. With increased sintering temperature, the X-ray density (D_x) was estimated to drop from 5.35–5.31 g/cm^3 . The microstructural insights via XPS spectra of the ferrite confirm the polycrystalline nature (low temperature) to the high crystalline single-phase (high temperature) at 1150 °C by showcasing the desired states of oxidation of every component included in the original samples. FESEM images exhibit a change in morphology from non-uniform coalesced globular grains (850 °C) to cuboidal-shaped particles (1150 °C), due to an increase in agglomeration with increased sintering temperature. Further, EDAX scans determined the elemental composition of prepared samples, where the observed values indicate the change between the experimental and theoretical values of the atomic percent (at. %) of as-synthesized samples for all sintering temperatures. Additionally, TEM images verify the morphology of cuboidal shape grains having a grain size (average) of about 84 nm for optimized $\text{Ni}_{0.5}\text{Co}_{0.5}\text{Fe}_2\text{O}_4$ sample at 1150 °C. Further, the high-resolution TEM images illustrate the single-direction oriented planes, followed by SAED patterns affirming the single-phase formation of the as-prepared samples at the high sintering temperature. Impedance and modulus spectroscopy were employed to evaluate the electrical response of the materials, which revealed the impact of grain boundaries and grains due to the influence of sintering temperature in the $\text{Ni}_{0.5}\text{Co}_{0.5}\text{Fe}_2\text{O}_4$ samples. The Nyquist plot estimated by the complex impedance spectroscopy demonstrates the rise of resistive properties with increasing sintering temperature. Owing to the presence of uneven semicircular arcs in complex modulus spectra the synthesized samples exhibit the non-Debye type of relaxation behavior. Thus, the synthesized $\text{Ni}_{0.5}\text{Co}_{0.5}\text{Fe}_2\text{O}_4$ ferrite at 1150 °C is regarded to be an optimized sintering temperature which can be an ideal candidate material for developing magneto-dielectrics, microwave devices, transformers, etc.

Chapter 8

Multiferroic Magnetoelectric Coupling in hybrid nanocomposite system

Abstract

Different compositions of nanocomposite lead-free multiferroic devices have been fabricated via the combination of piezoelectric polyaniline (PANI) and magnetostrictive $\text{Ni}_{0.5}\text{Co}_{0.5}\text{Fe}_2\text{O}_4$ (NCF) by changing the NCF weight fraction. The current work reports the synthesis of $x\text{NCF}:(1-x)\text{PANI}$ hybrid composite systems prepared via the physical blending method. X-ray powder diffraction (XRD) exhibits the presence of both; a polymeric amorphous phase of PANI (matrix) and a crystalline phase of inverse spinel ferrite NCF (filler) in the composites. EDAX and FESEM are used to investigate the microstructure and elemental composition of the samples, respectively. Here, frequency-dependent dielectric permittivity exhibits percolation-type behavior where permittivity (ϵ') attains a peak at a critical weight fraction ($x = 0.3$). The magnetic characteristics of the composite at the

specific stoichiometric concentration ($x = 0.3$) exhibit a significant increase in magnetization saturation (M_s) of 75.22 emu g^{-1} , while maintaining the soft ferromagnetism in the nanocomposite system. The switching behavior of electrical polarization in composite systems exhibits strong temperature dependence with a ferroelectric loop that appears to persist at even low temperatures (5 K). The remnant electrical polarization (P_r) appears to decline as the concentration of ferrite (NCF) increases. Hence, a synthesized composite system at the high electric field exhibits both ferroelectric and ferromagnetic characteristics without significant conductive losses making it suitable for potential multiferroic and capacitor applications.

8.1 Introduction

In recent years, hybrid (polymer/metal) nanocomposites have significantly emerged as prominent materials that merge optical, mechanical, and dielectric properties of polymers (organic) with magnetic characteristics as well as the high electrical conductivity of metallic (inorganic) inclusions. This configuration offers efficient performance and attractive usage of these materials for various energy storage, sensing applications, etc. [296][297][298][299][300][301]. To date, polymer components such as polyethylene, polypropylene, polyimide, and polystyrene blended with ceramics, carbon, and inorganic fillers including BaTiO_3 , MgO , Al_2O_3 , $\text{CaCu}_3\text{Ti}_4\text{O}_{12}$ shown to have the high dielectric breakdown of polymers and the high dielectric permittivity of the fillers exerting synergistic impacts. Additionally, various researchers have reported that the incorporation of metals into intrinsically conducting polymers (ICPs) has improved electron transfer via a direct or mediated method, leading to increased conductivity and stability [302][275][303]. Regardless of the type of filling in polymer nanocomposites, the size, aspect ratio, and shape of fillers are extremely significant in evaluating the intraparticle surface interaction mediated range of dielectric permittivity [304][305][258]. Polymer-based hybrid nanocomposites

are possibly developed by merging functional ceramic materials with polymers possessing magnetostrictive and piezoelectric characteristics, which further paves the research flow toward clean energy materials [306]. Moreover, fascinating phenomena have evolved when polymer-based multiferroic hybrid nanocomposites are taken into consideration and have further deepened the urge to understand the coupling between ferroelectricity and ferromagnetism at room temperature in these synthetic heterostructures [307][308].

Although the Maxwell-Wagner capacitor model, consisting of two leaky capacitors connected in series, has the potential to explain the multiferroic hybrid nanocomposite systems with heterogeneous structures [309], the mechanism for a true magnetodielectric response remains debatable. A disordered system with an appropriate blend of magnetic nanoparticles, insulating polymeric host matrix, and nanogranular structures can exhibit dielectric and magnetic properties. So far, in most of the reported polymer-based nanocomposite systems, PVDF or its derivatives have been used as polymer matrix since it exhibits good ferroelectric properties. The origin of ferroelectricity in PVDF arises from the switching of large ferroelectric domains induced by an applied electric field. Despite having a large dielectric permittivity resulting in the best energy density, the system has a large energy loss caused by electric conduction and broad ferroelectric hysteresis, generating unwanted heating and poor charging efficiency. To counteract the problem, various innovative approaches like layer-structured composites and surface-modified nanofillers have been used to optimize the molecular structure of the ferroelectric polymer. Although these techniques have helped ferroelectrics convert into relaxors and have diminished the remnant polarization to a certain limit, the polarization of PVDF depends on the interfacial coupling between the nanofillers and ferroelectric polymer. This limitation has urged us to explore new polymeric materials with better dielectric features that remain competitive in providing frequency-independent energy density.

In recent years, polyaniline (PANI), a polymer with unique properties has received enormous attention from various researchers in the field of science and nanotechnology. Due to its remarkable environmental stability, electrochemical activity, facile synthesis,

and good thermal resistance, PANI has the tendency to be synthesized and easily doped by different acids and dopants in any organic solvents or even in aqueous media. PANI usually occurs in three distinct forms depending on the oxidation and reduction process during synthesis. To date, in most of the PANI-based nanocomposite systems, PANI with high conductivity of around 10^{-4} Sm^{-1} is used which yields large permittivity of around 10^2 , but a considerable dielectric loss of 10^1 order at room temperature [310]. Various other research groups studied the effect of a polymer matrix including ceramic fillings [311] [312]. In order to improve the dielectric response in the hybrid nanocomposite, we have synthesized PANI of emeraldine base (EB) whose electrical conductivity is found to be in the order of 10^{-8} S m^{-1} at room temperature. As PANI is very sensitive to doping, applying silver paste as electrodes on the surface can modify the electrical properties. Polymers at the interface of conducting electrodes need a thorough investigation, which has been lacking in most of the literature.

The current study seeks to evaluate the dielectric property of insulating PANI in the presence of different weight fractions of ferromagnetic ceramic NCF. Though $\text{Ni}_{0.5}\text{Co}_{0.5}\text{Fe}_2\text{O}_4$ (NCF) is discovered to be a significant magnetic substance with high magneto-crystalline isotropy and high resistivity. In our composite system, at room temperature, NCF is ferromagnetic in behavior with a transition temperature of around 310 K and also exhibits novel multiferroic properties at room temperature. To the finest of our ability, such features have yet to be mentioned in the literature. Moreover, the purpose of introducing the magnetic ceramic fillers into the polymer host matrix is to increase the interaction between magnetic and dielectric particles which in turn can affect the charge dynamics that leads to lower charge leakage and enhance the charge density. In the context of the above discussion, we have synthesized and characterized flexible $x\text{NCF}:(1-x)\text{PANI}$ nanocomposites. The composites' microstructural, magnetic, structural, dielectric, and ferroelectric characteristics are investigated across broad temperature and magnetic limits of 5-300 K and $\pm 3 \text{ T}$ respectively.

8.2 Experimental

The chemicals and reagents used in the preparation were of analytical grade. Nitrates of Nickel, Cobalt, Iron (III), and Citric acid were purchased from Loba Chemie Pvt. Ltd. and utilized for the preparation of Ferrites. Ammonium persulfate (APS), Hydrochloric acid (37 %) (HCl), Ammonium Hydroxide (25 %) (NH_4OH) solution, and Aniline were purchased from Merck | Germany-Sigma-Aldrich, further used in the preparation of fine powders of Polyaniline. Distilled water was used throughout the preparation process. The connections between the electrodes were created using Ted Pella, Inc.'s Pelco conductive silver paint.

The hybrid composites $x\text{NCF}:(1-x)\text{PANI}$ are characterized by various techniques. X-ray Diffraction (XRD; Bruker) with $\text{Cu-K}\alpha$ ($\lambda = 1.5406 \text{ \AA}$) radiation analyzed the structural characteristics of the nanocomposites for 2θ ranging between 10° to 70° . The microstructure and elemental composition are studied via Field Emission Scanning Microscopy (FESEM; JEOL JSM-7610F, Au Coater; JEOL Smart Coater, plus Energy Dispersive X-ray Analysis (EDAX; OXFORD). For the study of electrical measurements, the flat surfaces of pellets acted as electrodes, where the polymer-ceramic samples on both sides were coated with conductive silver paste, which was further kept for air drying. Temperature and frequency-dependent dielectric measurements are performed for $x\text{Ni}_{0.5}\text{Co}_{0.5}\text{Fe}_2\text{O}_4:(1-x)\text{PANI}$ samples via 4 K CCR (closed cyclic refrigerator) instrument at temperature and frequency ranges of 5 K to 300 K and 100 Hz to 1 MHz respectively. The temperature and frequency-dependent (P-E) hysteresis loops are measured using a cryocooler model SRDK-205 circuit via 4 K CCR at 5 K-300 K and 50 Hz-250 Hz respectively. Room temperature magnetization measurements are made on a Lakeshore Applied Research (Model EZ9) vibrating sample magnetometer (VSM). Additionally, the magnetization hysteresis (M-H) and (M-T) loops are evaluated using a superconducting quantum interference device (SQUID) under magnetic fields in the range of -3 T to +3 T at a temperature range of 5 K-350 K

8.2.1 Polyaniline (PANI) Nanoparticles

In situ, chemical oxidative polymerization of aniline, ammonia persulphate (APS), and hydrochloric acid (HCl) were used in order to produce polyaniline (PANI). The oxidant monomer with 1.5 M of Aniline was dissolved in 0.1 M of HCl (2.09 mL) in 500 mL of distilled water in the container for homogenous stirring. The reaction mixture had been stored at an ambient temperature, and the precooled solution of APS (16 gms) in 500 ml distilled water was dissolved separately, which was further titrated over a period of 1 minute after the continuous stirring of 1 hr. The homogenous mixture of both reactions was allowed to proceed for 5-6 hrs and kept overnight for polymerization. It was then filtered using vacuum filtrate, washed with distilled water, and acetone, and followed by air drying for at least 36 hours. The dark-colored polymer powder obtained is green in color, confirming the synthesis of the Emeraldine salt form of Polyaniline (ES-PANI). Further, the synthesized ES- PANI along with 500 mL of distilled water and 1 M solutions of NH₄OH was kept under stirring at least for 7-8 hrs. The pH of 11 was maintained at ambient temperature, followed by the overnight resting of the solution. Hence, obtaining the dark blue colored Emeraldine base form of polyaniline (EB-PANI), was then thoroughly washed with distilled water, and acetone, followed by 250 mL of methanol, to remove the unreacted impurities and oligomers in the obtained polymer PANI. The obtained powder was heated overnight at 50 °C and further crushed using the mortar and pestle to obtain the fine PANI nanoparticles.

8.2.2 Ni_{0.5}Co_{0.5}Fe₂O₄ (NCF) Nanoparticles

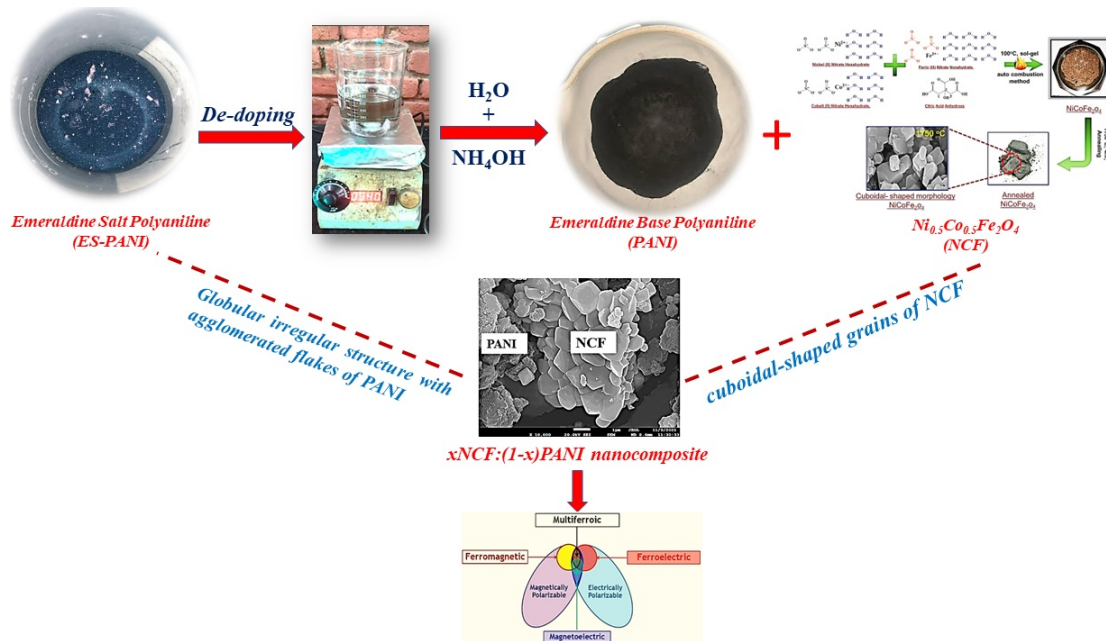
Synthesis of Ni_{0.5}Co_{0.5}Fe₂O₄ (NCF) is carried by one of the wet chemical methods known as, Pechini's process. The desired concentration of metal nitrates, Co(NO₃)₂.6H₂O, Ni(NO₃)₂.6H₂O with 0.5 wt. percent and Fe(NO₃)₂.9H₂O, (all AR grades) were employed as oxidizers, While citric acid was used as a fuel that acts as a reducing agent. To maintain a molar ratio of 1:1, the pulverized citric acid is introduced to the salt solution with cations. To

formulate a homogeneous solution, all metal nitrates and fuel were weighed, combined, heated continuously, and stirred in a hot magnetic stirrer in 100 ml of double-distilled water. A liquid ammonium hydroxide (NH_4OH) solution was also added to the mixture and agitated well to keep the pH level at 7. This homogenous mixture was further heated with continuous stirring, transforming the solution into xerogel. Heating the flammable xerogel until it ignites causes auto combustion, which results in the formation of fluffy, dark-colored powdered ferrites at the nanoscale. The charred powder was blended through grinding and then calcinated using a muffle furnace in the presence of air at $1150\text{ }^\circ\text{C}$ for 4 hours to evaporate any unburnt carbonaceous particles [28]. The dark-colored and fluffy powder is the obtained NCF nanoparticles.

The efficient production of spinel ferrite ($\text{Ni}_{0.5}\text{Co}_{0.5}\text{Fe}_2\text{O}_4$) powders via the sol-gel auto-combustion route, also known as Pechini's method have been reported. The aqueous solution of metal salts and iron is prepared homogeneously in distilled water with required stoichiometric proportions, under continuous magnetic stirring. To maintain a molar ratio of 1:1, the pulverized citric acid is introduced to the salt solution with cations. The solution's pH was maintained at 7 by adding ammonium hydroxide in droplet form at $90\text{ }^\circ\text{C}$ to $95\text{ }^\circ\text{C}$ for 2 h under continuous magnetic stirring. Due to excessive heating, surplus water evaporates and the liquid is turned into xerogel. Further, the xerogel is dried over a hot plate at $100\text{ }^\circ\text{C}$ for 1–2 h, which leads to an auto-combustion process, converting xerogel into brown fluffy powder forming the nanoparticles. Pre-sintering was done at $100\text{ }^\circ\text{C}$ for 48 h, in order to evaporate any excess moisture. By then, a pre-sintered powder sample was further sintered at different temperatures such as $850\text{ }^\circ\text{C}$, $1050\text{ }^\circ\text{C}$, and $1150\text{ }^\circ\text{C}$. Furthermore, the sintering temperature and heating rate of the $\text{Ni}_{0.5}\text{Co}_{0.5}\text{Fe}_2\text{O}_4$ sample are kept constant at $12\text{ }^\circ\text{C}$ per min for at least 4 hrs, respectively, to obtain the high crystalline and single-phase ferrite. The synthesis technique is depicted schematically in Figure 7.1. The required stoichiometric reaction occurring during the combustion synthesis is explained in Equation (7.1).

8.2.3 xNCF:(1-x)PANI Nanocomposite

The preparation of composites xNCF:(1-x)PANI was carried out via one of the ternary blend preparation methods known as physical blending. There are four different ways to prepare ternary blends: physical blending, surface-initiated polymerization, multi-branched PANI ternary composite, and thermos-responsive organic composite from sterically stabilized PANI. Out of all these, physical blending is the most simple, convenient, cost-effective, and composition-controlled method. Additionally, it is also expected that combining two components with different degradation characteristics would alter the original characteristics of the components. Thus, the composites here are prepared by fine grinding and homogenous mixing of NCF ferrite in the polymer PANI matrix via mortar and pestle. Additionally, followed by mechanically pressing the samples using the cold-press technique via KBr mechanical press instrument. The xNCF:(1-x)PANI nanocomposites are prepared with respective weight fractions (wt.) of $x = 0, 0.1, 0.3, 0.5, 0.7,$ and 1 , where x is the NCF ferrite in the polymer matrix of PANI (Figure 8.1).

FIGURE 8.1: Synthesis of $x\text{NCF}:(1-x)\text{PANI}$ Nanocomposite.

8.3 Results and Discussion

8.3.1 X-Ray Diffraction (XRD) Analysis

Figure 8.2 represents the XRD images of weight fraction dependent $x\text{NCF}:(1-x)\text{PANI}$ samples for $x = 0, 0.3,$ and 1 respectively. The XRD spectrum for pure PANI ($x=0$) indicates the appearance of a broad diffraction peak with an intense hump from 19° to 24° , thus confirming the emeraldine base form, an intermediate stable state of PANI polymer [313][152]. Also, the broad diffraction peak of PANI doesn't show any sharp peak characteristics indicating the impurity-free amorphous nature of the polymer. On the other hand, the XRD pattern of NCF ferrite ($x=1$) displays an inverse spinel crystal structure having diffraction peaks at 2θ values $18.46^\circ, 30.25^\circ, 35.58^\circ, 37.33^\circ, 43.29^\circ, 53.73^\circ, 57.24^\circ, 62.86^\circ$ ascribed to the diffraction planes of (111), (220), (311), (222), (400), (422), (511) and (440) respectively. The peaks and intensities for ferrites are matched and indexed using JCPDS diffraction data cards 74-2081 and 79-1744 [259][314]. There is no trace of

any intermediate phases such as α -Fe₂O₃ found, which again confirms the homogeneity and purity of NCF ferrites.

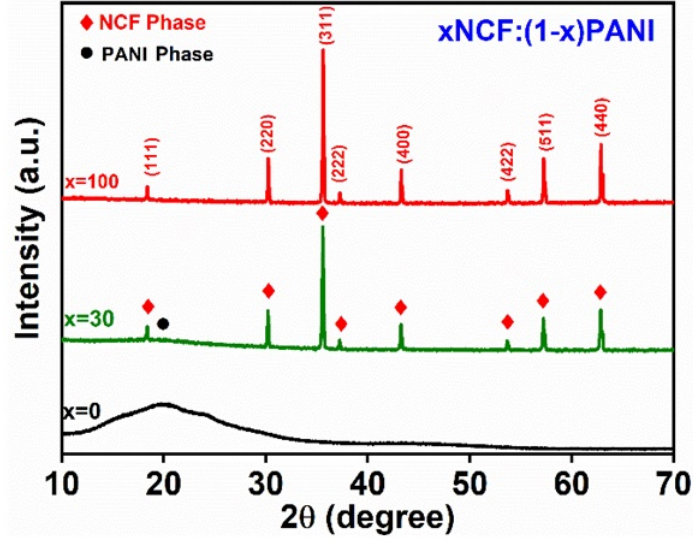


FIGURE 8.2: XRD patterns of NCF, PANI, and xNCF:(1-x)PANI nanocomposite.

The XRD spectrum for xNCF:(1-x)PANI composite (x=0.3) shows the dominant and highly crystalline diffraction peaks of NCF ferrite, eventually showing the variation in intensity. This shows that as composite formation takes place, it overshadows the broad peak of bulk matrix PANI and the peaks are more likely to appear as NCF ferrite. This behavior also confirms that the composite formation affects the interactions among particles, indicating a change in the amorphous nature of PANI as a result of its interaction with ferrite [312][315]. Further, the crystallite size (D) was calculated from the most intense peak of the diffraction plane (311) through the Debye-Scherrer formula, and the peak crystallinity of all samples by using Equation (8.1) and (8.2) respectively. Here θ represents Bragg's angle, β is the full width at half maxima (FWHM), λ is the X-ray radiation's wavelength, and K is a constant ($K=0.9$).

$$D = K\lambda/(\beta\cos\theta), \quad (8.1)$$

$$\text{Crystallinity} = (\text{Area of Crystalline Peaks} / \text{Area of All Peaks}) * 100 \quad (8.2)$$

Eventually, this interparticle interaction resulted in a crystallite decrease in size from 57 nm of as-prepared NCF ($x= 1$) to 51 nm for composite system $x= 0.3$ (Table 8.1). This overall decrease in crystallite size of a composite system along with a decrease in peak crystallinity is caused by the inclusion of NCF ferrite, which changes the PANI skeleton rings. Here the intensity and estimated peak crystallinity decrease, as it is found to be approximately 84 % for a pure sample of NCF ($x= 1$) which then reduces to 75 % for a composite system ($x= 0.3$). This overall decrease is attributed due to the PANI being absorbed by the strong adhesive force on the NCF surface [315].

Table 8.1. The structural parameters of NCF, PANI, and x NCF:(1- x)PANI nanocomposite.

Sample	Nature	$2\theta(^{\circ})$	D (nm)	Crystallinity (%)
NCF	Crystalline	35.6	57	84
x NCF:(1- x)PANI	Crystalline	35.6	51	75
PANI	Amorphous	20.0	25	50

8.3.2 Field Emission Scanning Electron Microscope (FE-SEM) and Energy Dispersive X-ray (EDAX) Analysis

Figure 8.3, displays the FESEM micrographs of x NCF:(1- x)PANI samples. Figure 8.3a displays the PANI ($x= 0$) microstructures which represent the large globular irregular structure of average size 10 μ m. The inset shows a magnified image of a single grain of PANI where sticky agglomerated flakes are seen to be separated by grain boundaries. The obtained microstructure is in accord with other research groups [316][317]. The morphology of the NCF ferrites (Figure 8.3b) has segregated cuboidal-shaped grains with defined edges [229]. This separation of grains is due to electrostatic interactions between grains [221]. The crystallite size of the dispersed NCF ferrites is 57.43 nm, whereas the average

grain size is found to be 316 nm and is estimated by using ImageJ software. Further, Figure 8.3c displays a noticeable change for the composite system $x=0.3$, which demonstrates the ferrites' uneven dispersion in the polymer matrix at the interface between NCF ferrite and PANI polymer [318]. Small magnetic filler nanoparticles grouped together in the composite system may lead to the onset of percolation at a critical fraction where a second-order jump can be expected in dielectric permittivity.

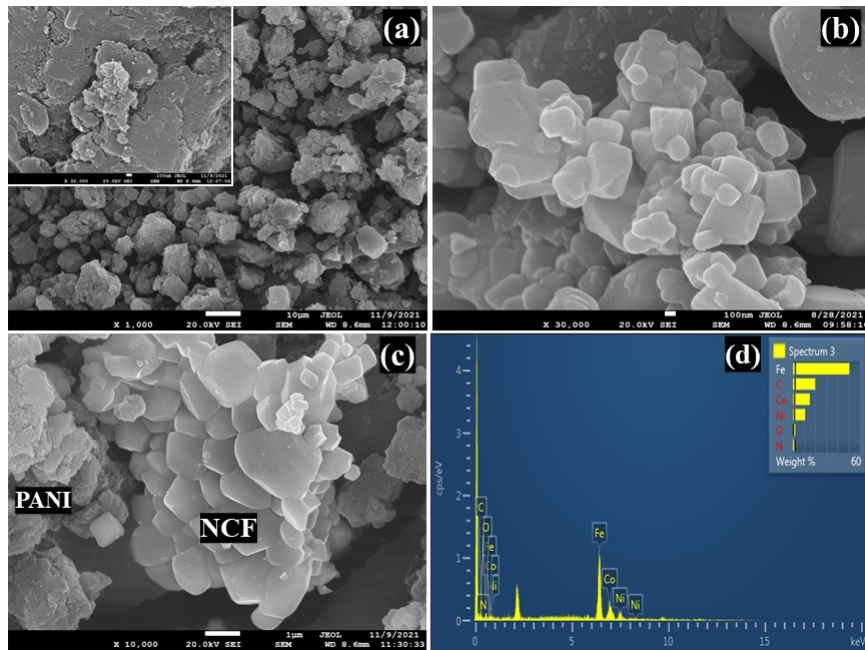


FIGURE 8.3: FESEM micrographs of (a) PANI, (b) NCF, (c) x NCF:(1- x)PANI; $x=0.3$ nanocomposite, and (d) EDAX scan of $x = 0.3$ nanocomposite.

Further, Figure 8.3d illustrates the energy dispersive X-ray analysis (EDAX) study for composite systems ($x=0.3$). The elements Co, Fe, Ni, O, C, and N are all confirmed by the EDAX spectrum. The presence of N, C, and O elements, which represent the emeraldine base form of the PANI polymer in a composite system, in addition to the elements Co, Ni, Fe, and O, serve as an indicative measure of NCF spinel ferrite.

8.3.3 Dielectric Analysis

Figure 8.4, shows the dielectric analysis of $x\text{NCF}:(1-x)\text{PANI}$ samples with respect to a temperature ranging from 5 K to 300 K at 30 kHz. Figure 8.4a displays the temperature-dependent dielectric permittivity for samples $x= 0, 0.1, 0.3, 0.5, 0.7,$ and 1. For pure PANI sample ($x= 0$), exhibits a higher dielectric constant with a structural phase transition of the first order at 150 K. The sudden rise could be due to PANI emeraldine base's (EB) glass transition temperature (T_g), which is in accord with the literature present for polymer ceramic composite systems [319][320]. Further, for the compositions ($x= 0.1, 0.5,$ and 0.7), the dielectric permittivity is found to decrease significantly between a wide range of temperatures, 5-300 K with a positive slope appearing beyond 200 K. This attributes to the fact that on increasing the NCF ferrite concentration, strong competition arises in between magnetic NCF particles and the terminal amide group of non-magnetic PANI that leads to the decrease in electrical polarization [319]. Whereas for the composite system ($x= 0.3$), it is observed that dielectric permittivity has significantly increased by a factor of 10 in magnitude which is primarily caused by the polymer matrix's divergence in cluster size. Hence, the variation of permittivity in the composite systems resembles percolation-type behavior where permittivity attains a peak at critical weight fraction ($x= 0.3$) at 30 kHz. Additionally, the sharp rise in the real dielectric permittivity as observed in PANI is found to shift towards the high-temperature regions with increasing NCF ferrite concentration. This observation indicates that the T_g of composites has increased because the chain mobility of PANI is constrained by the interfacial interaction between nanofiller and polymer matrix [321].

The temperature-dependent deviations of tangent loss for the prepared sample are depicted in Figure 8.4b. The increased tangent loss peak can be observed for PANI ($x= 0$) at T_g of 150 K and eventually drops off as the temperature rises. In contrast, the composite systems' tangent loss peaks ($x= 0.1, 0.3, 0.5,$ and 0.7) are more noticeable at temperatures

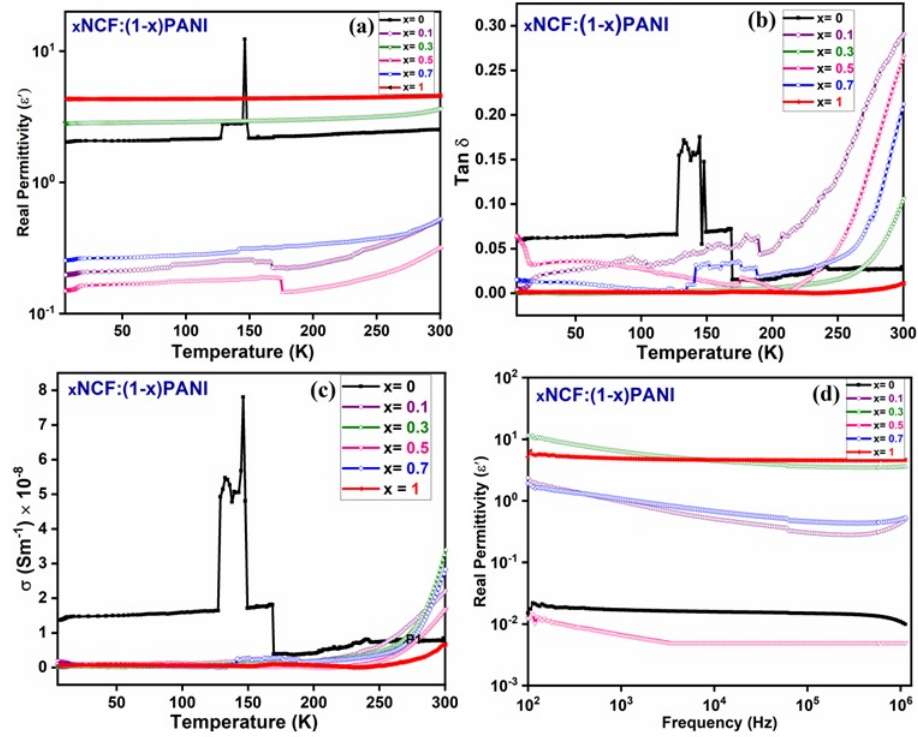


FIGURE 8.4: Dielectric analysis of xNCF:(1-x)PANI samples, (a) ϵ' vs T (K), (b) $\tan \delta$ vs T (K), (c) σ (Sm^{-1}) vs T (K), (d) Room temperature permittivity ϵ' vs Freq. (Hz) of samples.

above 150 K, and as a result, the tendency for losses to continue escalates, as the temperature rises. The increased loss peaks and their shifts suggest a thermally activated dielectric relaxation process that results in a harmonicity in the polarization mechanism [322][323]. The temperature dependence of the AC conductivity of the samples is illustrated in Figure 8.4c. The incorporation of NCF ferrite has the same influence on the conductivity properties, as compared to the real dielectric permittivity. As temperature rises above 150 K, it is seen that the AC conductivity also does, following a pattern observable in many polymer ceramic composites [324]. This is primarily caused by the composite systems' ability to generate thermally active charge carriers as the temperature rises.

Figure 8.4d shows the frequency-dependent variation of dielectric permittivity (ϵ') of as-prepared xNCF:(1-x)PANI samples, ranging from 100 Hz to 1 MHz at 300 K. For PANI ($x=0$), the dielectric permittivity is found to be one order less the value when PANI

is cycled through low temperature (5 K) to high temperature (300 K). This significant change is considered to be due to the diffusion of silver-paired complex ions from the electrode-sample interfacial surface to a few atomic layers of PANI, thus giving rise to the Maxwell-Wagner effect. The figure shows that for the composite systems, the value of ϵ' drops as the frequency rises, whereas, for pure NCF and PANI, the behavior is practically frequency-independent. In general, A material's dielectric response to an external electric field depends on the polarization effect that takes place within the matrix. The observed result is the normal dielectric dispersion which is usually found in ferrites [325]. Given the highest interfacial effect between an infinite cluster of NCF and dielectric PANI, among all composite systems, ($x= 0.3$) exhibits a high value of real permittivity. Because the relaxation mechanism is relatively slow in comparison to resonant electronic transitions in NCF, pure polyaniline, and all other composites exhibit low real permittivity (ϵ'). Due to this, it is relatively simple to pin the charge carriers at a close distance across the polymer chain, leading to an increased conductivity with respect to increasing frequency [326].

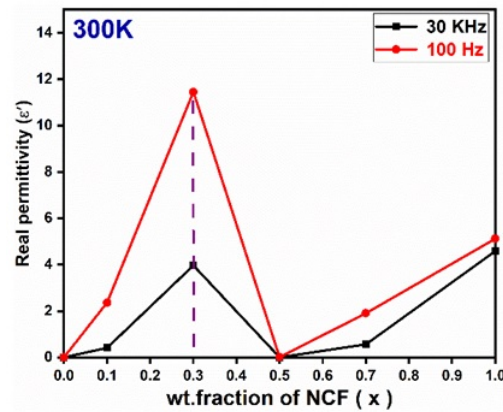


FIGURE 8.5: Real permittivity (ϵ') vs wt. fraction of NCF (x) samples at 300 K.

In addition, Figure 8.5 represents the room temperature variation of real permittivity (ϵ') vs the weight (wt.) fraction of NCF (x) in the polymer matrix at low (100 Hz) and high frequency (30 kHz) respectively. It confirms that the measured dielectric permittivity shows an instant increase, particularly for the composite system ($x= 0.3$) at room temperature. This instant increase supports the percolation phenomenon since the curve seems

to attain a peak at the percolation threshold [327][328][329][330]. Hence, dielectric permittivity is also expected to follow a power law behavior near the threshold independent of frequency.

8.3.4 Magnetic Analysis

The variation of the M-H curve is recorded for xNCF:(1-x)PANI samples at 300 K as shown in Figure 8.6a,b. Figure 8.6a illustrates the M-H curve, which depicts the NCF nanoparticles (blue line) having soft ferromagnetic behavior with magnetization saturation 14.18 emu g^{-1} and coercive field 391 Oe at room temperature (300 K). In addition, for the composite system $x= 0.3$ (red line), the magnetization saturation and coercive field at room temperature (300 K) have increased to 75.22 emu g^{-1} and 412 Oe respectively (Table 8.2). Here, PANI (green line) exhibits diamagnetic-type behavior at room temperature. It can be seen that the saturation magnetization M_s values of the investigated samples exhibit unique contrasting differences. Here, the composite system at $x= 0.3$ exhibits strong ferromagnetic behavior, with a sharp hysteresis curve. Composites with agglomerated magnetic fillers dispersed in a polymer matrix represent a complex system that is often influenced by the interaction at the ferrite-polymer interface [331]. In addition, the reported values of saturation magnetization were quite different from other groups. For instance, M_s is 35 emu g^{-1} for PANI/ Fe_3O_4 (32 wt. % of Fe_3O_4) [332], M_s for (1-x)PVDF-xNFO (15 wt. % of NiFe_2O_4) composite is 2.8 emu g^{-1} [333]. Clearly, the saturation magnetization (M_s) of prepared xNCF:(1-x)PANI samples is much higher than other groups. This increase in saturation magnetization (M_s) can be attributed due to the variation in the surface and size of magnetic nanoparticles and thickness of the nanocomposite [332][333]. Meanwhile, M_s values of the composite system ($x= 0.3$) fit well as the loops are normalized. It is anticipated that the existence of the PANI and interfacial effects will alter the asymmetric distribution of the magnetic ions and their spin orientation, particularly near interfaces, and hence have an impact on the magnetic interactions [334].

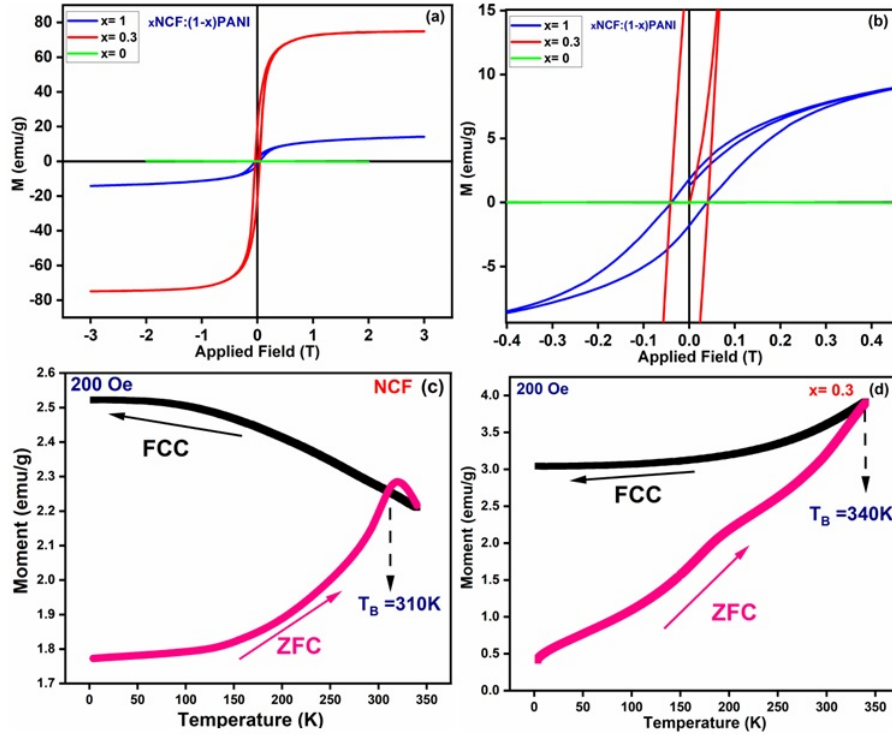


FIGURE 8.6: (a) Room temperature M-H curve of $x\text{NCF}:(1-x)\text{PANI}$ samples, (b) Magnified view of M-H curves. Temperature-dependent M-T curves (ZFC–FCC) of (c) NCF, and (d) $x = 0.3$ nanocomposite.

Table 8.2. Magnetic parameters of the hybrid composite $x\text{NCF}:(1-x)\text{PANI}$ measured at 300 K. For comparison, values reported in the literature, corresponding to other heterostructures, are also mentioned.

Sample	M_s (emu g^{-1})	M_s (emu g^{-1})	H_c (Oe)	$S^2 = M_r/M_s$
NCF	14.18	1.80	391	0.13
$x\text{NCF}:(1-x)\text{PANI}$ (30 % of $x\text{NCF}$)	75.22	20.22	412	0.26
$\text{PANI}/\text{Fe}_3\text{O}_4$ (32 % of Fe_3O_4), [44]	35.8	14.85	100	0.41

Moreover, the specific morphology and distribution of NCF and PANI strongly influence the surface interactions of the magnetic nanoparticles. Defects can be repaired by the PANI coating, and the ferrite surface is capable of remaining smooth, which eventually weakens the defects caused by ferrite surfaces leading to an increase in coercivity [335]. Further investigations on the magnetic properties are yet to be carried out for a detailed analysis. Hence, these types of composite materials filled with ferrite particles based on polymer matrix materials are called bonded magnets which are of current research interest due to their possible applications in EMI shielding materials, microwave absorption, magnetic storage, and spintronics devices. Figure 8.6b shows a magnified view of the M-H curve at room temperature affirming the presence of a hysteresis loop, which represents a difference of coercive field for samples ($x = 0.3$) and ($x = 1$) respectively.

Figure 8.6c displays the temperature-dependent polarisation curves (M-T) of the NCF nanoparticles in their as-prepared state and for the composite system ($x = 0.3$) (Figure 8.6d). In order to measure the field cool (FCC, black line), samples were cooled from 350 K to 5 K using a 200 Oe magnetic field, and data was collected as the samples were heated. Similar procedures were used for the zero-field cool (ZFC, red line) measurement, with the exception of adding the magnetic field during cooling. The interesting feature in the ZFC curves of the NCF nanoparticles and composite system $x = 0.3$ is the shift of maxima to a higher temperature (pink curves in Figure 8.6c, and 8.6d), which reflects the beginning of the superparamagnetic to ferromagnetic transition. The blocking temperature (T_B), which is attributed to NCF nanoparticles at around 310 K and the composite system ($x = 0.3$) at about 340 K, is the temperature at which the peak in ZFC curves occurs [336]. The FCC curve of as-prepared NCF nanoparticles shows a concave pattern that changes to convex type when the same NCF nanoparticles are used as fillers in a composite system ($x = 0.3$) (black curves in Figure 8.6(c), and 8.6(d)). Thus, NCF is confirmed to be in the superparamagnetic state, whereas the composite system ($x = 0.3$) exhibits non-negligible inter-particle interactions in a ferromagnetic state at ambient temperature [337]. The bifurcation between FCC and ZFC magnetization at higher temperatures in composite

systems for as-prepared NCF also signifies that with the change in inter-particle separation, the inter-particle interaction modifies which further increases the blocking temperature.

8.3.5 Ferroelectric Analysis

In general, ferroelectricity is linked to an empty outer shell of d electrons (known as d^0 configuration), whereas magnetic ordering typically requires unpaired d or f electrons, i.e., partially filled [338]. Here, Figure 8.7a depicts the PANI electric-field-dependent polarization (P-E) loop at room temperature, which displays a homogeneous hysteresis loop featuring a small area and remnant polarization suitable for energy discharge and storage applications.

Figure 8.7b displays, the P-E hysteresis loop at the room temperature (300 K) of $x\text{NCF}:(1-x)\text{PANI}$ samples with different compositions. In order to plot the loops, an electric field is used ranging from $\pm 0.2 \text{ kV cm}^{-1}$. It is discovered that when ferrite concentration increases, the composites' coercive field, remanent polarization, and saturation polarization all decrease. Similar to PVDF-based relaxor ferroelectric polymers, ferroelectric domains have a "critical size" below which macroscopic ferroelectric domains will become unstable, [339] ferroelectric domains can emerge from nanodomains at high electric fields. Ferroelectric domains can change back into nanodomains if the field is removed. The energy density of the composite is determined by the difference between the maximum and remanent polarisation, and nanodomains display substantially lower remanent polarisation than ferroelectric domains do (as can be observed for pure NCF; $x=1$). From a structural perspective, this conversion of nanodomains to ferroelectric domains is equivalent to the reversible change between polar and nonpolar conformations, which causes remanent polarization [340][341].

The temperature-dependent P-E hysteresis loop is observed for the composite system ($x=0.3$) from 5 K to 300 K (Figure 8.7c). In accordance with the microstructural analysis by FESEM, the hysteresis measurements show that at low temperatures, the value of remnant polarization (P_r) and saturation polarization (P_s) decreases, resulting in a

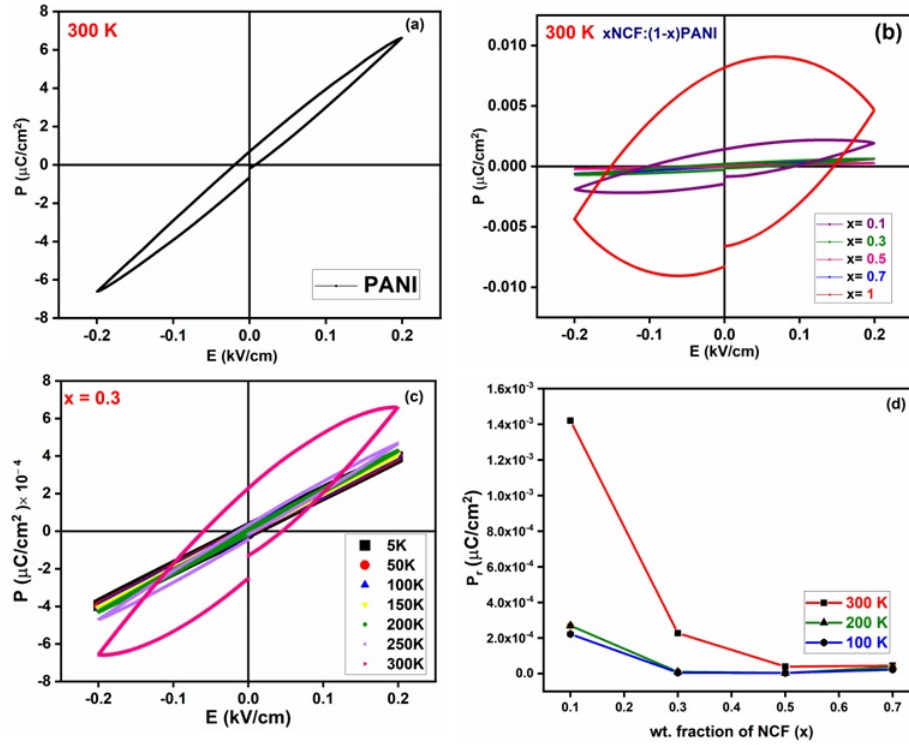


FIGURE 8.7: P–E hysteresis loop at room temperature (a) PANI, (b) $x\text{NCF}:(1-x)\text{PANI}$ samples, (c) Temperature-dependant P–E hysteresis loop for nanocomposite ($x=0.3$), and (d) Remnant Polarization P_r vs wt. fraction of NCF (x).

flattened loop that, in general, indicates compositional uniformity and inhomogeneity of the grain size of the component phases (Figure 8.3c) [16][342]. Due to the symmetrical distribution of the ferrite inclusion in a ferroelectric matrix, the analyzed composites had lower coercivity than the pure PANI (Figure 8.7a). Further, Figure 8.7d represents the temperature-dependent variation of remnant polarization P_r vs wt. fraction of NCF. The plotted graph affirms the decrease in remnant polarization (P_r) with respect to the rise in the concentration of ferrite, which is carefully scrutinized because of the robust paraelectric nature of NCF nanoparticles [343]. Therefore, the obtained investigations are in concurrence with those from the literature for composites at similar conditions [339].

Hence, the presence of both ferroelectric and magnetic characteristics confirms the multiferroic nature of $x\text{NCF}:(1-x)\text{PANI}$ samples. In addition, this interaction between the ferroelectric and magnetic domains is substantial for multiferroic applications, which can

also be achieved by magnetoelectric (ME) or Magneto-dielectric (MD) coupling. The MD coupling is achieved by evaluating the variation of the dielectric constant in the presence of a magnetic field or vice versa. In addition, this coupling can also be achieved by-product of the piezoelectric and magnetostriction characteristics present in ferroelectric and magnetic domains [344]. The preparation of xNCF:(1-x)PANI samples hold true justification for Magnetodielectric materials, as these magneto-polymer composites due to their specific mechanical properties, good formability, and toughness (typical for polymers) allow preparing the products for magnetic circuits of complicated shapes. In addition, these novel materials' fascinating multiferroic and magnetic characteristics have their use in many special applications, such as for the implementation of low-profile coils for identification systems, sensors, contactless smart cards, magnetic field-controlled, and energy storage devices [345].

8.4 Conclusion

The successful synthesis of xNCF:(1-x)PANI hybrid composites with different stoichiometric ratios ($x = 0, 0.1, 0.3, 0.5, 0.7,$ and 1) are carried out via the physical blending method. The XRD analysis confirms a decrease in crystallite size (57 nm to 51 nm) along with the peak crystallinity (84 % to 75 %) for nanocomposite is a result of PANI being absorbed on the NCF surface by the powerful adhesive force. The FESEM analysis shows a noticeable change in the composite, exhibiting both NCF and PANI morphology as irregular and aggregated globules structure. EDAX affirms the presence of homogenous and single-phase NCF in the composite system. Temperature-dependent dielectric analysis of xNCF:(1-x)PANI samples confirm the percolation type behavior of the threshold concentration ($x=0.3$). Whereas, frequency-dependent variation exhibits dielectric permittivity with low dielectric losses and low AC conductivity at 300 K. The magnetic characteristics illustrated by M-H and M-T hysteresis loops exhibit strong ferromagnetic properties of the composite, along with revealing the transition from the superparamagnetic phase of

NCF to the ferromagnetic phase of composite ($x=0.3$). Further, ferroelectricity has been observed for all the $x\text{NCF}:(1-x)\text{PANI}$ samples, since with an increase in ferrite concentration, there is a decline in remnant polarisation P_r , coercivity, and saturation polarisation P_s . Although ideal multiferroic properties have been observed for the sample ($x=0.3$). Hence, the successful synthesis of $x\text{NCF}:(1-x)\text{EB-PANI}$ multiferroic composites occurs as a suitable option for magnetodielectric applications, magnetic field-controlled devices, multiferroics, and energy storage devices.

Chapter 9

Summary and Future Scope

The current study focuses on the sol-gel auto-combustion method for synthesizing Nickel-Cobalt Ferrite powders with high efficiency utilizing citric acid as fuel. The nickel-cobalt ferrite particles are nano-crystalline in nature, as demonstrated by the applied characterization techniques such as XRD and FESEM. At an annealed temperature of 1150 °C, the average ferrite particle size is about ~ 71 nm. Also, the pure single phase of ferrites was observed at a high annealing temperature (1150 °C). Due to the annealing temperature, the dielectric constant is observed to be variable, and the maximum dielectric constant is obtained to be $\sim 15k$ at 1150 °C. Therefore, annealing at 1150 °C is promoted to be one of the most suitable temperatures for the effective study of structural, morphological, and dielectric analysis of (Ni-Co) ferrite NPs.

Due to the exceptional qualities of the obtained $\text{Ni}_{0.5}\text{Co}_{0.5}\text{Fe}_2\text{O}_4$ (spinel ferrite), nanoparticles were successfully synthesised using the sol-gel auto-combustion method. Scherrer's equation evaluates the crystallite size (D) (48.4-71.3 nm) in the nano-size range. The X-ray density (D_x) estimated a decrease from 5.35 g/cm³ to 5.31 g/cm³ with an increased sintering temperature. The microstructural insights via XPS spectra of the ferrite confirm the polycrystalline nature (low temperature) to the high crystalline single-phase (high temperature) at 1150 °C by showcasing all the elements of the prepared samples are in

the desired oxidation states. FESEM images exhibit a change in morphology from non-uniform coalesced globular grains (850 °C) to cuboidal-shaped particles (1150 °C), due to an increase in agglomeration with increased sintering temperature. The elemental composition of produced samples was also examined by EDAX scans; the observed values show a slight difference between experimental and theoretical values of the atomic percent (at. %) of as-synthesized samples for all sintering temperatures. Additionally, TEM images verify the morphology of cuboidal shape grains having a grain size (average) of about 84 nm for optimized $\text{Ni}_{0.5}\text{Co}_{0.5}\text{Fe}_2\text{O}_4$ sample at 1150 °C. Further, the high-resolution TEM images illustrate the single-direction oriented planes, followed by SAED patterns affirming the development of a single-phase of the as-prepared samples at the high sintering temperature. Impedance and modulus spectroscopy were used to analyze the materials' electrical response, and they were successful in determining how the $\text{Ni}_{0.5}\text{Co}_{0.5}\text{Fe}_2\text{O}_4$ samples' contributions from grains and grain boundaries were affected by the sintering temperature. Complex impedance spectroscopy estimates the Nyquist plot, which displays how resistive qualities grow as the sintering temperature rises. Owing to the presence of uneven semi-circular arcs in complex modulus spectra the synthesized samples exhibit the non-Debye type of relaxation behavior. Thus, the synthesized $\text{Ni}_{0.5}\text{Co}_{0.5}\text{Fe}_2\text{O}_4$ ferrite at 1150 °C is regarded to be an optimized sintering temperature which can be an ideal candidate material for developing magneto-dielectrics, microwave devices, transformers, etc.

Taking into consideration the findings of the above studies, The successful synthesis of $x\text{NCF}:(1-x)\text{PANI}$ hybrid composites with different stoichiometric ratios ($x = 0, 0.1, 0.3, 0.5, 0.7, \text{ and } 1$) are carried out via the physical blending method. The XRD investigation indicates a decrease both in peak crystallinity (84 % to 75 %) and in crystallite size (from 57 nm to 51 nm) of the nanocomposite, which results from PANI being absorbed on the NCF surface by its powerful adhesive force. The FESEM analysis shows a noticeable change in the composite, exhibiting both NCF and PANI morphology as irregular and aggregated globules in structure. EDAX affirms the presence of homogenous and single-phase NCF in the composite system. Temperature-dependent dielectric analysis

of xNCF:(1-x)PANI samples confirm the percolation type behavior at the threshold concentration ($x = 0.3$). Whereas, at room temperature, the frequency-dependent variation exhibits dielectric permittivity with low dielectric losses and a decrease in AC conductivity. The magnetic properties illustrated by the M-H and M-T hysteresis loops indicate strong ferromagnetic characteristics and also reveal the shift from the superparamagnetic behavior of NCF to the ferromagnetic phase of the composite system ($x = 0.3$). Further, ferroelectricity has been observed for all the xNCF:(1-x)PANI samples, along with a decline in remnant polarization P_r , coercivity, and saturation polarization P_s with an increase in ferrite concentration. Therefore, ideal multiferroic properties have been observed for the sample ($x = 0.3$). Therefore, the successful synthesis of xNCF:(1-x) PANI multiferroic composites emerges as a suitable candidate for magnetodielectric applications, multiferroics, magnetic field-controlled devices, and energy storage devices.

Future Scope

- To avoid exploitation of ferroelectric polymers such as polyvinylidene fluoride (PVDF) for energy storage applications, alternate options of the conducting polymers such as Polypyrrole (PPy), polyvinyl acetate (PVA) along with other ferrites such as hexaferrites may be explored for the fabrication of hybrid nanocomposites.
- The made composites can be used as an active electrode material for the fabrication of energy harvesters that could erase the need for external peripherals in the potential multiferroic industries.
- In addition, the substantial generation of multiferroicity can also be achieved without coupling of magnetoelectric (ME) or Magneto-dielectric (MD) phenomenos, using the materials such as (Chromates, aluminates and hexaferrites).

Hence, we hope the present work will provide the required impetus to a lot of future study. We believe that the aforementioned aspects will provide researchers working in this field more chances to look at cutting-edge hybrid nanocomposites for potential magnetic and dielectric applications in the future.

References

- [1] Adam Vaughan. Un climate change summit, 2019.
- [2] T Ibn-Mohammed, CA Randall, KB Mustapha, J Guo, J Walker, S Berbano, SCL Koh, D Wang, DC Sinclair, and IM Reaney. Decarbonising ceramic manufacturing: A techno-economic analysis of energy efficient sintering technologies in the functional materials sector. *Journal of the European ceramic society*, 39(16):5213–5235, 2019.
- [3] Rupam Mukherjee, Gavin Lawes, and Boris Nadgorny. Enhancement of high dielectric permittivity in $\text{CaCu}_3\text{Ti}_4\text{O}_{12}/\text{RuO}_2$ composites in the vicinity of the percolation threshold. *Applied Physics Letters*, 105(7):072901, 2014.
- [4] Stefanie A Sherrill, Parag Banerjee, Gary W Rubloff, and Sang Bok Lee. High to ultra-high power electrical energy storage. *Physical Chemistry Chemical Physics*, 13(46):20714–20723, 2011.
- [5] Chang Liu, Feng Li, Lai-Peng Ma, and Hui-Ming Cheng. Advanced materials for energy storage. *Advanced materials*, 22(8):E28–E62, 2010.
- [6] Graeme A Snook, Pon Kao, and Adam S Best. Conducting-polymer-based supercapacitor devices and electrodes. *Journal of power sources*, 196(1):1–12, 2011.
- [7] Hiroshi Kishi, Youichi Mizuno, and Hirokazu Chazono. Base-metal electrode-multilayer ceramic capacitors: past, present and future perspectives. *Japanese journal of applied physics*, 42(1R):1, 2003.

-
- [8] Ming-Jen Pan and Clive A Randall. A brief introduction to ceramic capacitors. *IEEE electrical insulation magazine*, 26(3):44–50, 2010.
- [9] Dawei Wang, Di Zhou, Kaixin Song, Antonio Feteira, Clive A Randall, and Ian M Reaney. Cold-sintered c0g multilayer ceramic capacitors. *Advanced Electronic Materials*, 5(7):1900025, 2019.
- [10] Yukio Sakabe. Multilayer ceramic capacitors. *Current Opinion in Solid State and Materials Science*, 2(5):584–587, 1997.
- [11] J Yamamatsu, N Kawano, T Arashi, A Sato, Y Nakano, and T Nomura. Reliability of multilayer ceramic capacitors with nickel electrodes. *Journal of Power Sources*, 60(2):199–203, 1996.
- [12] Hiroshi Saito, Hirokazu Chazono, Hiroshi Kishi Hiroshi Kishi, and Nobutatsu Yamaoka Nobutatsu Yamaoka. X7r multilayer ceramic capacitors with nickel electrodes. *Japanese journal of applied physics*, 30(9S):2307, 1991.
- [13] Thomas Christen and Martin W Carlen. Theory of ragone plots. *Journal of power sources*, 91(2):210–216, 2000.
- [14] Masao Yano and Ryouhei Uchida. History of power electronics in japan. *IEEJ Transactions on Fundamentals and Materials*, 121(1):2–10, 2001.
- [15] M Stanley Whittingham. Materials challenges facing electrical energy storage. *Mrs Bulletin*, 33(4):411–419, 2008.
- [16] Qi Li, Feihua Liu, Tiannan Yang, Matthew R Gadinski, Guangzu Zhang, Long-Qing Chen, and Qing Wang. Sandwich-structured polymer nanocomposites with high energy density and great charge–discharge efficiency at elevated temperatures. *Proceedings of the National Academy of Sciences*, 113(36):9995–10000, 2016.

-
- [17] A Serghei, M Tress, and F Kremer. The glass transition of thin polymer films in relation to the interfacial dynamics. *The Journal of chemical physics*, 131(15):154904, 2009.
- [18] Shaohui Liu, Bo Shen, Haoshan Hao, and Jiwei Zhai. Glass–ceramic dielectric materials with high energy density and ultra-fast discharge speed for high power energy storage applications. *Journal of Materials Chemistry C*, 7(48):15118–15135, 2019.
- [19] Michael G Todd and Frank G Shi. Complex permittivity of composite systems: a comprehensive interphase approach. *IEEE Transactions on Dielectrics and Electrical Insulation*, 12(3):601–611, 2005.
- [20] AL Efros. High volumetric capacitance near the insulator-metal percolation transition. *Physical Review B*, 84(15):155134, 2011.
- [21] Enis Tuncer, Adam J Rondinone, Jonathan Woodward, Isidor Sauers, D Randy James, and Alvin R Ellis. Cobalt iron-oxide nanoparticle modified poly (methyl methacrylate) nanodielectrics: Dielectric and electrical insulation properties. *Applied Physics A*, 94:843–852, 2009.
- [22] M Gich, C Frontera, A Roig, J Fontcuberta, E Molins, N Bellido, Ch Simon, and C Fleta. Magnetoelectric coupling in ϵ -fe₂o₃ nanoparticles. *Nanotechnology*, 17(3):687, 2006.
- [23] MP Singh, KD Truong, S Jandl, and P Fournier. Long-range ni/mn structural order in epitaxial double perovskite la₂ nimno₆ thin films. *Physical Review B*, 79(22):224421, 2009.
- [24] N Hur, S Park, S Guha, A Borissov, V Kiryukhin, and S-W Cheong. Low-field magnetodielectric effect in terbium iron garnets. *Applied Physics Letters*, 87(4):042901, 2005.
- [25] N Hur, S Park, PA Sharma, S Guha, and SW Cheong. Colossal magnetodielectric effects in d y m n₂ o₅. *Physical review letters*, 93(10):107207, 2004.

- [26] VJ Folen, GT Rado, and EW Stalder. Anisotropy of the magnetoelectric effect in Cr_2O_3 . *Physical Review Letters*, 6(11):607, 1961.
- [27] ZJ Huang, Y Cao, YY Sun, YY Xue, and CW Chu. Coupling between the ferroelectric and antiferromagnetic orders in ymno_3 . *Physical Review B*, 56(5):2623, 1997.
- [28] Yusuke Tokunaga, Nobuo Furukawa, Hideaki Sakai, Yasujiro Taguchi, Takahisa Arima, and Yoshinori Tokura. Composite domain walls in a multiferroic perovskite ferrite. *Nature materials*, 8(7):558–562, 2009.
- [29] NA Algarou, Y Slimani, MA Almessiere, FS Alahmari, MG Vakhitov, DS Klygach, SV Trukhanov, AV Trukhanov, and A Baykal. Magnetic and microwave properties of $\text{SrFe}_{12}\text{O}_{19}/\text{mCe}_0.04\text{Fe}_{1.96}\text{O}_4$ ($m = \text{Cu, Ni, Mn, Co}$ and Zn) hard/soft nanocomposites. *Journal of Materials Research and Technology*, 9(3):5858–5870, 2020.
- [30] Munirah A Almessiere, Sadik Güner, Yassine Slimani, Mohammed Hassan, Abdulhadi Baykal, Mohammed Ashraf Gondal, Umair Baig, Sergei V Trukhanov, and Alex V Trukhanov. Structural and magnetic properties of $\text{Co}_0.5\text{Ni}_0.5\text{Ga}_0.01\text{Gd}_0.01\text{Fe}_{1.98}\text{O}_4/\text{ZnFe}_2\text{O}_4$ spinel ferrite nanocomposites: Comparative study between sol-gel and pulsed laser ablation in liquid approaches. *Nanomaterials*, 11(9):2461, 2021.
- [31] MA Subramanian, Tao He, Jiazhong Chen, Nyrrisa S Rogado, Thomas G Calvarese, and Arthur W Sleight. Giant room-temperature magnetodielectric response in the electronic ferroelectric LuFe_2O_4 . *Advanced Materials*, 18(13):1737–1739, 2006.
- [32] IV Lisnevskaya, IA Bobrova, TG Lupeiko, MR Agamirzoeva, and KV Myagkaya. $\text{Y}_3\text{Fe}_5\text{O}_{12}/\text{Na, Bi, Sr}$ -doped PZT particulate magnetoelectric composites. *Journal of Magnetism and Magnetic Materials*, 405:62–65, 2016.
- [33] Y Wang. *Phys. rev. b: Condens. matter mater. phys.* 2006.
- [34] M Naveed Ul-Haq, Tayyaba Yunus, Arif Mumtaz, VV Shvartsman, and Doru C Lupascu. Magnetodielectric effect in relaxor/ferrimagnetic composites. *Journal of Alloys and Compounds*, 640:462–467, 2015.

-
- [35] YP Yao, Y Hou, SN Dong, and XG Li. Giant magnetodielectric effect in terfenol-d/pzt magnetoelectric laminate composite. *Journal of applied physics*, 110(1):014508, 2011.
- [36] Yemei Han, Lingxia Li, Dong Guo, Xiang Ren, and Wangsuo Xia. Magnetodielectric effect in $\text{nanbo}_3\text{-nife}_2\text{o}_4$ particulate composite. *Materials Letters*, 98:19–21, 2013.
- [37] Pedro Martins and Senentxu Lanceros-Méndez. Polymer-based magnetoelectric materials. *Advanced Functional Materials*, 23(27):3371–3385, 2013.
- [38] Debajyoti Nath, SK Mandal, and A Nath. Investigation of physical properties of magnetoelectric $\text{lafeo}_3\text{-ermno}_3$ lead-free nanocomposites. *Applied Physics A*, 124:1–7, 2018.
- [39] B Kumari, P R Mandal, and T K Nath. Magnetic, magnetocapacitance and dielectric properties of bifeo_3 nanoceramics. *Advanced Materials Letters*, 5(2):84–88, 2014.
- [40] Soumi Chatterjee, Ramaprasad Maiti, and Dipankar Chakravorty. Large magnetodielectric effect and negative magnetoresistance in nio nanoparticles at room temperature. *RSC advances*, 10(23):13708–13716, 2020.
- [41] G Lawes, R Tackett, B Adhikary, R Naik, O Masala, and R Seshadri. Positive and negative magnetocapacitance in magnetic nanoparticle systems. *Applied physics letters*, 88(24):242903, 2006.
- [42] Sanjay K Upadhyay, EV Sampathkumaran, S Rayaprol, and A Hoser. Magnetic and magnetodielectric behavior of the haldane spin-chain system, $\text{ho}_2\text{banio}_5$. *Materials Research Express*, 6(3):036107, 2018.
- [43] Pedro Martins, D Silva, M P. Silva, and S Lanceros-Mendez. Improved magnetodielectric coefficient on polymer based composites through enhanced indirect magnetoelectric coupling. *Applied Physics Letters*, 109(11):112905, 2016.

- [44] P Anithakumari, BP Mandal, Ehab Abdelhamid, R Naik, and AK Tyagi. Enhancement of dielectric, ferroelectric and magneto-dielectric properties in pvdF-baFe₁₂O₁₉ composites: a step towards miniaturized electronic devices. *RSC Advances*, 6(19):16073–16080, 2016.
- [45] Sang-Eui Lee, Seong Pil Choi, Kyung-Sub Oh, Jaehwan Kim, Sang Min Lee, and Kang Rae Cho. Flexible magnetic polymer composite substrate with Ba_{1.5}Sr_{1.5}Z hexaferrite particles of vhf/low uhf patch antennas for UAVs and medical implant devices. *Materials*, 13(4):1021, 2020.
- [46] Snehlata Aggarwal, KS Sreeja, S Chakrabarti, VR Palkar, and Arup R Bhattacharyya. Fabrication and characterization of flexible films of poly(vinylidene fluoride)/Pb(Fe_{0.5}Ti_{0.5})_{3- δ} multi-ferroic nano-composite. *RSC Advances*, 6(49):42892–42898, 2016.
- [47] Sang-Eui Lee, Han-Joon Kim, Jae-Ho Lee, Kyoung-Sub Oh, H Thomas Hahn, and Ji-Woong Choi. Magnetodielectric hexaferrite flake/polymer substrate for implantable antenna with an enhanced insensitivity to implant position. *Materials Letters*, 187:94–97, 2017.
- [48] Moustafa A Darwish, Alex V Trukhanov, Oleg S Senatov, Alexander T Morchenko, Samia A Saafan, Ksenia A Astapovich, Sergei V Trukhanov, Ekaterina L Trukhanova, Andrey A Pilyushkin, Antonio Sergio B Sombra, et al. Investigation of ac-measurements of epoxy/ferrite composites. *Nanomaterials*, 10(3):492, 2020.
- [49] Olena Yakovenko, Oleksandra Lazarenko, Ludmila Matzui, Ludmila Vovchenko, Mykola Borovoy, Petro Tesel'ko, Oleg Lozitsky, Ksenia Astapovich, Alexey Trukhanov, and Sergey Trukhanov. Effect of Ga content on magnetic properties of BaFe_{12-x}Ga_xO₁₉/epoxy composites. *Journal of Materials Science*, 55(22):9385–9395, 2020.

-
- [50] Bas B Van Aken, Jean-Pierre Rivera, Hans Schmid, and Manfred Fiebig. Observation of ferrotoroidic domains. *Nature*, 449(7163):702–705, 2007.
- [51] Nicola A Spaldin and Rammamoorthy Ramesh. Advances in magnetoelectric multiferroics. *Nature materials*, 18(3):203–212, 2019.
- [52] Nicola A Spaldin and Manfred Fiebig. The renaissance of magnetoelectric multiferroics. *Science*, 309(5733):391–392, 2005.
- [53] Néelson Pereira, Ana Catarina Lima, Senentxu Lanceros-Mendez, and Pedro Martins. Magnetoelectrics: Three centuries of research heading towards the 4.0 industrial revolution. *Materials*, 13(18):4033, 2020.
- [54] Qinghui Jiang, Futian Liu, Haixue Yan, Huanpo Ning, Zsuzsanna Libor, Qi Zhang, Markys Cain, and Michael J Reece. Magneto-electric properties of multiferroic pb (zr_{0.52}ti_{0.48}) o₃-nife₂o₄ nanoceramic composites. *Journal of the American Ceramic Society*, 94(8):2311–2314, 2011.
- [55] AI Stognij, NN Novitskii, SV Trukhanov, AV Trukhanov, LV Panina, SA Sharko, AI Serokurova, NN Poddubnaya, VA Ketsko, VP Dyakonov, et al. Interface magnetoelectric effect in elastically linked co/pzt/co layered structures. *Journal of Magnetism and Magnetic Materials*, 485:291–296, 2019.
- [56] Jitao Zhang, Ping Li, Yumei Wen, Wei He, Aichao Yang, and Caijiang Lu. Shear-mode self-biased magnetostrictive/piezoelectric laminate multiferroic heterostructures for magnetic field detecting and energy harvesting. *Sensors and Actuators A: Physical*, 214:149–155, 2014.
- [57] Alexander Omelyanchik, Valentina Antipova, Christina Gritsenko, Valeria Kolesnikova, Dmitry Murzin, Yilin Han, Andrei V Turutin, Ilya V Kubasov, Alexander M Kislyuk, Tatiana S Ilina, et al. Boosting magnetoelectric effect in polymer-based nanocomposites. *Nanomaterials*, 11(5):1154, 2021.

-
- [58] Jing Ma, Zhan Shi, and C-W Nan. Magnetolectric properties of composites of single pb (zr, ti) o3 rods and terfenol-d/epoxy with a single-period of 1-3-type structure. *Advanced Materials*, 19(18):2571–2573, 2007.
- [59] Valery V Vasiliev and Evgeny V Morozov. *Advanced mechanics of composite materials and structures*. Elsevier, 2018.
- [60] Mohammad Jawaid, Mohamed Thariq, and Naheed Saba. *Durability and life prediction in biocomposites, fibre-reinforced composites and hybrid composites*. Woodhead Publishing, 2018.
- [61] SM Sapuan. *Composite materials: Concurrent engineering approach*. Butterworth-Heinemann, 2017.
- [62] Julian Gustavo Renzo Sereni. Reference module in materials science and materials engineering. 2016.
- [63] Tri-Dung Ngo. *Composite and Nanocomposite Materials: From Knowledge to Industrial Applications*. BoD–Books on Demand, 2020.
- [64] Md Rezaur Rahman. *Silica and Clay Dispersed Polymer Nanocomposites: Preparation, Properties and Applications*. Woodhead Publishing, 2018.
- [65] Mohammad Jawaid, MT Paridah, and Naheed Saba. *Lignocellulosic fibre and biomass-based composite materials: processing, properties and applications*. Woodhead Publishing, 2017.
- [66] Vanessa F Cardoso, Daniela M Correia, Clarisse Ribeiro, Margarida M Fernandes, and Senentxu Lanceros-Méndez. Fluorinated polymers as smart materials for advanced biomedical applications. *Polymers*, 10(2):161, 2018.
- [67] Chaoying Wan and Christopher Rhys Bowen. Multiscale-structuring of polyvinylidene fluoride for energy harvesting: the impact of molecular-, micro-and macro-structure. *Journal of Materials Chemistry A*, 5(7):3091–3128, 2017.

- [68] Ehsan Ghafari, Xiaodong Jiang, and Na Lu. Surface morphology and beta-phase formation of single polyvinylidene fluoride (pvdf) composite nanofibers. *Advanced Composites and Hybrid Materials*, 1:332–340, 2018.
- [69] David Romero-Fierro, Moises Bustamante-Torres, Francisco Bravo-Plascencia, Héctor Magaña, and Emilio Bucio. Polymer-magnetic semiconductor nanocomposites for industrial electronic applications. *Polymers*, 14(12):2467, 2022.
- [70] Thanh-Hai Le, Yukyung Kim, and Hyeonseok Yoon. Electrical and electrochemical properties of conducting polymers. *Polymers*, 9(4):150, 2017.
- [71] Jorge G Ibanez, Marina E Rincón, Silvia Gutierrez-Granados, M’hamed Chahma, Oscar A Jaramillo-Quintero, and Bernardo A Frontana-Uribe. Conducting polymers in the fields of energy, environmental remediation, and chemical–chiral sensors. *Chemical reviews*, 118(9):4731–4816, 2018.
- [72] Jurgen Heinze, Bernardo A Frontana-Uribe, and Sabine Ludwigs. Electrochemistry of conducting polymers persistent models and new concepts. *Chemical Reviews*, 110(8):4724–4771, 2010.
- [73] AR Murad, A Iraqi, SB Aziz, SN Abdullah, and MA Brza. Conducting polymers for optoelectronic devices and organic solar cells: a review. *polymers* 12: 2627, 2020.
- [74] Samantha Phan and Christine K Luscombe. Recent advances in the green, sustainable synthesis of semiconducting polymers. *Trends in Chemistry*, 1(7):670–681, 2019.
- [75] Yongqin Han and Liming Dai. Conducting polymers for flexible supercapacitors. *Macromolecular chemistry and physics*, 220(3):1800355, 2019.
- [76] Somayeh Tajik, Hadi Beitollahi, Fariba Garkani Nejad, Iran Sheikh Shoaie, Mohammad A Khalilzadeh, Mehdi Shahedi Asl, Quyet Van Le, Kaiqiang Zhang, Ho Won Jang, and Mohammadreza Shokouhimehr. Recent developments in conducting polymers: Applications for electrochemistry. *RSC advances*, 10(62):37834–37856, 2020.

-
- [77] Álvaro Terán-Alcocer, Francisco Bravo-Plascencia, Carlos Cevallos-Morillo, and Alex Palma-Cando. Electrochemical sensors based on conducting polymers for the aqueous detection of biologically relevant molecules. *Nanomaterials*, 11(1):252, 2021.
- [78] V Arumugaprabu, TJ Ko, M Uthayakumar, and RD Joel Johnson. Failure analysis in biocomposites, fiber-reinforced composites and hybrid composites, 2019.
- [79] Zeaid Hasan. *Tooling for Composite Aerospace Structures: Manufacturing and Applications*. Butterworth-Heinemann, 2020.
- [80] Kishor Kumar Sadasivuni, John-John Cabibihan, Deepalekshmi Ponnamma, Mariam Ali SA Al-Maadeed, and Jaehwan Kim. *Biopolymer composites in electronics*. Elsevier, 2016.
- [81] Shao-Yun Fu, Xi-Qiao Feng, Bernd Lauke, and Yiu-Wing Mai. Effects of particle size, particle/matrix interface adhesion and particle loading on mechanical properties of particulate-polymer composites. *Composites Part B: Engineering*, 39(6):933–961, 2008.
- [82] Ibrahim Khan, Khalid Saeed, and Idrees Khan. Nanoparticles: Properties, applications and toxicities. *Arabian journal of chemistry*, 12(7):908–931, 2019.
- [83] Ana María Díez-Pascual. Nanoparticle reinforced polymers, 2019.
- [84] Moises Bustamante-Torres, David Romero-Fierro, Belén Arcentales-Vera, Samantha Pardo, and Emilio Bucio. Interaction between filler and polymeric matrix in nanocomposites: Magnetic approach and applications. *Polymers*, 13(17):2998, 2021.
- [85] G Yu Yurkov, DA Baranov, IP Dotsenko, and SP Gubin. New magnetic materials based on cobalt and iron-containing nanoparticles. *Composites Part B: Engineering*, 37(6):413–417, 2006.
- [86] M Saleem J Hashmi. *Comprehensive materials processing*. Newnes, 2014.

- [87] Chaudhery Mustansar Hussain. Handbook of nanomaterials in analytical chemistry: Modern trends in analysis. 2019.
- [88] Jong-Ryul Jeong, Sung-Chul Shin, Seung-Jun Lee, and Jong-Duk Kim. Magnetic properties of superparamagnetic γ -Fe₂O₃ nanoparticles prepared by coprecipitation technique. *Journal of magnetism and magnetic materials*, 286:5–9, 2005.
- [89] Havva Ya ci Acar, Rachel S Garaas, Faisal Syud, Peter Bonitatebus, and Amit M Kulkarni. Superparamagnetic nanoparticles stabilized by polymerized pegylated coatings. *Journal of magnetism and magnetic materials*, 293(1):1–7, 2005.
- [90] Maria Mikhaylova, Do Kyung Kim, Natalia Bobrysheva, Mikhail Osmolowsky, Valentin Semenov, Thomas Tsakalakos, and Mamoun Muhammed. Superparamagnetism of magnetite nanoparticles: dependence on surface modification. *Langmuir*, 20(6):2472–2477, 2004.
- [91] Moises Bustamante-Torres, David Romero-Fierro, Jocelyne Estrella-Nuñez, Belén Arcentales-Vera, Estefani Chichande-Proaño, and Emilio Bucio. Polymeric composite of magnetite iron oxide nanoparticles and their application in biomedicine: a review. *Polymers*, 14(4):752, 2022.
- [92] Jens Sommertune, Abhilash Sugunan, Anwar Ahniyaz, Rebecca Stjernberg Bejhed, Anna Sarwe, Christer Johansson, Christoph Balceris, Frank Ludwig, Oliver Posth, and Andrea Fornara. Polymer/iron oxide nanoparticle composites—a straight forward and scalable synthesis approach. *International journal of molecular sciences*, 16(8):19752–19768, 2015.
- [93] Shyam K Gore, Santosh S Jadhav, Umakant B Tumberphale, Shoyeb M Shaikh, Mu Naushad, and Rajaram S Mane. Cation distribution, magnetic properties and cubic-perovskite phase transition in bismuth-doped nickel ferrite. *Solid State Sciences*, 74:88–94, 2017.

- [94] Vladimir Tsurkan, Hans-Albrecht Krug Von Nidda, Joachim Deisenhofer, Peter Lunkenheimer, and Alois Loidl. On the complexity of spinels: Magnetic, electronic, and polar ground states. *Physics Reports*, 926:1–86, 2021.
- [95] RK Kotnala and Jyoti Shah. Ferrite materials: nano to spintronics regime. In *Handbook of magnetic materials*, volume 23, pages 291–379. Elsevier, 2015.
- [96] A El Khanchaoui, M Sajieddine, M Ounacer, A Fnidiki, F Richomme, Jean Juraszek, M Mansori, M Dib, and A Essoumhi. Structural, morphological, and magnetic studies of spinel ferrites derived from layered double hydroxides. *Applied Physics A*, 128(5):406, 2022.
- [97] K Maaz, S Karim, Kyu Joon Lee, Myung-Hwa Jung, and Gil-Ho Kim. Effect of temperature on the magnetic characteristics of $\text{Ni}_0.5\text{Co}_0.5\text{Fe}_2\text{O}_4$ nanoparticles. *Materials Chemistry and Physics*, 133(2-3):1006–1010, 2012.
- [98] Mehdi Delshad Chermahini, Hasan Ahmadian Baghbaderani, Mohammad Maleki Shahraki, and Mahdi Kazazi. Low temperature sintering of magnetic $\text{Ni}_0.5\text{Co}_0.5\text{Fe}_2\text{O}_4$ ceramics prepared from mechanochemically synthesized nanopowders. *Ceramics International*, 45(5):5491–5495, 2019.
- [99] Jose-Luis Ortiz-Quiñonez, Umapada Pal, and Martin Salazar Villanueva. Structural, magnetic, and catalytic evaluation of spinel Co , Ni , and Co-Ni ferrite nanoparticles fabricated by low-temperature solution combustion process. *ACS omega*, 3(11):14986–15001, 2018.
- [100] Kunal Pubby, SS Meena, SM Yusuf, and Sukhleen Bindra Narang. Cobalt substituted nickel ferrites via pechini’s sol-gel citrate route: X-band electromagnetic characterization. *Journal of Magnetism and Magnetic Materials*, 466:430–445, 2018.
- [101] Jalel Massoudi, Mourad Smari, Kamel Nouri, Essebti Dhahri, Kamel Khirouni, Sylvain Bertaina, Lotfi Bessais, et al. Magnetic and spectroscopic properties of Ni-Zn-Al

- ferrite spinel: from the nanoscale to microscale. *RSC advances*, 10(57):34556–34580, 2020.
- [102] JA Paulsen, AP Ring, CCH Lo, John Evan Snyder, and David C Jiles. Manganese-substituted cobalt ferrite magnetostrictive materials for magnetic stress sensor applications. *Journal of applied physics*, 97(4):044502, 2005.
- [103] E Veena Gopalan, PA Joy, IA Al-Omari, D Sakthi Kumar, Yasuhiko Yoshida, and MR Anantharaman. On the structural, magnetic and electrical properties of sol-gel derived nanosized cobalt ferrite. *Journal of Alloys and Compounds*, 485(1-2):711–717, 2009.
- [104] Seema Joshi, Manoj Kumar, Sandeep Chhoker, Geetika Srivastava, Mukesh Jewariya, and VN Singh. Structural, magnetic, dielectric and optical properties of nickel ferrite nanoparticles synthesized by co-precipitation method. *Journal of Molecular structure*, 1076:55–62, 2014.
- [105] MA Gabal and YM Al Angari. Effect of chromium ion substitution on the electromagnetic properties of nickel ferrite. *Materials Chemistry and Physics*, 118(1):153–160, 2009.
- [106] MK Anupama, B Rudraswamy, and N Dhananjaya. Investigation on impedance response and dielectric relaxation of ni-zn ferrites prepared by self-combustion technique. *Journal of Alloys and Compounds*, 706:554–561, 2017.
- [107] TP Sathishkumar, J Naveen, , and S Satheeshkumar. Hybrid fiber reinforced polymer composites—a review. *Journal of Reinforced Plastics and Composites*, 33(5):454–471, 2014.
- [108] BM Pirzada and S Sabir. Polymer-based nanocomposites for significantly enhanced dielectric properties and energy storage capability. In *Polymer-based Nanocomposites for Energy and Environmental Applications*, pages 131–183. Elsevier, 2018.

- [109] Rajesh Mishra and Jiri Militky. *Nanotechnology in textiles: theory and application*. Woodhead Publishing, 2018.
- [110] A Inamuddin and Ali Mohammad. Applications of nanocomposite materials in drug delivery. In *A Volume in Woodhead Publishing Series in Biomaterials, Book*. Elsevier, 2018.
- [111] Ana Paula Pereira Fulco, José Daniel Diniz Melo, Carlos Alberto Paskocimas, Suzana Nóbrega de Medeiros, Fernando Luis de Araujo Machado, and Alexandre Ricalde Rodrigues. Magnetic properties of polymer matrix composites with embedded ferrite particles. *NDT & E International*, 77:42–48, 2016.
- [112] Zakaria Chchiyai, Loubna Hdidou, Marwa Tayoury, Abdelwahed Chari, Youssef Tamraoui, Jones Alami, Mouad Dahbi, and Bouchaib Manoun. Synthesis and electrochemical properties of mn-doped porous $\text{mg}_0.9\text{zn}_0.1\text{fe}_2\text{-xmn}_x\text{o}_4$ ($0 < x < 1.25$) spinel oxides as anode materials for lithium-ion batteries. *Journal of Alloys and Compounds*, 935:167997, 2023.
- [113] G Vinod, K Rajashekhar, and J Laxman Naik. Dysprosium doped $\text{cu}_0.8\text{cd}_0.2\text{dy}_x\text{fe}_2\text{-x}_4$ nano ferrites: A combined impact of dy^{3+} on enhanced physical, optical, magnetic, and dc-electrical properties. *Ceramics International*, 49(2):2829–2851, 2023.
- [114] Nakiraboina Venkatesh, D Ravi Kumar, Shyamsunder Goud, Syed Ismail Ahmad, P Veerasomaiah, and D Ravinder. Structural, photocatalytic, electromagnetic properties of rare-earth metal gd-doped mg nanoferrites synthesized by citrate gel auto-combustion method. *Chemical Papers*, pages 1–19, 2023.
- [115] Dalia Hamad, Nasser Afify, Mohamed Omer, and Ghada Abbady. Structure and magnetic properties of cd (1- x) coxfe_2o_4 stoichiometric nanoferrite system. *Ceramics International*, 2023.

-
- [116] Bedanga Sapkota, Md Tanvir Hasan, Alix Martin, Rifat Mahbub, Jeffrey E Shield, and Vijaya Rangari. Fabrication and magnetoelectric investigation of flexible pvdft/rfe/cobalt ferrite nanocomposite films. *Materials Research Express*, 9(4):046302, 2022.
- [117] Syed Ismail Ahmad. Nano cobalt ferrites: Doping, structural, low-temperature, and room temperature magnetic and dielectric properties—a comprehensive review. *Journal of Magnetism and Magnetic Materials*, page 169840, 2022.
- [118] Deepa Rajendran Lekshmi, Sivan Pillai Adarsh, Manikanta Bayal, Swapna Shanmukhan Nair, and Kuzhichalil Peethambharan Surendran. Functionally graded magnetodielectric composite substrates for massive miniaturization of microstrip antennas. *Materials Advances*, 3(5):2380–2392, 2022.
- [119] Rekha Gupta and RK Kotnala. A review on current status and mechanisms of room-temperature magnetoelectric coupling in multiferroics for device applications. *Journal of Materials Science*, 57(27):12710–12737, 2022.
- [120] David Romero-Fierro, Moises Bustamante-Torres, Francisco Bravo-Plascencia, Aylin Esquivel-Lozano, Juan-Carlos Ruiz, and Emilio Bucio. Recent trends in magnetic polymer nanocomposites for aerospace applications: A review. *Polymers*, 14(19):4084, 2022.
- [121] S Kangishwar, N Radhika, Asad Amaan Sheik, Abhinav Chavali, and S Hariharan. A comprehensive review on polymer matrix composites: Material selection, fabrication, and application. *Polymer Bulletin*, 80(1):47–87, 2023.
- [122] Xianfeng Liang, Cunzheng Dong, Huaihao Chen, Jiawei Wang, Yuyi Wei, Mohsen Zaeimbashi, Yifan He, Alexei Matyushov, Changxing Sun, and Nianxiang Sun. A review of thin-film magnetoelastic materials for magnetoelectric applications. *Sensors*, 20(5):1532, 2020.

- [123] Iulian Petrila and Florin Tudorache. Effects of sintering temperature on the microstructure, electrical and magnetic characteristics of copper-zinc spinel ferrite with possibility use as humidity sensors. *Sensors and Actuators A: Physical*, 332:113060, 2021.
- [124] A Manikandan, M Yogasundari, K Thanrasu, A Dinesh, K Kanmani Raja, Y Slimani, SK Jaganathan, R Srinivasan, and A Baykal. Structural, morphological and optical properties of multifunctional magnetic-luminescent zno@ fe₃o₄ nanocomposite. *Physica E: Low-dimensional Systems and Nanostructures*, 124:114291, 2020.
- [125] Debajyoti Nath and SK Mandal. Magnetically influenced dielectric and electrical transport of inorganic–organic polymer-based hybrid nanocomposites. *International Journal of Modern Physics B*, 34(04):2050004, 2020.
- [126] Salma Ikram, Jolly Jacob, Khurram Mehboob, Khalid Mahmood, N Amin, MI Arshad, and M Ajaz un Nabi. Role of rare earth metal ions doping on structural, electrical, magnetic, and dielectric behavior of spinel ferrites: A comparative study. *Journal of Superconductivity and Novel Magnetism*, 34:1833–1842, 2021.
- [127] Rajendra P Patil, Prashant N Nikam, Sarjerao B Patil, Ramdas K Dhokale, Vijay S Sawant, and Satish B Shelke. Effect of sintering temperature on structural and morphological properties of mn-substituted lithium ferrite. In *Macromolecular Symposia*, volume 393, page 2000173. Wiley Online Library, 2020.
- [128] Ajith S Kumar, CS Chitra Lekha, S Vivek, K Nandakumar, MR Anantharaman, and Swapna S Nair. Effect of cofe₂o₄ weight fraction on multiferroic and magnetoelectric properties of (1- x) ba_{0.85}ca_{0.15}zr_{0.1}ti_{0.9}o_{3-x}cofe₂o₄ particulate composites. *Journal of Materials Science: Materials in Electronics*, 30:8239–8248, 2019.

- [129] Irfan Hussain Lone, Jeenat Aslam, Nagi RE Radwan, Ali Habib Bashal, Amin FA Ajlouni, and Arifa Akhter. Multiferroic abo₃ transition metal oxides: a rare interaction of ferroelectricity and magnetism. *Nanoscale research letters*, 14(1):1–12, 2019.
- [130] Dhiraj Kumar Rana, Shovan Kumar Kundu, Ram Janay Choudhary, and Soumen Basu. Enhancement of electrical and magnetodielectric properties of bifeo₃ incorporated pvdf flexible nanocomposite films. *Materials Research Express*, 6(8):0850d9, 2019.
- [131] Papia Dutta, SK Mandal, Rajesh Debnath, and A Nath. Enhanced magnetoimpedance and magnetodielectric effect in lafeo₃–organic paraffin wax hybrid nanocomposites. *Journal of Magnetism and Magnetic Materials*, 487:165332, 2019.
- [132] Balakrishnan Karthikeyan, R Govindhan, and M Amutheesan. Chemical methods for synthesis of hybrid nanoparticles. In *Noble Metal-Metal Oxide Hybrid Nanoparticles*, pages 179–188. Elsevier, 2019.
- [133] Sobhi Hcini, Noura Kouki, Aref Omri, Abdessalem Dhahri, and Mohamed Lamjed Bouazizi. Effect of sintering temperature on structural, magnetic, magnetocaloric and critical behaviors of ni-cd-zn ferrites prepared using sol-gel method. *Journal of Magnetism and Magnetic Materials*, 464:91–102, 2018.
- [134] F Madidi, Gelareh Momen, and Masoud Farzaneh. Dielectric properties of tio₂/silicone rubber micro-and nanocomposites. *Advances in Materials Science and Engineering*, 2018, 2018.
- [135] Haribabu Palneedi, Venkateswarlu Annapureddy, Shashank Priya, and Jungho Ryu. Status and perspectives of multiferroic magnetoelectric composite materials and applications. In *Actuators*, volume 5, page 9. MDPI, 2016.
- [136] VS Chaturmukha, CS Naveen, MP Rajeeva, BS Avinash, HS Jayanna, and Ashok R Lamani. Dielectrical properties of pani/tio₂ nanocomposites. In *AIP Conference Proceedings*, volume 1731, page 050066. AIP Publishing LLC, 2016.

- [137] Shrikant Thakur, Rakesh K Tekade, Prashant Kesharwani, and Narendra K Jain. The effect of polyethylene glycol spacer chain length on the tumor-targeting potential of folate-modified ppi dendrimers. *Journal of Nanoparticle Research*, 15:1–16, 2013.
- [138] Qian Liu, Xiao-Bing Bian, Jian-Ping Zhou, and Peng Liu. Colossal magnetodielectric effect caused by magnetoelectric effect under low magnetic field. *Bulletin of Materials Science*, 34:283–286, 2011.
- [139] Sreemanta Mitra, Oindrila Mondal, Dhriti Ranjan Saha, Anindya Datta, Sourish Banerjee, and Dipankar Chakravorty. Magnetodielectric effect in graphene-pva nanocomposites. *The Journal of Physical Chemistry C*, 115(29):14285–14289, 2011.
- [140] Cesar Morales, Julio Dewdney, Susmita Pal, Scott Skidmore, Kristen Stojak, Hariharan Srikanth, Thomas Weller, and Jing Wang. Tunable magneto-dielectric polymer nanocomposites for microwave applications. *IEEE transactions on microwave theory and techniques*, 59(2):302–310, 2010.
- [141] Shekhar D Bhame and Pattayil A Joy. Effect of sintering conditions and microstructure on the magnetostrictive properties of cobalt ferrite. *Journal of the American Ceramic Society*, 91(6):1976–1980, 2008.
- [142] OP Dimitriev. Doping of polyaniline by transition-metal salts. *Macromolecules*, 37(9):3388–3395, 2004.
- [143] Ashis Dey, Sukanta De, Amitabha De, and SK De. Characterization and dielectric properties of polyaniline–tio₂ nanocomposites. *Nanotechnology*, 15(9):1277, 2004.
- [144] Hamnesh Mahajan, Sachin Kumar Godara, and AK Srivastava. Synthesis and investigation of structural, morphological, and magnetic properties of the manganese doped cobalt-zinc spinel ferrite. *Journal of Alloys and Compounds*, 896:162966, 2022.
- [145] Andris Sutka and Gundars Mezinskis. Sol-gel auto-combustion synthesis of spinel-type ferrite nanomaterials. *Frontiers of Materials Science*, 6:128–141, 2012.

- [146] Ali A Jazie, Amar J Albaaji, and Suhad A Abed. A review on recent trends of antiviral nanoparticles and airborne filters: special insight on covid-19 virus. *Air Quality, Atmosphere & Health*, 14(11):1811–1824, 2021.
- [147] Subhendu Bhandari. Polyaniline: structure and properties relationship. In *Polyaniline Blends, Composites, and Nanocomposites*, pages 23–60. Elsevier, 2018.
- [148] Jaroslav Stejskal, Irina Sapurina, Jan Prokeš, and Josef Zemek. In-situ polymerized polyaniline films. *Synthetic Metals*, 105(3):195–202, 1999.
- [149] Muhammad Fayzan Shakir, Ahmad Nawaz Khan, Ramsha Khan, Sofia Javed, Asra Tariq, Muhammad Azeem, Adeel Riaz, Ahmed Shafqat, Hammad M Cheema, Muhammad Aftab Akram, et al. EMI shielding properties of polymer blends with inclusion of graphene nano platelets. *Results in Physics*, 14:102365, 2019.
- [150] John A Joule. *Heterocyclic chemistry*. CRC Press, 2020.
- [151] Shuxin Tan, Jin Zhai, Bofei Xue, Meixiang Wan, Qingbo Meng, Yuliang Li, Lei Jiang, and Daoben Zhu. Property influence of polyanilines on photovoltaic behaviors of dye-sensitized solar cells. *Langmuir*, 20(7):2934–2937, 2004.
- [152] Mahnoush Beygisangchin, Suraya Abdul Rashid, Suhaidi Shafie, Amir Reza Sadrolhosseini, and Hong Ngee Lim. Preparations, properties, and applications of polyaniline and polyaniline thin films—a review. *Polymers*, 13(12):2003, 2021.
- [153] Nirmala Kumari Jangid, Sapana Jadoun, and Navjeet Kaur. A review on high-throughput synthesis, deposition of thin films and properties of polyaniline. *European Polymer Journal*, 125:109485, 2020.
- [154] Michael O Akharam, Olalekan S Fatoki, Beatrice O Opeolu, Daniel I Olorunfemi, and Oghenechuko U Oputu. Polymeric nanocomposites (pnCs) for wastewater remediation: an overview. *Polymer-Plastics Technology and Engineering*, 57(17):1801–1827, 2018.

-
- [155] Sarita Kango, Susheel Kalia, Annamaria Celli, James Njuguna, Youssef Habibi, and Rajesh Kumar. Surface modification of inorganic nanoparticles for development of organic–inorganic nanocomposites—a review. *Progress in Polymer Science*, 38(8): 1232–1261, 2013.
- [156] C Suryanarayan and M Grant Norton. X-ray diffraction: a practical approach, 1998.
- [157] BD Cullity and SR Stock. Elements of x-ray diffraction, prentice hall. *Upper Saddle River, NJ*, page 388, 2001.
- [158] Yoshio Waseda, Eiichiro Matsubara, and Kozo Shinoda. *X-ray diffraction crystallography: introduction, examples and solved problems*. Springer Science & Business Media, 2011.
- [159] GEM Jauncey. The scattering of x-rays and bragg’s law. *Proceedings of the national academy of sciences*, 10(2):57–60, 1924.
- [160] LRB Elton and Daphne F Jackson. X-ray diffraction and the bragg law. *American Journal of Physics*, 34(11):1036–1038, 1966.
- [161] AL Patterson. The scherrer formula for x-ray particle size determination. *Physical review*, 56(10):978, 1939.
- [162] JJ Shea. Handbook of instrumental techniques for analytical chemistry. *IEEE Electrical Insulation Magazine*, 14(6):42–42, 1998.
- [163] T Vijaya Kumar, KV Ramana, and RB Choudary. Spectroscopic characterization of mechanically synthesized moo₃-tio₂ composite nano powders. *International Journal of Mechanical Engineering and Technology*, 8(5):1051–1063, 2017.
- [164] J Preudhomme and P Tarte. Spectrochimica acta part a: molecular spectroscopy. *Spectrochim. Acta*, 27:1817–1835, 1971.

- [165] Aurelio Ramírez-Hernández, Celia Aguilar-Flores, and Alejandro Aparicio-Saguilán. Fingerprint analysis of ftir spectra of polymers containing vinyl acetate. *Dyna*, 86 (209):198–205, 2019.
- [166] Joseph D Andrade. Surface and interfacial aspect of biomedical polymers. *Surface chemistry and physics*, 1, 1985.
- [167] D Nanda Gopala Krishna and John Philip. Review on surface-characterization applications of x-ray photoelectron spectroscopy (xps): Recent developments and challenges. *Applied Surface Science Advances*, 12:100332, 2022.
- [168] Stephen Klassen. The photoelectric effect: Reconstructing the story for the physics classroom. *Science & Education*, 20:719–731, 2011.
- [169] Philip R Davies and David J Morgan. Practical guide for x-ray photoelectron spectroscopy: Applications to the study of catalysts. *Journal of Vacuum Science & Technology A: Vacuum, Surfaces, and Films*, 38(3):033204, 2020.
- [170] Karen D Vernon-Parry. Scanning electron microscopy: an introduction. *III-Vs Review*, 13(4):40–44, 2000.
- [171] Kalsoom Akhtar, Shahid Ali Khan, Sher Bahadar Khan, and Abdullah M Asiri. Scanning electron microscopy: Principle and applications in nanomaterials characterization. *Handbook of materials characterization*, pages 113–145, 2018.
- [172] M Abd Mutalib, MA Rahman, MHD Othman, AF Ismail, and J Jaafar. Scanning electron microscopy (sem) and energy-dispersive x-ray (edx) spectroscopy. In *Membrane characterization*, pages 161–179. Elsevier, 2017.
- [173] Mohamed M El-Gomati and Christopher GH Walker. Toward quantitative scanning electron microscopy. In *Advances in Imaging and Electron Physics*, volume 183, pages 1–40. Elsevier, 2014.

-
- [174] Roy Bernstein, Yair Kaufman, and Viatcheslav Freger. Membrane characterization. *Encyclopedia of Membrane Science and Technology*, pages 1–41, 2013.
- [175] David C Joy and James B Pawley. High-resolution scanning electron microscopy. *Ultramicroscopy*, 47(1-3):80–100, 1992.
- [176] David J Smith. High resolution transmission electron microscopy. *Handbook of microscopy for nanotechnology*, pages 427–453, 2005.
- [177] Werner Grogger, Ferdinand Hofer, Gerald Kothleitner, and Bernhard Schaffer. An introduction to high-resolution eels in transmission electron microscopy. *Topics in catalysis*, 50:200–207, 2008.
- [178] JS Wu, AM Kim, R Bleher, BD Myers, RG Marvin, H Inada, K Nakamura, XF Zhang, E Roth, SY Li, et al. Imaging and elemental mapping of biological specimens with a dual-eds dedicated scanning transmission electron microscope. *Ultramicroscopy*, 128:24–31, 2013.
- [179] Nicolas Brodusch, Hendrix Demers, Alexandra Gellé, Audrey Moores, and Raynald Gauvin. Electron energy-loss spectroscopy (eels) with a cold-field emission scanning electron microscope at low accelerating voltage in transmission mode. *Ultramicroscopy*, 203:21–36, 2019.
- [180] G Lawes, T Kimura, CM Varma, MA Subramanian, N Rogado, RJ Cava, and AP Ramirez. Magnetodielectric effects at magnetic ordering transitions. *Progress in Solid State Chemistry*, 37(1):40–54, 2009.
- [181] G Lawes, AP Ramirez, CM Varma, and MA Subramanian. Magnetodielectric effects from spin fluctuations in isostructural ferromagnetic and antiferromagnetic systems. *Physical review letters*, 91(25):257208, 2003.
- [182] B Lorenz, YQ Wang, YY Sun, and CW Chu. Large magnetodielectric effects in orthorhombic HoMnO_3 and YMnO_3 . *Physical Review B*, 70(21):212412, 2004.

- [183] Li-Xia Pang, Hong Wang, Di Zhou, and Xi Yao. Low-temperature sintering and microwave dielectric properties of tio₂-based Itcc materials. *Journal of Materials Science: Materials in Electronics*, 21:1285–1292, 2010.
- [184] Maurizio Crippa, Alberto Bianchi, Davide Cristofori, Massimiliano D’Arienzo, Franco Merletti, Franca Morazzoni, Roberto Scotti, and Roberto Simonutti. High dielectric constant rutile–polystyrene composite with enhanced percolative threshold. *Journal of Materials Chemistry C*, 1(3):484–492, 2013.
- [185] Xu Huang, Zejun Pu, Lifen Tong, Zicheng Wang, and Xiaobo Liu. Preparation and dielectric properties of surface modified tio₂/pen composite films with high thermal stability and flexibility. *Journal of Materials Science: Materials in Electronics*, 23: 2089–2097, 2012.
- [186] Rocio Ponce Ortiz, Antonio Facchetti, and Tobin J Marks. High-k organic, inorganic, and hybrid dielectrics for low-voltage organic field-effect transistors. *Chemical reviews*, 110(1):205–239, 2010.
- [187] Kiran Kumar Ganta, Venkata Ramana Jeedi, K Vijaya Kumar, and E Laxmi Narasiah. Preparation, characterization and impedance spectroscopic studies of na⁺ ion conducting peo+ pvdf-blended polymer electrolytes. *International Journal of Polymer Analysis and Characterization*, 26(2):130–144, 2021.
- [188] Mohan L Verma and Homendra D Sahu. Study on ionic conductivity and dielectric properties of peo-based solid nanocomposite polymer electrolytes. *Ionics*, 23(9): 2339–2350, 2017.
- [189] Marie Bermeo, Nabil El Hadri, Florent Ravoux, Abdelali Zaki, Linda Zou, and Mustapha Jouiad. Adsorption capacities of hygroscopic materials based on nacl-tio₂ and nacl-sio₂ core/shell particles. *Journal of Nanotechnology*, 2020:1–16, 2020.
- [190] S Devikala, P Kamaraj, and M Arthanareeswari. Corrosion resistance behavior of pva/tio₂ composite in 3.5% nacl. *Materials today: proceedings*, 5(2):8672–8677, 2018.

- [191] Heng Su, Saddique Jaffer, and Haijun Yu. Transition metal oxides for sodium-ion batteries. *Energy storage materials*, 5:116–131, 2016.
- [192] Dino Aquilano, Fermín Otálora, Linda Pastero, and Juan Manuel García-Ruiz. Three study cases of growth morphology in minerals: Halite, calcite and gypsum. *Progress in Crystal Growth and Characterization of Materials*, 62(2):227–251, 2016.
- [193] Saleh M Abdou and Hany Moharam. Characterization of table salt samples from different origins and esr detection of the induced effects due to gamma irradiation. In *Journal of Physics: Conference Series*, volume 1253, page 012036. IOP Publishing, 2019.
- [194] Thirugnanasambandan Theivasanthi and Marimuthu Alagar. Titanium dioxide (tio2) nanoparticles xrd analyses: an insight. *arXiv preprint arXiv:1307.1091*, 2013.
- [195] Željka Antić, Radenka M Krsmanović, Marko G Nikolić, Milena Marinović-Cincović, Miodrag Mitrić, Stefano Polizzi, and Miroslav D Dramićanin. Multisite luminescence of rare earth doped tio2 anatase nanoparticles. *Materials Chemistry and Physics*, 135(2-3):1064–1069, 2012.
- [196] Qiang Zhang and Chaoyang Li. High temperature stable anatase phase titanium dioxide films synthesized by mist chemical vapor deposition. *Nanomaterials*, 10(5):911, 2020.
- [197] Muneer M Ba-Abbad, Abdul Amir H Kadhum, Abu Bakar Mohamad, Mohd S Takriff, and Kamaruzzaman Sopian. Synthesis and catalytic activity of tio2 nanoparticles for photochemical oxidation of concentrated chlorophenols under direct solar radiation. *Int. J. Electrochem. Sci*, 7(6):4871–4888, 2012.
- [198] Noemí Arconada, Lucía Arribas, Beatriz Lucio, José González-Aguilar, and Manuel Romero. Macroencapsulation of sodium chloride as phase change materials for thermal energy storage. *Solar Energy*, 167:1–9, 2018.

- [199] Min Gu Kim, Jeong Min Kang, Ji Eun Lee, Kang Seok Kim, Kwang Ho Kim, Min Cho, and Seung Geol Lee. Effects of calcination temperature on the phase composition, photocatalytic degradation, and virucidal activities of tio₂ nanoparticles. *ACS omega*, 6(16):10668–10678, 2021.
- [200] A Subrahmanyam. Dielectric properties of nacl and kcl single crystals x-irradiated under different dc fields. *Physica Status Solidi. A, Applied Research*, 69(2):773–778, 1982.
- [201] S Kaur, O Amin, B Sharma, M Kalyan, N Kumari, R Sharma, and R Mukherjee. Frequency dependent conductivity in vanadium intercalated mnpse₃ bulk single crystal. *Journal of Emerging Technologies and Innovative Research*, 6:738–43, 2019.
- [202] SV Ganesan, KK Mothilal, S Selvasekarapandian, and TK Ganesan. The effect of titanium dioxide nano-filler on the conductivity, morphology and thermal stability of poly (methyl methacrylate)—poly (styrene-co-acrylonitrile) based composite solid polymer electrolytes. *Journal of Materials Science: Materials in Electronics*, 29(10):8089–8099, 2018.
- [203] L TianKhoon, N Ataollahi, NH Hassan, and A Ahmad. Studies of porous solid polymeric electrolytes based on poly (vinylidene fluoride) and poly (methyl methacrylate) grafted natural rubber for applications in electrochemical devices. *Journal of Solid State Electrochemistry*, 20:203–213, 2016.
- [204] Rupam Mukherjee, Zhi-Feng Huang, and Boris Nadgorny. Multiple percolation tunneling staircase in metal-semiconductor nanoparticle composites. *Applied Physics Letters*, 105(17):173104, 2014.
- [205] Arsalan Hashemi, Hannu-Pekka Komsa, Martti Puska, and Arkady V Krasheninikov. Vibrational properties of metal phosphorus trichalcogenides from first-principles calculations. *The Journal of Physical Chemistry C*, 121(48):27207–27217, 2017.

- [206] S Ramesh and Ong Poh Ling. Effect of ethylene carbonate on the ionic conduction in poly (vinylidene fluoride-hexafluoropropylene) based solid polymer electrolytes. *Polymer Chemistry*, 1(5):702–707, 2010.
- [207] Thomas Dippong, Erika Andrea Levei, and Oana Cadar. Recent advances in synthesis and applications of MFe_2O_4 ($M = Co, Cu, Mn, Ni, Zn$) nanoparticles. *Nanomaterials*, 11(6):1560, 2021.
- [208] C Vidya, C Manjunatha, M Sudeep, S Ashoka, and MA Lourdu Antony Raj. Photo-assisted mineralisation of titan yellow dye using ZnO nanorods synthesised via environmental benign route. *SN Applied Sciences*, 2:1–15, 2020.
- [209] Channegowda Manjunatha, B Abhishek, BW Shivaraj, S Ashoka, M Shashank, and Ganganagappa Nagaraju. Engineering the $M_xZn_{1-x}O$ ($M = Al^{3+}, Fe^{3+}, Cr^{3+}$) nanoparticles for visible light-assisted catalytic mineralization of methylene blue dye using taguchi design. *Chemical Papers*, 74:2719–2731, 2020.
- [210] Rabia Ahmad, Iftikhar Hussain Gul, Muhammad Zarrar, Humaira Anwar, Muhammad Bilal Khan Niazi, and Azim Khan. Improved electrical properties of cadmium substituted cobalt ferrites nano-particles for microwave application. *Journal of magnetism and magnetic materials*, 405:28–35, 2016.
- [211] MT Farid, I Ahmad, Ss Aman, M Kanwal, G Murtaza, I Ali, I Ahmad, and M Ishfaq. Structural, electrical and dielectric behavior of $Ni_{1-x}Co_xFe_2O_4$ nano-ferrites synthesized by sol-gel method. *Digest Journal of Nanomaterials and Biostructures*, 10(1):265–275, 2015.
- [212] C Vidya, C Manjunatha, MN Chandrababha, Megha Rajshekar, and Antony Raj MAL. Hazard free green synthesis of ZnO nano-photo-catalyst using artocarpus heterophyllus leaf extract for the degradation of congo red dye in water treatment applications. *Journal of environmental chemical engineering*, 5(4):3172–3180, 2017.

- [213] M Jena, C Manjunatha, BW Shivaraj, G Nagaraju, S Ashoka, and MP Sham Aan. Optimization of parameters for maximizing photocatalytic behaviour of zn1-xfexo nanoparticles for methyl orange degradation using taguchi and grey relational analysis approach. *Materials Today Chemistry*, 12:187–199, 2019.
- [214] Anuja B Naik, Pranav P Naik, Snehal S Hasolkar, and Diksha Naik. Structural, magnetic and electrical properties along with antifungal activity & adsorption ability of cobalt doped manganese ferrite nanoparticles synthesized using combustion route. *Ceramics International*, 46(13):21046–21055, 2020.
- [215] Gangatharan Sathishkumar, Chidambaram Venkataraju, Kandasamy Sivakumar, et al. Synthesis, structural and dielectric studies of nickel substituted cobalt-zinc ferrite. *Materials Sciences and Applications*, 1(1):19–24, 2010.
- [216] Mangala U Sawal and VMS Verenkar. An insight into the nanosize and bulk ni 0.5 co 0.5 fe 2 o 4 ferrites through their comparative study: Structural and magnetic investigations. *Journal of Materials Science: Materials in Electronics*, 32:21350–21367, 2021.
- [217] Fakher Hcini, Sobhi Hcini, Bandar Alzahrani, Sadok Zemni, and Mohamed Lamjed Bouazizi. Effects of sintering temperature on structural, infrared, magnetic and electrical properties of cd 0.5 zn 0.5 fecro 4 ferrites prepared by sol–gel route. *Journal of Materials Science: Materials in Electronics*, 31:14986–14997, 2020.
- [218] Brajesh Nandan and MC Bhatnagar. Effect of sintering treatment on structural and magnetic properties of ni0. 5co0. 5fe2o4 ferrites. In *AIP Conference Proceedings*, volume 1728, page 020506. AIP Publishing LLC, 2016.
- [219] Alimohammad Mesbahinia, Mohammad Almasi-Kashi, Ali Ghasemi, and Abdolali Ramezani. First order reversal curve analysis of cobalt-nickel ferrite. *Journal of Magnetism and Magnetic Materials*, 473:161–168, 2019.

- [220] KB Modi, SJ Shah, NB Pujara, TK Pathak, NH Vasoya, and IG Jhala. Infrared spectral evolution, elastic, optical and thermodynamic properties study on mechanically milled $\text{Ni}_{0.5}\text{Zn}_{0.5}\text{Fe}_2\text{O}_4$ spinel ferrite. *Journal of Molecular Structure*, 1049: 250–262, 2013.
- [221] PA Asogekar and VMS Verenkar. Structural and magnetic properties of nanosized $\text{Co}_{1-x}\text{Zn}_x\text{Fe}_2\text{O}_4$ ($x = 0.0, 0.5, 1.0$) synthesized via autocatalytic thermal decomposition of hydrazinated cobalt zinc ferrous succinate. 2019.
- [222] Shahab Torkian, Ali Ghasemi, and Reza Shoja Razavi. Cation distribution and magnetic analysis of wideband microwave absorptive $\text{Co}_{0.9}\text{Ni}_{0.1}\text{Fe}_2\text{O}_4$ ferrites. *Ceramics International*, 43(9):6987–6995, 2017.
- [223] NM Deraz. Effects of magnesia addition on structural, morphological and magnetic properties of nano-crystalline nickel ferrite system. *Ceramics International*, 38(1): 511–516, 2012.
- [224] S Sendhilnathan et al. Enhancement in dielectric and magnetic properties of Mg^{2+} substituted highly porous super paramagnetic nickel ferrite nanoparticles with williamson-hall plots mechanistic view. *Ceramics International*, 43(17):15447–15453, 2017.
- [225] Marin Cernea, Pietro Galizia, Ioana Ciuchi, Gheorghe Aldica, Valentina Mihalache, Lucian Diamandescu, and Carmen Galassi. CoFe_2O_4 magnetic ceramic derived from gel and densified by spark plasma sintering. *Journal of Alloys and Compounds*, 656: 854–862, 2016.
- [226] Khalid Mujasam Battoo and M-S Abd El-sadek. Electrical and magnetic transport properties of Ni-Cu-Mg ferrite nanoparticles prepared by sol-gel method. *Journal of alloys and compounds*, 566:112–119, 2013.

- [227] Deepshikha Rathore, Rajnish Kurchania, and RK Pandey. Structural, magnetic and dielectric properties of $\text{Ni}_{1-x}\text{Zn}_x\text{Fe}_2\text{O}_4$ ($x = 0, 0.5$ and 1) nanoparticles synthesized by chemical co-precipitation method. *Journal of nanoscience and nanotechnology*, 13(3):1812–1819, 2013.
- [228] B Sharma, R Sharma, S Kour, MD Sharma, O Amin, AR Maity, and R Mukherjee. Fractional exponents of electrical and thermal conductivity of vanadium intercalated layered 2H-NbS_2 bulk crystal. *Indian Journal of Physics*, 96(5):1335–1339, 2022.
- [229] Simrandeep Kour, Rupam Mukherjee, and Nitish Kumar. Synthesis of $\text{Ni}_0.5\text{Co}_0.5\text{Fe}_2\text{O}_4$ ferrite and effect of annealing temperature on the structural, morphological and dielectric analysis. *ECS Transactions*, 107(1):19791, 2022.
- [230] Mathew George, Swapna S Nair, KA Malini, PA Joy, and MR Anantharaman. Finite size effects on the electrical properties of sol-gel synthesized CoFe_2O_4 powders: deviation from Maxwell-Wagner theory and evidence of surface polarization effects. *Journal of Physics D: Applied Physics*, 40(6):1593, 2007.
- [231] RC Kambale, PA Shaikh, CH Bhosale, KY Rajpure, and YD Kolekar. Dielectric properties and complex impedance spectroscopy studies of mixed Ni-Co ferrites. *Smart materials and structures*, 18(8):085014, 2009.
- [232] JH Joshi, DK Kanchan, MJ Joshi, HO Jethva, and KD Parikh. Dielectric relaxation, complex impedance and modulus spectroscopic studies of mix phase rod like cobalt sulfide nanoparticles. *Materials Research Bulletin*, 93:63–73, 2017.
- [233] RM Kershi and SH Aldirham. Transport and dielectric properties of nanocrystallite cobalt ferrites: Correlation with cations distribution and crystallite size. *Materials Chemistry and Physics*, 238:121902, 2019.
- [234] A Sathiya Priya, D Geetha, and N Kavitha. Effect of Al substitution on the structural, electric and impedance behavior of cobalt ferrite. *Vacuum*, 160:453–460, 2019.

- [235] Sandeep Arya, Prerna Mahajan, Sarika Mahajan, Ajit Khosla, Ram Datt, Vinay Gupta, Sheng-Joue Young, and Sai Kiran Oruganti. influence of processing parameters to control morphology and optical properties of sol-gel synthesized zno nanoparticles. *ECS Journal of Solid State Science and Technology*, 10(2):023002, 2021.
- [236] Kashif Ali, Ali Bahadur, Abdul Jabbar, Shahid Iqbal, Ijaz Ahmad, and Muhammad Imran Bashir. Synthesis, structural, dielectric and magnetic properties of $\text{CuFe}_2\text{O}_4/\text{MnO}_2$ nanocomposites. *Journal of Magnetism and Magnetic Materials*, 434: 30–36, 2017.
- [237] A Bahadur, A Saeed, S Iqbal, M Shoaib, and I Ahmad. ur rahman, ms; bashir, mi; yaseen, m.; hussain, w. morphological and magnetic properties of $\text{BaFe}_{12}\text{O}_{19}$ nanoferrite: A promising microwave absorbing material. *Ceram. Int*, 43:7346–7350, 2017.
- [238] Syed Tajammul Hussain, Syeda Rubina Gilani, Syed Danish Ali, and Humaira Safdar Bhatti. Decoration of carbon nanotubes with magnetic $\text{Ni}_1-\text{xCo}_x\text{Fe}_2\text{O}_4$ nanoparticles by microemulsion method. *Journal of alloys and compounds*, 544:99–104, 2012.
- [239] James E Huheey, Ellen A Keiter, Richard L Keiter, and Okhil K Medhi. *Inorganic chemistry: principles of structure and reactivity*. Pearson Education India, 2006.
- [240] Talat Zeeshan, Safia Anjum, Salma Waseem, and Lubna Mustufa. Tailoring of structural and magnetic properties by substitution of copper in cobalt chromium ferrites. *Ceramics International*, 44(15):17709–17715, 2018.
- [241] Charanjit Singh, Ankita Goyal, and Sonal Singhal. Nickel-doped cobalt ferrite nanoparticles: efficient catalysts for the reduction of nitroaromatic compounds and photo-oxidative degradation of toxic dyes. *Nanoscale*, 6(14):7959–7970, 2014.
- [242] Mircea Stefanescu, Marius Bozdog, Cornelia Muntean, Oana Stefanescu, and Titus Vlase. Synthesis and magnetic properties of $\text{Co}_{1-\text{x}}\text{Zn}_\text{x}\text{Fe}_2\text{O}_4$ ($\text{x} = 0 \div 1$) nanopowders

- by thermal decomposition of co (ii), zn (ii) and fe (iii) carboxylates. *Journal of Magnetism and Magnetic Materials*, 393:92–98, 2015.
- [243] MA Willard, LK Kurihara, EE Carpenter, S Calvin, and VG Harris. Chemically prepared magnetic nanoparticles. *International materials reviews*, 49(3-4):125–170, 2004.
- [244] K Ali, AK Sarfraz, IM Mirza, A Bahadur, and S Iqbal. ul haq, a.(2015). preparation of superparamagnetic maghemite (γ - Fe_2O_3) nanoparticles by wet chemical route and investigation of their magnetic and dielectric properties. *Curr. Appl. Phys*, 15:925–929.
- [245] S Iqbal, M Javed, SS Hassan, S Nadeem, A Akbar, MT Alotaibi, RM Alzhrani, NS Awwad, HA Ibrahim, and A Mohyuddin. Binary / s-scheme heterojunction enriching spatial charge carrier separation for efficient removal of organic pollutants under sunlight irradiation. *Colloids Surfaces A Physicochem. Eng. Asp*, 636:128177, 2022.
- [246] Muhammad Azam Qamar, Sammia Shahid, Mohsin Javed, Shahid Iqbal, Mudassar Sher, Ali Bahadur, Murefah Mana AL-Anazy, A Laref, and Dongxiang Li. Designing of highly active g-c₃n₄/ni-zno photocatalyst nanocomposite for the disinfection and degradation of the organic dye under sunlight radiations. *Colloids and Surfaces A: Physicochemical and Engineering Aspects*, 614:126176, 2021.
- [247] PP Hankare, SD Jadhav, UB Sankpal, SS Chavan, KJ Waghmare, and BK Chougule. Synthesis, characterization and effect of sintering temperature on magnetic properties of mg_{ni} ferrite prepared by co-precipitation method. *Journal of alloys and compounds*, 475(1-2):926–929, 2009.
- [248] Shahid Iqbal, Ali Bahadur, Shoaib Anwer, Shahid Ali, Rana Muhammad Irfan, Hao Li, Muhammad Shoaib, Muhammad Raheel, Tehseen Ali Anjum, and Muhammad Zulqarnain. Effect of temperature and reaction time on the morphology of l-cysteine

- surface capped chalcocite (Cu₂S) snowflakes dendrites nanoleaves and photodegradation study of methyl orange dye under visible light. *Colloids and Surfaces A: Physicochemical and Engineering Aspects*, 601:124984, 2020.
- [249] Kedar Marathe and Prashant Doshi. Localization and tracking under extreme and persistent sensory occlusion. In *2015 IEEE/RSJ International Conference on Intelligent Robots and Systems (IROS)*, pages 2550–2555. IEEE, 2015.
- [250] Chandana Rath, S Anand, RP Das, KK Sahu, SD Kulkarni, SK Date, and NC Mishra. Dependence on cation distribution of particle size, lattice parameter, and magnetic properties in nanosize Mn–Zn ferrite. *Journal of Applied Physics*, 91(4):2211–2215, 2002.
- [251] JM Yang and Fu-Su Yen. Evolution of intermediate phases in the synthesis of zinc ferrite nanopowders prepared by the tartrate precursor method. *Journal of alloys and compounds*, 450(1-2):387–394, 2008.
- [252] EJW Verwey, PW Haayman, and FC Romeijn. Physical properties and cation arrangement of oxides with spinel structures ii. electronic conductivity. *The Journal of Chemical Physics*, 15(4):181–187, 1947.
- [253] MM Rashad, RM Mohamed, and H El-Shall. Magnetic properties of nanocrystalline Mn-substituted CoFe₂O₄ synthesized by citrate precursor method. *Journal of Materials Processing Technology*, 198(1-3):139–146, 2008.
- [254] Lars Dörner, Claudia Cancellieri, Bastian Rheingans, Marc Walter, Ralf Kägi, Patrik Schmutz, Maksym V Kovalenko, and Lars PH Jeurgens. Cost-effective sol-gel synthesis of porous CuO nanoparticle aggregates with tunable specific surface area. *Scientific reports*, 9(1):1–13, 2019.
- [255] Vibha Verma, Manpreet Kaur, and Jean Marc Grenèche. Tailored structural, optical and magnetic properties of ternary nanohybrid Mn_{0.4}Co_{0.6}xCu_xFe₂O₄ (x= 0, 0.2, 0.4, 0.6) spinel ferrites. *Ceramics International*, 45(8):10865–10875, 2019.

- [256] N Murali, SJ Margarete, G Pavan Kumar, B Sailaja, S Yonatan Mulushoa, P Himakar, B Kishore Babu, and V Veeraiah. Effect of al substitution on the structural and magnetic properties of co-zn ferrites. *Physica B: Condensed Matter*, 522:1–6, 2017.
- [257] RK Panda and D Behera. Investigation of electric transport behavior of bulk cofe₂o₄ by complex impedance spectroscopy. *Journal of alloys and compounds*, 587:481–486, 2014.
- [258] Simrandeep Kour and Rupam Mukherjee. Effect of tio₂ as filler in nacl: Possible applications in ionic storage systems. In *Journal of Physics: Conference Series*, volume 2267, page 012092. IOP Publishing, 2022.
- [259] SB Gopale, GN Kakade, GD Kulkarni, V Vinayak, SP Jadhav, and KM Jadhav. X-ray diffraction, infrared and magnetic studies of nife₂o₄ nanoparticles. In *Journal of Physics: Conference Series*, volume 1644, page 012010. IOP Publishing, 2020.
- [260] Sagar Mitra, Pavan S Veluri, Antara Chakraborty, and Ramesh K Petla. Electrochemical properties of spinel cobalt ferrite nanoparticles with sodium alginate as interactive binder. *ChemElectroChem*, 1(6):1068–1074, 2014.
- [261] Timothy J Trentler, Kathleen M Hickman, Subhash C Goel, Ann M Viano, Patrick C Gibbons, and William E Buhro. Solution-liquid-solid growth of crystalline iii-v semiconductors: an analogy to vapor-liquid-solid growth. *Science*, 270(5243):1791–1794, 1995.
- [262] Yanping Sui, Xinfan Huang, Zhongyuan Ma, Wei Li, Feng Qiao, Kai Chen, and Kunji Chen. The effect of thermal annealing on crystallization in a-si: H/sio₂ multilayers by using layer by layer plasma oxidation. *Journal of Physics: Condensed Matter*, 15(34):5793, 2003.

- [263] ST Mahmud, AKM Akther Hossain, AKM Abdul Hakim, M Seki, T Kawai, and H Tabata. Influence of microstructure on the complex permeability of spinel type ni–zn ferrite. *Journal of Magnetism and Magnetic Materials*, 305(1):269–274, 2006.
- [264] Mamata Maisnam, Nandeibam Nilima, Maisnam Victory, and Sumitra Phanjoubam. Low dielectric loss in nano-li-ferrite spinels prepared by sol–gel auto-combustion technique. *Bulletin of Materials Science*, 39:249–254, 2016.
- [265] AP Grosvenor, BA Kobe, Mark C Biesinger, and NS McIntyre. Investigation of multiplet splitting of fe 2p xps spectra and bonding in iron compounds. *Surface and Interface Analysis: An International Journal devoted to the development and application of techniques for the analysis of surfaces, interfaces and thin films*, 36(12):1564–1574, 2004.
- [266] Mark C Biesinger. Advanced analysis of copper x-ray photoelectron spectra. *Surface and Interface Analysis*, 49(13):1325–1334, 2017.
- [267] JC Woicik, C Weiland, AK Rumaiz, M Brumbach, NF Quackenbush, JM Ablett, and EL Shirley. Revealing excitonic processes and chemical bonding in mo s₂ by x-ray spectroscopy. *Physical Review B*, 98(11):115149, 2018.
- [268] Mark C Biesinger, Brad P Payne, Andrew P Grosvenor, Leo WM Lau, Andrea R Gerson, and Roger St C Smart. Resolving surface chemical states in xps analysis of first row transition metals, oxides and hydroxides: Cr, mn, fe, co and ni. *Applied Surface Science*, 257(7):2717–2730, 2011.
- [269] Shahid Iqbal. Spatial charge separation and transfer in l-cysteine capped nicop/cds nano-heterojunction activated with intimate covalent bonding for high-quantum-yield photocatalytic hydrogen evolution. *Applied Catalysis B: Environmental*, 274:119097, 2020.

- [270] Chandan C Naik and AV Salker. Tailoring magnetic and dielectric properties of $\text{Co}_{0.9}\text{Cu}_{0.1}\text{Fe}_2\text{O}_4$ with substitution of small fractions of Gd^{3+} ions. *Journal of Materials Science: Materials in Electronics*, 29:5380–5390, 2018.
- [271] Raghvendra Singh Yadav, Jaromir Havlica, Jiri Masilko, Lukas Kalina, Miroslava Hajdúchová, Vojtěch Enev, Jaromir Wasserbauer, Ivo Kuřitka, and Zuzana Koza-kova. Structural, cation distribution, and magnetic properties of CoFe_2O_4 spinel ferrite nanoparticles synthesized using a starch-assisted sol–gel auto-combustion method. *Journal of Superconductivity and Novel Magnetism*, 28:1851–1861, 2015.
- [272] SR Naik, AV Salker, SM Yusuf, and SS Meena. Influence of Co^{2+} distribution and spin–orbit coupling on the resultant magnetic properties of spinel cobalt ferrite nanocrystals. *Journal of alloys and compounds*, 566:54–61, 2013.
- [273] Florin Tudorache, Paul Dorin Popa, Marius Dobromir, and Felicia Iacomi. Studies on the structure and gas sensing properties of nickel–cobalt ferrite thin films prepared by spin coating. *Materials Science and Engineering: B*, 178(19):1334–1338, 2013.
- [274] R Verma and A Chauhan. Neha; batoo, km; kumar, r.; hadhi, m.; raslan, eh effect of calcination temperature on structural and morphological properties of bismuth ferrite nanoparticles. *Ceram. Int*, 47(3):3680–3691, 2021.
- [275] Hammesh Mahajan, Shammi Kumar, Anjori Sharma, Ibrahim Mohammed, Manisha Thakur, Simrandeep Kour, Amarjeet Kaur, and Ajeet Kumar Srivastava. Structural, morphological, and electrochemical investigation of $\text{Mn}_{0.3}\text{Co}_{0.2}\text{Zn}_{0.5}\text{Fe}_2\text{O}_4$ -polyaniline nanocomposite for supercapacitor application. *Journal of Materials Science: Materials in Electronics*, pages 1–14, 2022.
- [276] Asmaa AH El-Bassuony. Enhancement of structural and electrical properties of novelty nanoferrite materials. *Journal of Materials Science: Materials in Electronics*, 28(19):14489–14498, 2017.

- [277] Asmaa AH El-Bassuony. A comparative study of physical properties of er and yb nanophase ferrite for industrial application. *Journal of Superconductivity and Novel Magnetism*, 31:2829–2840, 2018.
- [278] Idza Riati Ibrahim, Mansor Hashim, Rodziah Nazlan, Ismayadi Ismail, Samikannu Kanagesan, Wan Norailiana Wan Ab Rahman, Nor Hapishah Abdullah, Fadzi-dah Mohd Idris, and Ghazaleh Bahmanrokh. A comparative study of different sintering routes effects on evolving microstructure and b–h magnetic hysteresis in mechanically-alloyed ni–zn ferrite, ni_{0.3}zn_{0.7}fe₂o₄. *Journal of Materials Science: Materials in Electronics*, 26:59–65, 2015.
- [279] SR Gibin and P Sivagurunathan. Synthesis and characterization of nickel cobalt ferrite (ni_{1-x}co_xfe₂o₄) nano particles by co-precipitation method with citrate as chelating agent. *Journal of Materials Science: Materials in Electronics*, 28:1985–1996, 2017.
- [280] H Moradmard, S Farjami Shayesteh, P Tohidi, Z Abbas, and M Khaleghi. Structural, magnetic and dielectric properties of magnesium doped nickel ferrite nanoparticles. *Journal of Alloys and Compounds*, 650:116–122, 2015.
- [281] JH Joshi, KP Dixit, MJ Joshi, and KD Parikh. Study on ac electrical properties of pure and l-serine doped adp crystals. In *AIP Conference Proceedings*, volume 1728, page 020219. AIP Publishing LLC, 2016.
- [282] NH Vasoya, VK Lakhani, PU Sharma, KB Modi, Ravi Kumar, and HH Joshi. Study on the electrical and dielectric behaviour of zn-substituted cobalt ferrialuminates. *Journal of Physics: Condensed Matter*, 18(34):8063, 2006.
- [283] Manish S Jayswal, DK Kanchan, Poonam Sharma, and Nirali Gondaliya. Relaxation process in pbi₂–ag₂o–v₂o₅–b₂o₃ system: dielectric, ac conductivity and modulus studies. *Materials Science and Engineering: B*, 178(11):775–784, 2013.

- [284] S Yonatan Mulushoa, N Murali, Paulos Taddesse, A Ramakrishna, D Parajuli, Khalid Mujasam Bato, Ritesh Verma, Rajesh Kumar, YB Shankar Rao, Sajjad Hussain, et al. Structural, dielectric and magnetic properties of nickel-chromium substituted magnesium ferrites, $\text{mg}_{1-x}\text{ni}_x\text{fe}_2\text{-xcr}_x\text{o}_4$ ($0 < x < 0.7$). *Inorganic Chemistry Communications*, 138:109289, 2022.
- [285] A Kaushal, SM Olhero, Budhendra Singh, Duncan P Fagg, Igor Bdikin, and JMF Ferreira. Impedance analysis of $0.5 \text{ ba} (\text{zr}_{0.2}\text{ti}_{0.8}) \text{o}_3$ – $0.5 (\text{ba}_{0.7}\text{ca}_{0.3}) \text{tio}_3$ ceramics consolidated from micro-granules. *Ceramics International*, 40(7):10593–10600, 2014.
- [286] MM Rahman, N Hasan, MA Hoque, MB Hossen, and M Arifuzzaman. Structural, dielectric, and electrical transport properties of al^{3+} substituted nanocrystalline ni-cu spinel ferrites prepared through the sol–gel route. *Results in Physics*, 38:105610, 2022.
- [287] Haitao Ye, Richard B Jackman, and Peter Hing. Spectroscopic impedance study of nanocrystalline diamond films. *Journal of applied physics*, 94(12):7878–7882, 2003.
- [288] Dalibor L Sekulić, Zorica Z Lazarević, Čedomir D Jovalekić, Aleksandra N Milutinović, and Nebojša Z Romčević. Impedance spectroscopy of nanocrystalline mgfe_2o_4 and mnfe_2o_4 ferrite ceramics: effect of grain boundaries on the electrical properties. *Science of Sintering*, 48(1), 2016.
- [289] Gagan Kumar, Sucheta Sharma, RK Kotnala, Jyoti Shah, Sagar E Shirsath, Khalid M Bato, and M Singh. Electric, dielectric and ac electrical conductivity study of nanocrystalline cobalt substituted mg-mn ferrites synthesized via solution combustion technique. *Journal of Molecular Structure*, 1051:336–344, 2013.
- [290] Khalid Mujasam Bato, Shalendra Kumar, Chan Gyu Lee, et al. Finite size effect and influence of temperature on electrical properties of nanocrystalline ni-cd ferrites. *Current Applied Physics*, 9(5):1072–1078, 2009.

- [291] Karishma Kumari, Ashutosh Prasad, and Kamal Prasad. Dielectric, impedance/modulus and conductivity studies on $[\text{Bi}_{0.5}(\text{Na}_{1-x}\text{K}_x)_{0.5}]_{0.94}\text{Ba}_{0.06}\text{TiO}_3$ ($0.16 < x < 0.20$) lead-free ceramics. *Am. J. Mater. Sci.*, 6(1):1–18, 2016.
- [292] SK Ahmed, M Faishal Mahmood, M Arifuzzaman, and M Belal Hossen. Enhancement of electrical and magnetic properties of Al^{3+} substituted CuZn nano ferrites with structural rietveld refinement. *Results in Physics*, 30:104833, 2021.
- [293] Anu Rana et al. Study of anneal-tuned dielectric properties, ac conductivity, complex impedance, and modulus of cobalt ferrite nanoparticles. *Materials Today: Proceedings*, 45:5444–5448, 2021.
- [294] Elaa Oumezzine, Sobhi Hcini, FIH Rhouma, and Mohamed Oumezzine. Frequency and temperature dependence of conductance, impedance and electrical modulus studies of $\text{Ni}_{0.6}\text{Cu}_{0.4}\text{Fe}_2\text{O}_4$ spinel ferrite. *Journal of Alloys and Compounds*, 726:187–194, 2017.
- [295] Ch Rayssi, S El Kossi, J Dhahri, and K Khirouni. *Rsc adv.* 8, 17139 (2018).
- [296] Yuezhong Xian, Yi Hu, Fang Liu, Yang Xian, Haiting Wang, and Litong Jin. Glucose biosensor based on au nanoparticles–conductive polyaniline nanocomposite. *Biosensors and Bioelectronics*, 21(10):1996–2000, 2006.
- [297] PilliSatyananda Kishore, Balasubramanian Viswanathan, and ThirukkallamKanthadai Varadarajan. Synthesis and characterization of metal nanoparticle embedded conducting polymer–polyoxometalate composites. *Nanoscale Research Letters*, 3(1):14–20, 2008.
- [298] Ricky J Tseng, Jiaying Huang, Jianyong Ouyang, Richard B Kaner, and Yang Yang. Polyaniline nanofiber/gold nanoparticle nonvolatile memory. *Nano letters*, 5(6):1077–1080, 2005.
- [299] Wendy U Huynh, Janke J Dittmer, and A Paul Alivisatos. Hybrid nanorod-polymer solar cells. *science*, 295(5564):2425–2427, 2002.

- [300] Asgar Kayan. Synthesis, characterization, and application of hybrid inorganic–organic composites (k/na) zrsi (r) o x. *Journal of Inorganic and Organometallic Polymers and Materials*, 26:640–647, 2016.
- [301] Chi-Chang Hu, Eve Chen, and Jeng-Yan Lin. Capacitive and textural characteristics of polyaniline–platinum composite films. *Electrochimica acta*, 47(17):2741–2749, 2002.
- [302] Süleyman Köytepe, Turgay Seçkin, Nilüfer Kıvrılcım, and H İbrahim Adıgüzel. Synthesis and dielectric properties of polyimide–titania hybrid composites. *Journal of Inorganic and Organometallic Polymers and Materials*, 18:222–228, 2008.
- [303] Songhua Wu, Jianzheng Zhang, Chao Sun, and Jingshuai Chen. Synthesis of mno₂/nico-layered double hydroxide hybrid as electrode materials for supercapacitor. *Journal of Inorganic and Organometallic Polymers and Materials*, 30:3179–3187, 2020.
- [304] S Firmino Mendes, Carlos M Costa, Cristina Caparrós, Vitor Sencadas, and Senentxu Lanceros-Méndez. Effect of filler size and concentration on the structure and properties of poly (vinylidene fluoride)/batio 3 nanocomposites. *Journal of Materials Science*, 47:1378–1388, 2012.
- [305] R Gregorio, M Cestari, and FE Bernardino. Dielectric behaviour of thin films of β -pvdf/pzt and β -pvdf/batio 3 composites. *Journal of Materials Science*, 31:2925–2930, 1996.
- [306] Dhiraj Kumar Rana, Suresh Kumar Singh, Shovan Kumar Kundu, Subir Roy, S Angappane, and Soumen Basu. Electrical and room temperature multiferroic properties of polyvinylidene fluoride nanocomposites doped with nickel ferrite nanoparticles. *New Journal of Chemistry*, 43(7):3128–3138, 2019.
- [307] M Salah, Ibrahim Morad, H Elhosiny Ali, MM Mostafa, and MM El-Desoky. Influence of bao doping on the structural, ac conductivity, and dielectric properties of

- bifeo 3 multiferroic nanoparticles. *Journal of Inorganic and Organometallic Polymers and Materials*, 31:3700–3710, 2021.
- [308] M Saleem, BR Bhagat, and A Mishra. Influence of lead free bi 0.5 na 0.5 tio 3 substitution on the structural and electrical properties of ferromagnetic metallic phase la 0.8 sr 0.2 mno 3. *Journal of Inorganic and Organometallic Polymers and Materials*, 29:2103–2115, 2019.
- [309] G Catalan. Magnetodielectric effect without multiferroic coupling. *arXiv preprint cond-mat/0510313*, 2005.
- [310] Jing Yan, Ying Huang, Xuefang Chen, and Chao Wei. Conducting polymers-nife2o4 coated on reduced graphene oxide sheets as electromagnetic (em) wave absorption materials. *Synthetic Metals*, 221:291–298, 2016.
- [311] Muhammad Ajmal and MU Islam. Structural, optical and dielectric properties of polyaniline-nio. 5 zno. 5fe2o4 nano-composites. *Physica B: Condensed Matter*, 521:355–360, 2017.
- [312] M Khairy and ME Gouda. Electrical and optical properties of nickel ferrite/polyaniline nanocomposite. *Journal of advanced research*, 6(4):555–562, 2015.
- [313] Shama Islam, GBVS Lakshmi, Azher M Siddiqui, M Husain, and M Zulfequar. Synthesis, electrical conductivity, and dielectric behavior of polyaniline/v2o5 composites. *International Journal of Polymer Science*, 2013, 2013.
- [314] Yinglin Xiao, Xiaomin Li, Jiantao Zai, Kaixue Wang, Yong Gong, Bo Li, Qianyan Han, and Xuefeng Qian. Cofe 2 o 4-graphene nanocomposites synthesized through an ultrasonic method with enhanced performances as anode materials for li-ion batteries. *Nano-micro letters*, 6:307–315, 2014.
- [315] Özlem Yavuz, Manoj K Ram, Matt Aldissi, Pankaj Poddar, and Srikanth Hariharan. Synthesis and the physical properties of mnzn ferrite and nimnzn ferrite–polyaniline nanocomposite particles. *Journal of Materials Chemistry*, 15(7):810–817, 2005.

- [316] Nassim Nasser Ali, Yomen Atassi, Akil Salloum, Abdulkarim Charba, Adnan Malki, and Mojtaba Jafarian. Comparative study of microwave absorption characteristics of (polyaniline/nizn ferrite) nanocomposites with different ferrite percentages. *Materials Chemistry and Physics*, 211:79–87, 2018.
- [317] Ajai Kumar S Molakeri and Sangshetty Kalyane. Preparation, structural and dielectric properties of polyaniline-nickel ferrite composites. *Int. J. Mater. Sci*, 12:47–56, 2017.
- [318] S Kotresh, YT Ravikiran, SC Vijaya Kumari, CH VV Ramana, AS Anu, and KM Battoo. Optimised polyaniline–cadmium ferrite nanocomposite: synthesis, characterisation and alternating current response. *Polymer Bulletin*, 75(6):2475–2490, 2018.
- [319] KS Hemalatha, G Sriprakash, MVN Ambika Prasad, R Damle, and K Rukmani. Temperature dependent dielectric and conductivity studies of polyvinyl alcohol-zno nanocomposite films by impedance spectroscopy. *Journal of Applied physics*, 118(15):154103, 2015.
- [320] Aikaterini Sanida, Sotirios G Stavropoulos, Thanassis Speliotis, and Georgios C Psarras. Investigating the effect of zn ferrite nanoparticles on the thermomechanical, dielectric and magnetic properties of polymer nanocomposites. *Materials*, 12(18):3015, 2019.
- [321] S El-Sayed, TA Abdel-Baset, and A Hassen. Dielectric properties of pvdf thin films doped with 3 wt.% of r cl3 (r= gd or er). *AIP advances*, 4(3):037114, 2014.
- [322] VM Mohan, Weiliang Qiu, Jie Shen, and Wen Chen. Electrical properties of poly (vinyl alcohol)(pva) based on lifepo 4 complex polymer electrolyte films. *Journal of polymer research*, 17:143–150, 2010.
- [323] Lizhen Fan, Zhimin Dang, Guodan Wei, Ce-Wen Nan, and Ming Li. Effect of nanosized zno on the electrical properties of (peo) 16liclo4 electrolytes. *Materials Science and Engineering: B*, 99(1-3):340–343, 2003.

- [324] P Dutta, S Biswas, M Ghosh, SK De, and S Chatterjee. The dc and ac conductivity of polyaniline–polyvinyl alcohol blends. *Synthetic metals*, 122(2):455–461, 2001.
- [325] IH Gul, W Ahmed, and A Maqsood. Electrical and magnetic characterization of nanocrystalline ni–zn ferrite synthesis by co-precipitation route. *Journal of Magnetism and Magnetic Materials*, 320(3-4):270–275, 2008.
- [326] Ramesh Patil, Aashis S Roy, Koppalkar R Anilkumar, KM Jadhav, and Shrikant Ekhelkar. Dielectric relaxation and ac conductivity of polyaniline–zinc ferrite composite. *Composites Part B: Engineering*, 43(8):3406–3411, 2012.
- [327] Hui Zheng, Yanling Dong, Xin Wang, Wenjian Weng, Gaorong Han, Ning Ma, and Piyi Du. Super high threshold percolative ferroelectric/ferrimagnetic composite ceramics with outstanding permittivity and initial permeability. *Angewandte Chemie International Edition*, 48(47):8927–8930, 2009.
- [328] JQ Huang, PY Du, LX Hong, YL Dong, and MC Hong. A novel percolative ferromagnetic–ferroelectric composite with significant dielectric and magnetic properties. *Advanced Materials*, 19(3):437–440, 2007.
- [329] Hui Zheng, Lu Li, Zhaojun Xu, Wenjian Weng, Gaorong Han, Ning Ma, and Piyi Du. Ferroelectric/ferromagnetic ceramic composite and its hybrid permittivity stemming from hopping charge and conductivity inhomogeneity. *Journal of Applied Physics*, 113(4):044101, 2013.
- [330] Yang Wang, Jerry W Shan, and George J Weng. Percolation threshold and electrical conductivity of graphene-based nanocomposites with filler agglomeration and interfacial tunneling. *Journal of Applied Physics*, 118(6):065101, 2015.
- [331] Juan C Apesteguy and Silvia E Jacobo. Synthesis of a soluble polyaniline–ferrite composite: magnetic and electric properties. *Journal of materials science*, 42:7062–7068, 2007.

- [332] Yunze Long, Zhaojia Chen, Jean Luc Duvail, Zhiming Zhang, and Meixiang Wan. Electrical and magnetic properties of polyaniline/fe₃o₄ nanostructures. *Physica B: Condensed Matter*, 370(1-4):121–130, 2005.
- [333] C Behera, RNP Choudhary, and Piyush R Das. Development of ni-ferrite-based pvdf nanomultiferroics. *Journal of Electronic Materials*, 46:6009–6022, 2017.
- [334] M Kryszewski and JK Jeszka. Nanostructured conducting polymer composites—superparamagnetic particles in conducting polymers. *Synthetic Metals*, 94(1):99–104, 1998.
- [335] Natalia E Kazantseva, Jarmila Vilčáková, V Křesálek, P Saha, I Sapurina, and J Stejskal. Magnetic behaviour of composites containing polyaniline-coated manganese–zinc ferrite. *Journal of Magnetism and Magnetic Materials*, 269(1):30–37, 2004.
- [336] Cristian Iacovita, Gabriela Fabiola Stiufig, Roxana Dudric, Nicoleta Vedeanu, Romulus Tetean, Rares Ionut Stiufig, and Constantin Mihai Lucaciu. Saturation of specific absorption rate for soft and hard spinel ferrite nanoparticles synthesized by polyol process. *Magnetochemistry*, 6(2):23, 2020.
- [337] Ayan Mukherjee, Soumen Basu, PK Manna, SM Yusuf, and Mrinal Pal. Giant magnetodielectric and enhanced multiferroic properties of sm doped bismuth ferrite nanoparticles. *Journal of Materials Chemistry C*, 2(29):5885–5891, 2014.
- [338] Ramaroorthy Ramesh and Nicola A Spaldin. Multiferroics: progress and prospects in thin films. *Nature materials*, 6(1):21–29, 2007.
- [339] Giovanni Moggi, Piergiorgio Bonardelli, and Jan CJ Bart. Copolymers of 1, 1-difluoroethene with tetrafluoroethene, chlorotrifluoroethene, and bromotrifluoroethene. *Journal of Polymer Science: Polymer Physics Edition*, 22(3):357–365, 1984.

- [340] Haisheng Xu, Z-Y Cheng, Dana Olson, T Mai, QM Zhang, and G Kavarnos. Ferroelectric and electromechanical properties of poly (vinylidene-fluoride–trifluoroethylene–chlorotrifluoroethylene) terpolymer. *Applied Physics Letters*, 78(16):2360–2362, 2001.
- [341] P Durga Prasad and J Hemalatha. Enhanced dielectric and ferroelectric properties of cobalt ferrite (cofe₂o₄) fiber embedded polyvinylidene fluoride (pvdf) multiferroic composite films. *Materials Research Express*, 6(9):094007, 2019.
- [342] Gang Liu, Shujun Zhang, Wenhua Jiang, and Wenwu Cao. Losses in ferroelectric materials. *Materials Science and Engineering: R: Reports*, 89:1–48, 2015.
- [343] Chuntian Chen, Lei Wang, Xinmei Liu, Wenlong Yang, Jiaqi Lin, Gaoru Chen, and Xinrui Yang. K_{0.5}Na_{0.5}NbO₃-SrTiO₃/pvdf polymer composite film with low remnant polarization and high discharge energy storage density. *Polymers*, 11(2):310, 2019.
- [344] Yiping Guo, Yun Liu, Jianli Wang, Ray L Withers, Hua Chen, Lu Jin, and Paul Smith. Giant magnetodielectric effect in 0-3 Ni_{0.5}Zn_{0.5}Fe₂O₄-poly (vinylidene-fluoride) nanocomposite films. *The Journal of Physical Chemistry C*, 114(32):13861–13866, 2010.
- [345] Simrandeep Kour, Hammesh Mahajan, and Rupam Mukherjee. Influence of sintering temperature on impedance and modulus spectroscopy of nickel-substituted cobalt ferrite. *Journal of Materials Science: Materials in Electronics*, 34(7):594, 2023.
- [346] Thomas Hanemann and Dorothée Vinga Szabó. Polymer-nanoparticle composites: from synthesis to modern applications. *Materials*, 3(6):3468–3517, 2010.
- [347] Yo-Rhin Rhim, Dajie Zhang, D Howard Fairbrother, Kevin A Wepasnick, Kenneth J Livi, Robert J Bodnar, and Dennis C Nagle. Changes in electrical and microstructural properties of microcrystalline cellulose as function of carbonization temperature. *Carbon*, 48(4):1012–1024, 2010.

- [348] Tom G Mackay and Akhlesh Lakhtakia. Percolation thresholds in the homogenization of spheroidal particles oriented in two directions. *Optics communications*, 259(2):727–737, 2006.
- [349] Liudmila A Makarova, Danil A Isaev, Alexander S Omelyanchik, Iuliia A Alekhina, Matvey B Isaenko, Valeria V Rodionova, Yuriy L Raikher, and Nikolai S Perov. Multiferroic coupling of ferromagnetic and ferroelectric particles through elastic polymers. *Polymers*, 14(1):153, 2022.
- [350] Oriol Gavalda Diaz, Gonzalo Garcia Luna, Zhirong Liao, and Dragos Axinte. The new challenges of machining ceramic matrix composites (cmcs): Review of surface integrity. *International Journal of Machine Tools and Manufacture*, 139:24–36, 2019.
- [351] Hongbo Gu, Jiang Guo, Huige Wei, Xi Zhang, Jiahua Zhu, Lu Shao, Yudong Huang, Neel Haldolaarachchige, David P Young, Suying Wei, et al. Magnetoresistive conductive polymer-tungsten trioxide nanocomposites with ultrahigh sensitivity at low magnetic field. *Polymer*, 55(3):944–950, 2014.
- [352] Shilpi Banerjee, Partha Hajra, Asim Bhaumik, Sri Bandyopadhyay, and Dipankar Chakravorty. Large magnetodielectric effect in nickel zinc ferrite–lithium niobate nanocomposite. *Chemical Physics Letters*, 541:96–100, 2012.
- [353] Biwei Qiu, Jingyun Wang, Zhoujing Li, Xia Wang, and Xiaoyan Li. Influence of acidity and oxidant concentration on the nanostructures and electrochemical performance of polyaniline during fast microwave-assisted chemical polymerization. *Polymers*, 12(2):310, 2020.
- [354] Murat Akarsu, Meltem Asiltürk, Funda Sayilkan, Nadir Kiraz, Ertuğrul Arpaç, and Hikmet Sayilkan. A novel approach to the hydrothermal synthesis of anatase titania nanoparticles and the photocatalytic degradation of rhodamine b. *Turkish Journal of Chemistry*, 30(3):333–343, 2006.

- [355] Arunas Ramanavicius, Povilas Genys, Yasemin Oztekin, and Almira Ramanaviciene. Evaluation of the redox mediating properties of 1, 10-phenanthroline-5, 6-dione for glucose oxidase modified graphite electrodes. *Journal of the Electrochemical Society*, 161(3):B31, 2013.
- [356] Arunas Ramanavicius, Povilas Genys, and Almira Ramanaviciene. Electrochemical impedance spectroscopy based evaluation of 1, 10-phenanthroline-5, 6-dione and glucose oxidase modified graphite electrode. *Electrochimica Acta*, 146:659–665, 2014.
- [357] Manjunatha Channegowda. Recent advances in environmentally benign hierarchical inorganic nano-adsorbents for the removal of poisonous metal ions in water: a review with mechanistic insight into toxicity and adsorption. *Nanoscale Advances*, 2(12): 5529–5554, 2020.
- [358] Duy Thanh Tran, Huu Tuan Le, Nam Hoon Kim, Joong Hee Lee, et al. Highly efficient overall water splitting over a porous interconnected network by nickel cobalt oxysulfide interfacial assembled $\text{Cu@Cu}_2\text{S}$ nanowires. *Journal of Materials Chemistry A*, 8(29):14746–14756, 2020.
- [359] Philseok Kim, Natalie M Doss, John P Tillotson, Peter J Hotchkiss, Ming-Jen Pan, Seth R Marder, Jiangyu Li, Jeffery P Calame, and Joseph W Perry. High energy density nanocomposites based on surface-modified BaTiO_3 and a ferroelectric polymer. *ACS nano*, 3(9):2581–2592, 2009.
- [360] Shiyang Li, Zhaojiang Chen, and Wenwu Cao. Switching $70\text{pm} \times (100\text{nm}/3\text{nm}^2/3) \times 0.30\text{p} \times \text{BaTiO}_3$ single crystal by 3 mhz bipolar field. *Applied Physics Letters*, 108(23): 232901, 2016.

List of Publications

Journals

1. Publication

Journal of Inorganic and Organometallic Polymers and Materials
<https://doi.org/10.1007/s10904-023-02602-2>

RESEARCH



The Dielectric, Magnetic, and Ferroelectric Analysis of $x\text{Ni}_{0.5}\text{Co}_{0.5}\text{Fe}_2\text{O}_4:(1-x)\text{PANI}$ Multiferroic Composites

Simrandeep Kour¹ · Sanat Kumar Adhikari² · Maheshika Paliwadana³ · Rupam Mukherjee¹

Received: 27 December 2022 / Accepted: 28 February 2023
© The Author(s), under exclusive licence to Springer Science+Business Media, LLC, part of Springer Nature 2023

Abstract

Different compositions of the nanocomposite lead-free multiferroic systems are fabricated by employing piezoelectric poly-aniline (PANI) and magnetostrictive $\text{Ni}_{0.5}\text{Co}_{0.5}\text{Fe}_2\text{O}_4$ (NCF) by varying the NCF weight fraction. The current work reports the synthesis of $x\text{NCF}:(1-x)\text{PANI}$ hybrid composite systems prepared via the physical blending method. X-ray powder diffraction (XRD) exhibits the presence of both; a polymeric amorphous phase of PANI (matrix) and a crystalline phase of inverse spinel ferrite NCF (filler) in the composites. The microstructure analysis along with the elemental composition of the samples are studied via Field emission scanning electron microscopy (FESEM) and Energy Dispersive X-ray Analysis (EDAX) respectively. Here, frequency-dependent dielectric permittivity exhibits percolation-type behavior where permittivity (ϵ') attains a peak at a critical weight fraction ($x = 0.3$). The magnetic properties for the particular stoichiometric concentration ($x = 0.3$) of the composite exhibit a large enhancement in the saturation magnetization (M_s) of 75.22 emu g^{-1} , while maintaining the soft ferromagnetism in the nanocomposite system. The switching behavior of electrical polarization in composite systems exhibits strong temperature dependence with a ferroelectric loop that appears to persist at even low temperatures (5 K). The remnant electrical polarization (P_r) is found to decrease with the increase in ferrite (NCF) concentration. Hence, the developed composite system at the high electric field exhibits both ferroelectric and ferromagnetic characteristics without significant conductive losses making it suitable for potential multiferroic and capacitor applications.

Keywords Hybrid composites · Multiferroic · Remnant Polarization · Weight fraction · Dielectric response

1 Introduction

In recent years, hybrid (polymer/metal) nanocomposites have significantly emerged as prominent materials that merge optical, mechanical, and dielectric properties of polymers (organic) with magnetic characteristics as well as the high electrical conductivity of metallic (inorganic) inclusions. This configuration offers efficient performance and attractive usage of these materials for various applications

and many more [1–6]. To date, polymer components such as polyethylene, polypropylene, polyimide, and polystyrene blended with ceramics, carbon, and inorganic fillers including BaTiO_3 , MgO , Al_2O_3 , $\text{CaCu}_2\text{Ti}_4\text{O}_{12}$ shown to have synergistic effects from the high dielectric breakdown of polymers and large dielectric permittivity of the fillers. Additionally, various researchers have reported that the incorporation of metals into intrinsically conducting polymers (ICPs) has improved electron transfer via a direct or

2. Publication

J Mater Sci: Mater Electron (2023)34:594



Influence of sintering temperature on impedance and modulus spectroscopy of nickel-substituted cobalt ferrite

Simrandeep Kour¹, Hamnesh Mahajan¹, and Rupam Mukherjee^{1,*}

¹Department of Physics, Lovely Professional University, Phagwara 144411, Punjab, India

Received: 5 August 2022

Accepted: 2 February 2023

© The Author(s), under exclusive licence to Springer Science+Business Media, LLC, part of Springer Nature 2023

ABSTRACT

In this paper, the author reports the productive synthesis of spinel ferrite samples with composition $\text{Ni}_{0.5}\text{Co}_{0.5}\text{Fe}_2\text{O}_4$ using the sol-gel auto-combustion method. The crystal structure of inverse spinel ferrite was confirmed by X-ray Diffraction (XRD) for all the $\text{Ni}_{0.5}\text{Co}_{0.5}\text{Fe}_2\text{O}_4$ samples. Here, the crystallize size (D) and theoretical density (D_t) calculated are found to be inversely proportional to each other. Crystallize size (D) increases with increasing sintering temperature from 850 °C to 1150 °C. The X-ray Photoelectron Spectroscopy (XPS) confirms the presence of a single-phase of synthesized samples at the highest sintering temperature of 1150 °C. The change in morphology and the elemental composition of $\text{Ni}_{0.5}\text{Co}_{0.5}\text{Fe}_2\text{O}_4$ is confirmed by Field Emission Scanning Electron Microscope (FESEM) and Energy-Dispersive X-ray Analysis (EDAX), respectively. Additionally, Transmission Electron Microscopy (TEM) confirms the uniformity of cuboidal shape grains having an average grain size of about 84 nm for the $\text{Ni}_{0.5}\text{Co}_{0.5}\text{Fe}_2\text{O}_4$ sample at an optimized temperature of 1150 °C. Also, the Selective Area Electron Diffraction (SAED) pattern designates the regular distribution of bright spots, affirming the high degree of crystallinity and single-phase formation. Furthermore, Complex Impedance Spectroscopy (CIS) along with complex dielectric modulus studies reveal a relaxation phenomenon with non-Debye-type nature originating from grain boundaries. Frequency-dependent complex impedance and modulus studies exhibit space charge polarization effect with increasing sintering temperature. It is suggested that sintering the compound at the requisite temperature is the significant reason for the improved dielectric properties, which can be further useful for magnetodielectric materials, spintronic devices, sensors, and many more.

3. Publication


Indian J Phys

<https://doi.org/10.1007/s12648-021-02045-w>



ORIGINAL PAPER

Fractional exponents of electrical and thermal conductivity of vanadium intercalated layered 2H-NbS₂ bulk crystal

B Sharma¹, R Sharma¹, S Kour¹, M D Sharma¹, O Amin¹, A R Maity² and R Mukherjee^{1*} 

¹Department of Physics, School of Chemical Engineering and Physical Science, Lovely Professional University, Phagwara, Punjab 144001, India

²Amity Institute of Biotechnology, Amity University, Newtown, Kolkata 700135, India

Received: 11 April 2020 / Accepted: 18 February 2021

Abstract: Intercalation of transition metal dichalcogenides (TMDs) by 3d or 4d transition metal elements are of considerable interest as the intercalated atoms can finely tune the physical and chemical properties of host TMDs. On addition, these intercalation complexes show interesting magnetic property and displays anomalous transport behavior at the magnetic ordering temperature. Here, we have synthesized and measured transport properties of single crystal vanadium intercalated Niobium Di-sulphide. At 300 K, electrical resistivity and thermal conductivity of V_{0.3}NbS₂ is found to be $\sim 10^{-6} \Omega \text{ m}$ and $36 \text{ W m}^{-1} \text{ K}^{-1}$ respectively. Unlike phonon scattering, the spin scattering is found to affect both electrical and phonon conduction at low temperature. The electrical resistivity at temperature $T < 45 \text{ K}$ follows $T^{3/2}$ behavior, whereas the electronic part of thermal conductivity shows exponent of 0.8. Using steady-state method, the temperature dependent lattice part of thermal conductivity shows exponents of 0.5 and -0.5 at $T < 45 \text{ K}$ and $T > 45 \text{ K}$ respectively. Moreover, the peak of the total thermal conductivity also overlaps with the magnetic transition temperature, indicating the participation of spin dependent phonon dynamics below 45 K.

Keywords: Transport; Intercalation; Single crystal; Spin scattering; Lattice

1. Introduction

The layered transitional metal dichalcogenides (TMDC) have drawn a immense interest since the discovery of graphene [1–3]. Unlike graphene, the presence of band gap in Van der Waals layered materials have provided more opportunities for the development of scientific and tech-

structural stability of host material [13]. Over the past decade, 2D layered materials have proved to be the building blocks for constructing various electrical, opto-electronic, energy conversion and storage-based devices [14, 15]. Thermal and electrical properties in these thin devices needs a comprehensive understanding as the heat dissipation and device performance are coupled together.

4. Publication

J Mater Sci: Mater Electron

Structural, morphological, and electrochemical investigation of $\text{Mn}_{0.3}\text{Co}_{0.2}\text{Zn}_{0.5}\text{Fe}_2\text{O}_4$ -polyaniline nanocomposite for supercapacitor application

Hamnesh Mahajan¹, Shammi Kumar², Anjori Sharma¹, Ibrahim Mohammed¹, Manisha Thakur¹, Simrandeep Kour¹, Amarjeet Kaur³, and Ajeet Kumar Srivastava^{1,*}

¹ Department of Physics, Lovely Professional University, Phagwara, Punjab 144411, India

² Department of Physics, GCET, Chak Bhalwal, Jammu 181122, India

³ Central Instrumentation Facility, Lovely Professional University, Phagwara, Punjab 144411, India

Received: 1 June 2022

Accepted: 12 October 2022

© The Author(s), under exclusive licence to Springer Science+Business Media, LLC, part of Springer Nature 2022

ABSTRACT

The present research deals in preparing $\text{Mn}_{0.3}\text{Co}_{0.2}\text{Zn}_{0.5}\text{Fe}_2\text{O}_4$ (spinel ferrite) by sol-gel procedure, polyaniline (PANI) by chemical oxidative method, and $\text{Mn}_{0.3}\text{Co}_{0.2}\text{Zn}_{0.5}\text{Fe}_2\text{O}_4$ -PANI nanocomposite by physical blending method. X-ray diffraction (XRD) study affirms the formation of $\text{Mn}_{0.3}\text{Co}_{0.2}\text{Zn}_{0.5}\text{Fe}_2\text{O}_4$ -PANI nanocomposite owing to the appearance of two different types of peaks: sharp $\text{Mn}_{0.3}\text{Co}_{0.2}\text{Zn}_{0.5}\text{Fe}_2\text{O}_4$ peaks, and broader PANI peaks. Fourier transform infrared spectroscopy (FTIR) of $\text{Mn}_{0.3}\text{Co}_{0.2}\text{Zn}_{0.5}\text{Fe}_2\text{O}_4$ -PANI nanocomposite shows all characteristic vibrational bands, which are observed in the $\text{Mn}_{0.3}\text{Co}_{0.2}\text{Zn}_{0.5}\text{Fe}_2\text{O}_4$ and PANI spectra. Field emission scanning electron microscopy (FESEM) micrographs have been employed for measuring the average particle size by using ImageJ software. The encapsulation of the synthesized ferrite nanoparticle with the PANI matrix is exhibited by the FESEM micrograph of $\text{Mn}_{0.3}\text{Co}_{0.2}\text{Zn}_{0.5}\text{Fe}_2\text{O}_4$ -PANI nanocomposite. The electrochemical activity of the novel $\text{Mn}_{0.3}\text{Co}_{0.2}\text{Zn}_{0.5}\text{Fe}_2\text{O}_4$ -PANI nanocomposite is manifested to be higher as compared to their counterparts on account of synergistic impact, continual movement of electrons toward the electrode, and multiple redox reactions.

Publication proceedings in International Conferences

- Publication Proceeding 1

RAFAS-2021 IOP Publishing
Journal of Physics: Conference Series 2267 (2022) 012092 doi:10.1088/1742-6596/2267/1/012092

Effect of TiO₂ as Filler in NaCl: Possible Applications in Ionic Storage Systems

Simrandeep Kour and Rupam Mukherjee*

Department of Physics, School of Chemical Engineering and Physical Science, Lovely Professional University, Phagwara, Punjab-144411, India

*E-mail: rupam.23644@lpu.co.in

Abstract. High dielectric capacitors are increasingly used for energy storage in sustainable nanotechnologies. Here, we observed large enhancement of dielectric constant by 3 order at frequency 1kHz with moderate loss when TiO₂ is added as a filler in NaCl bulk matrix. The TiO₂ nanoparticles are synthesized via sol gel process and is subsequently added in varying weight percentage x in the ionic matrix of NaCl, which is represented as TiO_{2(x)}NaCl. The parameters like dielectric constant, dissipation Loss and ac conductivity are measured with varying fraction of TiO₂ in frequency range less than 25 KHz. The steady increase of dielectric constant with increasing filler content at low frequency indicates percolation type behavior which accounts for the first dielectric peak at $x=50$. The dielectric loss is found to be around 1 for $x < 45$ whereas it tends to increase with higher filler fraction. Moreover, the frequency dependent polarization in this composite system also accounts for hopping type behavior of mobile charge carriers contributed by TiO₂ as confirmed from ac conductivity measurement. Further, the samples are characterized by X-ray diffraction and Field emission scanning electron microscopy in order to study the structure and morphology of the samples. Overall, TiO₂ incorporation strongly improves the dielectric behavior of the ionic matrix at low frequency, making it suitable for super dielectric material (SDM).

Keywords: High dielectric capacitors, Ionic matrix, Percolation, Mobile charge carriers.

1. Introduction

Green technology is currently a rapidly growing field aiming to improve our surroundings by making us less dependent on non-renewable energy resources as they are furiously consumed in faster rate than ever [1-3]. Large volumetric capacitors are one such green device which is used in multitude of applications such as energy storage and renewable energy source. Earlier, it had been widely observed that storage devices like Memory chips which uses just a single capacitor to represent 1 or 0 illustrates unsustainable approach for the green technology. Since, millions of capacitors tend to occupy at least a few tenths of a square μm of the total area, the situation has been alarming considering the growing demand of miniature devices in form of ICs (Integrated circuits). This has left us with no other alternative rather by putting billions of transistors on 1mm*1mm chip responsible for the functioning of nearly all modern devices from an automobile to supercomputers. Given the above, storage devices with efficient storage and low power consumption and losses should be considered.

Capacitors being one of them, with large volumetric capacitance or High-k dielectric materials can be a prominent as well as effective way out. Capacitors on other hand can prove detrimental to the whole gadget if the size is shrunked below a limiting thickness. On reducing the thickness, capacitor either

- Publication Proceeding 2

ECS Transactions, 107 (1) 19791-19801 (2022)
10.1149/10701.19791ecst ©The Electrochemical Society

Synthesis of $\text{Ni}_{0.5}\text{Co}_{0.5}\text{Fe}_2\text{O}_4$ Ferrite and Effect of Annealing Temperature on the Structural, Morphological and Dielectric Analysis

Simrandeep Kour^a, Nitish Kumar^b, Rupam Mukherjee^{a*}

^a Department of Physics, Lovely Professional University, Punjab-144411, India

^b Department of Physics, Indian Institute of Technology, Jammu-181221, India

* Email: rupam.23644@lpu.co.in

In the current work, we have synthesized nickel substituted cobalt ferrite nanoparticles using Pechini's method. The presence of single-phase synthesized nanoparticle is confirmed at annealing temperature around 1000 °C and the crystallinity nature further improves at 1150 °C. The average crystallite size is found to increase with increasing annealing temperature. The strain in the crystalline particles also found to decrease with increasing temperature as confirmed through XRD analysis. The cuboidal morphology with considerable size is observed in nanoparticles by FESEM images. The EDAX spectrum further confirms the presence of pure single phase of desired elements in grown nanoparticles. The dielectric properties were studied using impedance spectroscopy, recorded from 100 Hz to 1 MHz at room temperature for different annealed temperatures. The change in the frequency dependent dielectric properties with increasing annealing temperature are in accordance with the Maxwell-Wagner two layers model for space charge theory and correlated barrier hopping (CBH) model.

Introduction

Over the past few decades, research on the synthesis and characterization of nanosized ferrites have increased, and a wide range of new technological applications for these materials have been identified. The ability to tailor ferrites' structural, chemical, optical, magnetic, and electrical properties by selecting the synthesis parameter carefully have enhanced their widespread potential technological applications (1-3). Ferrites have specialized characteristics like low electrical resistivity, high dielectric losses, etc., and variation at low to high frequencies creates distinguished industrial employment with advanced technology. The nano-ferrites being confined to microwave device applications (phase shifters, circulators, isolators) due to their considerable low electrical conductivity

1. Conference 1

 <p>LOVELY PROFESSIONAL UNIVERSITY <i>Transforming Education Transforming India</i></p>	Certificate No. <u>225303</u>		
			
<h3>Certificate of Participation</h3>			
<p>This is to certify that <u>Ms. Simrandeep Kour</u> of <u>Lovely Professional University Phagwara Punjab</u> has given oral presentation on <u>Effect of TiO₂ as filler in NaCl: Possible applications in Ionic storage systems</u> in the International Conference on "Recent Advances in Fundamental and Applied Sciences" (RAFAS 2021) held on June 25-26, 2021, organized by School of Chemical Engineering and Physical Sciences, Lovely Faculty of Technology and Sciences, Lovely Professional University, Punjab.</p>			
<p>Date of Issue : 15-07-2021 Place of Issue: Phagwara (India)</p>	 <p>Prepared by (Administrative Officer-Records)</p>	 <p>Organizing Secretary (RAFAS 2021)</p>	 <p>Convener (RAFAS 2021)</p>

2. Conference 2

**INTERNATIONAL CONFERENCE ON TECHNOLOGIES FOR
SMART GREEN CONNECTED SOCIETIES 2021
NOVEMBER 29-30, 2021 | ONLINE | WORLDWIDE**

SIMRANDEEP KOUR

LOVELY PROFESSIONAL UNIVERSITY, PHAGWARA, PUNJAB-144411, INDIA

Presented a paper titled **Synthesis of Ni_{0.5}Co_{0.5}Fe₂O₄ Ferrite and Effect of Annealing Temperature on the Structural, Morphological and Dielectric Analysis.**
at the ICTSGS-1 conference led by Yamagata University Japan.

ICTSGS-1 IS ORGANIZED BY SPAST FOUNDATION AND ASSOCIATED PARTNER INSTITUTIONS.



SPAST FOUNDATION

Hidemitsu Furukawa,
YAMAGATA UNIVERSITY, JAPAN



Ajit Khosla,
YAMAGATA UNIVERSITY, JAPAN



3. Award in Conference 2

First International Conference on Technologies for Smart Green Connected Society 2021
November 29-30, 2021 | Online | Worldwide

ACS Best Oral and Poster Presentation Certificate

Simrandeep Kaur
LPU, India

Paper Title: Synthesis of $\text{Ni}_{0.5}\text{Co}_{0.5}\text{Fe}_2\text{O}_4$ ferrite and effect of annealing temperature on the structural, morphological and dielectric analysis.

Sponsored Award

 **ACS Publications**
Most Trusted. Most Cited. Most Read.

 **The Electrochemical Society**
Advancing solid state & electrochemical science & technology


Sustainability Begins Here
SPAST FOUNDATION

Conference Secretariat

Reference number: ICTSGS/21/16



ICTSGS-1